Molecular Simulation Applied to Formic Acid Production

PROEFSCHRIFT

ter verkrijging van de graad van doctor aan de Technische Universiteit Eindhoven, op gezag van de rector magnificus prof.dr. S.K. Lenaerts, voor een commissie aangewezen door het College voor Promoties, in het openbaar te verdedigen op maandag 28 oktober 2024 om 13:30 uur

door

Dominika Oliwia Wasik

geboren te Wrocław, Polen

Dit proefschrift is goedgekeurd door de promotoren en de samenstelling van de promotiecommissie is als volgt:

Voorzitter:	prof.dr. F. Toschi
1^e promotor:	prof.dr. S. Calero
2^e promotor:	prof.dr.ir. T.J.H. Vlugt (Technische Universiteit Delft)
Leden:	prof.dr. P.A. Bobbert
	prof.dr.ir. B. Kuchta (Politechnika Wrocławska)
	prof.dr. K. Hooman (Technische Universiteit Delft)
	dr. D. Dubbeldam (Universiteit van Amsterdam)

Het onderzoek dat in dit proefschrift wordt beschreven is uitgevoerd in overeenstemming met de TU/e Gedragscode Wetenschapsbeoefening.

ORCID iD: 0000-0002-9903-941X

The work presented in this thesis has been supported by the Eindhoven Institute for Renewable Energy Systems (EIRES). The research was conducted in the Materials Simulation & Modelling (MSM) group, Department of Applied Physics and Science Education, Eindhoven University of Technology, The Netherlands.

A catalogue record is available from the Eindhoven University of Technology Library ISBN: 978-90-386-6158-2

Printing: ADC DEREUMAUX

Contents

Chapter 1

Introduction

Growing concern about the increase of carbon dioxide emissions and their impact on climate change has raised significant interest in developing economically viable technologies for carbon dioxide reduction [1–4]. Among various strategies, converting carbon dioxide into valuable chemicals such as formic acid has garnered attention due to its wide range of applications in industries ranging from pharmaceuticals to fuel cells [5–11]. One of the possible routes for carbon dioxide conversion is the electrochemical reduction to formic acid in aqueous solutions [12–15], which is not optimal due to the low solubility of this gas [16]. It is crucial to investigate the possibilities of improving the solubility of carbon dioxide and thus the efficiency of its conversion without decreasing the ionic conductivity of an electrolyte solution that leads to a pH drop due to higher carbon dioxide dissolution favoring the hydrogen evolution reaction (HER) [17]. Another method for formic acid production is the carbon dioxide hydrogenation reaction in which a catalyst is needed to mediate the reduction [18]. The cost of transition metal catalysts and the toxicity of the transition elements are two major limitations in their usage [19]. This thesis explores advanced methods for formic acid production through molecular simulation studies. The possibilities of improving both the electrochemical reduction of carbon dioxide to formic acid in an aqueous solution and the carbon dioxide hydrogenation reaction are investigated and alternative approaches are proposed.

1.1 — Reduction of Carbon Emissions

Reducing greenhouse gas emissions has become an urgent priority, as mandated by the European Climate Law, which requires the European Union to achieve climate neutrality by 2050 [20]. Between 2019 and 2023, global energy-related carbon dioxide emissions increased by approximately 4.2 billion tonnes (Gt) from 33.2 Gt [21] to 37.4 Gt [22]. The implementation of clean energy technologies prevented the carbon dioxide emissions from energy combustion

from increasing threefold [22]. In the Netherlands, the central objective of the government's National Climate Agreement [23] is to reduce greenhouse gas emissions by 49% compared to 1990 levels. On a European scale, the government is pushing for a 55% reduction in greenhouse gas emissions by 2030, and several initiatives are underway in the Netherlands to achieve these carbon dioxide reduction targets [23]. In the built environment of the Netherlands, efforts are focused on enhancing the energy efficiency of 1.5 million homes and reducing carbon dioxide emissions by an additional 1 Mt for utility buildings to achieve the goal of reducing total emissions by 3.4 Mt by 2030 [23]. New buildings will no longer be heated with natural gas, and existing buildings are being upgraded to enable fossil-free heating. Municipalities are spearheading local, participative approaches to achieve emission-free housing, neighborhood by neighborhood. In the traffic and transport sector, the goal is for all new passenger cars to be emission-free by 2035 [24]. This initiative is supported by various taxation measures to incentivize electric vehicles. Encouraging a shift from cars to bicycles and public transport, along with smart solutions for more efficient and sustainable logistics are also key components of this strategy [23]. In the electricity sector, coal-fired electricity generation is expected to be phased out by 2025/2030 [23]. Offshore wind power is being accelerated, along with the growth of onshore wind and solar energy. Subsidies for additional renewable energy capacity are in place until 2025, aiming for an estimated 70% renewable share in electricity production by 2030 [23]. Agriculture and land use are also important areas for emission reduction. Initiatives include sustainable heating in greenhouse horticulture, reducing methane emissions from livestock through improved manure processing, and carbon storage in soil and vegetation through pilot programs for climate-friendly land use [23].

The industrial sector is set to introduce a targeted carbon levy, starting at €30 per tonne in 2021 and rising to €125-150 per tonne by 2030, which includes the Emissions Trading System (ETS) price for every tonne emitted beyond a fixed reduction path [20]. The Renewable Energy Grant Scheme (SDE) and other carbon dioxide-reducing options, such as carbon capture, utilization, and storage (CC(U)S), are being implemented [23]. Funding is also directed towards innovation in hydrogen and other sustainable fuels [23]. Advancing sustainable energy technologies that significantly decrease emissions remains a crucial area for future research. One economically attractive method to reduce carbon dioxide emissions is capturing it at the source of production and converting into valuable chemicals such as formic acid, salicylic acid, methanol, urea, propylene, and polyols [1–4]. The focus of this work is to propose advancements in methods for the conversion of carbon dioxide to formic acid,

primarily because formic acid has significant industrial applications, a higher market value, and a relatively simpler conversion process compared to other products [4, 25, 26].

1.2 — Formic Acid Production

Formic acid, also known as methanoic acid (HCOOH, FA), is a colorless and corrosive liquid with a sharp, pungent odor [8]. A schematic representation of the molecule model is shown in Figure 1.1. It is the strongest unsubstituted alkyl carboxylic acid, with a pKa of 3.745 [27]. The acid is fully miscible with water and many polar solvents, but it only partially mixes with hydrocarbons [8]. In the vapor phase, formic acid molecules tend to dimerize, resulting in non-ideal gas behavior, with about 95% of the vapor existing in dimerized form at room temperature and normal pressure [8]. While formic acid remains stable at room temperature, it exhibits thermal instability, leading to decomposition [28].

Formic acid has a variety of industrial applications, see Figure 1.2. It is predominantly used in the animal feed industry and grass silage (27%), where it is used for ensiling difficult-to-ensile materials, limiting fermentation when ensiling crimped high-moisture grain, and as a preservative and antibacterial agent, helping to improve the storage and quality of feed and silage [8]. In leather tanning (22%), formic acid is used as a leveling agent that facilitates the movement of dye across the leather surface, ensuring a more consistent and even distribution for a smoother appearance [8]. In the pharmaceuticals and food chemicals industry (14%), it acts as an intermediate in the synthesis of various drugs including insulin, caffeine, aspartame, or vitamin B1, and as a preservative in food products [8, 29]. It is also used for Salmonella decontamination [8]. In textiles (9%), formic acid is used to adjust pH in dyeing wool, nylon, and other natural and synthetic fibers with acid and chrome dyes, neutralize alkaline solutions and aid in rinsing during laundering processes [8]. In the natural rubber industry (7%), it is used for coagulating latex, which is essential in rubber production [8]. In drilling fluids (4%), formic acid functions as a component of drilling muds, which are used in oil and gas extraction to cool and lubricate drilling equipment and to carry cuttings to the surface [30]. The remaining 17% is utilized in other miscellaneous applications, such as in cleaning products, electroplating, and as a reducing agent in various chemical processes [8, 31]. In the chemical industry, formic acid is a primary product with a production capacity of 800,000 tons per year as of 2017 [18, 32]. The formic acid global market value is forecast to increase from 1.8 billion dollars in 2023 to 2.8 billion dollars by 2033 [33]. The current main method of

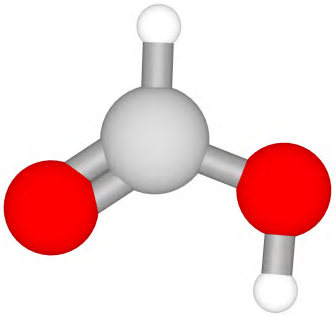

Fig. 1.1. Schematic representation of the formic acid model visualized using iRASPA [38], where red atoms represent oxygen, grey atoms represent carbon, and white atoms represent hydrogen.

producing formic acid is through methanol carbonylation, which generates a formate ester that is hydrolyzed to formic acid [8, 34–36]. This process, which became economically viable in the 1970s, was the basis for around 81% of the world's formic acid production capacity in 2014 [8]. Major producers using this method include BASF in Germany and Kemira in Finland, as well as Chinese companies like Feicheng Acid Chemicals and Luxi Chemical Group [8]. Another method involves producing formic acid from its salts, primarily sodium formate and calcium formate, through acidolysis with sulfuric or phosphoric acid [8]. Although the market share of this method has decreased, it is still practiced by companies like Perstorp in Sweden and some smaller producers in China, accounting for 19% of production capacity in 2014 [8]. Historically, formic acid was also a byproduct of acetic acid production from the liquid-phase oxidation of butane or naphtha, but this process has largely been replaced by methanol carbonylation, which does not produce formic acid [37]. The hydrolysis of formamide was another significant production method until the 1970s, but it became economically less viable due to the consumption of ammonia and sulfuric acid and the byproduct ammonium sulfate [8].

Several electrochemical methods for producing formic acid or formate salts from carbon dioxide are currently under development [14]. Significant advancements in catalyst systems and electrode designs in recent years have led to substantially higher formic acid production yields [8]. Within the scope of this thesis, two methods for producing formic acid are examined. The first method is an electrochemical reduction of carbon dioxide in aqueous electrolyte solutions. This method uses renewable electricity to convert carbon dioxide into formic acid aiding carbon capture and utilization [39, 40]. While obtained

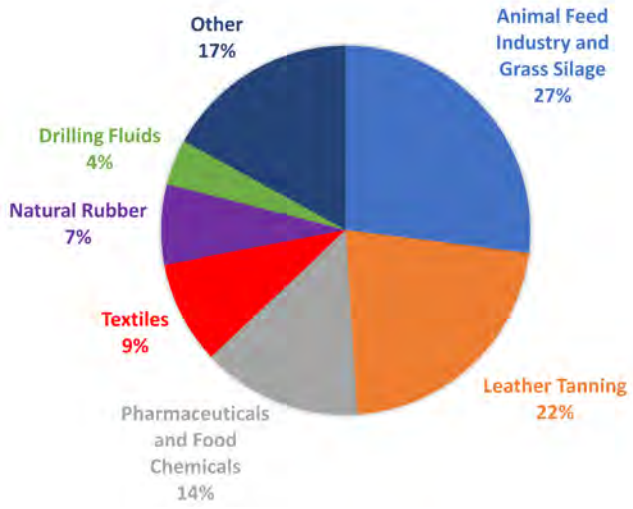

Fig. 1.2. Distribution of formic acid application across various industries in 2021 [8, 31]. Formic acid is predominantly used in the animal feed industry and grass silage (27%), leather tanning (22%), pharmaceuticals and food chemicals (14%), textiles (9%), natural rubber (7%), drilling fluids (4%), and other miscellaneous applications (17%).

formic acid is a useful carrier for hydrogen and carbon monoxide contributing to energy storage [41], this process faces challenges in competing with traditional fossil-fuel-based methods, such as complexity of mixtures, dilute products, high pH solutions favoring the formation of formate, and high-cost downstream processing [17, 42, 43]. The second method is carbon dioxide hydrogenation to formic acid [18] in the confinement of metal-organic frameworks. The effects of confinement affect reaction equilibrium by Le Chatelier's principle [44] enhancing the yield of formic acid, and potentially offering a less toxic and less expensive alternative or addition to conventional transition metal catalysts [19].

1.2.1 – Electrochemical Reduction of Carbon Dioxide

The electrochemical reduction of carbon dioxide in aqueous electrolyte solutions is a promising method for producing formic acid and formate salts [12–15]. This process is less resource-intensive than traditional methods such as methanol carbonylation and utilizes carbon dioxide, a widely available resource while avoiding the production of intermediates [12–15]. Carbon dioxide is reduced at the cathode in an electrolyzer, while the oxygen evolution reaction

occurs at the anode. At low pH, the competing cathodic hydrogen evolution reaction (HER) dominates over the carbon dioxide reduction, decreasing the efficiency and selectivity of formic acid production [12]. Additionally, tin-based electrodes commonly used for carbon dioxide reduction can be affected by degradation/deactivation through the formation of alkali metals under solution acidification [17, 45, 46]. Suppressing the HER by performing the reduction of carbon dioxide in alkaline media leads to improved selectivity towards the production of formate and hydroxide ions [17]:

$$CO_2 + H_2O + 2e^- \rightarrow HCOO^- + OH^- \tag{1.1}$$

The product can be formic acid or formate depending on the pH [12]. The molecular form of formic acid and its ionic formate form exhibit slight differences, yet their dissociation state significantly influences the choice of downstream separation processes [17]. Ramdin et al. [17] conducted an economic analysis on methods for processing formic acid and formate, demonstrating the higher value of formic acid as a product compared to formate. Converting formate solutions into formic acid incurs significant costs due to the necessary separation, concentration, and acidification processes [17]. Although electrochemical reduction of carbon dioxide is traditionally performed in alkaline solutions, which favors formate production, market demands for formic acid have driven research towards acidic conditions with pH-neutral electrolytes like sodium chloride, which become slightly acidic upon carbon dioxide dissolution [17]. Additionally, it has been observed that at high pH levels, the electrode materials can be affected by degradation/dissolution under cathodic polarization, which can compromise the stability and efficiency of the process [46]. However, challenges such as trade-offs between increasing carbon dioxide solubility without compromising ionic conductivity remain, highlighting the necessity for further investigation. High-pressure carbon dioxide and gas diffusion electrodes have been explored to improve yield, but the problems of fouling and crystallization persist [16, 47–49]. Research has shown that adding salts can affect carbon dioxide solubility, with studies focusing on pure water solutions [50–53]. Economic evaluations using potassium hydroxide and potassium sulfate as electrolytes indicate the need for optimized process designs to enhance carbon dioxide solubility and conversion efficiency [17].

1.2.2 – Carbon Dioxide Hydrogenation

The hydrogenation of carbon dioxide into formic acid is a challenging process due to the high kinetic and thermodynamic stability of carbon dioxide [18]. The reaction can be represented as:

$$CO_2 + H_2 \rightleftarrows HCOOH \tag{1.2}$$

Ghara et al. [19] calculated the free energy change for carbon dioxide hydrogenation to formic acid to be ca. 42 kJ mol^{-1}. Additionally, the free energy barrier for carbon dioxide hydrogenation in the gas phase was determined as ca. 351 kJ mol^{-1} [19]. Due to the high free energy barrier of carbon dioxide hydrogenation, the use of a catalyst is needed [19]. Over the past few decades, various transition metal-based catalysts have been developed for carbon dioxide hydrogenation, including catalysts with phosphine ligands [54–58], pincer ligands [59–61], N-heterocyclic carbene ligands [62–64], and half-sandwich catalysts with or without proton-responsive ligands [65–69]. However, the cost and toxicity of transition metal catalysts are significant limitations [19], needing further research to improve carbon dioxide hydrogenation efficiency while reducing costs and toxicity.

An alternative or supplement to transition metal catalysts is the use of porous materials such as metal-organic frameworks, which can shift the thermodynamic equilibrium of the reaction. The confinement effects in porous materials can affect reaction equilibrium via several mechanisms: (a) the higher density of the pore phase compared to the bulk phase, which increases the yield for reactions where the total number of moles decreases, according to Le Chatelier's principle [44]; (b) the molecular orientation of reactants and reaction products influenced by the vicinity of the neighboring pore walls; and (c) the selective adsorption of favored components on solid surfaces [70]. The interactions between the framework and adsorbates can favor the formation of certain components. The separation of favored components from the mixture promotes their increased formation by Le Chatelier's principle [44]. To reach favorable thermodynamic equilibrium in MOFs, a low free energy barrier for the reaction is still essential. Therefore, either the simultaneous use of MOFs with catalysts to enhance formic acid formation is necessary, or future research should focus on improving the catalytic effects of MOFs to potentially eliminate the need for transitional metal catalysts.

1.3 — Metal-Organic Frameworks

Metal-organic frameworks (MOFs) are extended one, two, or three-dimensional porous structures composed of transition metal ions, linked together by rigid rod-like organic linkers [71, 72]. These structures are prepared as crystalline solids through the solution reaction of metal ion salts with organic bridges [73]. The exploration of these novel materials began with Tomic in 1965, who investigated MOFs as thermally stable coordination polymers [74]. Later, Yaghi and his coworkers significantly advanced the field by designing and synthesizing an exceptionally stable and highly porous MOF called MOF-5 [75].

The most important advantages of MOFs are relatively good stability, porosity, organic functionality, and tunable properties. The ability to control the pore structure makes functionalized MOFs more attractive microporous materials than zeolites and microporous carbons [76–78]. This flexibility in modifying physicochemical properties has led to the design of approximately 100,000 MOF structures, constituting about 8% entries of the Cambridge Structural Database, which contains over 1 million structures in total [79]. The primary objective of developing new MOF structures is to explore their applications in various fields, including gas storage [80, 81], separation [82, 83], catalysis [84, 85], drug delivery [86, 87], enzyme immobilization [88, 89], sensing [90, 91], and water sustainability [92]. The potential advantages of MOF-based catalysts include easier separation and recycling of the catalyst, reduced costs due to metal-free catalytic sites, high thermal stability, the combination of carbon dioxide capture and conversion steps, pore-confinement effects, and mild conditions for carbon dioxide reduction due to low reaction barriers [93]. The metal-organic frameworks investigated in this thesis are UiO-66, IRMOF-1, Cu-BTC, and M-MOF-74 (M = Ni, Cu, Co, Fe, Mn, Zn), see Figure 1.3. The metal-organic frameworks UiO-66, IRMOF-1, and Cu-BTC were chosen for their varying pore sizes, which enable the assessment of confinement impact on the carbon dioxide hydrogenation reaction. The M-MOF-74 series, due to its isostructural nature and open metal centers, allows for the evaluation of the effects of different types of metal cations on carbon dioxide hydrogenation independently of pore size.

UiO-66

UiO-66 consists of hexa-nuclear $Zr_6O_4(OH)_4$ inorganic nodes which form lattices by 1,4-benzene-dicarboxylate linker [96]. This MOF is notable for its high surface area, porosity, and the catalytic properties of its zirconium oxide node. It also shows superior stability in mechanical, thermal, acidic, aqueous, and water vapor environments, and can be synthesized easily on a laboratory scale [96]. The inorganic center contains polar hydroxy groups, contributing to the exceptional stability of UiO-66, particularly its ability to undergo reversible changes between its hydroxylated and dehydroxylated forms without altering the linked carboxylate ligands [97]. This stability is likely due to narrow pores and sterically hindered metal carboxylate sites, which reduce accessibility to water [98]. Unlike structures with open-metal sites, the fully saturated metal centers cannot coordinate with other molecules. UiO-66 is known for containing a significant number of defects in the form of missing linkers, which can considerably affect its adsorption properties [99]. Nevertheless, it has been determined to be an effective adsorbent for both carbon dioxide and hydro-

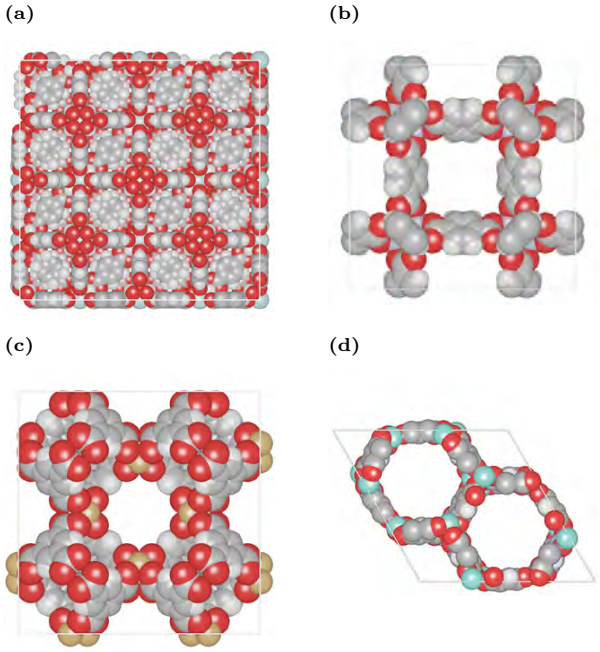

Fig. 1.3. Schematic representation of several MOFs visualized using iRASPA [38]: (a) UiO-66, (b) IRMOF-1, (c) Cu-BTC, and (d) M-MOF-74. The pore distributions and the void fractions of the structures were computed using the RASPA software package [94, 95]. UiO-66 has two types of micropores with diameters of 3.5 Å and 7 Å, and the void fraction of 0.507. IRMOF-1 contains larger micropores with diameters of 11 Å and 15 Å, with the void fraction of 0.815. Cu-BTC is characterized by micropores with diameters of 5 Å, 11 Å, and 13 Å, and the void fraction of 0.746. The M-MOF-74 series has micropores with a diameter of 11 Å, and the void fractions of ca. 0.7.

gen, demonstrating significant adsorption capacity under high-pressure and low-temperature conditions for hydrogen (4.2 wt% at 60 bar, 77 K) [100], and notable efficiency for carbon dioxide adsorption at moderate pressures and temperatures (35.6 wt% at 9.8 bar and 273 K) [101].

IRMOF-1

IRMOF-1 belongs to an isoreticular class of MOFs with a cubic topology. First reported in 1999, IRMOF-1 forms a network consisting of Zn_4O units joined by linear 1,4-benzenedicarboxylate links [102]. Despite not containing open-metal sites, IRMOF-1 is highly water unstable, similar to other structures with Zn as a central atom, which limits its potential applications [103].

IRMOF-1 is one of the most widely studied MOFs in scientific literature due to its well-defined structure and potential in gas storage applications, especially for hydrogen [80, 104–108].

Cu-BTC

Cu-BTC, also known as MOF-199 and HKUST-1, was first reported by Chui et al. [109] in 1999. Cu-BTC consists of metal coordination polymers where copper ions act as nodes and benzene-1,3,5-tricarboxylate (BTC) ligands act as linkers, forming a porous crystalline structure. Each copper ion is typically bound to four BTC ligands, with each ligand contributing through two oxygen atoms. Additionally, each copper ion may coordinate with solvent molecules, usually water, through two additional oxygen atoms. When Cu-BTC is activated, solvent molecules are removed, making two copper ions with unsaturated sites available for binding. The open-metal sites exhibit a strong affinity and selectivity for electron-donating adsorbates, such as water [103]. The strongest carbon dioxide adsorption was found to occur around the open-metal centers, reaching up to 40% of the total uptake for Cu-BTC at low pressures (0.1 MPa) [110]. Cu-BTC shows relatively good thermal stability and reversible adsorption-desorption properties without damage to the crystal structure [103]. It is commercially sold as Basolite C300 and is a frequently studied MOF, noted for its open-metal sites, high surface area, and pore volume [111, 112].

M-MOF-74

The M-MOF-74 series (CPO-27-M), where M = Ni, Cu, Co, Fe, Mn, Mg, or Zn [113–122], is a well-known family of metal-organic frameworks. These frameworks are synthesized through a reaction between M^{2+} ions and 2,5-dioxido-1,4-benzenedicarboxylate ($dobdc^{4-}$) ligands, resulting in a structure with hexagonal channels. The metal ions act as favored adsorption sites, accessible for the molecules through cylindrical pores. Despite the large pores (ca. 11 Å) [122], the density of metal cations remains high due to the negative charge of the $dobdc^{4-}$ ligand. The abundant open-metal sites in M-MOF-74 enhance selectivity [123] and the surface packing density of adsorbates [124], while also offering reactive sites for chemical reactions such as oxygenation [125] and size-selective Lewis acid catalysis [126]. M-MOF-74 structures exhibit low water stability, with degradation occurring upon exposure to even minimal moisture [98].

1.4 — Scope of the Thesis

This thesis addresses the challenges of formic acid production using two methods: (1) the electrochemical reduction of carbon dioxide in an aqueous electrolyte solution, and (2) the hydrogenation of carbon dioxide to formic acid. The perspectives of both methods are examined and the alternative approaches are proposed. Given the complex behavior of formic acid mixtures and the lack of experimental data, classical force field-based molecular simulations are used to determine thermodynamic properties. The electrochemical reduction of carbon dioxide is studied by Monte Carlo simulations in search of chemicals that enhance the carbon dioxide solubility in aqueous electrolyte solutions and thus the efficiency of the carbon dioxide conversion without decreasing the ionic conductivity of an electrolyte solution. Molecular simulations also allow for the exploration of confinement effects independently from catalytic effects. To assess the impact of different pore sizes and types of metal centers on formic acid production, the thermodynamic confinement effects of the metal-organic frameworks on the carbon dioxide hydrogenation reaction equilibrium are studied by Monte Carlo simulations. The microscopic mechanisms governing adsorption processes are comprehensively addressed, including molecular configurations within porous materials, using energy optimization techniques.

This thesis is structured as follows. The introduction to the field of formic acid production in this chapter is followed by Chapter 2, where the applied methodology is summarized and the concepts related to Monte Carlo simulations are explained. The conventional and expanded ensembles are provided together with the corresponding partition functions. The functional form of the force field is described and the molecular properties computed in this work are listed. In Chapter 3, the dependence of the carbon dioxide solubility in aqueous formic acid solutions on the composition and the electrolyte concentration is studied for a higher yield of formic acid from the electrochemical reduction of carbon dioxide. The formic acid force field used in all remaining chapters of this thesis is selected and validated through simulations of vapor-liquid equilibrium, vapor pressures, and the densities of $HCOOH/H_2O$ systems. The dependence of the Henry coefficient of carbon dioxide on the mole fraction of formic acid and the sodium chloride concentration in the mixture is determined. The solubility of carbon dioxide is found to decrease with increasing sodium chloride concentration in the solution but increase with formic acid concentration. In Chapter 4, the effect of UiO-66 confinement on the carbon dioxide hydrogenation reaction equilibrium is studied to investigate the performance of MOFs as an alternative for transition metal catalysts. The results are compared with the confinement effects resulting

from Cu-BTC and IRMOF-1 to assess the impact of different pore sizes and metal centers on the carbon dioxide hydrogenation reaction. It is observed that the MOF confinement increases the equilibrium concentration of formic acid, due to the higher density of the pore phase compared to the gas phase by Le Chatelier's principle and the selective adsorption of formic acid as the preferred component. By comparing the performance of MOFs with different pore size distributions and metal centers, it is shown that the type of metal center in the metal-organic framework plays a crucial role in formic acid production yield. The most significant enhancement in formic acid production by ca. 2000 times higher compared to the gas phase is achieved using Cu-BTC at 298.15 K and 60 bar. In Chapter 5, a non-polarizable carbon dioxide and hydrogen force field for adsorption in M-MOF-74 (M = Ni, Cu, Co, Fe, Mn, Zn) is proposed by scaling the Coulombic interactions of M-MOF-74 atoms and Lennard-Jones interaction potentials between the center of mass of hydrogen molecules and the open-metal centers. The force field is validated by reproducing experimental adsorption data of carbon dioxide and hydrogen, such as isotherms, enthalpies of adsorption, and binding geometries. The adsorption of CO_2/H_2 mixtures in M-MOF-74 is studied, and breakthrough curves, which represent the concentration of the adsorbate in the fluid phase at the exit of a fixed bed adsorber as a function of time, are generated to analyze the performance of CO_2/H_2 mixture separation. The non-polarizable force field can describe the adsorption behavior in computational studies of the capture, and separation processes, and allow the simulation of the carbon dioxide hydrogenation reaction to formic acid in confinement for a better understanding of the effect of open-metal centers. In Chapter 6, the effect of the type of metal center in M-MOF-74 (M = Ni, Cu, Co, Fe, Mn, Zn) on the carbon dioxide hydrogenation reaction to formic acid is investigated. The compatibility of the non-polarizable force field for carbon dioxide and hydrogen adsorption in M-MOF-74 with the formic acid force field is evaluated by the simulation of formic acid binding geometries. The single-component adsorption isotherms of formic acid and the adsorption isobars of the carbon dioxide hydrogenation components are computed. Depending on the metal center, the enhancement in formic acid production decreases in the same order as its uptake and isosteric heat of adsorption: Ni > Co > Fe > Mn > Zn > Cu. The most significant influence on the carbon dioxide hydrogenation thermodynamics, enhancing formic acid production by ca. 10^5 times higher compared to the gas phase is achieved using Ni-MOF-74 at 298.15 K, 60 bar. In Chapter 7, a multi-scale methodology is introduced to investigate the thermodynamics of formic acid dimerization to explore its potential as a reactive fluid in thermodynamic cycles. This methodology combines force field-based Monte

Carlo simulations, quantum mechanics, and equations of state. The umbrella sampling is implemented in Monte Carlo simulations, and two computational methods are used to compute the reaction equilibrium constants, and subsequently enthalpy and entropy of dimerization: dimer counter and potential of mean force. Both methods demonstrated strong agreement, resulting in the enthalpy of dimerization of -60.46 kJ mol^{-1} and -62.91 kJ mol^{-1} for the dimer counter and PMF methods, respectively, with the quantum mechanics calculations yielding an enthalpy of -60.48 kJ mol^{-1}. The cubic Peng-Robinson equation of state coupled with advanced mixing rules is applied to determine thermodynamic phase equilibrium properties. This includes the Global Phase Equilibrium of the system, vaporization enthalpy, phase composition, vapor and liquid densities of the coexisting phases as a function of temperature, and entropy as a function of temperature. Comparisons with Monte Carlo simulations in the Gibbs ensemble indicate that the simulations align well with the thermodynamic model, proving the accuracy of the presented methodology. Chapter 8 provides the conclusions and outlook of the work presented in this thesis.

Chapter 2

Methodology

This chapter provides an overview of the methodology applied in this thesis, summarizing the theoretical foundations of key concepts related to molecular simulation. Detailed explanations of all specific calculation methods are provided in each relevant chapter of the thesis. The Monte Carlo method was used as the main technique to compute thermodynamic properties of bulk and confined systems, using classical force fields to model atomic interactions. When considering classical versus quantum mechanics, methods like Monte Carlo with classical force fields are advantageous for studying large-scale systems due to their computational efficiency and ability to capture collective behaviors and thermodynamic properties [127, 128]. Quantum mechanics offers a more accurate description of atomic-level interactions but at a significantly higher computational cost, often reserved for smaller systems or specific quantum effects beyond classical modelling capabilities [127]. Thus, this thesis focuses on classical methods suited for the scale and scope of the simulations conducted.

2.1 — Monte Carlo Method

Molecular simulation is an efficient tool for understanding and predicting the properties of systems [128, 129]. Computational techniques offer significant advantages over experimental methods by providing a detailed microscopic perspective that is challenging or even impossible to achieve experimentally [128, 129]. Molecular simulation enables the testing of theories and validation of molecular models, as well as serves as an alternative approach in cases involving challenging conditions, hazardous materials, or lack of experimental synthesis of the materials/molecules. Two primary branches of force field-based molecular simulation exist: Molecular Dynamics and Monte Carlo simulations [128, 129]. In Molecular Dynamics simulations, Newton's equations of motion are numerically integrated to generate a representative trajectory of the system over time [128]. Monte Carlo is a numerical stochastic tech-

nique that uses random numbers and probability theory to solve problems with probabilistic interpretations by computing phase space averages instead of time averages [128]. Monte Carlo simulations involve the dimensions of energy, length, and temperature, but not mass and time. This method is applied to calculate the thermodynamic properties of a system, enabling accurate evaluation of complex and costly processes [128]. Statistical Mechanics is essential for relating molecular simulations with real-world systems by connecting a collection of interacting molecules to the macroscopic properties of materials [127, 130, 131]. While molecular simulations can compute various quantities, not all of these quantities correspond directly to experimentally measurable properties. Properties, such as temperature, pressure, volume, and energy can be measured experimentally. The relation between microscopic and macroscopic properties is established using Statistical Mechanics, which applies probability theory to study the thermodynamic behavior of systems composed of a large number of particles [127, 130, 131]. The simulation data can be translated into macroscopic properties, effectively linking theoretical models with observable experimental data and bridging classical mechanics and thermodynamics. In statistical mechanics, many different configurations of a system (microstates) are compatible with a macrostate, constituting an ensemble. In an isolated system at thermodynamic equilibrium, each microstate with the same total energy can be found with equal probability. The probability density function for a classical system is:

$$\wp(p^N, r^N) = \delta(H(p^N, r^N) - E) \tag{2.1}$$

where r^N denotes the x, y, z coordinates of the N atoms in the system, and p^N denotes the corresponding momenta, H is the Hamiltonian function of the total energy of the system in the microstate (p^N, r^N), E is the total energy of the system, and $\delta(x)$ is the Dirac delta function. To calculate the macroscopic property of non-isolated systems, the value of this property has to be averaged over all possible microstates. The thermodynamic average of the property A is computed using a numeral technique by Metropolis et al. [132]:

$$\langle A \rangle = \frac{\int \exp\left[-\frac{U(r^N)}{k_\mathrm{B}T}\right] A(r^N)\,\mathrm{d}r^N}{\int \exp\left[-\frac{U(r^N)}{k_\mathrm{B}T}\right]\,\mathrm{d}r^N} \tag{2.2}$$

where $U(r^N)$ is the potential energy of configuration r^N. The probability density of finding the system in a configuration around r^N is:

$$\wp(r^N) = \frac{\exp\left[-\frac{U(r^N)}{k_\mathrm{B}T}\right]}{Z} \tag{2.3}$$

where $Z = \int \exp\left[-\frac{U(r^N)}{k_B T}\right] \mathrm{d}r^N$ is the configurational part of the partition function. Since the partition function can rarely be obtained analytically or numerically, Monte Carlo simulations need to be used to compute ensemble averages. It is important to note that the vast majority of microstates have $U = \infty$ so these states do not contribute to Z and $\langle A \rangle$.

2.1.1 – Ensembles

The thermodynamic averages of the property can be computed using Monte Carlo methods at certain statistical ensemble to obtain the thermodynamic quantities of a system, as well as other equilibrium and dynamic properties [127]. In statistical mechanics, all thermodynamic properties are related to the partition function Q of the system [133]. All properties of the system can be derived if the partition function of the applied ensemble is known. The statistical ensembles used in this thesis are summarized below.

Canonical ensemble

In the canonical ensemble (NVT), the number of particles N, temperature T, and volume V are fixed. This represents a closed system that can exchange heat, but not particles, with its surroundings. The partition function of the NVT ensemble is [128]:

$$Q_{NVT} = \frac{V^N}{\Lambda^{3N} N!} \int \mathrm{d}s^N \exp(-\beta U(s^N)) \tag{2.4}$$

where N is the number of molecules, V is the volume of the system, $\beta = \frac{1}{k_B T}$, Λ is the thermal wavelength, U is the potential energy, and s^N is the scaled coordinate vector of all atoms by:

$$s_i = \frac{r_i}{L} \quad \text{for} \quad i = 1, 2, \ldots, N \tag{2.5}$$

where it is assumed that the system is contained in a cubic box with a volume V and a diameter $L = V^{1/3}$.

The NVT ensemble is a useful tool for computational studies, offering insights into the thermodynamic properties and behaviors of systems. Many experimental setups control the temperature and volume while keeping the number of particles fixed, and the NVT ensemble directly corresponds to these conditions, making theoretical results applicable to real-world situations. The canonical ensemble allows for the simplification of complex systems by providing a framework in which the probability of each microstate can be determined using the Boltzmann factor [128]. It is also well-suited for studying phase transitions at constant volume, allowing for the observation of changes in state (e.g.,

from liquid to gas), thus providing insights into the conditions at which these transitions occur, although phase transitions are more commonly studied at constant pressure [128]. Within the scope of this thesis, the NVT ensemble was used to compute the enthalpy of adsorption at infinite dilution, see Chapter 2.3.5.

Isobaric-isothermal ensemble

In the isobaric-isothermal ensemble (NPT), the number of atoms N, imposed pressure P, and temperature T are fixed. The volume is a dynamic variable that changes during the simulation in a closed system. The partition function of the NPT ensemble is [128]:

$$Q_{NPT} = \frac{\beta P}{\Lambda^{3N} N!} \int \mathrm{d}V V^N \exp(-\beta P V) \int \mathrm{d}s^N \exp(-\beta U(s^N)) \tag{2.6}$$

where N is the number of molecules, V is the volume of the system, P is the imposed pressure, $\beta = \frac{1}{k_\mathrm{B} T}$, Λ is the thermal wavelength, s^N is the scaled coordinate vector of all molecules, and U is the potential energy.

The NPT ensemble is one of the most important ensembles for studying the behavior of materials and substances as it reflects conditions common in experimental setups and real-world applications [127]. By allowing the volume to fluctuate, the NPT ensemble provides more realistic simulations of natural processes compared to the NVT ensemble, which keeps the volume constant [129]. The NPT ensemble provides insights into thermodynamic properties, including standard enthalpies, entropies and free energies of formation, redox potentials, equilibrium constants (e.g., acid ionization constants, solubility products, inhibition constants), etc., at conditions of constant temperature and pressure [127]. Additionally, this ensemble is well-suited for investigating phase transitions, such as the vaporization of liquids, where the volume of the system changes significantly, studying mechanical properties of materials, and understanding the pressure-dependent solvation and dissolution processes [127, 129, 134].

Grand-canonical ensemble

In the grand-canonical ensemble (GC, μVT), the temperature T, volume V, and chemical potential μ are fixed. This represents an open system that can exchange heat and mass with the surroundings. The partition function of the μVT ensemble is [128]:

$$Q_{\mu VT} = \sum_{N=0}^{\infty} \frac{\exp(\beta \mu N) V^N}{\Lambda^{3N} N!} \int \mathrm{d}\mathbf{s}^N \exp\left[-\beta U\left(\mathbf{s}^N\right)\right] \tag{2.7}$$

where N is the number of molecules, V is the volume of the system, μ is the imposed chemical potential, $\beta = \frac{1}{k_B T}$, Λ is the thermal wavelength, s^N is the scaled coordinate vector of all molecules, and U is the potential energy.

The grand-canonical ensemble is necessary for simulating open systems where the number of molecules varies, including the modelling of adsorption processes, molecular electronics, batteries, phase transitions, and the effect of Bose-Einstein condensation in quantum systems [127, 134].

Gibbs ensemble

The Gibbs ensemble (GE) describes a system where two coexisting phases (vapor and liquid) are in thermodynamic equilibrium [128]. In the Gibbs ensemble, the system consists of two simulation boxes that can exchange molecules and volume, maintaining a fixed total number of particles N and, in the NVT version, total volume V. Each phase within the system is internally equilibrated with a uniform temperature T, pressure P, and chemical potential μ across both phases. The partition function of the single-component GE ensemble (NVT version) is [128]:

$$\begin{aligned} Q_{\mathrm{GE}}(N,V,T) \equiv \sum_{n_1=0}^{N} \frac{1}{V\Lambda^{3N} n_1!(N-n_1)!} \int_0^V \mathrm{d}V_1 V_1^{n_1} (V-V_1)^{N-n_1} \\ \times \int \mathrm{d}\mathbf{s}_1^{n_1} \exp[-\beta U(\mathbf{s}_1^{n_1})] \int \mathrm{d}\mathbf{s}_2^{N-n_1} \exp[-\beta U(\mathbf{s}_2^{N-n_1})] \end{aligned} \tag{2.8}$$

where n_j and V_j are the number of molecules and volume of simulation box j, N is the total number of molecules in the two simulation boxes, V is the total volume of the two simulation boxes, $\beta = \frac{1}{k_B T}$, Λ is the thermal wavelength, s^N is the scaled coordinate vector of all molecules, and U is the potential energy.

This ensemble is particularly useful for simulating phase coexistence and transitions, providing insights into the thermodynamic properties and phase behavior of diverse systems ranging from simple fluids to complex mixtures and biological systems [128, 129].

Reaction ensemble

In the Reaction ensemble (RxMC) at constant pressure, the pressure P is imposed, and the number of atoms is fixed, while the number of molecules of individual species can vary due to chemical reactions. This ensemble is used to simulate chemical reaction equilibrium by introducing additional Monte Carlo trial moves that transform reactants into products and vice versa [129]. These moves mimic the exchange of atoms and molecules, exploring the composition

adjustments necessary to achieve thermodynamic equilibrium. The partition function of the Reaction ensemble is [135, 136]:

$$
\begin{aligned}
&Q_{\mathrm{RxMC},P} = \\
&\beta P \sum_{N_1=0}^{\infty} \cdots \sum_{N_S=0}^{\infty} \int \mathrm{d}V \exp[-\beta P V] \exp\left[\sum_{i=1}^{S} \left(\beta \mu_i N_i + N_i \ln \frac{V q_i}{\Lambda_i^3} - \ln N_i!\right)\right] \\
&\times \int \mathrm{d}\mathbf{s}^N \exp[-\beta U(\mathbf{s}^N)]
\end{aligned}
\tag{2.9}
$$

where S is the number of components, $\beta = \frac{1}{k_\mathrm{B}T}$, s^N is the scaled coordinate vector of all molecules, V is the volume, P is the imposed pressure, N is the total number of molecules in the simulation box, and U is the potential energy. q_i, μ_i, N_i, and Λ_i are the ideal gas partition function excluding the translational part, the chemical potential, the number of molecules, and the thermal wavelength of component type i, respectively. The Reaction ensemble at constant pressure is used to compute the thermodynamic equilibrium compositions of a gas-phase chemical reaction, which are essential for investigating the confinement effects on thermodynamic reaction equilibrium. This ensemble addresses only the thermodynamic equilibrium and does not provide insights into the kinetics of the reaction.

2.1.2 – Monte Carlo Trial Moves

MC simulations consist of cycles, with each cycle involving different types of MC moves, varying according to the statistical ensemble chosen to characterize the system [128]. One MC cycle consists of N MC trial moves, where N is the total number of molecules at the start of the simulation. A trial move refers to a proposed modification of the system, such as moving, rotating, inserting, or deleting a molecule. Each trial move is evaluated and accepted or rejected based on the criteria of the chosen MC algorithm, which ensures that the system explores different configurations and ultimately samples the desired probability distribution. Markov Chain Monte Carlo (MCMC) method generates configurations with a probability proportional to the Boltzmann weight $\exp[-\beta U(s^N)]$ [132] to ensure that only relevant microstates are considered. The Boltzmann weight determines the probability of a system being in a particular configuration based on its energy and the system temperature. When the number of possible configurations is too vast to compute exhaustively, MCMC methods, such as the Metropolis algorithm, provide a practical solution. Random trial moves are generated by the Metropolis algorithm from the current

microscopic state to a new state, with the acceptance probability depending on the ratio of Boltzmann weights between the new and current states [132]. This ensures that the generated configurations have probabilities proportional to their Boltzmann weights. By satisfying the detailed balance condition, the MCMC method ensures that the Markov chain equilibrium distribution matches the desired Boltzmann distribution, allowing accurate sampling of the system thermodynamic properties. The detailed balance condition is given by [128]:

$$P_B(o)\alpha(o \to n)P_{\text{acc}}(o \to n) = P_B(n)\alpha(n \to o)P_{\text{acc}}(n \to o) \tag{2.10}$$

where $P_B(o)$ and $P_B(n)$ are probabilities of finding the system in the current microscopic state (o) and the new state (n), respectively. P_{acc} is the probability of leaving/entering a state by accepting a trial move, and $\alpha(o \to n)$ is the probability that a trial move is selected from o to n. Quite often (but not always), α is symmetric, i.e., $\alpha(o \to n) = \alpha(n \to o)$ [132]. The trial moves are accepted or rejected based on the acceptance rule to ensure that system states are generated according to the probability distribution derived from the partition function [132], imposing equilibrium [128]. The acceptance probability of performing a trial move from the current microscopic state to the new state is defined by Metropolis et al. [132] as:

$$P_{\text{acc}}(o \to n) = \min\left(1, \frac{P_B(n)}{P_B(o)}\right) \tag{2.11}$$

where $P_B(o)$ and $P_B(n)$ are probabilities of finding the system in the current microscopic state (o) and the new state (n).

To enhance the statistical accuracy of Monte Carlo simulations for long-chain molecules, the Configurational-Bias Monte Carlo (CBMC) method is used [137]. This approach reduces computational time, prevents overlaps with the framework, and increases the success rate of molecule insertions. The molecule is grown inside the simulation box segment by segment. For each segment, k trial orientations are generated according to the bonded energy, then based on the non-bonded energy the most favorable orientation is selected according to:

$$P_i(j) = \frac{\exp[-\beta U_i^{\text{ext}}(j)]}{\sum_{l=1}^{k} \exp[-\beta U_i^{\text{ext}}(l)]} = \frac{\exp[-\beta U_i^{\text{ext}}(j)]}{\omega_i} \tag{2.12}$$

where ω_i is the Rosenbluth weight [138]. The selected trial orientation is added to the chain and the procedure is repeated until the entire molecule is grown.

The Rosenbluth factor for the newly grown molecule is computed by [138]:

$$W = \prod_i \omega_i \tag{2.13}$$

The Rosenbluth factor of the new configuration is related to the free energy:

$$F = -\frac{1}{\beta} \ln \frac{\langle W \rangle}{\langle W^{\mathrm{id}} \rangle} \tag{2.14}$$

where $\langle W^{\mathrm{id}} \rangle$ is the Rosenbluth factor of an isolated molecule that has only internal interactions. The rules for accepting or rejecting the grown molecule are chosen to eliminate the bias introduced by this growth method precisely.

In a MC simulation, each molecule is selected at random, and one of the trial moves is applied to it:

- Translations – move a randomly selected molecule in a random direction.
- Rotations – rotate a randomly selected molecule around its center of mass by a random rotation angle.
- Insertions – randomly place a molecule in the simulation box. The CBMC technique is used for efficient insertion of molecules by adjusting the probability of insertion based on the local configuration and avoiding over-counting.
- Deletions – remove a randomly selected molecule from the simulation box. The CBMC technique is used for efficient deletions by adjusting probabilities based on the resulting configuration after a molecule is removed.
- Identity changes – alter the identity of a randomly chosen molecule to that of another component in the mixture.
- Volume changes – expand or reduce the volume of the simulation box.
- Reaction swap moves – remove randomly selected molecules of the reactants and insert molecules of the reaction products at random positions with a random orientation for the conversion of the reactant molecules into reaction product molecules according to a specified chemical reaction.

An extensive overview of molecular simulations can be found in the books by Frenkel and Smit [128] and Allen and Tildesley [129].

2.1.3 – Continuous Fractional Component Monte Carlo

The Continuous Fractional Component (CFC) Monte Carlo method [139–142] can be seen as an expanded version of the conventional ensembles, where

instead of inserting molecules in a single Monte Carlo trial move, molecules are inserted gradually. This method significantly enhances the efficiency of molecule transfers by introducing so-called fractional molecules into the system [139]. Each fractional molecule is assigned a continuous fractional parameter, $\lambda \in [0, 1]$, which controls the interaction strength with surrounding molecules. When $\lambda = 0$, there are no interactions between the fractional molecule and its surroundings, meaning the molecule behaves as an ideal gas molecule, allowing efficient insertions and deletions. For $\lambda = 1$, the fractional molecule interacts with its surroundings like any other non-fractional molecule, facilitating trial moves that change its identity and enable molecule exchanges [139, 143]. The surroundings can easily adapt to the inserted/deleted fractional molecules, which is important at high densities, e.g. adsorption simulations in porous materials near the saturation loading [144] or reaction equilibria of complex systems [145]. The CFC method uses the probability distribution of λ to directly calculate chemical potentials, fugacity coefficients, partial molar enthalpies, and partial molar volumes [143, 146]. To prevent the system from getting stuck at specific λ values, it is necessary to bias the sampling of λ using a weight function $[W(\lambda)]$ [139]. This weight function can be obtained using the Wang-Landau algorithm or an iterative scheme [143]. Four additional trial moves can be used in the CFC method to allow the gradual insertion/deletion of fractional molecules [143]:

- λ changes – the parameter λ is changed by a random value in a way that it remains in the range $[0, 1]$, resulting in scaled interactions between the fractional molecule and the surroundings.
- Reinsertions – removal of the fractional molecules from the system and insertion at a random position with a random orientation.
- Identity changes for fractional molecules – the transformation of the fractional molecule into a whole molecule and the transformation of a randomly selected whole molecule into a fractional molecule.
- Reaction swap moves for fractional molecules – removal of fractional molecules of reactants/products and insertion of fractional molecules of products/reactants at random positions.
- Swapping the fractional – transfer of the fractional molecule from one simulation box to the other in the Gibbs ensemble. The value of λ remains constant. The acceptance probability for this trial move is high when λ is close to 0.

The expanded partition functions for the ensembles combined with the CFC method used in this thesis are listed below.

Canonical ensemble

The NVT ensemble combined with the CFC method has the following partition function [143]:

$$Q_{NVT}^{\mathrm{CFC}} = \frac{V^{N+1}}{\Lambda^{3(N+1)}N!}\int_0^1 \mathrm{d}\lambda \int \mathrm{d}\mathbf{s}^N \exp\left[-\beta U(\mathbf{s}^N)\right] \times \int \mathrm{d}\mathbf{s}_{\mathrm{frac}} \exp\left[-\beta U_{\mathrm{frac}}(\mathbf{s}_{\mathrm{frac}}, \mathbf{s}^N, \lambda)\right] \tag{2.15}$$

where N is the number of whole molecules, V is the volume of the system, $\beta = \frac{1}{k_{\mathrm{B}}T}$, Λ is the thermal wavelength, s^N is the scaled coordinate vector of all molecules, and U is the potential energy (excluding the interactions of the fractional molecule), U_{frac} is the potential energy of the fractional molecule, $\lambda \in [0, 1]$ is the fractional parameter, and s_{frac} is the scaled coordinate vector of the fractional molecule.

In Monte Carlo simulations in the NVT ensemble with the CFC method, three additional trial moves (λ changes, reinsertions, and identity changes for fractional molecules), together with the conventional trial moves for thermalization such as translations, rotations, and volume changes, allow for efficient sampling of the different system states. Within this ensemble, one can calculate various thermodynamic properties such as the Helmholtz free energy, internal energy, enthalpy, entropy, and heat capacity, which are essential for understanding the equilibrium behavior of the system [128, 129].

Isobaric-isothermal ensemble

The NPT ensemble combined with the CFC method has the following partition function [143]:

$$Q_{NPT}^{\mathrm{CFC}} = \frac{\beta P}{\Lambda^{3(N+1)}N!}\int_0^1 \mathrm{d}\lambda \int \mathrm{d}V V^{N+1} \exp(-\beta P V) \times \int \mathrm{d}\mathbf{s}^N \exp\left[-\beta U(\mathbf{s}^N)\right] \int \mathrm{d}\mathbf{s}_{\mathrm{frac}} \exp\left[-\beta U_{\mathrm{frac}}(\mathbf{s}_{\mathrm{frac}}, \mathbf{s}^N, \lambda)\right] \tag{2.16}$$

where N is the number of molecules, V is the volume of the system, P is the imposed pressure, $\beta = \frac{1}{k_{\mathrm{B}}T}$, Λ is the thermal wavelength, s^N is the scaled coordinate vector of all molecules, and U is the potential energy (excluding the interactions of the fractional molecule), U_{frac} is the potential energy of the fractional molecule, $\lambda \in [0, 1]$ is the fractional parameter, and s_{frac} is the scaled coordinate vector of the fractional molecule.

In Monte Carlo simulations in the NPT ensemble with the CFC method, three additional trial moves (λ changes, reinsertions, and identity changes for fractional molecules) are used together with the conventional trial moves such

as translations and rotations. In this thesis, the NPT ensemble is used to compute the densities of mixtures and pure components and the excess chemical potential (see Chapter 2.3.1) necessary to obtain several thermodynamic properties, such as activity coefficients, saturated vapor pressures, and Henry coefficients.

Grand-canonical ensemble

The GC ensemble combined with the CFC method has the following partition function [139, 143]:

$$Q_{\mu VT}^{\mathrm{CFC}} = \sum_{N=0}^{\infty} \frac{\exp[\beta\mu N] V^{N+1}}{\Lambda^{3(N+1)} N!} \int_0^1 \mathrm{d}\lambda \int \mathrm{d}\mathbf{s}^N \exp\left[-\beta U(\mathbf{s}^N)\right] \times \int \mathrm{d}\mathbf{s}_{\mathrm{frac}} \exp\left[-\beta U_{\mathrm{frac}}(\mathbf{s}_{\mathrm{frac}}, \mathbf{s}^N, \lambda)\right] \tag{2.17}$$

where N is the number of whole molecules, V is the volume of the system, μ is the imposed chemical potential, $\beta = \frac{1}{k_{\mathrm{B}}T}$, Λ is the thermal wavelength, s^N is the scaled coordinate vector of all molecules, and U is the potential energy (excluding the interactions of the fractional molecule), U_{frac} is the potential energy of the fractional molecule, $\lambda \in [0, 1]$ is the fractional parameter, and s_{frac} is the scaled coordinate vector of the fractional molecule.

In the grand-canonical ensemble, the value of the fractional parameter λ is randomly changed. There are three scenarios:

1. $\lambda < 0$: The fractional molecule is removed from the system, and a randomly chosen whole molecule is converted into a fractional molecule with $\lambda \to \lambda + 1$.

2. $0 < \lambda < 1$: This trial move corresponds to a normal change in λ.

3. $\lambda > 1$: A new fractional molecule is taken from an ideal gas reservoir and introduced into the system at a random position, with a random orientation and internal configuration. The new fractional parameter for this molecule is set to $\lambda \to \lambda - 1$.

In this thesis, the GC ensemble was used to study the effect of thermodynamic confinement on the chemical reaction equilibrium, and for the computation of adsorption isotherms and isobars with the corresponding enthalpies of adsorption, see Chapter 2.3.4.

Gibbs ensemble

The GE ensemble combined with the CFC method has the following partition function [143, 146]:

$$
\begin{aligned}
Q_{\mathrm{GE},NVT}^{\mathrm{CFC}} = \frac{1}{\Lambda^{3(N+1)} N!} \sum_{i=1}^{2} \sum_{n_1=0}^{N} \frac{N!}{n_1!(N-n_1)!} \int_0^1 \mathrm{d}\lambda \\
\times \int_0^V \mathrm{d}V_1 V_1^{n_1+\delta_{i1}} (V - V_1)^{N-n_1+\delta_{i2}} \\
\times \int \mathrm{d}\mathbf{s}^{n_1} \exp\left[-\beta U_1(\mathbf{s}^{n_1})\right] \\
\times \int \mathrm{d}\mathbf{s}^{N-n_1} \exp\left[-\beta U_2(\mathbf{s}^{N-n_1})\right] \\
\times (\delta_{i1} \int \mathrm{d}\mathbf{s}_{\mathrm{frac}} \exp\left[-\beta U_{\mathrm{frac},1}(\mathbf{s}_{\mathrm{frac}}, \mathbf{s}^{n_1}, \lambda)\right] \\
+ \delta_{i2} \int \mathrm{d}\mathbf{s}_{\mathrm{frac}} \exp\left[-\beta U_{\mathrm{frac},2}(\mathbf{s}_{\mathrm{frac}}, \mathbf{s}^{N-n_1}, \lambda)\right])
\end{aligned}
\tag{2.18}
$$

where n_j and V_j are the number of molecules and volume of simulation box j, N is the total number of molecules in the two simulation boxes, V is the total volume of the two simulation boxes, $\beta = \frac{1}{k_{\mathrm{B}}T}$, Λ is the thermal wavelength, s^N is the scaled coordinate vector of all molecules, and U is the potential energy (excluding the interactions of the fractional molecule), U_{frac} is the potential energy of the fractional molecule, $\lambda \in [0, 1]$ is the fractional parameter, s_{frac} is the scaled coordinate vector of the fractional molecule, and the δ-function is used to indicate if the fractional molecule is in simulation box j ($\delta_{ij} = 0$ if $i \neq j$ and $\delta_{ij} = 1$ if $i = j$).

In the Gibbs Ensemble simulations combined with the CFC method, in addition to the conventional Monte Carlo trial moves for thermalization and volume changes, there are trial moves used to facilitate molecule transfer between the boxes: λ changes, swapping the fractional, and identity changes for fractional molecules [146]. In this thesis, the Gibbs Ensemble was used to compute vapor-liquid equilibrium and critical constants, see Chapter 2.3.2.

Reaction ensemble

The RxMC ensemble combined with the CFC method has the following partition function [142, 143]:

$$
\begin{aligned}
Q^{\mathrm{CFC}}_{\mathrm{RxMC},P} = \beta P \sum_{N_1=0}^{\infty} \cdots \sum_{N_S=0}^{\infty} \sum_{\delta=0}^{1} \int_0^1 \mathrm{d}\lambda \int \mathrm{d}V \exp(-\beta P V) \\
\times \exp\left[\sum_{i=1}^{R} \beta\mu_i(N_i+\delta\nu_i) + (N_i+\delta\nu_i)\ln\left(\frac{V q_i}{\Lambda_i^3}\right) - \ln N_i!\right] \\
\times \exp\left[\sum_{i=R+1}^{S} \beta\mu_i(N_i+(1-\delta)\nu_i) + (N_i+(1-\delta)\nu_i)\ln\left(\frac{V q_i}{\Lambda_i^3}\right) - \ln N_i!\right] \\
\times \int \mathrm{d}\mathbf{s}^N \exp\left[-\beta U(\mathbf{s}^N)\right] \int \mathrm{d}\mathbf{s}_{\mathrm{frac}}^{N_{\mathrm{frac}}} \exp\left[-\beta U_{\mathrm{frac}}(\mathbf{s}_{\mathrm{frac}}^{N_{\mathrm{frac}}}, \mathbf{s}^N, \lambda, \delta)\right]
\end{aligned}
\tag{2.19}
$$

where S is the number of components, $\beta = \frac{1}{k_{\mathrm{B}}T}$, s^N is the scaled coordinate vector of all molecules, V is the volume, P is the imposed pressure, N is the total number of molecules in the simulation box, U is the potential energy, U_{frac} is the potential energy of the fractional molecule, $\lambda \in [0,1]$ is the fractional parameter, and s_{frac} is the scaled coordinate vector of the fractional molecule. q_i, μ_i, N_i, ν_i, and Λ_i are the ideal gas partition function excluding the translational part, the chemical potential, the number of molecules, the stoichiometric coefficient, and the thermal wavelength of component type i, respectively. δ is the reaction step of fractional molecules ($\delta = 0$ for reactants and $\delta = 1$ for products). Components 1 to R are reactants, and components $R+1$ to S are products.

In Rx/CFC simulations, in addition to the conventional Monte Carlo trial moves for thermalization and volume changes, there are trial moves used to mimic the chemical reaction [142]: λ changes, and reaction swap moves for fractional molecule. In this thesis, the Reaction ensemble at constant pressure is used to compute the thermodynamic equilibrium compositions of a gas-phase chemical reaction (see Chapter 2.3.3), needed as an input in the simulations of the confinement effects of metal-organic frameworks on thermodynamic reaction equilibrium.

2.2 — Force fields

A classical force field is a set of functions and corresponding parameters used to describe the interactions in a molecular system during simulations. In this thesis, several force fields are applied, including the generic Universal Force Field (UFF) [147], DREIDING [148], and OPLS/AA [149], as well as custom force fields developed for particular systems. In this section, the functional

form of the force fields is described. The sets of used and developed parameters are discussed in detail in each chapter.

The total potential energy of a system includes two terms: bonded and non-bonded interactions:

$$U = U_{\text{bonded}} + U_{\text{non-bonded}} \tag{2.20}$$

Intramolecular interactions refer to the forces that hold atoms together within a molecule and involve both bonded and non-bonded interactions. Bonded interactions arise from chemical bonds, such as covalent bonds, and include bond stretching (interactions between two atoms), angle bending (interactions between three atoms), and torsional interactions (interactions between four atoms). Two types of non-bonded intramolecular interactions occuring between atoms within the same molecule are considered: Van der Waals (VdW) and electrostatic interactions. In this work, all molecular and framework models are considered rigid, with the total potential energy of the system determined solely by non-bonded interactions ($U_{\text{bonded}} = 0$). Intermolecular interactions occur between different molecules and are dominated by non-bonded forces, including Van der Waals and electrostatic interactions. While Van der Waals interactions sufficiently describe non-polar fluids, a comprehensive description of the potential energy for polar systems also requires considering electrostatic interactions:

$$U_{\text{non-bonded}} = U_{\text{VdW}} + U_{\text{electrostatic}} \tag{2.21}$$

Van der Waals interactions result from the fluctuating electron densities around atoms. As two atoms come close to each other, these fluctuations become correlated, leading to an attractive force. The Van der Waals interactions are modeled using the Lennard-Jones (LJ) pair potential [150] (see Figure 2.1) as a combination of attraction and repulsion forces:

$$U^{\text{LJ}}(r_{ij}) = 4\epsilon_{ij}\left[\left(\frac{\sigma_{ij}}{r_{ij}}\right)^{12} - \left(\frac{\sigma_{ij}}{r_{ij}}\right)^{6}\right] \tag{2.22}$$

where ϵ_{ij} is the depth of the energy minimum, σ_{ij} is the distance at which the interatomic potential is zero, and r_{ij} the distance between particles i and j. The interaction parameters for identical atoms, ϵ_{ii} and σ_{ii}, are fixed using an effective potential. For interactions between different types of atoms, the cross-terms are estimated via the Lorentz-Berthelot mixing rules [129], with arithmetic and geometric means used for the calculations, respectively:

$$\epsilon_{ij} = \sqrt{\epsilon_{ii}\epsilon_{jj}} \tag{2.23}$$

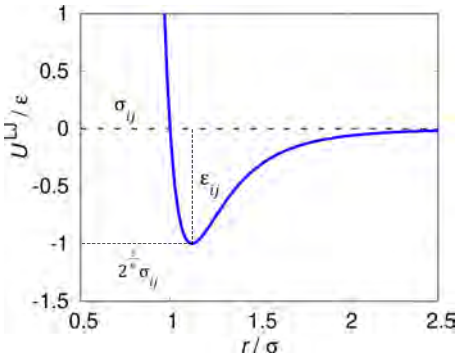

Fig. 2.1. The intermolecular potential energy U_{LJ} as a function of the distance between a pair of particles is given by the Lennard-Jones potential, where σ, $\epsilon = 1$. The potential has a minimum at a distance $r_{\min} = 2^{1/6}\sigma$.

$$\sigma_{ij} = \frac{\sigma_{ii} + \sigma_{jj}}{2} \tag{2.24}$$

LJ interactions are truncated at a certain distance (cut-off) with analytic tail corrections applied to the energy or cut and shifted to zero with the tail corrections omitted [128]. The electrostatic interactions between charged molecules, which involve both attractive and repulsive forces, are modeled using a static Coulombic potential:

$$U^{\mathrm{elec}}(r_{ij}) = \frac{1}{4\pi\epsilon_0\epsilon_r}\frac{q_i q_j}{r_{ij}} \tag{2.25}$$

where ϵ_0 is the permittivity of the vacuum, ϵ_r is the relative permittivity of the material, q_i and q_j are the charges of the atoms i and j, and r_{ij} the distance between the atoms. Due to their long-range nature, Coulombic forces require specialized methods for accurate calculation within finite systems that use periodic boundary conditions. In this thesis, the Ewald summation method [151] is used for calculating electrostatic interactions. To reduce deviations in the behavior or properties of a simulated system due to its finite size and maintain continuity, periodic boundary conditions are used for modelling an infinite system by replicating a small simulation box in all directions [128].

2.3 — Computed Thermodynamic Properties

2.3.1 – Excess Chemical Potential

The computation of excess chemical potentials (μ^{ex}) is performed using the

Continuous Fractional Component (CFC) Monte Carlo method in the NPT ensemble [143]. The excess chemical potential can be calculated using two different routes [143, 152]. The first route is based on the probability distribution of the scaling factor for the fractional molecule (i.e., continuous fractional parameter, $\lambda \in [0,1]$), regulating the interaction strength with surrounding molecules $[p(\lambda)]$:

$$\mu_i^{\text{ex}} = -k_{\text{B}}T \ln\left(\frac{p(\lambda=1)}{p(\lambda=0)}\right) \tag{2.26}$$

where k_{B} is the Boltzmann constant, T is temperature, and $p(\lambda_i = 1)$ and $p(\lambda_i = 0)$ are the probabilities of the scaling factor λ_i taking the value 1 and 0, respectively [146, 153].

The second route uses the computation of μ_{ex} via thermodynamic integration [152]:

$$\mu_i^{\text{ex}} = \int_0^1 \left\langle \frac{\partial U}{\partial \lambda} \right\rangle \mathrm{d}\lambda \tag{2.27}$$

where the term $\langle \frac{\partial U}{\partial \lambda} \rangle$ is the ensemble average derivative of the potential energy with respect to the interaction scaling factor λ.

2.3.2 – Vapor-Liquid Equilibrium

Simulating vapor-liquid equilibrium (VLE) is crucial for understanding the phase behavior of substances. VLE data provides essential insights into the thermodynamic properties and phase transitions of materials, which are fundamental for the design and optimization of chemical processes such as distillation, extraction, and crystallization. The simulations of phase coexistence are performed using the Continuous Fractional Component (CFC) Monte Carlo method in the Gibbs ensemble [143, 146]. In this method, two distinct microscopic regions, representing the vapor and liquid phases, are simulated concurrently. These regions are allowed to exchange both particles and volume to achieve internal equilibrium. At equilibrium, the temperature remains constant across both regions, as specified in the simulation input. As the simulation progresses, the system adjusts such that the pressure and chemical potential of the components equilibrate between the two phases. In the NVT version of the Gibbs ensemble, the pressure and chemical potential are not predefined inputs but the outcomes of the equilibration process in the simulation that satisfy the equilibrium conditions for both phases. The temperature, total number of molecules, and total volume (NVT version) remain constant as specified in the simulation input. The critical values of temperature and density can be determined from the vapor-liquid equilibrium curve using the Schröer-Pottlacher approach [154].

2.3.3 – Chemical Reaction Equilibrium

The computation of the thermodynamic equilibrium composition of a chemical reaction is performed using Continuous Fractional Component (CFC) Monte Carlo simulations in the Reaction Ensemble (Rx/CFC). This method allows for the interconversion of reactants and products through a series of stochastic trial moves, which propagate the system towards thermodynamic equilibrium. By using the Rx/CFC method, the equilibrium compositions of the reactants and products can be accurately predicted, providing valuable insights into the thermodynamic properties and behavior of chemical reactions under various conditions. In Rx/CFC simulations, the following input data are required:

- A force field that describes the interactions between molecules. This includes parameters for bonding, non-bonding, and electrostatic interactions which are crucial for accurately modelling the system.
- The isolated molecule gas partition functions of all reactants and reaction products. These partition functions account for the contributions of rotational and vibrational degrees of freedom, and are necessary for calculating the thermodynamic properties of the molecules in their isolated states.
- The stoichiometry of the chemical reactions in the system, which specifies the reactants and products involved and their respective coefficients in the balanced chemical equations.

The ideal gas partition functions can be obtained based on vibrational and rotational experimental data available from sources such as the NIST database, or through quantum mechanical calculations [155]. These functions play a critical role in determining the standard Gibbs free energy changes for the reactions. The details about computation and prediction of ideal-gas partition functions can be found in the book by McQuarrie et al. [156].

2.3.4 – Adsorption Isotherm

The computation of adsorption isotherms and isobars is performed using grand-canonical Monte Carlo (GCMC) simulations. GCMC simulations provide a detailed microscopic view of adsorption processes, allowing for the accurate computation of adsorption isotherms and isobars, which are essential for the design and optimization of adsorption systems in various industrial applications. In GCMC simulations, molecules are exchanged with a reservoir at the same temperature and chemical potential, allowing the system to reach adsorption equilibrium. The chemical potential of the adsorbate is computed using the fugacity f, which provides a more accurate description of real gas

behavior compared to the ideal gas assumption. The chemical potential μ is given by:

$$\mu = \mu^0 + RT \ln \left(\frac{f}{p^0} \right) \tag{2.28}$$

where μ^0 is the reference chemical potential, and p^0 is the reference pressure. The fugacity f is related to the pressure p by the fugacity coefficient ϕ:

$$f = \phi p \tag{2.29}$$

The fugacity coefficient ϕ accounts for deviations from ideal gas behavior and can be determined from equations of state (e.g. Peng-Robinson Equation of State [157] used by the RASPA software package [94, 95]) or experimental data. During the GCMC simulations, the number of adsorbate molecules within the pores of the adsorbent structure fluctuates. The average number of molecules adsorbed, or the adsorption loading, is computed as an output of the simulation. This average provides insight into the capacity of the material for gas adsorption at different conditions. To construct an adsorption isotherm, a series of GCMC simulations are run at increasing pressures and constant temperature. Each simulation point represents the equilibrium adsorption loading at a specific pressure. By plotting these equilibrium loadings against their corresponding pressures, the adsorption isotherm is obtained. This isotherm is crucial for understanding the adsorption capacity and behavior of the material over a range of pressures.

2.3.5 – Enthalpy of Adsorption

The enthalpy of adsorption at infinite dilution, representing the affinity between the molecule and the framework, is obtained from the average energies of the guest molecule in the host framework, the host framework itself, and the guest molecule. This is determined by [158]:

$$\Delta H = \Delta U - RT = \langle U_{hg} \rangle - \langle U_h \rangle - \langle U_g \rangle - RT \tag{2.30}$$

where, ΔU is the internal energy of the system, $\langle U_{hg} \rangle$ is the average energy of the guest molecule in the host framework, $\langle U_h \rangle$ is the average energy of the host framework (0 J for rigid frameworks), $\langle U_g \rangle$ is the average energy of the guest molecule (0 J for rigid molecules), R is the universal gas constant, and T is the temperature.

2.3.6 – Radial Distribution Function

The Radial Distribution Function (RDF) is a measure used in statistical mechanics to describe how the local particle density varies as a function of

distance from a reference particle. It provides insight into the structure of a system at the atomic level. The RDF, $g_{AB}(r)$, which describes the distribution of particles of type B around a particle of type A, is defined as the ratio of the probability density of finding a particle B at a distance between r and $r + \mathrm{d}r$ from a particle A to the expected density for an ideal gas, given by [128]:

$$g_{AB}(r) = \frac{1}{\langle \rho_b \rangle} \frac{1}{N_A} \sum_{i=1}^{N_A} \sum_{j=1}^{N_B} \frac{\delta(r_{ij} - r)}{4\pi r^2} \tag{2.31}$$

where $\langle \rho_b \rangle$ is the average density of the B-type particles, and N_i is the number of i-type particles.

2.3.7 – Average Density Profiles

The average density profiles are histograms representing the positions of adsorbed molecules within the pores of the adsorbent during simulations. The average position probability of each molecule is obtained from the adsorption simulation for every cycle and the number of times a specific location in the framework is taken by a guest molecule is determined. The projection of the 3-dimensional histogram onto a plane is constructed, with the probability of finding a molecule at a given position indicated by a color scale.

2.3.8 – Binding Energy and Geometry

The computation of the minimum state of energy in the system allows finding the most stable binding configurations of the adsorbed molecule in the pores of the structure. The minimum in the potential energy hypersurface is defined as [159]:

$$\frac{\partial U(s^N)}{\partial s_i} = 0 \quad \text{for} \quad i = 1, 2, \ldots, N \tag{2.32}$$

where $U(s^N)$ is the total potential energy of the system for N particles. To ensure that this point is a true minimum (and not a maximum or saddle point), it is necessary to calculate the second derivative of the potential energy, which corresponds to the Hessian matrix. The Hessian matrix provides information about the curvature of the potential energy surface. A true minimum is confirmed when all the eigenvalues of the Hessian are positive, indicating that the energy increases in all directions around the minimum. This calculation is crucial for identifying the global minimum energy state of the system, which represents the most stable configuration. In this work, Baker's minimization method [160] is selected for energy minimizations. This method is advantageous because it utilizes not only the energy and first derivatives but also the second derivatives and the eigenvalues/vectors of the Hessian matrix. Baker's

method employs a combination of the Newton-Raphson and quasi-Newton approaches, which ensures rapid convergence to the minimum by effectively using the curvature information provided by the Hessian. The method involves iteratively updating the coordinates by solving the Newton-Raphson equations, which take into account the gradient and curvature of the potential energy surface. This approach allows Baker's method to efficiently and accurately locate true minima on the energy surface. This leads to enhanced numerical stability and faster convergence, making it a reliable and effective approach for determining equilibrium geometries in complex systems.

Chapter 3

Solubility of Carbon Dioxide in Aqueous Formic Acid Solutions and the Effect of Sodium Chloride Addition

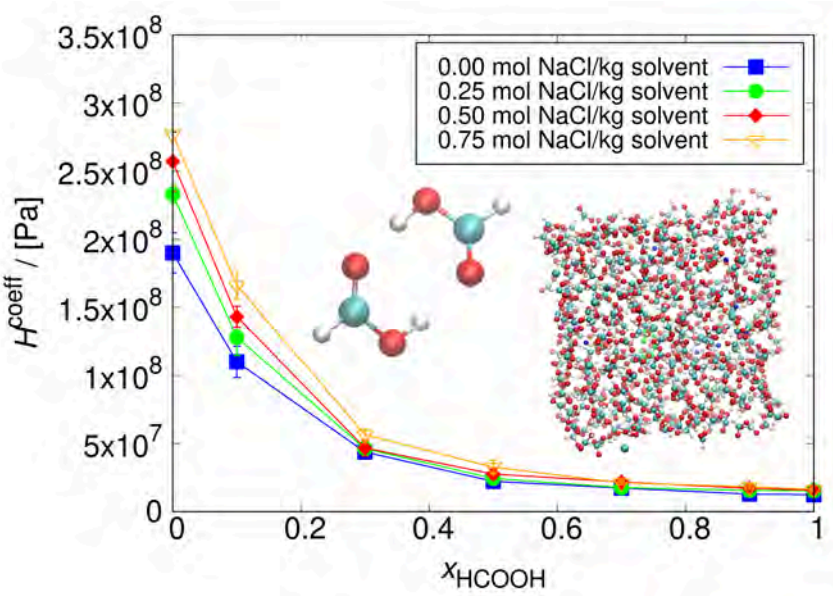

There is a growing interest in the development of routes to produce formic acid from CO_2, like the electrochemical reduction of CO_2 to formic acid. The solubility of CO_2 in the electrolyte influences the production rate of formic acid. Here, the dependence of the CO_2 solubility in aqueous HCOOH solutions with electrolytes on the composition and the NaCl concentration was studied by Continuous Fractional Component Monte Carlo simulations at 298.15 K. The chemical potentials of CO_2, H_2O and HCOOH were obtained directly from single simulations, enabling the calculation of Henry coefficients, and subsequently considering salting in or salting out effects. As the force fields for HCOOH and H_2O may not be compatible due to the presence of strong hydrogen bonds, the Gibbs-Duhem integration test was used to test this compatibility. The combination of the OPLS/AA force field with a new set of parameters, in combination with the SPC/E force field for water, was selected. It was found that the solubility of CO_2 decreases with increasing NaCl concentration in the solution and increases with increasing of HCOOH concentration. This continues up to a certain concentration of HCOOH in the solution, after which the CO_2 solubility is high and the NaCl concentration has no significant effect.

This chapter is based on the following publication:
Wasik, D. O., Polat, H. M., Ramdin, M., Moultos, O. A., Calero, S., Vlugt, T. J. H. Solubility of CO_2 in Aqueous Formic Acid Solutions and the Effect of NaCl Addition: A Molecular Simulation Study. *Journal of Physical Chemistry C* **2022**, *126*, 19424-19434.

3.1 — Introduction

The industrial revolution started an extensive use of fossil fuels, resulting in the release of alarming amounts of CO_2 gas into the atmosphere [1]. In the past years, the development of technologies for reducing CO_2 emissions have been in the forefront of research. From an economical point of view, a promising way of decreasing CO_2 emissions is the capture of CO_2 at the source of production (e.g., at industrial sites) and the conversion to value-added products, e.g., formic acid, methanol, propylene, urea [1–3]. In the chemical industry, formic acid (FA, HCOOH) is a primary product with a production capacity of 800,000 tons per year as of 2017 [18, 32]. A wide range of products are synthesized from FA [5, 7, 9, 10]. It is, e.g., used for the hydrothermal decarbonylation and decarboxylation in the water-gas-shift reaction [9], as a preservative (antibacterial cocktail in the prevention of potato spoilage [10]), as antibacterial in livestock feed (control of luminous vibriosis disease in shrimp aquaculture [5]), in the process of leather tanning and textiles dyeing [11], the production of rubber [8], and as hydrogen storage material [7].

Predominantly, formic acid is synthesized by methanol carbonylation resulting in a formate ester which undergoes a hydrolysis process with an excess of water [8, 34–36]. Another method for producing formic acid is the electrochemical reduction of CO_2 in an aqueous electrolyte solution [12–15]. The electrochemical conversion of CO_2 in a single step using H_2O is less resource intensive than methanol carbonylation, uses an abundant resource (CO_2), and avoids the production of intermediates. Electrochemical reduction of CO_2 is typically performed in alkaline media to suppress the competing hydrogen evolution reaction (HER) [17]. The reduction of CO_2 at the cathode results in formate ($HCOO^-$) and hydroxide (OH^-) ions [12]:

$$CO_2 + H_2O + 2e^- \rightarrow HCOO^- + OH^- \tag{3.1}$$

Depending on the pH, either formic acid or formate is produced. CO_2 reduction is mostly performed in alkaline solutions [12], but this results in formate, which is not the desired product from a market perspective [17]. To obtain FA, researchers are shifting to CO_2 reduction in (slightly) acidic conditions using pH neutral electrolytes (such as NaCl), which become acidic upon CO_2 dissolution [17]. Due to possible salting-out effects, there is a trade-off between CO_2 solubility and electric conductivity as a function of the NaCl concentration.

Currently, electrocatalytic reduction of CO_2 to HCOOH is not optimal due to the low solubility of CO_2 in aqueous solutions [16]. One possible solution is to use CO_2 at high pressures [14]. Another solution is to use a gas diffusion electrode, but in this case fouling and/or undesired crystallization takes

place [47–49]. This is a problem for producing HCOOH as the low solubility of CO_2 decreases the yield of the process. It is therefore crucial to investigate the possibilities of improving the solubility of CO_2 in the electrolyte. Formic acid/water systems are difficult to study experimentally because FA is susceptible to decomposition at relatively low temperatures and exhibits complex behavior with mixtures [161, 162]. FA forms strong hydrogen bonds [162–164]. There are two types of hydrogen bonds formed between FA monomers and water molecules: C-H$\cdots$O and O-H$\cdots$O [163, 165]. Due to the complex behavior of FA mixtures, force field-based molecular simulations are alternative approach to obtain thermodynamic properties, in cases where there is a lack of experimental data. In this work, molecular simulations have been used to study the CO_2 solubility in aqueous FA solutions and the effect of salting in/out. The modelling of hydrogen bonds is challenging in simulations because their presence leads to density and structural anomalies, such as a tetrahedral coordination in water [166]. Due to the strong H-bonds of FA, systems of FA – water are difficult to model due to the structure of the liquid phase [163, 167–169]. To the best of our knowledge, the effect of salt addition on the CO_2 solubility was investigated in pure water [50–53] and not in aqueous FA solutions. The first attempt to make an economic evaluation of electrochemical reduction of CO_2 with the use of potassium hydroxide and potassium sulfate (K_2SO_4) as electrolytes is described by Ramdin et al. [17] The results of our work can be used for a better design of processes for the electrochemical reduction of CO_2, in search of chemicals that enhance the CO_2 solubility and thus the efficiency of the CO_2 conversion without decreasing ionic conductivity of an electrolyte solution. Here, we will show the salting out effect of NaCl electrolyte on CO_2 solubility and CO_2 solubility dependence on HCOOH fraction in the solution.

This chapter is organized as follows: in section 3.2, we define the HCOOH model and force fields. In section 3.3, we provide technical details of the molecular simulation methods. In section 3.4 we specify detailed information on the simulations. In section 3.5 we present and discuss the results. The selected HCOOH force field is validated by simulations of vapor-liquid equilibria (VLE) and vapor pressure as a function of temperature. The densities of HCOOH/H_2O systems with different mole fractions of FA are compared to the experimental values. The dependence of the Henry coefficient of CO_2 on the mole fraction of HCOOH and the NaCl concentration in the mixture is determined. The solubility of CO_2 decreases with increasing NaCl concentration in the solution but increases with HCOOH concentration. Our findings are summarized in section 3.6.

3.2 — Force Field

The HCOOH molecule was constructed using the Avogadro molecule editor [170] and its geometry optimization was performed at the B3LYP/6-31G(d) level of theory using Gaussian09 [171]. The resulting geometry is shown in Figure 3.1. The model is rigid, and all interaction sites are at the atom positions (in sharp contrast to the anisotropic force field in the study by Schnabel et al. [172]).

Equilibration of systems containing both HCOOH and H_2O is not straightforward due to the presence of strong hydrogen bonds [173]. The compatibility of force fields for formic acid and water is unknown. For this reason, it is necessary to conduct a test verifying if the force field results in molecular simulations that are in thermodynamic equilibrium. Four force fields for HCOOH (FF-0, FF-1, FF-2, FF-3) in combination with the SPC/E force field for water were studied here. In the literature, there are three variants of the OPLS/AA force field [174] available for HCOOH, as well as a force field developed by Schnabel et al [172]. The OPLS/AA force fields are here named FF-0, FF-1 and FF-2. They correspond to the so-called 'Original', P1 and P2 force fields from the study of Salas et al [174], respectively. FF-3 is the force field by Schnabel et al [172]. All studied force fields use a functional form for intermolecular interactions based on Coulombic and Lennard-Jones (LJ) interactions:

$$U_{\text{inter}}\left(r_{ij}\right) = \frac{q_i q_j}{4\pi\varepsilon_0 r_{ij}} + 4\varepsilon_{ij}\left[\left(\frac{\sigma_{ij}}{r_{ij}}\right)^{12} - \left(\frac{\sigma_{ij}}{r_{ij}}\right)^{6}\right] \tag{3.2}$$

where r_{ij} is the distance between atoms i and j, q_i is the partial charge of atom i, and ϵ_0 is the permittivity of vacuum. ϵ_{ij} and σ_{ij} are the Lennard-Jones energy and size parameters, respectively [174]. Interactions between unlike Lennard–Jones sites are defined by the Lorentz–Berthelot mixing rules [129]. The interaction parameters for all studied HCOOH force fields are shown in Tables A.2 – A.5 of Appendix A, and references to the original publications of these force fields are provided. The interaction parameters of the HCOOH force field FF-2 selected for further simulations are in Table A.4 of Appendix A, together with the SPC/E force field for water [175], the García-Sánchez et al. force field for CO_2 [176] and the Joung–Cheatham force field for NaCl [177], that were used in this work.

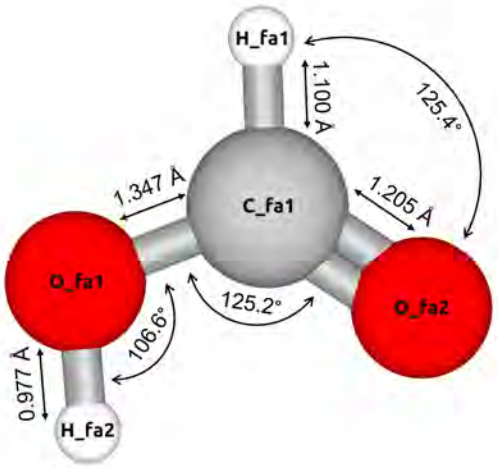

Fig. 3.1. Schematic representation of the HCOOH model optimized using Gaussian09 [171] at the B3LYP/6-31G(d) level of theory. The visualization is created using iRASPA [38]. The atoms labels and the respective atomic positions are listed in Table A.1 of Appendix A. The listed bond lengths are in Å.

3.3 — Methodology

The computation of excess chemical potentials (μ^{ex}) enables to test the compatibility of force fields, and subsequently, the calculation of Henry coefficients for CO_2 in aqueous solutions of HCOOH. The aim is to consider the salting in/salting out effects of NaCl addition to increase the electric conductivity and therefore the efficiency of the electrochemical reduction of CO_2.

For all simulations, the Monte Carlo (MC) Software Brick-CFCMC [143, 152] was used. This is an open-source molecular simulation code for the calculation of phase and reaction equilibria using state-of-the-art force field-based MC simulations in different ensembles, such as the NVT, NPT, grand-canonical, reaction, and the Gibbs ensemble [152]. The Continuous Fractional Component (CFC) Monte Carlo [139, 141] method in the NPT ensemble can be considered as an expanded ensemble version of the conventional NPT ensemble, in which a fractional molecule is introduced to the system. The interactions of the fractional molecule are scaled by a parameter $\lambda \in [0, 1]$. There

are no interactions of the fractional molecule with the surroundings when $\lambda = 0$, which means that the molecule is treated as an ideal gas molecule. For $\lambda = 1$, the fractional molecule has the same interactions as the other molecules not being a fractional molecule [139, 143]. The biasing of λ using a weight function $[W(\lambda)]$ is necessary to prevent the system from getting stuck at certain values of λ [139]. The weight function can be obtained via the Wang-Landau algorithm or an iterative scheme [143]. The excess chemical potential can be calculated using two different routes [143, 152]. The first route is based on the probability distribution of the scaling factor $[p(\lambda)]$ of the fractional molecule:

$$\mu_i^{\mathrm{ex}} = -k_{\mathrm{B}} T \ln\left(\frac{p(\lambda = 1)}{p(\lambda = 0)}\right) \tag{3.3}$$

where k_{B} is the Boltzmann constant, T is temperature, and $p(\lambda_i = 1)$ and $p(\lambda_i = 0)$ are the probabilities of the scaling factor λ_i taking the value 1 and 0, respectively [146, 153]. A flat probability distribution of λ is ensured by adding a biasing weight function, which is easily achieved for small molecules (low uncertainty for μ_{ex}). The second route is recommended in case of large and/or strongly polar molecules and uses the computation of μ_{ex} via thermodynamic integration [152]:

$$\mu_i^{\mathrm{ex}} = \int_0^1 \left\langle \frac{\partial U}{\partial \lambda} \right\rangle \mathrm{d}\lambda \tag{3.4}$$

The application of thermodynamic integration eliminates the need for sampling the full λ-space with equal probability in a single simulation. The term $\langle \frac{\partial U}{\partial \lambda} \rangle$ is the ensemble average derivative of the potential energy with respect to the interaction scaling factor λ. Values for $\langle \frac{\partial U}{\partial \lambda} \rangle$ can be computed from several independent simulations at different fixed values of λ [152, 178].

The excess chemical potentials for HCOOH and H_2O were calculated using the probability distribution of the scaling factor $p(\lambda)$, as well as from thermodynamic integration. A series of NPT simulations of HCOOH/H_2O systems were performed with mole fractions $x_{\mathrm{HCOOH}} = 0$, 0.1, 0.3, 0.5, 0.7, 0.9, 1. The compositions and average box volumes of all 7 systems simulated for the Gibbs-Duhem integration test are shown in Table A.6 of Appendix A. The value of μ^{ex} computed from the probability distribution $p(\lambda)$ was obtained directly from a single simulation of each system. Two fractional molecules (one for HCOOH and one for H_2O) were introduced in those simulations. For the thermodynamic integration, simulations of each system had to be computed separately for a HCOOH fractional molecule and a H_2O fractional molecule. In Brick-CFCMC, the value $\langle \frac{\partial U}{\partial \lambda} \rangle$ can only be computed for a single charge-neutral group of fractional molecules [152]. Series of 99 simulations were performed at

values of λ ranging from 0.01 to 0.99. The resulting values of $\langle \frac{\partial U}{\partial \lambda} \rangle$ as a function of λ were used in the thermodynamic integration (Eq. 3.4) to compute μ^{ex}.

The computed values of μ^{ex} and the activity coefficient γ_i for component i depend on the composition of the system. The activity coefficient can be computed from [179]:

$$\gamma_i = \frac{\rho_i}{x_i \cdot \rho_{i0}} \cdot \exp\left[\frac{\mu_i^{\mathrm{ex}} - \mu_{i0}^{\mathrm{ex}}}{k_{\mathrm{B}} T}\right] \tag{3.5}$$

where ρ_i and ρ_{i0} are the number densities of component i in the mixture and the reference number density of the pure solvent, respectively. μ_i^{ex} is the excess chemical potential of component i in the mixture and μ_{i0}^{ex} is the excess chemical potential of i in the pure fluid i. The derivation of Eq. 3.5 is provided in Appendix A.

The Gibbs-Duhem integration test [180] is a convenient tool to verify that the calculated activity coefficients of a system correspond to a system at equilibrium. Four studied HCOOH force fields [172, 174] in combination with the SPC/E force field for water were checked for thermodynamic consistency using the Gibbs-Duhem integration test [180]:

$$\int_0^1 \ln\left(\frac{\gamma_1}{\gamma_2}\right) \mathrm{d}x_1 = 0 \tag{3.6}$$

where γ_1 and γ_2 are the activity coefficients of component 1 and component 2, respectively, and x_1 is a mole fraction of component 1. The trapezoidal rule [181] was used for approximating the definite integral:

$$\int_a^b f(x)\mathrm{d}x \approx \sum_{k=1}^{N} \frac{f\left(x_{k-1}\right) + f\left(x_k\right)}{2} \cdot \left(x_k - x_{k-1}\right) \tag{3.7}$$

where N is the number of the subintervals. The uncertainties of the Gibbs-Duhem integrals were calculated using error propagation. The uncertainty for k^{th} subinterval of the integral is calculated by:

$$\mathrm{ERR}_k = \frac{\sqrt{\delta_{f(x_{k-1})}^2 + \delta_{f(x_k)}^2}}{2} \cdot \left(x_k - x_{k-1}\right) \tag{3.8}$$

where $\delta_{f(x_k)}$ is an uncertainty of $\ln\left(\frac{\gamma_1}{\gamma_2}\right)$ computed as the standard deviation from five independent simulations and x_k is a mole fraction of component 1, considered in k^{th} subinterval. The uncertainty of the Gibbs-Duhem integral is calculated using all subintervals by:

$$\mathrm{ERR_{G\ -\ D}} = \sqrt{\mathrm{ERR}_k^2 + \mathrm{ERR}_{k+1}^2 + \ \ldots\ + \ \mathrm{ERR}_N^2} \tag{3.9}$$

The densities of simulated $HCOOH/H_2O$ binary mixtures with different HCOOH mole fractions were compared with the experimental data [175] at temperatures 288.15 K, 298 K, and 303.15 K. The VLE curve for pure HCOOH was simulated using the Gibbs Ensemble at constant total volume, combined with the CFC method [143]. In this ensemble, there are two simulation boxes that can exchange molecules and volume. The phase equilibrium densities were reproduced for a temperature range from 335 K to 560 K and compared to experimental data [172]. At the start of the simulation, the total number of molecules in each simulation was equal to 400. Both simulation boxes were identical in terms of number of molecules and volume. The critical values of temperature and density were determined using the Schröer-Pottlacher approach [154]. The densities of the gas phase from the Gibbs Ensemble simulations were used to compute saturated vapor pressures. For the temperature range 335 K to 560 K, a series of NPT simulations for the gas phase were performed as a function of pressure. From these simulations, HCOOH vapor pressures were calculated using interpolation of the pressure as a function of density. Additionally, vapor pressures of HCOOH were calculated by assuming an ideal gas phase [182]:

$$P^{\mathrm{sat}} = \rho_{\mathrm{L}} \cdot k_{\mathrm{B}} T \cdot \exp\left(\frac{\mu_L^{\mathrm{ex}}}{k_{\mathrm{B}} T}\right) \tag{3.10}$$

where ρ_{L} and $\mu_{\mathrm{L}}^{\mathrm{ex}}$ are the number density and the excess chemical potential of the liquid phase from Gibbs Ensemble simulations, respectively. This approximation is investigated in Appendix A by the calculation of HCOOH dimer and monomer partial vapor pressures.

The solubilities of CO_2 in aqueous HCOOH solutions were determined from the Henry coefficient which are calculated by [183]:

$$H^{\mathrm{coeff}} = \rho_{\mathrm{mix}} \cdot k_{\mathrm{B}} T \cdot \exp\left(\frac{\mu_{\mathrm{CO2}}^{\mathrm{ex}}}{k_{\mathrm{B}} T}\right) \tag{3.11}$$

where ρ_{mix} is a number density of the mixture, and μ_{CO2} is the excess chemical potential of CO_2 at infinite dilution. To investigate the dependence of the CO_2 solubility on the salt content, NPT simulations of systems containing $HCOOH/H_2O/CO_2/NaCl$ were performed. To characterize the HCOOH content, HCOOH pseudo-mole fractions were used that are defined by:

$$x_{\mathrm{HCOOH}} = \frac{N_{\mathrm{HCOOH}}}{N_{\mathrm{HCOOH}} + N_{\mathrm{H_2O}}} \tag{3.12}$$

For each HCOOH pseudo-mole fraction $x_{\mathrm{HCOOH}} = 0$, 0.1, 0.3, 0.5, 0.7, 0.9, 1, four concentrations of NaCl have been studied: 0, 0.25, 0.5, 0.75 mol NaCl per kilogram of solvent (HCOOH + H_2O). The exact number of molecules used in each system is shown in Table A.7 of Appendix A. To enable the calculation of the excess chemical potential of CO_2, a fractional molecule of CO_2 is added to all systems.

As this is our first estimate for the HCOOH/H_2O/NaCl mixture, the ideal gas behavior was assumed. The computations are performed in the limit where the pressure approaches zero and hence the volume tends to infinity. In this limit, the side of monomers is favored by the reaction equilibrium in the gas phase. The increase of the volume leads to the decrease of the density. To counteract this, the number of monomers increases in the system resulting in the increase of the density. The appearance of monomers only allows to approximate the ideal gas behavior. The vapor pressures of H_2O and HCOOH were calculated by [184]:

$$P_i = \gamma_i \cdot x_i \cdot P_i^* \tag{3.13}$$

where γ_i is an activity coefficient of component i, x_i is a mole fraction of component i, P_i is actual partial vapor pressure and P_i^* is the vapor pressure of the pure solvent at the same temperature. The values of P_i^* for HCOOH and H_2O used in Eq. 3.13 were computed at 298.15 K using Gibbs Ensemble simulations (at constant total volume). The computed values were equal to the experimental data at 298 K [185, 186] within the error bars. The values of P_i^* for HCOOH and H_2O used in Eq. 3.13 were 5678.2 Pa [185] and 3169.0 Pa [186], respectively. The total pressure of the system was calculated according to the additivity of the partial pressures:

$$P_{\mathrm{total}} = P_{\mathrm{HCOOH}} + P_{\mathrm{H_2O}} \tag{3.14}$$

where P_{HCOOH} and $P_{\mathrm{H_2O}}$ are the partial pressures of HCOOH and H_2O, respectively. The results were compared with experimentally measured total pressures of the HCOOH/H_2O mixture at 291.15 K [187] and 303.15 K [188, 189] without NaCl added. The HCOOH vapor mole fraction was calculated by:

$$y_{\mathrm{HCOOH}} = \frac{P_{\mathrm{HCOOH}}}{P_{\mathrm{total}}} \tag{3.15}$$

The azeotropic behavior of simulated HCOOH/H_2O system without NaCl addition was analyzed using $P(x,y)$ and y-x diagrams. The results were compared with the NRTL-HOC method [190, 191] using parameters from Ref. [17].

The effect of salt on the solubility of CO_2 can be described by engineering models, e.g. the study by Weisenberger and Schumpe [192]. The solubility of CO_2 was compared with an engineering model for estimation of gas solubilities in salt solutions [192]. The Sechenov constant K was computed for each HCOOH pseudo-mole fraction from the slope of linear function, according to:

$$\log_{10} \frac{c_{G,o}}{c_G} = K \cdot c_S \tag{3.16}$$

where $c_{G,o}$ and c_G are the gas solubilities in pure water and in the salt solution, respectively, and c_S is the molar concentration of the salt. The solubility is related to Henry coefficients computed in the simulations of $HCOOH/H_2O/CO_2/$ NaCl mixtures and expressed as $H^{\text{coeff -1}}$. The solubility of gases in the solvent is inversely proportional to the Henry coefficient. Obtained values for K were compared with the Sechenov constant for CO_2/NaCl system calculated based on engineering model parameters [192].

3.4 — Simulation Details

In all simulations, the cutoff radius for intermolecular interactions is set to 10 Å. Interactions are truncated with analytic tail corrections applied. Periodic boundary conditions are exerted in all three directions. The Ewald summation method [151] is used for calculating electrostatic interactions. The number of k-vectors in each direction $K_{\max}$ equals 8 and the damping parameter a equals 0.32 $Å^{-1}$. The parameters for the Ewald summation correspond to a relative precision of 10^{-6}. One single MC cycle consists of N MC trial moves, where N is the total number of molecules at the start of the simulation. Each simulation was carried out with 200 000 equilibration cycles. In the production phase, 400 000 to 500 000 MC cycles were performed, depending on the energy equilibration of individual systems and a reaching flat probability distribution of the observed value of λ. The probabilities of selecting trial moves were 30% translations, 30% rotations, 1% volume changes, 15% λ changes and 30% CFC hybrid moves that combine the swap and identity changes [143]. To calculate the standard deviations of the computed values, all sets of simulations were performed five times starting from independent configurations and using different random number seeds. The algorithms provided in Brick-CFCMC [143, 152] are used to generate random initial configurations. The dissociation of formic acid in water was neglected in the simulations due to the low pKa value of formic acid (3.745 [27]). As a rough guide, for an ideal solution model the equilibrium reaction extent for the dissociation reaction (H^+ and $HCOO^-$) would be equal to only 0.026. We also neglected the soluble [186] sodium form-

ate since it forms at very low concentrations by reaction between the formate product of CO_2 reduction and the cell electrolyte.

3.5 — Results and Discussion

We first validated for which combinations of the SPC/E – HCOOH force fields the Gibbs-Duhem integration is passed within the error bars. In Table A.8 of Appendix A, the excess chemical potentials obtained from the probability distribution of λ and thermodynamic integration are compared. It turns out that both routes for obtaining μ^{ex} (i.e., from the probability distribution of λ and thermodynamic integration) lead to nearly identical results. The conceptually simpler route of using the probability distribution of λ turned out to be sufficiently accurate. The relative difference between μ^{ex} computed from the probability distribution of λ and μ^{ex} from thermodynamic integration is below 0.5%. The average uncertainties of μ^{ex} are 0.31 kJ mol^{-1} and 0.13 kJ mol^{-1} in case of probability distribution of λ and thermodynamic integration, respectively. A typical example of $\langle \frac{\partial U}{\partial \lambda} \rangle$ as a function of λ is shown in Figure 3.2.

The Gibbs-Duhem integration test was performed based on the values of μ_{ex} of HCOOH and H_2O computed from the probability distribution of λ. The values of $\ln\left(\frac{\gamma_1}{\gamma_2}\right)$ for four studied force fields as a function of HCOOH mole fraction are shown in Figure A.1 of Appendix A. Table 3.1 shows the results of this integration. For further studies, we selected the FF-2 force field [174], as the OPLS/AA force field is a well-established, broadly applicable and extensively developed force field for organic molecules [149]. The HCOOH force field FF-2 is used for all simulations in the remainder of this chapter. The activity coefficients and densities for HCOOH and H_2O obtained using all the studied force fields, are listed in Tables A.9 and A.10 of Appendix A.

For validation of the FF-2 HCOOH/H_2O SPC/E force fields the simulated HCOOH/H_2O densities were compared with experimental densities found in literature [193] in Figure 3.3. Three temperatures were considered: 288.15 K, 298 K, and 308.15 K. The values of the calculated densities differ from the experimental ones by 0.52% – 4.82%. The order of magnitude for uncertainty values is ca. 1 g cm^{-3}.

The FF-2 force field was further validated for a pure HCOOH system. The VLE phase diagram was simulated for a temperature range from 335 K to 560 K and compared with experimental values [172] and simulation results of Miná ry et al. [194] (see Figure 3.4). The computed VLE curve fits well with the experimental values up to 510 K. At higher temperatures, the line starts to diverge from the experimental values. The average uncertainty of computed densities is 0.021 mol L^{-1}. The VLE curve obtained using FF-2 force field is

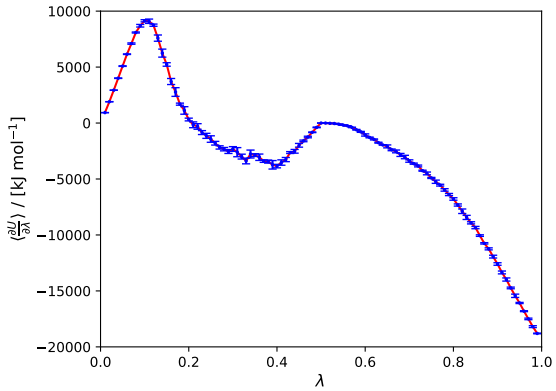

Fig. 3.2. $\langle \frac{\partial U}{\partial \lambda} \rangle$ as a function of λ for a HCOOH/H_2O system containing a fractional molecule of HCOOH. $x_{\mathrm{HCOOH}} = 0.1$, $T = 298$ K, and $P = 1$ bar. The values of $\langle \frac{\partial U}{\partial \lambda} \rangle$ were obtained from 99 independent simulations at different fixed values of λ. The blue points represent the values of $\langle \frac{\partial U}{\partial \lambda} \rangle$ and the red line is a fitted spline. The error bars of $\langle \frac{\partial U}{\partial \lambda} \rangle$ were computed as the standard deviation from five independent simulations. The integration of the fitted spline resulted in μ_{ex} of HCOOH equals to -24.5 ± 0.1 kJ mol^{-1}.

Table 3.1: Gibbs-Duhem integration test results for the four studied HCOOH/H_2O force fields. All the studied force field resulted in the Gibbs-Duhem integral equals to zero within the error bars. The subscripts show uncertainties computed using error propagation rules.

Force field	$-\int_{\mathbf{0}}^{\mathbf{1}} \ln\left(\frac{\gamma_1}{\gamma_2}\right)\mathbf{dx_1}$
FF-0	$0.08_{0.10}$
FF-1	$0.01_{0.13}$
FF-2	$-0.03_{0.11}$
FF-3	$0.02_{0.16}$

less deflected from the experimental data than the simulation results of Mináry et al. [194] using the HCOOH model of Jedlovszky and Turi [163].

The saturated vapor pressure of pure FA was computed from series of *NPT* simulations of vapor phase and calculated using the liquid phase properties from Gibbs Ensemble simulations using Eq. 3.10. The results were compared with experimental data [172] as a function of temperature, as shown in Figure 3.5. In the case of vapor phase simulations, the vapor pressures of pure FA differ from the experimental ones by 13.26% – 64.74%. The average deviation equals to 29.66%. The uncertainties are close to zero, due to the small

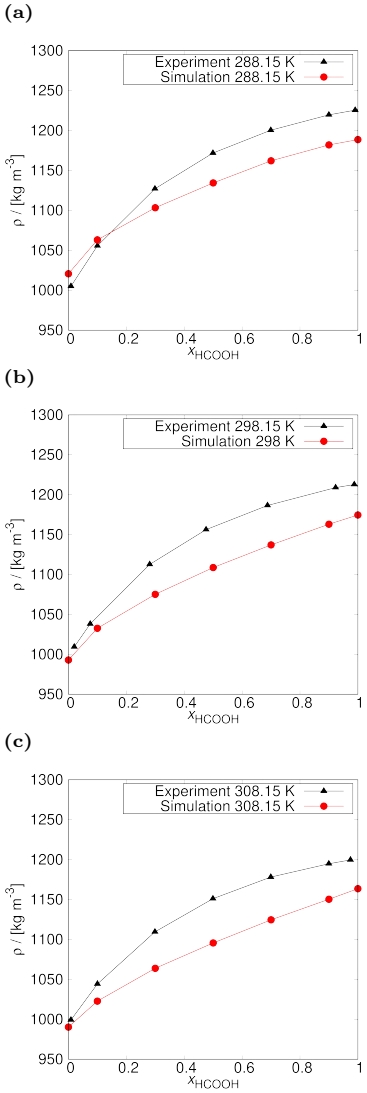

Fig. 3.3. Densities of HCOOH/H_2O systems as a function of the mole fraction of HCOOH compared to the experimental values [193], at (a) 288.15 K, (b) 298 K, and (c) 308.15 K and 1 bar. Calculated values of density differ from experimental by 0.71% – 3.19% for 288.15 K, 0.52% – 4.16% for 298 K, and 0.90% – 4.82% for 308.15 K. The uncertainties were computed as the standard deviation from five independent simulations. The error bars are smaller than the size of the symbols.

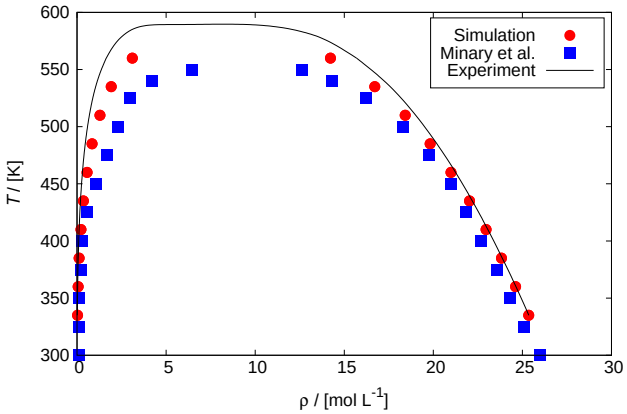

Fig. 3.4. Vapor-liquid equilibrium curve of pure HCOOH. The coexistence densities were reproduced for a temperature range from 335 K to 560 K and compared with experimental data [172] and simulation results of Mináry et al [194]. The uncertainties were computed as the standard deviation from five independent simulations. The error bars are smaller than the size of the symbols. The average uncertainty of the computed densities is 0.021 mol L^{-1}. The simulated VLE curve fits well with the experimental values up to 510 K, after which values start to diverge. The critical values of temperature and density were determined (experimental values in parentheses): T_c = 610.19 (588.00) [172] K, ρ_c = 7.39 (8.00) [172] mol L^{-1}, leading to the differences relative to the experimental values respectively 3.8% and 7.6%.

number of molecules used in the simulation of the vapor box. The average uncertainty equals to 0.1 MPa. The configurations of computed systems were visualized, and the presence of dimers was confirmed in the gas phase of our simulations (see Figure A.2 in Appendix A). The formation of dimers in FA is experimentally proven and leads to non-ideal gas behavior [162, 169]. The values of saturated vapor pressures calculated using Eq. 3.10, differ from experimental data by 37.84% - 1.19%. The difference decreases with increasing vapor pressure. The average uncertainty of the calculated pressures is equal to 0.02 MPa.

The dependence of the Henry coefficient of CO_2 on the mole fraction of HCOOH and NaCl concentration in the mixture was computed. The results are presented in Figures 3.6 and 3.7. In Figure 3.7, literature values for CO_2 solubility in H_2O/NaCl system are shown for comparison. These are as follows: (1) experimental Henry coefficients of CO_2 for H_2O/NaCl system at 293.8 K from a study of Weiss et al. [196], (2) Henry coefficients calculated from experimental solubilities at 298.15 K from a study of Harned et al. [197], (3) Henry

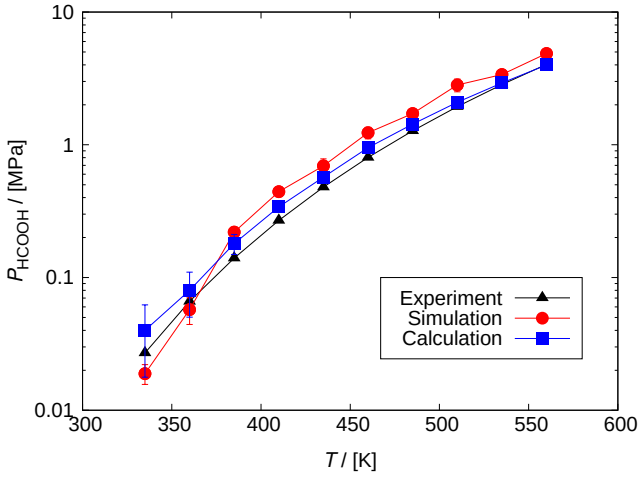

Fig. 3.5. Comparison of the saturated vapor pressures of HCOOH computed from series of *NPT* simulations of vapor phase and calculated using the liquid phase properties from Gibbs Ensemble simulations with experimental values [172] as a function of temperature. In the case of the vapor phase simulations, the differences between simulations and experiments vary by 13.26% - 64.74%, due to the small number of molecules used in the simulation. The saturated vapor pressures calculated using Eq. 3.10 differ from experimental values by 37.84% - 1.19%, whereby with increasing vapor pressure, the difference decreases. The values of the HCOOH vapor pressures are shown in Table A.11 of Appendix A. The uncertainties are computed as the standard deviation obtained from five independent Gibbs Ensemble simulations. In case of the vapor pressures of pure HCOOH computed from the series of *NPT* simulations ($P_{\mathrm{HCOOH,sim}}$), the average uncertainty equals to 0.1 MPa. The average uncertainty of the values calculated by Eq. 3.10 is equal to 0.02 MPa.

coefficients calculated from experimental solubilities at 303.15 K from a model of Duan et al. [50]. From the comparison with literature, it is shown that the Henry coefficient of CO_2 computed in this study are in the correct range. The average deviation from the experimental values at 298.15 K [197] is 31%. The reason of deviations from the experimental data is non-ideal gas behavior.

In Figure 3.8, vapor pressures for systems with different NaCl concentrations are shown as a function of the pseudo-mole fraction of HCOOH. Due to the lack of experimental data at 298.15 K, the experimental vapor pressures for a system without added NaCl are shown for comparison at 291.15 K [187] and 303.15 K [188, 189]. The difference between temperature used in our study and temperature of the experimental vapor pressures for a system without NaCl is very small and the resulting vapor pressures are comparable.

The computed vapor pressures are in the correct range but show a relat-

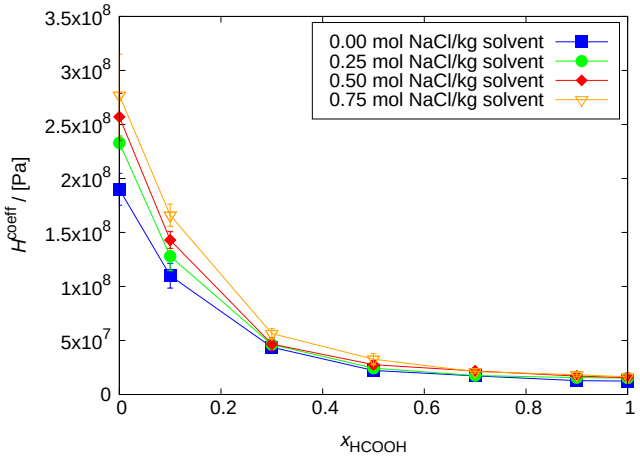

Fig. 3.6. Henry coefficients of CO_2 computed for several NaCl concentration as a function of the pseudo-mole fraction of HCOOH at 298.15 K. The lines connecting the symbols are used to guide the eye. The solubility of CO_2 decreases with the increase of the NaCl concentration in the solution, but increases with the HCOOH concentration. The uncertainties were computed as the standard deviation from five independent simulations. The uncertainty decreases with the increase of HCOOH concentration. For $x_{\mathrm{HCOOH}} = 0$, the order of magnitude of the error bars is $1 \cdot 10^7$ Pa, for $x_{\mathrm{HCOOH}} = 0.3$ this drops to $1 \cdot 10^6$. Compared to the experimental Henry coefficient for CO_2 in water, which is $1.62 \cdot 10^8$ Pa at 298.15 K [195], simulated value differs by 16.9% and equals to $1.90 \cdot 10^8 \pm 1 \cdot 10^7$ Pa.

ively high deviation from experimental values. The simulations result in a low-boiling azeotrope in sharp contrast to the NRTL-HOC computations [17] that indicate high-boiling azeotrope behavior of the HCOOH/H_2O system (see Figure A.3 of Appendix A). Our first estimate of the HCOOH/H_2O/NaCl model did not describe the azeotrope accurately due to the non-ideal gas behavior caused by dimer formation, which was confirmed by visually inspecting characteristic configurations of the simulations as shown in Figure A.4 of Appendix A. Achieving the same magnitude of computed and experimentally measured vapor pressures is considered as sufficient for our for HCOOH/H_2O/NaCl model without any adjustments. Additionally, the calculation of HCOOH dimer and monomer partial vapor pressures are presented in Table A.12 of Appendix A. The calculated dimer partial vapor pressures are found to be higher than monomer partial vapor pressures, confirming that the non-ideal dimer formation behavior is the reason why our model does not reproduce vapor pressures and azeotropic behavior more precisely than the order of magnitude. The Sechenov constants for each studied pseudo-mole fraction of HCOOH are lis-

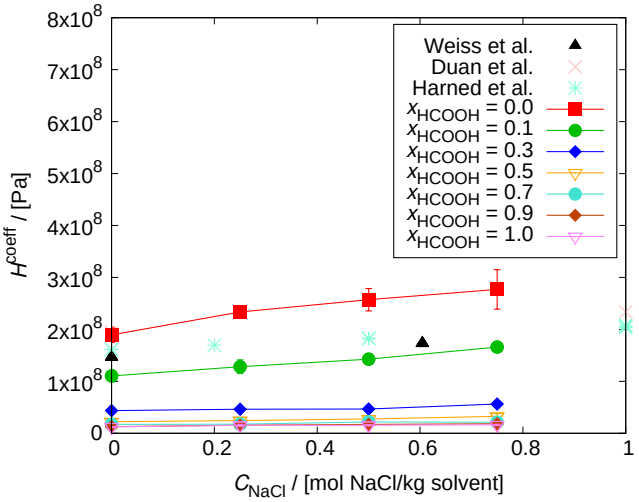

Fig. 3.7. Henry coefficients of CO_2 computed for different HCOOH pseudo-mole fractions as a function of the NaCl concentration in the solution at 298.15 K. The lines connecting the symbols are used to guide the eye. The solubility of CO_2 decreases with the increase of the NaCl concentration in the solution but increases with the HCOOH concentration. The uncertainties were computed as the standard deviation from five independent simulations. The uncertainty decreases with the increase of HCOOH concentration. The experimental Henry coefficients of CO_2 for the H_2O/NaCl system at 293.8 K from a study of Weiss et al. [196] are displayed as black points. The Henry coefficients calculated from experimental solubilities at 298.15 K from a study of Harned et al. [197] are displayed as yellow points. The calculated Henry coefficients from a model of Duan et al. [50] at 303.15 K are displayed as grey points.

ted in Table 3.2. The value of K calculated using model parameters [192] for CO_2/NaCl system is 0.1117 m^3 $kmol^{-1}$. The computed K for different pseudo-mole fraction of HCOOH show a scattering but are of the same order of magnitude. The experimental solubility of NaCl in pure formic acid is 0.89 mol per kg of solvent at 298.15 K [198]. NaCl is still soluble for all studied concentrations in the simulated systems.

The solubility of CO_2 increases with the HCOOH concentration (decrease in Henry constant), leading to the highest solubility for pure formic acid and the lowest in the case of pure water. The CO_2 solubility decreases with the increase of NaCl concentration in the solution. This trend continues up to $x_{\mathrm{HCOOH}} = 0.3$ in the solution, after which the concentration of NaCl has no significant effect on the CO_2 solubility. This effect is described as salting out, where an increase in the ionic strength of a solution decreases the solubility of a

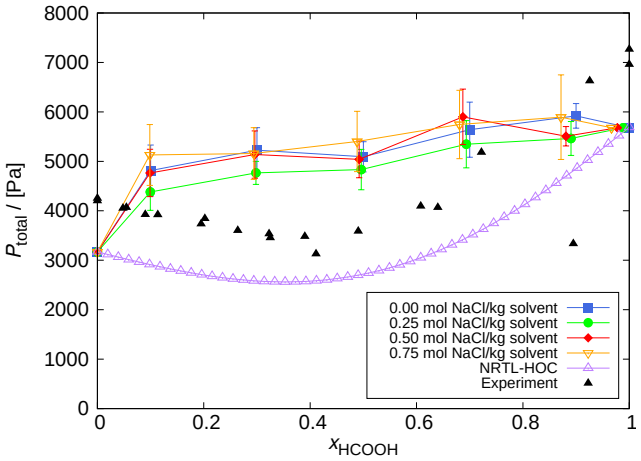

Fig. 3.8. The total vapor pressure (P_{H2O} + P_{HCOOH}) for systems of certain NaCl concentrations, as a function of the HCOOH mole fraction at 298.15 K. The lines connecting the symbols are used to guide the eye. For comparison, vapor pressures of the NRTL-HOC model at 298.15 K [17] and experimental vapor pressures at 291.15 K [187] and 303.15 K [188, 189] for a system without NaCl are also shown. The uncertainties were computed as the standard deviation from five independent simulations.

Table 3.2: Sechenov constants for each studied pseudo-mole fraction of HCOOH. The value of K calculated using model parameters [192] for the CO_2/NaCl system is 0.1117 m^3 $kmol^{-1}$. The error bars were computed as the standard deviation from 5 independent simulations. The computed values of K for different pseudo-mole fractions of HCOOH are in the same order of magnitude.

x_{HCOOH}	$K/[m^3\ kmol^{-1}]$
0	$0.2_{0.1}$
0.1	$0.23_{0.08}$
0.3	$0.11_{0.04}$
0.5	$0.19_{0.06}$
0.7	$0.13_{0.09}$
0.9	$0.19_{0.06}$
1	$0.16_{0.05}$

solute. The more notable decrease in the CO_2 solubility for systems consisting predominantly of water can be explained by the fact that when salt ions such as NaCl are added to water, water molecules are bound to "solvates", leaving fewer water molecules for CO_2 to adhere to. Upon salt addition, weak attractions of CO_2 molecules to water are decreased and dissolved CO_2 is displaced from

polar water. Studies on the hydration of ions and the interaction of ions with water molecules have shown that, at a high density, smaller ions tend to bind the molecules of water more effectively, while larger ions with a low charge density bind the water molecules weakly [199, 200]. Similar results for CO_2 solubility in water in the presence of salt ions are presented in the literature [50–53]. Salting out effects were shown in a study by Liu et al. [51], where systems consisting of distilled water and various concentrations of NaCl, $MgCl_2$, $CaCl_2$ and $MgCl_2$ + $CaCl_2$ were studied. The solubilities of CO_2 were measured in pure distilled water and salinities of 1000, 10000 and 15000 ppm at 298 K. In all cases, a decrease in CO_2 solubility was observed as salinity increases. In a study by Koschel [52], the effect of NaCl concentrations on CO_2 solubility in water was studied at 323.1 K and 2 – 20 MPa, and at 373.1 K and 5 – 20 MPa. For both temperatures salting out was observed, in line with the findings by Liu et al. [53] on the effects of NaCl + KCl + $CaCl_2$ at various temperatures.

An interesting research topic is to investigate if other chemicals may enhance the CO_2 solubility. Salting-in effects are possible by using salts like $NaClO_4$ [201]. In the aqueous $NaClO_4$ solutions, mutual affinity occurs between the ClO^{4-} anion and CO_2 [202]. This results in an increase in the solubility of CO_2. For most salting-out salts, the salting effect is possible to predict based on the viscosity B-coefficients [203], that describe the change of water mobility induced by salts. The salting-in effect is more specific and complex than the salting-out. It cannot be predicted by the viscosity B-coefficients of salts. In the most of cases there is a correlation between salting out Sechenov constant and viscosity B-coefficient [201]. The structure maker ions (positive value of viscosity B-coefficients) strengthen the water-water hydrogen bond network and reduce the entropy of water. The solubility of the non-polar solutes decreases. The salting-in $NaClO_4$ is an exception. It has a positive value of the viscosity B-coefficient (0.012 [203]), which inconsistency is not well understood due to the lack of knowledge on the underlying molecular mechanism [201].

3.6 — Conclusions

We present a study on the solubility of CO_2 in aqueous solutions of HCOOH and the effect of adding NaCl to the system. All the studied HCOOH/SPC/E force fields resulted in the Gibbs-Duhem integral equals to zero within the error bars, even though they were not parameterized explicitly for mixtures with water. To investigate the compatibility of the other HCOOH force fields with the SPC/E force field, more research is required. The Continuous Frac-

tional Component Monte Carlo method turns out to be able to compute excess chemical potential with sufficient accuracy. The routes used to compute the excess chemical potentials of HCOOH and H_2O i.e., (1) from the probability distribution of the scaling factor, and (2) thermodynamic integration, resulted in excess chemical potentials that differ by approximately less than 0.5%. The method using $p(\lambda)$ is precise enough to reproduce μ^{ex}. Validation of the selected force field by comparing the density, vapor-liquid equilibrium and vapor pressure with the experimental values showed a high accuracy of the model. Based on the most compatible model FF-2 HCOOH/H_2O SPC/E, we observe the salting out effect of NaCl on CO_2 solubility, which should be considered in further research in the field of CO_2 reduction. From an economical point of view, the salting out effect is unprofitable because it reduces the amount of product obtained. It is also disadvantageous from an ecological point of view, as less CO_2 would be reduced and removed from the environment. It would be interesting to investigate if other chemicals may enhance the CO_2 solubility and hence the efficiency of the CO_2 conversion without decreasing ionic conductivity of an electrolyte solution. An important observation is that CO_2 solubility increases (Henry coefficient decreases) with HCOOH fraction in the solution. HCOOH production may be a better alternative to elevating CO_2 pressure to modify solubility.

Chapter 4

Enhancement of Formic Acid Production from Carbon Dioxide Hydrogenation Using Metal-Organic Frameworks

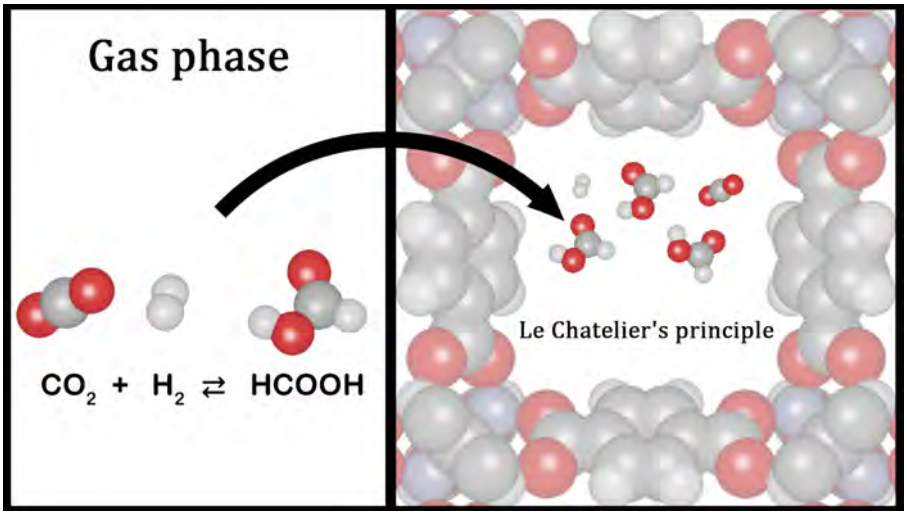

Formic acid production from CO_2 allows the reduction of carbon dioxide emissions while synthesizing a product with a wide range of applications. CO_2 hydrogenation is challenging due to the cost of transition metal catalysts and the toxicity of the transition elements. In this work, the thermodynamic confinement effects of the metal-organic framework UiO-66 on the CO_2 hydrogenation to formic acid were studied by force field-based molecular simulations. The confinement effects of UiO-66 and the metal-organic frameworks Cu-BTC, and IRMOF-1 were compared, to assess the impact of different pore size and metal centers on the production of HCOOH. Monte Carlo simulations in the grand-canonical ensemble were performed in the frameworks, using gas phase mole fractions of CO_2, H_2, and HCOOH at chemical equilibrium, obtained from Continuous Fractional Component Monte Carlo simulations in the Reaction Ensemble. The adsorption isobars of the components in metal-organic frameworks were computed at 298.15 - 800 K, 1 - 60 bar. The enhancement of HCOOH production due to preferential adsorption of HCOOH in metal-organic frameworks was calculated for all studied conditions. UiO-66, Cu-BTC, and IRMOF-1 affect CO_2 hydrogenation reaction, shifting the thermodynamical equilibrium towards HCOOH formation. The prevailing factor is the type of metal center in the metal-organic framework. The confinement effect of Cu-BTC turns out to exceed the enhancement caused by UiO-66, and IRMOF-1. The resulting mole fraction of HCOOH increased by ca. 2000 times compared to the gas phase at 298.15 K, 60 bar. Cu-BTC can be considered as an alternative to improve the production of HCOOH due to elimination of the high-cost temperature elevation, cost reduction of downstream processing methods, and comparable final concentration of HCOOH to the reported concentrations of formate obtained using transition metal catalysts.

This chapter is based on the following publication:
Wasik, D. O., Martín-Calvo, A., Gutiérrez-Sevillano, J. J., Dubbeldam, D., Vlugt, T. J. H., Calero, S. Enhancement of Formic Acid Production from Carbon Dioxide Hydrogenation Using Metal-Organic Frameworks: Monte Carlo Simulation Study. *Chemical Engineering Journal* **2023**, *467*, 143432.

4.1 — Introduction

Since the beginning of the industrial era in 1750, the carbon dioxide level in the atmosphere has increased from ca. 277 parts per million (ppm) [204] to ca. 412.4 ppm in 2020 [205]. Technological efforts are made to reduce CO_2 emissions by the capture at the source and conversion to useful feedstock chemicals, such as formic acid [4]. The market value of HCOOH is expected to increase from 1.5 billion dollars to 4 billion dollars in the next 10 years [31], which corresponds to the increase in the expected market demand. One of the methods for producing HCOOH is the electrochemical reduction of CO_2 in an aqueous electrolyte solution [12, 14, 15, 17, 206]. The electrocatalytic reduction of CO_2 to HCOOH has disadvantages due to the low solubility of CO_2 in aqueous solutions, being a consequence of salting-out effects [16]. The possible solutions to increase the yield of the process include high-cost elevation of the CO_2 pressure [14] or the use of a gas diffusion electrode, but in this case fouling and/or undesired crystallization takes place [47–49].

The hydrogenation of CO_2 into HCOOH is challenging due to the high kinetic and thermodynamic stability of CO_2 [18]:

$$CO_2 + H_2 \rightleftarrows HCOOH \tag{4.1}$$

The carbon atom in CO_2 is in the highest formal oxidation state (+4) [19]. In a study by Ghara et al. [19], the free energy change for CO_2 hydrogenation to HCOOH was computed as 41.84 kJ mol^{-1}. The free energy barrier of CO_2 hydrogenation in the gas phase was found to be 351.46 kJ mol^{-1}. This high value indicates that the use of catalyst is needed to mediate the reduction. Over the past few decades, transition metal based catalysts for CO_2 hydrogenation have been developed. The most efficient catalytic systems consist of catalysts with phosphine ligands [54–58], pincer ligands [59–61], N-heterocyclic carbene ligands [62–64] and half-sandwich catalysts with/without proton-responsive ligands [65–69]. The cost of transition metal catalysts and the toxicity of the transition elements are two major limitations in their usage [19]. It is therefore crucial to investigate the possibilities of improving the CO_2 hydrogenation efficiency with a simultaneous decrease of cost and toxicity. Attempts to design transition metal-free homogeneous catalysts have been made by, e.g. studies on the potential application of frustrated Lewis pairs (FLPs) [19, 207, 208]. The FLPs have the ability to activate small, and stable molecules as an alternative strategy. In a study by Stephan et al. [207], it was shown that $B(C_6F_5)_3$ and tBu$_3$P in C_6H_5Br can bind CO_2 reversibly under mild conditions. The activation of H_2 and insertion of CO_2 into a B-H bond in the first homogeneous process for hydrogenation of CO_2 to CH_3OH

was presented in a study by Ashley et al. [208] However further investigation on the stability of the system was necessary. The first catalytic process of CO_2 hydrogenation to formate in the presence of transition metal-free catalyst (BCF/M_2CO_3 , M = Na, K, and Cs) was disclosed by Zhao et al. [209], resulting in high turnover number (ca. 4000). The confinement effect of porous materials on the thermodynamical equilibrium of the reaction may also be considered as an alternative to the transition metal catalysts. The effects of confinement that might affect reaction equilibrium are: (a) the higher density of pore phase compared to the bulk-phase, resulting in an increase in yield for reactions in which there is a decrease in the total number of moles, by Le Chatelier's principle [44], (b) vicinity of the neighboring pore walls affecting the molecular orientation, (c) the selective adsorption of favored components on the solid surfaces [70]. The interactions between the framework and the adsorbates result in favoring some components and disfavoring others. The separation of favored components from the other components of the mixture causes their enhanced formation by Le Chatelier's principle [44]. Previous studies on the reactions carried out in confinement showed a shift in the thermodynamic equilibrium [70, 210–215].

Metal-organic frameworks (MOFs) are a class of porous materials that contain organic ligands and metal clusters linked by coordination bonds [100]. The high density of catalytic sites in high-area porous solids and the controllable porous structure initiated intensive research in the area of MOFs [92, 216, 217]. The main goal is preparing new MOF structures to investigate their applications mainly in gas storage [80] and separation [82]. Recently, MOFs have gained attention as potential catalysts [84, 85, 218–220]. The application of MOFs in catalysis has been already been successful, e.g., in a process of methane reforming [221], palladium-catalyzed reactions (alcohol oxidation, Suzuki C–C coupling, and olefin hydrogenation) [84], and isomerizations of terpenes, terpene epoxides, and ketals [85]. MOF-based catalysts show a better economic performance, recyclability, longer life span, and relatively lower carbon emissions than previously used Ni-based catalysts [93, 221]. In the study of Ong et al. [221], MOF-based catalysts were considered as an alternative to conventional transition metal catalysts in dry methane reforming. These catalysts have net present values of ca. 62%, 140%, and 560% higher than Ni-Ce/Al_2O_3, Ni/Al_2O_3, and Ni-HTNT, respectively, and carbon emissions of ca. 13%, 20%, and 76% lower than Ni/Al_2O_3, Ni-HTNT, and unsupported Ni, respectively. The potential advantages of MOF-based catalysts include easier catalyst separation, recycling, and recovery of a product, reduced cost of the catalyst due to metal-free catalytic sites, high thermal stability, the combination of CO_2 capture and conversion steps, pore-confinement effects, and

mild conditions of CO_2 reduction due to low reaction barriers [93]. There is a considerable interest in a metal-organic framework UiO-66 due to its superior mechanical, thermal, acidic, aqueous, and water vapor stability, high porosity, and catalytic properties of the zirconium oxide node and an easy lab-scale synthesis [96]. UiO-66 is a framework containing metal nodes composed of a zirconium oxide complex bridged by terepthalic acid (1,4-benzenedicarboxylic acid) ligands [96]. The adsorption of H_2 and CO_2 in UiO-66 was studied experimentally [100, 222] and computationally [223]. As a result, UiO-66 has been determined as an effective adsorbent with an adsorption of H_2 as high as 4.2 wt% at 60 bar, 77 K, and CO_2 adsorption of 35.6 wt% at 9.8 bar and 273 K [100, 101]. The adsorption performance of both reactants makes the application of UiO-66 in the CO_2 hydrogenation to HCOOH potentially promising. To the best of our knowledge, there are no literature data regarding the confinement effect of UiO-66 on the production yield of HCOOH from CO_2 and H_2. In a study by Ye and Johnson [93, 224], the catalytic activity of functionalized UiO-66 toward CO_2 hydrogenation was evaluated based on reaction energies, barriers, and geometries for the CO_2 reduction steps, computed using Density Functional Theory (DFT). Several non-metal frustrated Lewis pairs were incorporated into the linkers of the MOF. The ease of recovery, high mass transfer, and low reaction barriers make the application of the catalysts potentially promising [93, 224]. UiO-66 was also found to be an effective catalyst for CO_2 hydrogenation to CH_3OH [225]. In a study by Yang and Jiang [225], the defective UiO-66 with a frustrated Lewis pair was successfully used in a three-stage transformation of CO_2: (a) CO_2 hydrogenation to HCOOH, (b) HCOOH conversion to formaldehyde (HCHO), (c) HCHO hydrogenation to CH_3OH [225]. Given the literature data on the catalytic activity of UiO-66, an interesting research topic is to verify whether its confinement effect causes a shift in the thermodynamic equilibrium of the CO_2 hydrogenation to HCOOH. The "confinement effect" should be studied independently from the "catalytic effect", otherwise it is unclear what is caused by confinement, and what is caused by catalysis. Molecular simulations are a natural tool that allows us to "switch off" the catalysis and exclusively consider the confinement effects. The resulting shift in the thermodynamic equilibrium of the CO_2 hydrogenation can be evaluated by comparison to the gas phase studied at 400 - 1400 K and 1 bar [41]. In this work, the effect of UiO-66 confinement on the CO_2 hydrogenation reaction is studied at less industrially expensive temperatures 298.15 - 800 K and higher pressures 1 - 60 bar, which allow more molecules to enter the structure. The results were compared with the confinement effects of metal-organic frameworks Cu-BTC and IRMOF-1 to assess the impact of different pore size and metal centers on CO_2 hydrogenation reaction.

This chapter is organized as follows: in section 4.2, we provide technical details of the molecular simulation methods. In section 4.3, we define the metal-organic frameworks, and the force fields for CO_2, H_2 and HCOOH. In section 4.4, we provide detailed information on the simulations. In section 4.5, we present and discuss the results. The adsorption isobars are computed by Monte Carlo simulations in the grand-canonical ensemble, using the initial CO_2, H_2 and HCOOH mole fractions at reaction equilibrium obtained from Continuous Fractional Component Monte Carlo simulations [139–141] in the Reaction Ensemble [135, 136, 142]. The HCOOH production enhancement is calculated for all systems. The effects of UiO-66, Cu-BTC, and IRMOF-1 confinement are shown to increase the HCOOH production. Our findings are summarized in section 4.6.

4.2 — Methodology

The confinement effect by Le Chatelier's principle on the thermodynamic equilibrium of the studied reaction is analyzed using force field-based molecular simulations. The catalytic effects are absent in our model, and we fully focus on the equilibrium thermodynamics of the chemical reaction. We use the Monte Carlo (MC) Software Brick-CFCMC [143, 152] and the RASPA software package [94, 95] to perform simulations in the bulk-phase and confinement, respectively. Continuous Fractional Component Monte Carlo simulations [139–141] in the Reaction Ensemble [135, 136, 142] (Rx/CFC) were used to simulate the thermodynamic equilibrium of CO_2 hydrogenation reaction in the bulk-phase. In the Monte Carlo simulations in the Reaction Ensemble (RxMC), the reactants and products are interconverted using a series of stochastic trial moves [226]. The insertion and deletion of the reactants and reaction products during Monte Carlo (MC) trial moves in RxMC propagate the system to thermodynamic equilibrium. The activation energy barriers related to transition states are not considered as the dimention time is absent in the simulations [226]. The application of RxMC in reaction equilibrium predictions was already successful for many systems [41, 70, 227–231]. The RxMC technique is difficult to apply for high density systems since it critically relies on insertion and deletion of reactants and reaction products [142]. To improve the acceptance probabilities for insertion and deletion trial moves in RxMC, the Continuous Fractional Component Monte Carlo (CFCMC) method [139–142] is applied. Fractional molecules are introduced to the system and their interactions with the surroundings are scaled by a parameter $\lambda \in [0, 1]$. When $\lambda = 0$, fractional molecules are considered as ideal gas molecules. For $\lambda = 1$, fractional molecules have the same interactions with the surroundings as the

other molecules (not being a fractional molecule). The surroundings can easily adapt to the inserted/deleted molecules, which is of particular importance at high densities (e.g., computation of the loading and enthalpy of adsorption of guest molecules in porous materials near the saturation loading [144] and reaction equilibria of complex systems [145]). The chemical reaction is a MC trial move to ensure chemical reaction equilibrium. The required ideal-gas partition functions in combination with the medium/surrounding of molecules effects are used to describe the chemical reaction equilibrium [142]. The force field describing interactions between molecules, the ideal gas partition functions of all reactants and reaction products and the stoichiometry of the chemical reactions in the system are used as input for Rx/CFC simulations [142]. The stoichiometry of the studied CO_2 hydrogenation (Eq. 4.1) is 1:1:1 for CO_2:H_2:HCOOH. The ideal gas partition functions were obtained based on the vibrational and rotational experimental data from the NIST database [232–236], see Table B.1 of Appendix B. For details about computation and prediction of ideal-gas partition functions the reader is referred to the book by McQuarrie et al. [156]. To validate our approach, the equilibrium composition of syngas from the study of Rahbari et al. [41] was reproduced assuming the ideal gas behavior by Rx/CFC simulations, see Figure B.1 of Appendix B. The composition of the systems studied in this work by Rx/CFC simulations consists of equal number of CO_2 and H_2 molecules (200) according to the stoichiometry of the CO_2 hydrogenation reaction. Simulations were performed at 298.15 - 800 K and 1 - 60 bar.

The next step is to investigate the effect of UiO-66 on the equilibrium of the CO_2 hydrogenation reaction. The combination of the force fields of HCOOH and MOFs cannot be investigated due to the lack of adsorption data available. For the estimation, the compatibility of the HCOOH force field with the framework was validated by simulating the HCOOH density in the pores of the framework close to the maximum loading and comparing to the experimental data. It is necessary to compute the helium void fraction (ξ) of the framework to perform simulations of the system in confinement. This is required to calculate the HCOOH density taking into account the empty space of a structure. These simulations use a probe helium atom exploring the structure using Widom's particle insertion method to measure the energy required for insertion of the particle in the system or the energy obtained by inserting the particle [94, 237]. The computed value of the ξ was compared to literature data [238]. To reach the maximum pore loading, the GCMC simulation of HCOOH adsorption in UiO-66 was performed at low temperature (77 K, 1000 bar). The obtained density of HCOOH was compared to the experimental [186] and simulated [206] density of liquid HCOOH. The HCOOH

density at the maximum pore loading in units of kg m^{-3} was calculated by:

$$\rho = \frac{M \cdot N}{\xi \cdot V \cdot N_A} \tag{4.2}$$

where M is the molar mass of HCOOH in units of kg mol^{-1}, N is the number of molecules in the unit cell, ξ is the helium void fraction, V is the volume of the UiO-66 unit cell in units of m^3, and N_A is Avogadro's constant.

The adsorption isobars of the studied systems were computed from Monte Carlo simulations in the grand-canonical ensemble (GCMC) [128]. In the GCMC ensemble, the chemical potential, volume, and temperature are fixed. The mole fractions of CO_2, H_2 and HCOOH at the reaction equilibrium obtained from Rx/CFC simulations were used in the GCMC simulations as the input data. The fugacity coefficients are computed using the Peng-Robinson Equation of State (PR-EoS) [157] to convert pressure to fugacity, using the RASPA software package [94, 95]. The chemical potential is directly obtained from the fugacity [94]:

$$\beta\mu_i = \beta\mu_{i0} + \ln\left(\beta\frac{f}{P_0}\right) \tag{4.3}$$

where μ is the chemical potential of component i for a non-ideal gas, $\beta = 1/(k_B T)$, f is the fugacity of the mixture, P_0 is the reference pressure equal to 1 bar, μ_{i0} is the reference state of the chemical potential of component i. The initial mole fractions and fugacity coefficients are listed in Tables B.4 and B.5 of Appendix B. The fugacity coefficients for the mixtures of CO_2, H_2, and HCOOH computed using the Peng-Robinson equation of state [157] were compared with the fugacity coefficients for binary mixtures of CO_2, and H_2 obtained from the NIST Standard Reference Database REFPROP [239]. Very good agreement between the computed fugacity coefficients and the database is shown in Table B.5 of Appendix B. The mole fractions obtained from Rx/CFC simulations are used as input in simulations in the GCMC ensemble, as in the study by Matito-Martos et al. [240]

To calculate the standard deviations of the computed number of molecules in the bulk-phase, the Brick-CFCMC simulations were performed five times starting from independent configurations and using different random number seeds. The algorithms provided in Brick-CFCMC [143, 152] are used to generate random initial configurations. The uncertainties in the computed number of molecules adsorbed in a unit cell were provided by the RASPA software package [94] and were used in the case of simulations in UiO-66. The simulation is divided into five blocks and the error is computed by calculating the standard

deviation. Due to the high uncertainties in simulations using Cu-BTC and IRMOF-1, the simulations in both the MOFs were performed five times to calculate the standard deviations of the computed number of molecules adsorbed in the confinement. The uncertainty of the HCOOH density at the maximum pore loading (Err_ρ) is calculated based on error propagation [241]:

$$Err_\rho = \frac{M}{V \cdot N_\mathrm{A}} \cdot \rho \cdot \sqrt{\left(\frac{Err_N}{N}\right)^2 + \left(\frac{Err_\xi}{\xi}\right)^2} \tag{4.4}$$

where M is the molar mass of HCOOH, V is the average volume of the UiO-66 unit cell, N_A is Avogadro's constant, N is the number of molecules in the unit cell, ξ is the helium void fraction, ρ is the HCOOH density, Err_N is the uncertainty of the computed number of molecules adsorbed in a unit cell, and Err_ξ is the uncertainty of the helium void fraction.

The uncertainties in the obtained mole fractions are expressed by Err_x and calculated as:

$$Err_{\sum N} = \sqrt{{Err_{N_{\mathrm{CO_2}}}}^2 + {Err_{N_{\mathrm{H_2}}}}^2 + {Err_{N_{\mathrm{HCOOH}}}}^2} \tag{4.5}$$

$$Err_x = x \cdot \sqrt{\left(\frac{Err_N}{N}\right)^2 + \left(\frac{Err_{\sum N}}{\sum N}\right)^2} \tag{4.6}$$

where Err_N is the uncertainty of the computed number of molecules adsorbed in a unit cell, $Err_{\sum N}$ is the uncertainty of the total number of molecules of all components adsorbed in a unit cell, x is a mole fraction of the component, and N is the computed number of molecules of the component.

To analyze the resulting production of HCOOH, the interactions between an adsorbate molecule and the framework were studied. The isosteric heat of adsorption [242] was computed for CO_2, H_2 and HCOOH in UiO-66 at 298.15 - 800 K. The affinity of the molecule with the framework can be expressed as the binding energy. The enthalpy of adsorption at infinite dilution is calculated by [158]:

$$\Delta H = \Delta U - RT = \langle U_{hg} \rangle - \langle U_h \rangle - \langle U_g \rangle - RT \tag{4.7}$$

where ΔU is the internal energy of the system, $\langle U_{hg} \rangle$ is the average energy of the guest molecule inside the host framework, $\langle U_h \rangle$ is the average energy of the host framework which is equal to 0 J for rigid frameworks, $\langle U_g \rangle$ is the average energy of the guest molecule which is equal to 0 J for rigid molecules, R is the universal gas constant and T is the temperature.

To compare the mole fractions of HCOOH obtained from GCMC simulations to the bulk-phase at the same chemical potential, the enhancement

(*ENH*) of HCOOH production is calculated as:

$$ENH = \frac{x_{\mathrm{GCMC}}}{x_{\mathrm{Rx/CFC}}} \tag{4.8}$$

where x_{GCMC} and $x_{\mathrm{Rx/CFC}}$ are mole fractions of HCOOH obtained from GCMC simulations and Rx/CFC simulations, respectively. The pore size distributions of the studied UiO-66, Cu-BTC, and IRMOF-1 frameworks were computed to analyze, whether the enhancement in the production of HCOOH in MOFs results from increased confinement or different metal centers, see Figure B.2 of Appendix B.

4.3 — Force Field

The guest-host and guest-guest intermolecular interactions are modeled by Coulombic and Lennard-Jones (LJ) interaction potentials, except for the interaction between C and O atoms of CO_2 molecules that are specified by an override. The Lorentz–Berthelot mixing rules [129] are used to define interactions between unlike Lennard–Jones sites. Explicit polarization effects are neglected and accounted for in the LJ interactions. The so-called 'P2' variant of the OPLS/AA force field for HCOOH from the study of Salas et al. [174] was used. The HCOOH molecule was constructed and its geometry was optimized at the B3LYP/6-31G(d) level of theory [206]. The interaction sites of the model are at the atom positions. The cutoff radius for intermolecular interactions is set to 12 Å. In the Rx/CFC simulations, LJ interactions are truncated with analytic tail corrections applied. In the GCMC simulations, LJ interactions are cut and shifted to zero at the cutoff with the tail corrections omitted, due to the generic force field for MOFs being used. Periodic boundary conditions are exerted in all three directions. The Ewald summation method [151] is used for calculating electrostatic interactions. The Ewald summation method parameters correspond to a relative precision of 10^{-6}. The so-called 'P2' variant of the OPLS/AA force field for HCOOH [174] was validated in our previous work [206] by reproducing the vapor-liquid equilibrium coexistence curve, saturated vapor pressures, and densities at different temperatures. The interaction parameters of the HCOOH force field are used in this work together with the three-site charge-quadrupole model by Darkrim and Levesque for H_2 [243] and the García-Sánchez et al. force field for CO_2 [176]. The models of the framework and guest-host interaction used in this work are rigid, and all atoms of the molecules have point charges assigned. The atomic positions of HCOOH are listed in Table A.1 of Appendix A. The atomic positions of CO_2, and H_2 molecules are listed in Table B.2 of Appendix B. The structures of triclinic UiO-66, cubic Cu-BTC, and cubic IRMOF-1 crystal sys-

tems are rigid, with the atoms of the frameworks at crystallographic positions. The UiO-66, Cu-BTC, and IRMOF-1 cell parameters are listed in Table B.3 of Appendix B. LJ parameters for the atoms of the framework are from the DREIDING force field [148], except for zirconium and copper, which is from the UFF force field [147]. The force fields for UiO-66, and Cu-BTC containing parameters from DREIDING, and UFF were already validated with experimental data by Jajko et al. [238], Frost et al. [158], Dubbeldam et al. [244], Jajko et al. [245], and Gutiérrez-Sevillano et al. [246] Point charges for UiO-66 were obtained using the EQeq method [247] and modified as in the study of Jajko et al. [238] The atomic charges for the Cu-BTC and IRMOF-1 were taken from Frost et al. and Dubbeldam et al. [244] The LJ parameters and partial charges for all components, the framework and the probe helium atom [248] used in this work are listed in Table 4.1.

Table 4.1: LJ interaction parameters for the UiO-66, Cu-BTC, and IRMOF-1 frameworks [147, 148], a probe helium atom [248], HCOOH [174], CO_2 [176], and H_2 [243]. Figure 3.1 of Chapter 3 shows a schematic representation of the HCOOH model with all atoms labeled.

Atom	ϵ/k_B /[K]	σ /[Å]	q /[e$^-$]
He	10.9	2.64	0
O_{CO_2}	85.671	3.017	-0.3256
C_{CO_2}	29.93	2.742	0.6512
C_{fa1}	49.6728	3.67	0.52
O_{fa2}	99.34559	2.9	-0.44
H_{fa1}	7.09611	2.37	0
O_{fa1}	80.46271	2.94	-0.53
H_{fa2}	1	1	0.45
H_{com}	36.7	2.958	-0.936
H_{H_2}	0	0	0.468
UiO-66			
Zr	34.7221	2.78317	4.503
C1	47.86	3.473	0.529571
C2	47.86	3.473	0.0131923
C3	47.86	3.473	-0.137721
O1	48.19	3.0331	-0.739224
O2	48.19	3.0331	-3.30054
H1	7.65	2.8464	0.0373778
H2	7.65	2.8464	0.241634
Cu-BTC			
Cu	2.518	3.114	1.248
O	48.19	3.0331	-0.624
C1	47.86	3.473	0.494
C2	47.86	3.473	0.13
C3	47.86	3.473	-0.156
H	7.65	2.8464	0.156
IRMOF-1			
Zn	27.7	4.04	1.275
O1	48.19	3.0331	-1.5
O2	48.19	3.0331	-0.6
C1	47.86	3.473	0.475
C2	47.86	3.473	0.125
C3	47.86	3.473	-0.15
H	7.65	2.8464	0.150

4.4 — Simulation Details

Each simulation in the Rx/CFC ensemble was carried out with $5 \cdot 10^4$ equilibration cycles. In the production phase, 10^6 MC cycles were performed. One single MC cycle consists of N MC trial moves, where N is the total number of molecules at the start of the simulation. The probabilities for selecting trial moves in Rx/CFC simulations were: 24.8% translations, 24.8% rotations, 0.8% volume changes, 24.8% CFC λ change trial moves [143], and 24.8% Reaction Ensemble trial moves [142], in which reactants are removed and reaction products are inserted in the system, in a such way that an equilibrium distribution of reactants and reaction products is obtained. The GCMC simulation of the HCOOH density at the maximum pore loading, used for the model validation, consisted of 10^4 equilibration MC cycles and $1.495 \cdot 10^5$ production MC cycles. The GCMC simulations of the adsorption of CO_2, H_2, and HCOOH in MOFs were carried out with $1 \cdot 10^4$ equilibration cycles, and $4 \cdot 10^5$ MC production cycles. The probabilities of selecting trial moves in GCMC simulations were 16.7% translations, 16.7% rotations, 16.7% reinsertions, 16.7% identity changes (changing the identity of the selected molecule) and 33.2% swap trial moves (exchanging molecules with the reservoir). The simulations of the enthalpy of adsorption at infinite dilution were carried out with $1 \cdot 10^5$ initialization cycles and $1 \cdot 10^5$ production cycles.

4.5 — Results and Discussion

We first computed the helium void fraction of UiO-66, which is used to calculate the HCOOH density. The obtained value equals 0.5070 ± 0.0002 and agrees with literature data (0.5071 [238]). The compatibility of HCOOH with the framework was tested by computing the density of HCOOH at the maximum pore loading. The computed value of the density was found to be ca. 1073 kg m^{-3} at 77 K and 1000 bar. There is a relative difference of 12% between the computed value and the experimental density of the liquid HCOOH at 293.15 K [186] (1220 kg m^{-3}) and a relative difference of 9% compared to the simulated value of the HCOOH density in the bulk-phase at 298.15 K from our previous work [206] (1177 ± 1 kg m^{-3}). The differences between the HCOOH density at the maximum pore loading and in the bulk-phase are due to the relatively large size of the HCOOH molecule compared to the pore size of UiO-66 and the formation of hydrogen bonds between HCOOH and the framework. There are two types of micropores with a diameter at 3.5 Å and 7 Å present in the UiO-66 structure, see Figure B.2 of Appendix B. The length between the most distant HCOOH atoms (H_{fa1} and H_{fa2}) is 2.804 Å and can affect the adsorption, which is be most consequential at low pressure.

Before studying the effect of the UiO-66 on the reaction yield, we simulated the CO_2 hydrogenation reaction in the gas phase at 298.15 - 800 K and 1 - 60 bar. In Figure 4.1, the mole fractions of HCOOH computed from the Rx/CFC simulations at 1 bar were compared to literature values calculated from equilibrium constants of the CO_2 hydrogenation reaction from the study of Rahbari et al. [41]. The isobars of simulated and calculated mole fractions of HCOOH overlap within the error bars. The results were obtained with high accuracy even when the values are of the order of magnitude 10^{-8}. It was shown that the simulations reproduce the mole fractions of HCOOH calculated from the literature [41].

The HCOOH reaction yield obtained from the Rx/CFC simulations at 298.15 - 800 K and 1 - 60 bar is shown in Figure 4.2. The obtained mole fractions of all components in the system are listed in Table B.4 of Appendix B. The production of HCOOH from the uncatalyzed CO_2 hydrogenation turns out to be challenging, as a low amount of product is obtained - the mole fractions of HCOOH are of the order of magnitude 10^{-6}. Increasing the temperature from 298.15 K to 800 K has an effect on the resulting mole fraction of FA: it increases approximately 13.2 times in all the studied systems. The reaction of CO_2 hydrogenation requires energy to be driven, due to its endergonicity (the free energy change is equal to 41.84 kJ mol^{-1} [19]). The HCOOH mole fraction increases approximately 56 times with pressure in the range from 1 bar to 60 bar. When the pressure increases, the reaction proceeds in that direction in which the volume decreases, by Le Chatelier's principle [44]. The highest HCOOH mole fraction, obtained at 800 K and 60 bar, is equal to $1.09 \cdot 10^{-5}$. The order of magnitude for uncertainty values is from $1 \cdot 10^{-9}$ to $1 \cdot 10^{-7}$.

In Figure 4.3, the location of the equilibrium of the CO_2 hydrogenation in the gas phase is shown as a function of T and P. The color code of the scale is the mole fraction of HCOOH starting from an equimolar mixture of CO_2 and H_2. The presence of orange color at 800 K and 60 bar indicate the highest production of HCOOH, equal to $1.09 \cdot 10^{-5}$. The conditions in which the mole fraction of HCOOH reaches the equivalent values are possible to distinguish: a similar result can be obtained, e.g., at 800 K, 30 bar and 500 K, 60 bar. This comparison can be useful when there is a need to lower the production temperature for economic reasons.

An attempt to improve HCOOH production was made by studying the effect of a confinement on the equilibrium of the CO_2 hydrogenation. GCMC simulations were carried out using the mole fractions of the components from the Rx/CFC simulations in the bulk-phase. The mole fractions obtained from GCMC simulations are listed in Table B.6 of Appendix B. In Figure 4.4, the HCOOH production enhancement (*ENH*, Eq. 4.8) obtained from GCMC sim-

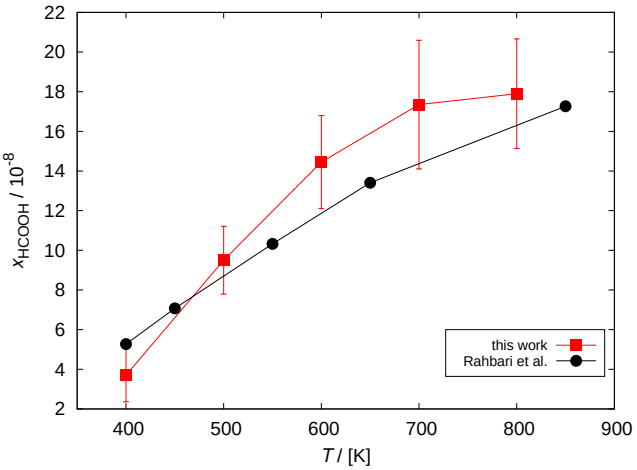

Fig. 4.1. HCOOH mole fractions computed from the Rx/CFC simulations in the bulk-phase and calculated from equilibrium constants of CO_2 hydrogenation reaction from the study of Rahbari et al. [41]. The Rx/CFC simulations were carried out at 400 - 800 K and 1 bar. As the equilibrium constants reported in the study of Rahbari et al. [41] lack uncertainty values, it is assumed that the isobars of simulated and calculated HCOOH mole fractions overlap within the error bars.

ulations in the UiO-66 framework is shown.

The effect of the UiO-66 confinement caused an average enhancement in HCOOH production by ca. 37 times compared to the gas phase. The enhancement in HCOOH production decreases with increasing temperature from approximately 212 at 298.15 K to 3 at 800 K. The most efficient conditions resulting in the highest mole fraction of HCOOH are at 298.15 K, 60 bar. The confinement effect of UiO-66 increases the HCOOH production by 176 times compared to the gas phase. The obtained mole fraction of HCOOH equals to $1.5{\cdot}10^{-4}$. Figure B.3 of Appendix B shows that the HCOOH mole fractions increase with pressure and decrease with the increasing temperature. The increasing pressure allows more molecules to enter the structure and fill the pores. The temperature has an opposite effect on mole fractions of HCOOH obtained in UiO-66 comparing to the bulk-phase. In the confinement, the exothermic reaction of CO_2 hydrogenation does not require energy to be absorbed from the surroundings, the enthalpy change has a negative value. There is a sharp drop in the mole fractions of HCOOH from 298.15 K to 400 K - the values decrease ca. 6 times in the pressure range from 1 to 60 bar. Above 400 K, mole fractions of HCOOH does not decrease. At 1 bar, HCOOH is pro-

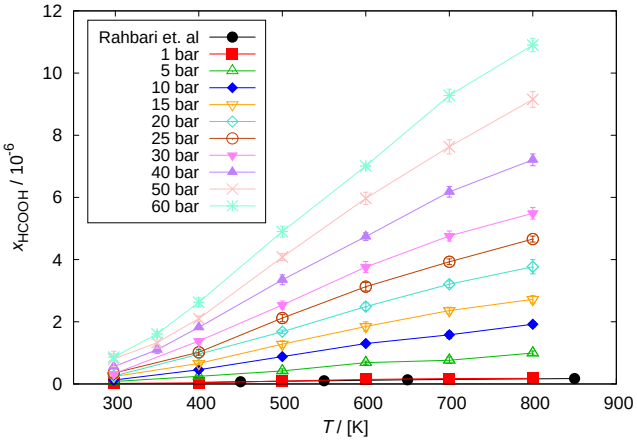

Fig. 4.2. HCOOH mole fractions computed from the Rx/CFC simulations in the bulk-phase. The mole fractions of HCOOH computed from the Rx/CFC simulations at 1 bar were compared to literature values, calculated from equilibrium constants of CO_2 hydrogenation reaction from the study of Rahbari et al. [41]. The simulations were carried out at 298.15 - 800 K and 1 - 60 bar. The mole fractions of HCOOH increase with temperature and pressure. The order of magnitude for the uncertainties are ranging from $1{\cdot}10^{-9}$ to $1{\cdot}10^{-7}$.

duced only up to 500 K. Above 500 K, the HCOOH mole fraction values are equal to 0 within the error bars. Although all the mole fractions of HCOOH obtained in the UiO-66 framework are of the order of magnitude 10^{-6} - 10^{-4}, the increase up to 300 times comparing to the bulk-phase was observed. This increase in the mole fraction of HCOOH points to the existing effect of UiO-66 on the CO_2 hydrogenation reaction. This effect is most likely extendable to lower temperatures and higher pressures. Further studies at these conditions are needed to investigate the maximum production of HCOOH to be obtained using UiO-66. We found that UiO-66, that was characterized by high CO_2 and H_2 adsorption [100, 222, 223], has positive influence on the CO_2 hydrogenation reaction due to the increased formation of a favored HCOOH product.

The adsorption of CO_2 and H_2 in UiO-66 is shown in Figure 4.5. The highest mole fraction of CO_2 is obtained at 298.15 K and 1 bar and equals 0.994. The adsorption of CO_2 in UiO-66 decreases ca. 1.3 times within the temperature range from 298.15 to 800 K, and also decreases with increasing pressure by ca. 1.02 times in the range from 1 to 60 bar. The adsorptions of CO_2 and H_2 are inversely related: as the mole fraction of CO_2 decreases, more H_2 is adsorbed. The adsorption of H_2 in UiO-66 increases ca. 35 times within the temperature range from 298.15 to 800 K and ca. 1.4 times within the

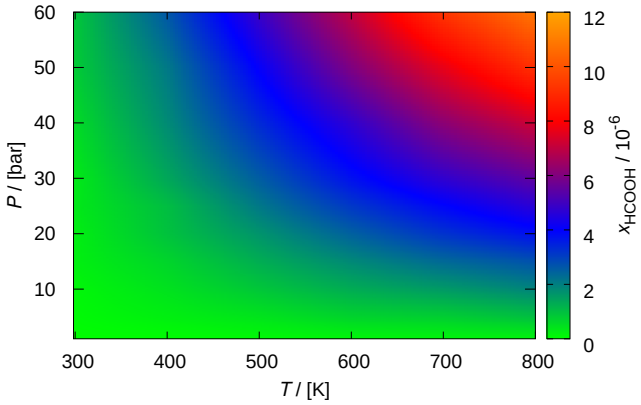

Fig. 4.3. Location of the equilibrium of the CO_2 hydrogenation in the gas phase as a function of T and P. The color gradation on the scale relates with the highest and lowest production of HCOOH. The highest production of HCOOH equal to $1.09{\cdot}10^{-5}$ is obtained at 800 K and 60 bar. The mole fractions of HCOOH increase with temperature and pressure, due to the endergonicity of CO_2 hydrogenation reaction and Le Chatelier's principle, respectively.

pressure range from 1 to 60 bar. The highest mole fraction of H_2 is obtained at 800 K and 60 bar and equals 0.27. The increasing temperature strengthens the interactions between the framework and H_2. The adsorption of H_2 is favored by UiO-66 with increasing temperature, resulting in the decrease of mole fractions of CO_2 and HCOOH. The amount of adsorbed reagents in UiO-66 varies, and the production of HCOOH is limited to the least adsorbed compound (H_2), due to the stoichiometry of the CO_2 hydrogenation reaction. The adsorption of H_2 increases with pressure, resulting in an increase in the production of HCOOH. Despite the increased adsorption of H_2 with temperature, the production of HCOOH decreases, which suggests that the interaction of HCOOH with the adsorbent becomes weaker.

To understand the reason for the decrease of mole fractions of HCOOH with increasing temperature and the increase of mole fractions of H_2, the infinite dilution was assumed and the isosteric heat of adsorption was computed at 298.15 - 800 K. In Figure 4.6, the isosteric heat of adsorption for CO_2, H_2 and HCOOH is shown, that is a measure of the change of enthalpy when adsorbate molecules are adsorbed from the bulk-phase to the adsorbed phase. The adsorbate molecules are at a lower energy state on the adsorbent surface than in the bulk-phase, causing the liberation of heat. The enthalpy of adsorption of HCOOH noticeably decrease by 2.7 kJ mol^{-1} in the temperature range from

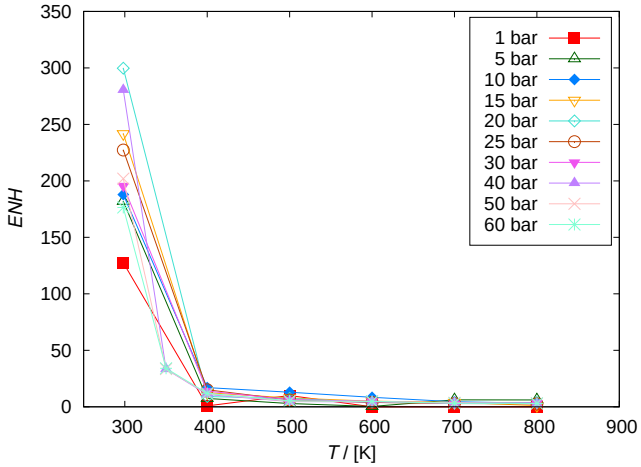

Fig. 4.4. Enhancement (*ENH*, Eq. 4.8) in the production of HCOOH obtained from GCMC simulations in UiO-66 framework. The simulations were carried out at 298.15 - 800 K and 1 - 60 bar. The mole fractions of HCOOH computed from the Rx/CFC simulations (see Table B.4 of Appendix B) are used as an input for GCMC ensemble. The mole fractions obtained from GCMC simulations are listed in Table B.6 of Appendix B. The enhancement in HCOOH production decreases with increasing temperature. HCOOH production increases ca. 37 times compared to the gas phase for all studied conditions. The resulting value at 800 K and 1 bar was discarded due to high uncertainty.

298.15 to 400 K. The increase in temperature leads to higher energy state of HCOOH on the adsorbent surface. The interactions between the host (UiO-66) and guest (HCOOH) become weaker, resulting in less heat released. This behavior is reflected in the decreasing production of HCOOH with increasing temperature in Figure 4.4. The increase of temperature causes the decrease in the enthalpy of adsorption of CO_2 by 0.5 kJ mol^{-1} in the temperature range from 298.15 to 400 K. However, in the temperature range from 600 to 800 K, the slight increase by 0.4 kJ mol^{-1} is observed. The enthalpy of adsorption of H_2 increases by 3 kJ mol^{-1} with temperature in the range from 298.15 to 800 K. The linear behavior of the heat of adsorption at increasing temperature results from the fact that the increment of RT is larger than the variation of the hydrogen adsorption energy ΔU inside the host-framework (see Table B.7 of Appendix B) according to $-\Delta H = -(\Delta U - RT) = RT - \Delta U$. This behavior has been previously reported by Martín-Calvo et al. [249]. These authors showed that above 200 K, the heat of adsorption of hydrogen in all the zeolites linearly increases as a function of temperature. In this work, we also observe that despite differences between pore sizes, the trend and the obtained values

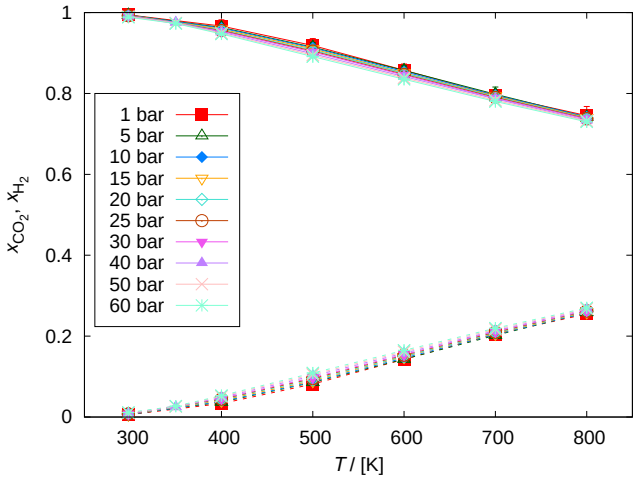

Fig. 4.5. CO_2 and H_2 mole fractions computed from GCMC simulations in UiO-66 framework. The data points of CO_2 mole fractions are connected to guide the eye by the solid lines and the data points of H_2 mole fractions by the dashed lines. The mole fractions of CO_2 and H_2 computed from the Rx/CFC simulations are used as an input for GCMC ensemble. The simulations were carried out at 298.15 - 800 K and 1 - 60 bar. The mole fractions of CO_2 decrease with increasing pressure and temperature. The mole fractions of H_2 increase with pressure and temperature.

of heat of adsorption of H_2 are similar for all three MOFs.

The distribution of CO_2, H_2 and HCOOH molecules at 298.15 K, 60 bar can be analyzed inside UiO-66 with the average density profiles (Figure 4.7). The center of mass of the molecules that are adsorbed was projected onto the XY plane, which is the same as YZ and ZX planes in isotropic UiO-66. Figure 4.7a is a reference structure of the UiO-66 framework. The average density profiles of HCOOH in Figure 4.7b in UiO-66 show a very low adsorption loading compared to CO_2 ($x_{\mathrm{HCOOH}} = 1.5{\cdot}10^{-4}$). HCOOH molecules tends to be located surrounding the carbon hexagonal structure connected to the oxygen and hydrogen atoms and near the zirconium centers. Figures 4.7c and 4.7d show the distributions of CO_2 and H_2 molecules in the structure. CO_2 ($x_{CO_2} = 0.99$) is densely located surrounding the carbon hexagonal structure and near the zirconium centers. These positions in the pores have been filled, because CO_2 can form hydrogen bonds with H atoms belonging to the framework. The visualization of the CO_2 molecule interacting with H atom of the framework is shown in Figure B.4 of Appendix B. The access of HCOOH molecules to their preferential sites is difficult due to the high loading of CO_2 molecules,

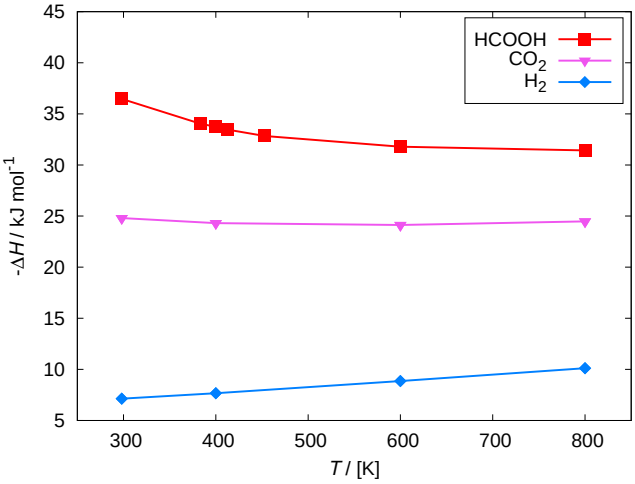

Fig. 4.6. Isosteric heat of adsorption of CO_2, H_2 and HCOOH at 298.15 - 800 K in UiO-66. The isosteric heat of adsorption of HCOOH decreases in the temperature range from 298.15 to 400 K. The energy state of HCOOH on the adsorbent surface increases, leading to weaker interactions between the framework and adsorbate. The increase of temperature causes the decrease in the enthalpy of adsorption of CO_2 in the temperature range from 298.15 to 400 K. The opposite effect is in the case of H_2, which enthalpy of adsorption increases with temperature in the range from 298.15 to 800 K. The error bars are smaller than the size of the symbols.

competing for the same location. The amount of the H_2 molecules adsorbed is lower than for CO_2 ($x_{H_2} = 0.01116$), but preferential sites can be described as surrounding the carbon hexagonal structure.

The enhancement in HCOOH production resulting from the UiO-66 confinement was compared with the Cu-BTC and IRMOF-1, see Figure 4.8. The mole fractions obtained from GCMC simulations in Cu-BTC and IRMOF-1 frameworks are listed in Tables B.8 and B.9 of Appendix B, respectively. The mole fractions of HCOOH are shown as a function of temperature and pressure in Figures B.5 and B.6 of Appendix B. The comparison of HCOOH mole fractions obtained in UiO-66, Cu-BTC, and IRMOF-1 at 60 bar is shown in Figure B.7 of Appendix B. The mole fractions of HCOOH increase with pressure and decrease with the increasing temperature, due to the host-guest interactions becoming weaker (see isosteric heat of adsorption shown in Figures B.8 and B.9 of Appendix B). The calculated *ENH* results for UiO-66, Cu-BTC, and IRMOF-1 frameworks at 298.15 - 800 K and 1 - 60 bar are listed in Table 4.2. The most efficient conditions for all the systems resulting in the

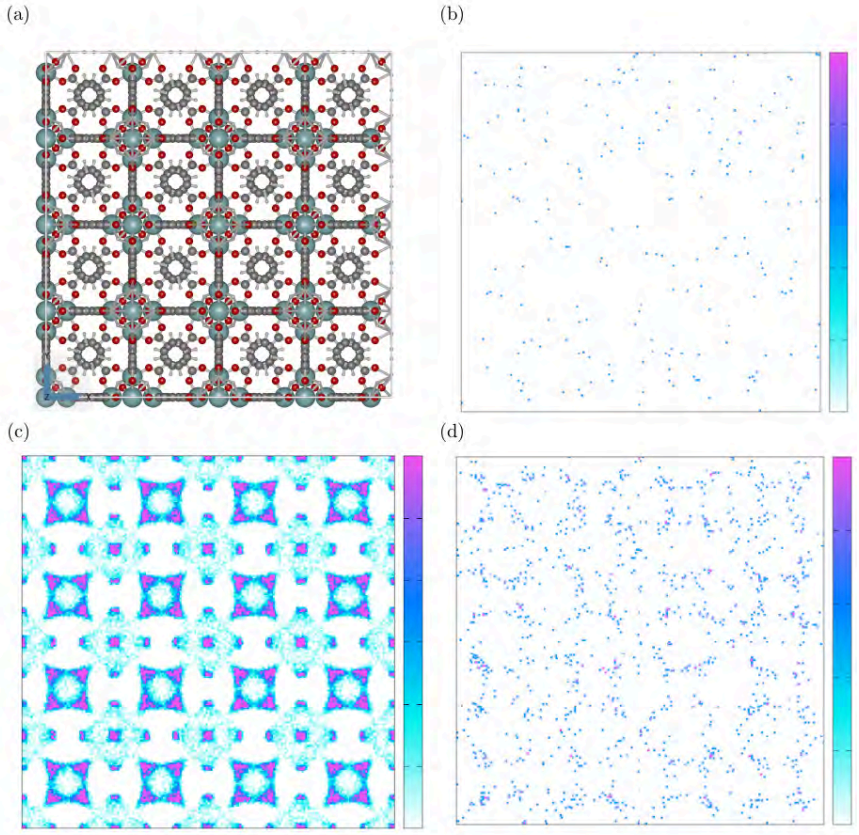

Fig. 4.7. The distribution of the HCOOH, CO_2 and H_2 molecules inside UiO-66, analyzed using density profiles from GCMC simulation at 298.15 K, 60 bar: (a) an atomistic reference structure of UiO-66 empty framework, visualized using iRASPA [38], (b) the distribution of HCOOH molecules ($x_{HCOOH} = 1.5{\cdot}10^{-4}$), (c) the distribution of CO_2 molecules ($x_{CO_2} = 0.99$), (d) the distribution of H_2 molecules ($x_{H_2} = 0.01116$). The center of mass of the molecules that are adsorbed was projected onto the XY plane. The projections onto YZ and ZX planes are identical due to the isotropy of UiO-66. The color gradation of the scales relates to the most and least populated regions of the structure, which is relative in each case. The preferential sites of CO_2 molecules (colored magenta) are surroundings of the zirconium centers and carbon hexagonal structures connected to the oxygen and hydrogen atoms. H_2 molecules are adsorbed surrounding the carbon hexagonal structure. The adsorption loading of HCOOH in UiO-66 is very low and the molecules of HCOOH tend to be located near carbon hexagonal structures and the zirconium centers, which are occupied by CO_2 molecules. The color scale is shown as a reference of the molecules loading.

highest mole fraction of HCOOH are at 298.15 K, 60 bar. The enhancement in the HCOOH production is the highest in Cu-BTC framework. The obtained mole fraction of HCOOH equals 0.0016 at 298.15 K, reaching a value 1819 times higher compared to the bulk-phase. A large discrepancy is noticeable between the enhancement in HCOOH production caused by Cu-BTC and the effect of UiO-66 (x_{HCOOH} is 176 times higher compared to the gas phase) and IRMOF-1 (x_{HCOOH} is 67 times higher compared to the gas phase). To assess if this difference is caused by the impact of different pore size or metal centers of the studied MOFs, the pore size distributions were compared in Figure B.2 of Appendix B. There are two types of micropores with a diameter at 3.5 Å and 7 Å present in the UiO-66. Cu-BTC is characterized by larger micropores with diameters at 5, 11, and 13 Å. The diameters of micropores in IRMOF-1 are at 11, and 15 Å. UiO-66 causes the strongest confinement, although in Cu-BTC the production of HCOOH is ca. 10 times bigger than in UiO-66. The stronger confinement resulting from the smaller pore size is found to not improve the production of HCOOH in CO_2 hydrogenation reaction.

Radial distribution functions were computed to analyze the effect of metal centers on HCOOH adsorption in UiO-66, Cu-BTC, and IRMOF-1 at 298.15 K, see Figures B.10 – B.12 of Appendix B. The preferential distance of the adsorbed molecules of HCOOH to the metal centers is the closest in Cu-BTC framework and equals to 2.4 Å. Simultaneously, the highest number of molecules (6) are noticeable in Cu-BTC within the preferential distance to the metal centers. This indicates a significant influence of the type of metal center on CO_2 hydrogenation reaction, exceeding the influence of the pore size in the structure. The application of Cu-BTC makes it possible to eliminate the high-cost temperature elevation, which is necessary in most of the analyzed cases to obtain a higher purity of the product.

In Table 4.3, the effect of confinement on the CO_2 hydrogenation using Cu-BTC at 298.15 K and 60 bar was compared with the performance of transition metal catalysts with phosphine ligands [55, 58], pincer ligands [59], N-heterocyclic carbene ligands [56, 63, 64], and half-sandwich catalysts with proton-responsive ligands [65, 66, 68, 69]. From each considered study, two types of catalysts were selected based on the highest and lowest concentration of the product of CO_2 hydrogenation. The final concentration of HCOOH obtained from the Cu-BTC confinement is ca. 80 times lower than the highest reported concentration obtained with the use of the Wilkinson complex [55], and ca. 30 times higher than the lowest reported concentration obtained using a catalyst with N-heterocyclic carbene ligands [63]. The concentration of HCOOH obtained from the confinement effect is between the highest and lowest concentration of the product obtained with the use of transition metal

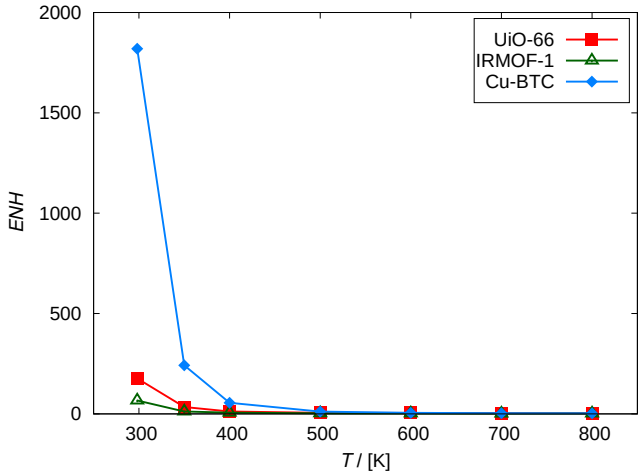

Fig. 4.8. Enhancement (*ENH*, Eq. 4.8) in the production of HCOOH obtained from GCMC simulations in UiO-66, Cu-BTC, and IRMOF-1 frameworks at 298.15 - 800 K and 60 bar. The enhancement in HCOOH production resulting from the effect of confinement decreases with increasing temperature. The enhancement in the HCOOH production is the highest in Cu-BTC framework. The obtained mole fraction of HCOOH is 1819 times higher compared to the bulk-phase at 298.15 K.

catalysts. Despite the minor difference between the molecular form of HCOOH and the ionic form (formate), the dissociation state of the acid significantly affects the selection of a proper downstream separation process [17]. An economic analysis for formic acid/formate downstream processing methods has been performed by Ramdin et al. [17], which shows that HCOOH is more valuable as a product than formate. The processes of separation, concentration, and acidification of formate solutions are challenging. The conversion and concentration of 10 wt% formate to 85 wt% formic acid add around \$380/ton of FA to the total production costs [17]. The application of Cu-BTC has the potential to improve the economically more attractive direct method of CO_2 conversion through downstream separation cost reduction. Further studies of Cu-BTC towards its functionalization may be a promising subject of research in the field of CO_2 hydrogenation.

Table 4.2: Enhancement (*ENH*, Eq. 4.8) in the production of HCOOH obtained from GCMC simulations in UiO-66, Cu-BTC, and IRMOF-1 frameworks at 298.15 - 800 K and 1 - 60 bar. The HCOOH mole fractions computed from Rx/CFC simulations are used as an input for GCMC ensemble. The enhancement in HCOOH production resulting from the effect of confinement decreases with increasing temperature. The enhancement in the HCOOH production is the highest in Cu-BTC framework. The subscripts show uncertainties computed using error propagation rules. The enhancement value obtained in UiO-66 at 800 K and 1 bar was rejected due to high uncertainty.

P/[bar]	T/[K]	$ENH_{\text{UiO-66}}$	$ENH_{\text{Cu-BTC}}$	$ENH_{\text{IRMOF-1}}$
1	298.15	$127.5_{180.9}$	$668.9_{635.3}$	$3.6_{7.3}$
	400	$0.8_{1.7}$	$8.2_{8.8}$	0_{0}
	500	$10.0_{27.8}$	$12.4_{15.0}$	0_{0}
	600	0_{0}	0_{0}	0_{0}
	700	0_{0}	0_{0}	0_{0}
	800	0_{0}	0_{0}	0_{0}
5	298.15	$181.9_{82.5}$	$1514.3_{509.0}$	$46.0_{52.4}$
	400	$7.4_{7.7}$	$34.4_{10.1}$	$7.8_{10.4}$
	500	$2.9_{7.9}$	$17.9_{11.6}$	$2.9_{3.1}$
	600	$0.3_{0.8}$	$12.3_{5.2}$	$2.1_{2.7}$
	700	$6.2_{9.7}$	$1.9_{2.5}$	$1.2_{1.7}$
	800	$6.1_{11.8}$	$0.2_{0.4}$	$0.9_{1.8}$
10	298.15	$187.9_{99.1}$	$2748.3_{591.2}$	$38.5_{18.4}$
	400	$17.0_{14.2}$	$48.6_{10.8}$	$4.2_{3.1}$
	500	$12.9_{10.0}$	$14.7_{4.2}$	$3.2_{1.5}$
	600	$8.4_{10.1}$	$4.1_{1.8}$	$2.7_{1.1}$
	700	$4.5_{4.1}$	$4.6_{2.1}$	$1.3_{1.2}$
	800	$3.2_{4.9}$	$3.7_{1.5}$	$1.8_{0.9}$
15	298.15	$241.8_{54.0}$	$2750.8_{412.2}$	$43.1_{13.1}$
	400	$12.5_{10.3}$	$73.8_{23.6}$	$4.6_{1.2}$
	500	$7.8_{6.6}$	$12.2_{4.6}$	$3.1_{0.7}$
	600	$5.0_{4.5}$	$5.3_{1.7}$	$2.3_{0.6}$
	700	$4.0_{4.8}$	$3.7_{1.0}$	$1.8_{1.0}$
	800	$1.1_{1.4}$	$2.0_{1.0}$	$1.9_{0.5}$
20	298.15	$299.7_{257.2}$	$2460.5_{333.5}$	$44.3_{12.8}$
	400	$9.1_{5.3}$	$49.8_{5.1}$	$4.8_{1.2}$
	500	$7.5_{5.9}$	$12.7_{1.3}$	$2.1_{0.6}$
	600	$3.8_{2.0}$	$5.9_{2.8}$	$2.0_{0.7}$
	700	$3.4_{2.0}$	$3.7_{1.0}$	$2.1_{0.4}$
	800	$3.8_{1.8}$	$2.8_{0.5}$	$1.6_{0.3}$

25	298.15	$227.3_{83.3}$	$2543.1_{698.3}$	$62.2_{22.8}$
	400	$15.1_{8.6}$	$48.9_{8.2}$	$5.3_{1.4}$
	500	$6.1_{4.1}$	$10.4_{2.2}$	$3.0_{0.8}$
	600	$3.9_{2.4}$	$5.9_{0.6}$	$2.5_{0.5}$
	700	$2.9_{1.5}$	$4.2_{0.6}$	$2.1_{0.6}$
	800	$2.7_{3.1}$	$2.7_{0.3}$	$1.5_{0.4}$
30	298.15	$195.6_{133.4}$	$2461.4_{372.4}$	$72.2_{25.9}$
	400	$13.9_{4.5}$	$45.3_{9.9}$	$5.1_{0.9}$
	500	$6.3_{1.6}$	$11.0_{1.2}$	$3.6_{0.6}$
	600	$5.0_{2.8}$	$5.4_{0.8}$	$2.1_{0.2}$
	700	$2.8_{1.0}$	$3.8_{0.5}$	$1.5_{0.6}$
	800	$3.5_{0.7}$	$2.4_{0.5}$	$1.6_{0.5}$
40	298.15	$280.5_{53.5}$	$2415.7_{315.1}$	$86.1_{24.0}$
	350	$33.3_{15.6}$	$264.8_{30.3}$	$11.3_{2.4}$
	400	$10.9_{3.9}$	$52.4_{8.0}$	$5.9_{1.7}$
	500	$4.7_{2.0}$	$13.4_{1.5}$	$2.6_{0.4}$
	600	$4.3_{1.7}$	$4.8_{0.6}$	$2.1_{0.5}$
	700	$3.7_{0.7}$	$3.5_{0.2}$	$2.0_{0.3}$
	800	$2.7_{0.6}$	$2.6_{0.2}$	$1.6_{0.4}$
50	298.15	$202.0_{96.1}$	$2020.8_{631.6}$	$80.7_{36.4}$
	350	$33.4_{13.4}$	$249.1_{41.1}$	$12.3_{2.5}$
	400	$11.6_{3.4}$	$56.8_{3.9}$	$5.9_{0.9}$
	500	$4.9_{1.3}$	$11.9_{1.0}$	$2.8_{0.5}$
	600	$4.7_{1.8}$	$5.7_{0.9}$	$2.4_{0.3}$
	700	$3.6_{0.9}$	$3.6_{0.3}$	$2.0_{0.3}$
	800	$3.0_{0.8}$	$2.6_{0.3}$	$1.7_{0.2}$
60	298.15	$176.5_{73.9}$	$1819.3_{229.8}$	$66.6_{12.1}$
	350	$34.1_{8.2}$	$241.9_{17.1}$	$12.0_{1.9}$
	400	$11.9_{3.5}$	$55.2_{3.8}$	$6.0_{1.1}$
	500	$5.3_{1.5}$	$11.3_{0.8}$	$3.1_{0.4}$
	600	$4.8_{2.3}$	$5.3_{0.5}$	$2.4_{0.4}$
	700	$3.1_{0.4}$	$3.5_{0.5}$	$1.6_{0.1}$
	800	$2.9_{0.7}$	$2.7_{0.1}$	$1.8_{0.3}$

Table 4.3: CO_2 hydrogenation using transition metal catalysts. The final concentration of HCOOH obtained in this work using Cu-BTC at 298.15 K and 60 bar was ca. 80 times lower than the highest reported concentration obtained with the use of Wilkinson complex [55], and ca. 30 times higher than the lowest reported concentration obtained using a catalyst with N-heterocyclic carbene ligands [63]. The final concentration of HCOOH in the adsorbed phase was calculated as $c_{\mathrm{HCOOH}} = \frac{n_{\mathrm{HCOOH}}}{(\xi \cdot V)}$, where n_{HCOOH} is the number of moles of HCOOH adsorbed in a unit cell, V is the volume of the unit cell, and ξ is the helium void fraction.

Catalyst	**Conditions**	**Product**	**Concentration / [mol L^{-1}]**	**Reference**
none	Cu-BTC confinement, 298.15 K, 60 bar	HCOOH	0.031	this work
4DHBP Ir(III) complex no. 1	298.15 K, 1 bar, 24h	formate	0.005	[69]
4DHBP Ir(III) complex no. 4	353.15 K, 30 bar 8h	formate	0.687	[69]
[Cp*Ir(6,6'-R_2-bpy)(OH_2)]SO_4 (R=OMe)	353.15 K, 10 bar, 8h	formate	0.004	[68]
Cp*Ir, thbpym ligand	323.15 K, 10 bar, 8h	formate	0.480	[68]
Ir(III) complex $[3(OH_2)_2]^{4+}$	323.15 K, 10 bar, 2h	formate	0.006	[66]
Ir(III) complex 2'$(OH_2)_2$	323.15 K, 30 bar, 48h	formate	1.7	[66]
[RhCl(η^4 C_8H_12)]$_2$	298.15 K, 40 bar, 22h	formate	1.55	[56]
Ir(PNP), pincer ligand	473.15 K, 50 bar, 2h	formate	0.6	[59]
Cp*Ir(III) complex no. 5	303.15 K, 1 bar, 30h	formate	0.016	[65]
(C_6Me_6)*Ru(II) complex no. 6	393.15 K, 60 bar, 24h	formate	1.54	[65]
Cp*Rh(III) complex no. 4	353.15 K, 40 bar, 32h	formate	0.24	[65]

[Ir(bis-NHC)(AcO)I_2] complex no. 1, N-heterocyclic carbene ligand	353.15 K, 60 bar, 20h	formate	0.01	[64]
[Ir(bis-NHC)(AcO)I_2] complex no. 3, N-heterocyclic carbene ligand	473.15 K, 60 bar, 75h	formate	0.38	[64]
(η^6-arene)Ru(bis-NHC) complex no. 1	353.15 K, 40 bar, 1h	formate	0.001	[63]
(η^6-arene)Ru(bis-NHC) complex no. 1	473.15 K, 40 bar, 20h	formate	0.13	[63]
[RhCl(mtppms)$_3$]	323.15 K, 60 bar, 24h, $CaCO_3$	HCOOH	0.01	[58]
[RhCl(mtppms)$_3$]	323.15 K, 100 bar, 20h, HCOONa	HCOOH	0.12	[58]
Rh(acac)$(CO)_2$, Dppe ligand	298.15 K, p_{CO_2} = 40 bar, p_{H_2} = 20 bar, 20h	HCOOH·NEt_3	0.03	[55]
Wilkinson complex $RhCl(PPh_3)_3$ + 3 PPh_3	298.15 K, p_{CO_2} = 40 bar, p_{H_2} = 20 bar, 20h	HCOOH	2.50	[55]

4.6 — Conclusions

We carried out molecular simulations to study the performance of UiO-66 for the production process of formic acid, followed by comparison with the performance of Cu-BTC, and IRMOF-1. The effect of confinement on the yield of HCOOH from the CO_2 hydrogenation reaction was analyzed. The adsorption isobars of the studied systems were computed with Monte Carlo simulations in the grand-canonical ensemble. It was shown that the confinement increases the HCOOH production, due to the higher density of pore phase compared to the bulk-phase and the selective adsorption of HCOOH as a favored component, by Le Chatelier's principle. The HCOOH mole fractions increase with pressure and decrease with the increasing temperature. The most efficient conditions for the HCOOH production in the confinement are at 298.15 K and 60 bar. The production of HCOOH in UiO-66 framework is ca. 200 times higher compared to the gas phase. The most significant enhancement in HCOOH production (ca. 2000 times higher compared to the gas phase) is achieved using Cu-BTC, resulting in $x_{\mathrm{GCMC}} = 0.0016$ from $x_{\mathrm{Rx/CFC}} = 8.63{\cdot}10^{-7}$ at 298.15 K and 60 bar. The increase in temperature leads to the higher energy state of HCOOH on the adsorbent surface and weaker interactions between the framework and adsorbate, causing the decrease of enhancement. At 1 bar, HCOOH is obtained in UiO-66 and Cu-BTC up to 500 K and in IRMOF-1 only at 298.15 K. By comparing the performance of MOFs with different pore size distributions and metal centers, it is found that the stronger confinement resulting from the smaller pores does not guarantee the improvement of HCOOH production in CO_2 hydrogenation reaction. The prevailing factor is the type of metal center in the metal-organic framework. The highest number of HCOOH molecules in the closest distance to the metal center is located near the Cu center in Cu-BTC. The metal-organic framework Cu-BTC has the potential to be a useful alternative or supplement to transition metal catalysts for improving the efficiency of CO_2 hydrogenation due to: (a) elimination of the high-cost temperature elevation, (b) more valuable final product enabling cost reduction of downstream processing methods, and (c) comparable final concentration of HCOOH to the reported concentrations of formate obtained using transition metal catalysts. To fully investigate its performance, a techno-economic and carbon emission analysis should be conducted. An interesting topic for future research would be a kinetic study of the Cu-BTC catalytic performance in CO_2 hydrogenation and the functionalization of Cu-BTC structure to improve the adsorption of HCOOH. This would allow a better understanding of the CO_2 hydrogenation reaction to HCOOH in confinement.

Chapter 5

The Impact of Metal Centers in the M-MOF-74 Series on Carbon Dioxide and Hydrogen Separation

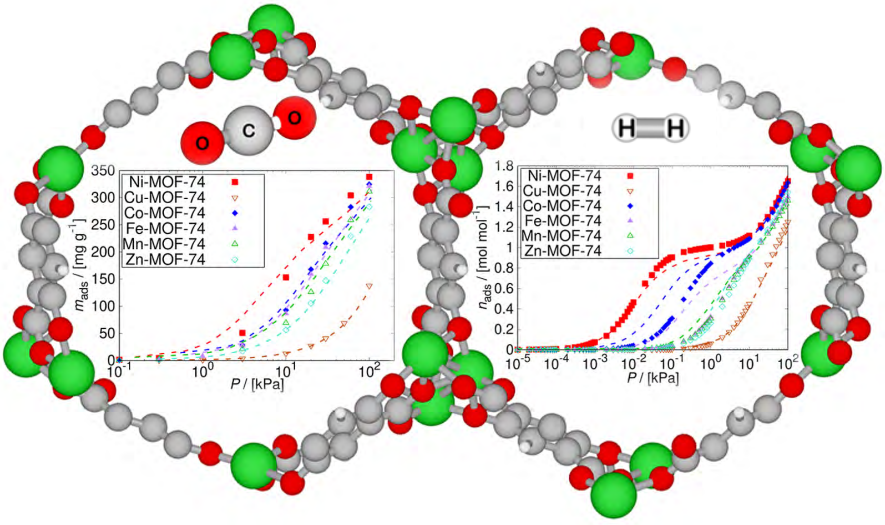

The series of metal-organic frameworks M-MOF-74 gained popularity in the field of capture and separation of CO_2 due to the presence of numerous, highly reactive open-metal sites. The description of effective interactions between guest molecules and open-metal sites without accounting for polarization effects is challenging but it can significantly reduce the computational cost of simulations. In this study, we propose a non-polarizable force field for CO_2, and H_2 adsorption in M-MOF-74 (M = Ni, Cu, Co, Fe, Mn, Zn) by scaling the Coulombic interactions of M-MOF-74 atoms, and Lennard-Jones interaction potentials between the center of mass of H_2 and the open-metal centers. The presented force field is based on UFF and DREIDING parameters, characterized by high transferability and efficiency. The quantum behavior of H_2 at cryogenic temperatures is considered by incorporating Feynman-Hibbs quantum corrections. To validate the force field, the experimental isotherms of CO_2 at 298 K and 10^{-1} - 10^{2} kPa, the isotherms of H_2 at 77 K and 10^{-5} - 10^{2} kPa, the corresponding enthalpy of adsorption, and the binding geometries in the M-MOF-74 series were reproduced using Monte Carlo simulations in the grand-canonical ensemble. The computed loadings, heats of CO_2 and H_2 adsorption, and binding geometries in M-MOF-74 are in very good agreement with the experimental values. The temperature transferability of the force field from 77 K to 87 K, and 298 K was shown for adsorption of H_2. The validated force field was used to study the adsorption and separation of CO_2/H_2 mixtures at 298 K. The adsorption of H_2 practically does not occur when CO_2 is present in the mixture. As indicated from simulated breakthrough curves, the breakthrough time of CO_2 in M-MOF-74 follows the same order as the uptake and the heat of CO_2 adsorption: Ni > Co > Fe > Mn > Zn > Cu. Increasing the feed mole fraction of CO_2 in the breakthrough simulations from 0.1 to 0.9 speeds up the saturation of the adsorbent, leading to a faster exit of CO_2 with the column effluent. The application of the non-polarizable force field allows full investigation of the capture and separation of CO_2 in M-MOF-74, and can be expanded to study multi-component mixtures or industrial reactions in future research.

This chapter is based on the following publication:

Wasik, D. O., Vicent-Luna, J. M., Luna-Triguero, A., Dubbeldam, D., Vlugt, T. J. H., Calero, S. The Impact of Metal Centers in the M-MOF-74 Series on Carbon Dioxide and Hydrogen Separation. *Separation and Purification Technology* **2024**, *339*, 126539.

5.1 — Introduction

Since metal-organic frameworks (MOFs) emerged in 1995 [250], this class of porous materials has gained attention in a wide variety of applications such as gas storage [80, 81], separation [82, 83], catalysis [84, 85], drug delivery [86, 87], enzyme immobilization [88, 89], sensing [90, 91], and water sustainability [92]. The crystalline structures of MOFs are composed of organic ligands, and metal clusters linked by coordination bonds [100]. The flexibility in modification of physicochemical properties has led to the design of more than 20,000 different MOFs [251]. One of the most popular families of MOFs is M-MOF-74, also known as CPO-27-M, where M = Ni, Cu, Co, Fe, Mn, Mg, or Zn [113–122]. M-MOF-74 series is synthesized by combining M^{2+} ions with 2,5-dioxido-1,4-benzenedicarboxylate ($dobdc^{4-}$) ligands, resulting in hexagonal array of channels, see Figure 5.1. Metal ions are favorable sorption sites for sorbate molecules, accessible through cylindrical pores. Despite the large pores with a diameter of ca. 11 Å [122], the metal cation density is relatively high, due to the negative charge of the $dobdc^{4-}$ ligand [122]. The presence of numerous open-metal sites enhances selectivity [123] and the surface packing density of adsorbates [124], as well as provides reactive sites for chemical reactions, e.g. oxygenation [125], or size-selective Lewis acid catalysis [126]. The stability of metal-ligand complexes for first-row transition metals is described by the empirical Irving–William series [252] and follows the order: $Mn^{2+} < Fe^{2+} < Co^{2+} < Ni^{2+} < Cu^{2+} > Zn^{2+}$. The binding strength between metal cations and ligands, as well as their stability, is related to the lattice constants. The smaller lattice constants correspond to more stable structures and the larger constants to less stable structures [253]. In the study of Yu et al. [253], the experimental lattice constants of M-MOF-74 were compared to the computed from Density Functional Theory (DFT) calculations. The study revealed that the experimental lattice constants a and c for Mn-, Fe-, Co-, Ni-, and Zn-MOF-74 obey the order of the Irving–William series, as well as the computed lattice constants a, however, DFT calculations do not predict this trend correctly for the lattice constants c of Fe-, Co-, and Ni-MOF-74.

As effective adsorbents, M-MOF-74 series raised the interest in CO_2 capture, and storage due to alarming fossil CO_2 emmisions leading to global warming. Total emissions are estimated at 37.9 Gtons of CO_2 in 2021, with 14% of these emissions from Europe, 13% from the United States, and 33% from China [254]. Liquid absorbent processes are more expensive, and less efficient compared to solid adsorbent processes [255]. In search of an alternative, in the study of Queen et al. [122] the adsorption of CO_2 in M-MOF-74 was analyzed experimentally, and computationally using DFT calculations. The affinity of

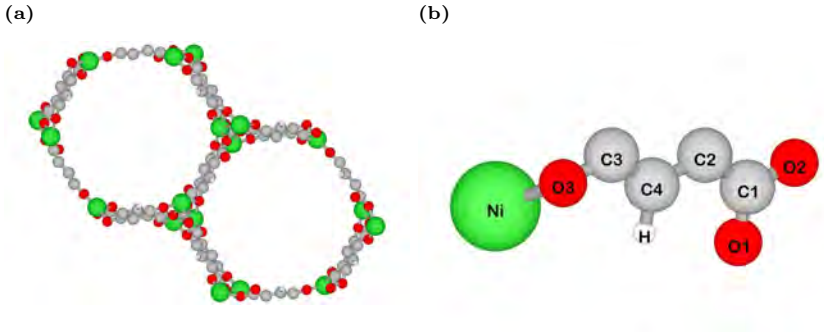

Fig. 5.1. Schematic representation of M-MOF-74 series on the example of Ni-MOF-74, visualized using iRASPA [38]: (a) an atomistic reference structure of Ni-MOF-74 empty framework, and (b) Ni-MOF-74 building block showing the different uniquely charged atoms. The corresponding charges and LJ interaction potentials are listed in Table C.2 of Appendix C.

CO_2 in M-MOF-74, quantified by the isosteric heat of adsorption is in the range from ca. 20 to ca. 40 kJ mol^{-1} [122], resulting in adsorption of CO_2 in M-MOF-74 from ca. 130 mg g^{-1} of framework for M = Cu to as high as ca. 310 mg g^{-1} of framework for M = Mg at 100 kPa, 298 K. Depending on the open-metal site, the isosteric heat of CO_2 adsorption measured at the loading of 0.1 CO_2 per M^{2+} decreases as follows: Mg > Ni > Co > Fe > Mn > Zn > Cu. As the metal-ligand complex stability for the first-row transition metals obeys the Irving–William series order [252]: $Mn^{2+} < Fe^{2+} < Co^{2+} < Ni^{2+} < Cu^{2+} > Zn^{2+}$, ideally the energies of the guest molecule of CO_2 inside the host-MOF and the MOF complexes follow the same trend. The study by Yu et al. [253] revealed that the CO_2 binding strength does not necessarily follow the Irving–William series order, as it is a relative energy to the interaction strength between the CO_2 molecule and the metal centers within the MOF structure: $E_{\text{binding}} = E(\text{MOF–CO}_2)$ - $E(\text{MOF})$ - $E(\text{CO}_2)$. Natural bond order charge analysis showed that the charge transfer from the CO_2 molecule to the metal ions is minimal (0.06–0.07 electron) [253]. This indicates that CO_2 adsorption is predominantly influenced by the electrostatic interactions dependent on the effective charge of the M^{2+} ion at the open-metal site where CO_2 adsorbs. The higher charge on the metal ion leads to the stronger CO_2 binding energy, which correlates with the increased isosteric heat of CO_2 adsorption. The experimental CO_2 binding geometries at different open-metal sites were shown to be in good agreement with DFT computations in the study of Queen et al. [122] The adsorption performance makes the capture and separ-

ation of CO_2 from gas mixtures in M-MOF-74 promising [256–260], leading to an idea about the potential application of this MOF series in, e.g., separation of CO_2/H_2 mixtures from the water-gas-shift reaction [261]:

$$CO + H_2O \rightleftarrows CO_2 + H_2 \tag{5.1}$$

The presence of CO_2 in H_2 significantly decreases the heat value of produced H_2 as an energy carrier [262]. The separation of H_2 from CO_2/H_2 mixtures is typically performed by pressure swing adsorption (PSA) [263], amine scrubbing [264], and membrane processes [265], although none are commercially used [266]. The improvement of industrial adsorptive H_2 purification efficiency is needed to minimize energy usage in the mass transport of the gas and regeneration of the adsorbents. As further optimization of zeolites and activated carbons is unlikely to result in major enhancements in CO_2/H_2 separation [267], MOFs show promise in this context. In the computational screening study of Aksu et al. [268], the molecular simulation results for zeolites, MOFs, and hypothetical MOFs are compared for syngas separation. The highest CO_2/H_2 selectivity in the range of 24700 - 84000 was reported for MOFs, surpassing zeolites up to ca. 5000 times. In the experimental study of Herm et al. [267], the utility of five MOFs was compared for high-pressure CO_2/H_2 separation by PSA. The highest CO_2/H_2 selectivity in the range of 400 - 800 at 313 K, 0 - 40 bar was achieved using Mg-MOF-74, which was chosen as a representative of MOFs with exposed metal cations. The CO_2/H_2 selectivity obtained using Mg-MOF-74 surpassed the performance of the reference activated carbon by ca. 4 - 8 times. Moreover, the Mg-MOF-74 selectivity exceeded also the representative of MOFs with high surface area and a rigid framework structure, i.e. Be-BTB, by ca. 60 - 130 times. The observed performance can be associated with interactions involving the open-metal sites, making the M-MOF-74 series an interesting subject for further research. Extensive experimental studies on the adsorption of H_2 using MOFs revealed that the adsorbed H_2 molecules favor the open-metal site over the alternative adsorption site [269]. Due to the open-metal sites present in M-MOF-74 series, H_2 sorption has been studied for M = Ni [113, 270, 271], Co [115, 117, 271], Mg [117, 271], Zn [118, 121, 272], Mn [117, 271, 273], Cu [114, 271], and Fe [116, 271, 274, 275]. The two-step mechanism of adsorption, wherein adsorbate molecules first adsorb at the metal centers, followed by adsorption above a triangle of oxygen atoms within the framework, is especially noticeable in the adsorption isotherm and heat of adsorption for Ni-MOF-74 [269]. In the experimental study of Rosnes et al. [271] the uptake of H_2 in M-MOF-74 (M = Ni, Cu, Co, Fe, Mn, Mg) is determined as ca. 20 mg g^{-1} of framework for M = Ni at 100 kPa, 77 K, and the differences in interactions between H_2 and the metal centers in the

structure are examined. A comparison of the isosteric heat of adsorption that quantifies the affinity of H_2, shows the decrease depending on the open-metal site as follows: Ni > Co > Mg > Fe > Zn ≈ Mn > Cu. The difference in affinity compared to CO_2 is attributed to the prevalence of polarization interactions in H_2 sorption, in contrast to electrostatic interactions characterizing CO_2 sorption [119]. Considering that both adsorbates CO_2 and H_2 undergo adsorption in M-MOF-74 with different affinity, an interesting topic for future research is to check, whether the separation of the CO_2/H_2 mixture would be effective.

Apart from the separation of CO_2/H_2 mixtures, another potential application of MOFs is the capture of CO_2 followed by the conversion to useful feedstock chemicals, e.g., formic acid, methanol, urea, propylene, salicylic acid, and polyols [1–4]. The hydrogenation reaction of CO_2 into HCOOH carried out in MOF confinement recently gained interest of scientists [276]. Due to the high kinetic and thermodynamic stability of CO_2 the use of a catalyst is needed to mediate the reduction [18], see Eq. 4.1.

In Chapter 4, the confinement effect of porous materials on the thermodynamical equilibrium of the CO_2 hydrogenation reaction can be considered as an alternative to high-cost, toxic transition metal catalysts [19]. The performed Monte Carlo simulations of this study proved that the confinement effect of MOFs affects CO_2 hydrogenation reaction, shifting the thermodynamical equilibrium towards HCOOH formation by Le Chatelier's principle [44]. The evaluation of the influence of pore size and metal centers on the HCOOH yield showed that the type of metal center is the prevailing factor. The M-MOF-74 series potentially allows to fully investigate the dependence of HCOOH production enhancement on the type of metal center, minimizing the effect of pore size. Molecular simulations are a natural tool to investigate confinement effects independently from catalytic effects. To the best of our knowledge, there is no literature data regarding force field-based molecular simulations of CO_2/H_2/HCOOH systems in the M-MOF-74 framework. Due to the specific interactions between open-metal sites and polarizable guest molecules, the description of such is challenging. In the studies of Becker et al. [277–279] a polarizable force field for CO_2 in M-MOF-74 was developed. A non-polarizable force field for the adsorption of CO_2 in M-MOF-74 was derived from DFT by Mercado et al. [280, 281] by adjusting not only the Lennard-Jones (LJ) interaction potentials of the metal site but all interaction sites. This approach is elaborated and results in many fitting parameters of the force field, possibly leading to lower transferability. An attempt to reproduce experimental data on adsorption of H_2 in M-MOF-74 [271] was made in the study of Pham et al. [119], where the Buch model [282], Belof Stern Space model [283], Darkrim-

Levesque model [243], and polarizable Belof Stern Space Polar model [283] of H_2 were tested. Only the polarizable Belof Stern Space Polar model successfully reproduced the experimental adsorption data [271] for all the studied metal centers. Polarizable force fields improve the description of the enhanced interactions between guest molecules and open-metal sites, however, excessive computational costs are generated unless back-polarization is ignored [277]. In the recent study of Becker et al. [279] a polarizable force field for CO_2 in M-MOF-74 is derived directly from quantum mechanics and back-polarization is neglected, resulting in a decrease of the computation time to a level comparable to non-polarizable force fields. In case of systems that include not only CO_2 and H_2 adsorption but also the hydrogenation reaction of CO_2 to HCOOH, the size of the considered system, and the complexity of its description can affect computational time, and accuracy. The development of a non-polarizable force field would be beneficial for further investigation on the dependence of HCOOH production enhancement on the type of metal center in M-MOF-74. Another advantage is the transferability of the non-polarizable force field from one component to another, while polarizable force fields are non-transferable unless they are specifically developed for transferability [119, 279]. In this work, we present a non-polarizable force field for molecular simulations of CO_2 and H_2 adsorption in M-MOF-74, where M = Ni, Cu, Co, Fe, Mn, Zn, after introducing two modifications to the existing parameters for CO_2, H_2, and M-MOF-74: (1) Coulombic interactions of M-MOF-74 are scaled to reproduce experimental data on CO_2 adsorption [122] using a non-polarizable force field for CO_2 [176, 284] at 298 K, (2) LJ interaction potentials between the center of mass of H_2 in the Darkrim-Levesque model [243], and the open-metal centers are scaled to reproduce experimental data on H_2 adsorption [271] at 77 K. The force field is transferable from cryogenic temperatures (77 K, 87 K) to 298 K, where the separation of CO_2/H_2 mixtures is studied in the M-MOF-74 series. As there is no force field available that would reproduce the adsorption of HCOOH in M-MOF-74, the adjustment of the already existing force field of HCOOH [174] validated in our previous studies [206, 276] remains a separated subject of our future research.

This chapter is organized as follows: in section 5.2, we provide technical details of the molecular simulation methods, the force fields for CO_2, H_2, and the metal-organic frameworks. The force field is adjusted by scaling the Coulombic interaction potentials of M-MOF-74 and scaling the LJ interaction potentials between the center of mass of H_2, and the open-metal centers. The isotherms, and enthalpy of adsorption are computed using Monte Carlo simulations in the grand-canonical ensemble. The force field is validated by reproducing experimental data of CO_2, and H_2 isotherms, enthalpies of adsorption, and binding

geometries. The adsorption of CO_2/H_2 mixtures in M-MOF-74 is studied, and the breakthrough curves are generated to analyze the performance of CO_2/H_2 mixtures separation. In section 5.3, we present and discuss our results. The non-polarizable force field is able to describe the adsorption behavior and can be applied in computational studies of the capture, and separation processes. Our findings are summarized in section 5.4.

5.2 — Methodology

The non-polarizable force field for the adsorption of CO_2 and H_2 in M-MOF-74, where M = Ni, Cu, Co, Fe, Mn, Zn is adjusted, and validated using force field-based molecular simulations. The guest-host and guest-guest intermolecular interactions are modeled by Coulombic and LJ interaction potentials. The Lorentz–Berthelot mixing rules [129] are used to define interactions between unlike Lennard–Jones sites, except for the interactions between the center of mass of H_2 molecules and the open-metal centers, that are scaled and specified by an override. Explicit polarization effects are neglected and accounted for in the LJ and Coulombic interactions. The cutoff radius for intermolecular interactions is set to 12 Å. LJ interactions are cut and shifted to zero at the cutoff without tail corrections. Periodic boundary conditions are exerted in all three directions. The Ewald summation method [151] is used for calculating electrostatic interactions. The Ewald summation method parameters correspond to a relative precision of 10^{-6}. The bond length and the point charges from the model for CO_2 by Harris and Yung [284] are used together with LJ interactions parameters modeled by García-Sánchez et al. [176]. The three-site charge-quadrupole model for H_2 by Darkrim and Levesque [243] was chosen as the closest non-polarizable model to the experimental data studied by Pham et al. [119]. The models of CO_2 and H_2 are rigid. LJ parameters for the atoms of the framework are from the DREIDING force field [148], except for metal centers, which are from the UFF force field [147]. The models of the framework and guest-host interactions used in this work are rigid, and all atoms of the molecules have point charges assigned. All the structures are charge-neutral before and after modification. Each MOF crystal structures for M-MOF-74 were obtained from a different experimental synthesis [113–118]. The parameters of M-MOF-74 trigonal cells are listed in Table C.1 of Appendix C. The simulated systems are composed of $1 \times 1 \times 4$ unit cells to ensure a minimum distance of more than twice the cutoff radius between periodic images. The LJ parameters, partial charges for all the components, and frameworks used in this work are listed in Table C.2 of Appendix C.

The first modification to the existing force field is the scaling of Coulombic

interaction potentials of M-MOF-74 to reproduce experimental data on CO_2 adsorption [122]. We implement the RASPA software package [94, 95] to perform simulations using the M-MOF-74 frameworks. The adsorption isotherms and the enthalpy of CO_2 adsorption were computed from Monte Carlo simulations in the grand-canonical ensemble (GCMC) [128]. The chemical potential, volume, and temperature are fixed and imposed in the GCMC ensemble. The uncertainties in the computed number of molecules adsorbed in a unit cell were provided by the RASPA software package [94]. The simulation is divided into five blocks, and the error is computed by calculating the standard deviation. The initial charges of the M-MOF-74 frameworks are computed using the 'charge-equilibration' method of Wilmer and Snurr [247, 285] at 298 K, and subsequently adjusted through multiplication by a scaling factor within the range of 0.5 - 1.5. To compare the resulting uptakes and the enthalpies of CO_2 adsorption to the experimental data [122], a series of adsorption isotherms of CO_2 is computed at 298 K, 10^{-1} - 10^2 kPa. The set of charges leading to the closest results to the experimental data was selected for further study as a part of the final force field.

The second modification to the force field is the scaling of LJ interaction potentials between the center of mass of H_2, and the open-metal centers, to reproduce experimental data on the adsorption of H_2 [271]. The LJ interaction potentials were adjusted through multiplication by a scaling factor within the range of 0.8 - 1.2. However, an exception was made for the potential between the center of mass of H_2 and the open-metal centers in Ni-MOF-74, where a scaling factor of 13 was applied, because of the stronger interaction of H_2 with the metal centers of this MOF [271]. To determine the scaling that leads to the closest values to the experimental loadings and heats of adsorption [271], a series of adsorption isotherms and the enthalpy of H_2 adsorption is computed from GCMC simulations at 77 K, 10^{-5} - 10^2 kPa. Additionally, Henry coefficients computed from the adjusted force field using Widom's test particle insertions [128] at 77 K were compared to the coefficients calculated from the slope of experimental isotherms [271] in the linear region at low pressures [286]. The selected scaling was also validated by simulating the adsorption isotherms of H_2 at 87 K, and 298 K. The quantum behavior that is non-negligible at cryogenic temperatures (i.e. 77 K) was taken into account by incorporating Feynman-Hibbs quantum correction [287] to the interaction potentials between the center of mass of H_2 molecules at 77 K, and 87 K. The influence of Feynman–Hibbs effect on the H_2 adsorption behavior has been already shown to reduce the saturation capacity and change the shape of the isotherms in zeolites and other nanomaterials [249, 288–290]. The original and scaled Coulombic and LJ interaction potentials are provided in Table 5.1 and

Table 5.2, respectively.

The adjusted non-polarizable force field for the adsorption of CO_2, and H_2 in M-MOF-74 was further validated by analysis of the behavior of molecules inside the frameworks at 298 K. To generate binding geometries, Baker's minimization scheme [160] is applied, which uses the eigenvalues/vectors of the Hessian matrix to locate true minima on the energy surface, corresponding to equilibrium geometries. The distance between the metal center and O atom of CO_2 molecule (M - O_{CO_2}) was compared with experimental data and DFT [122]. In case of H_2, the simulated distance between the metal center and the center of mass of H_2 (M - H_{com}) was compared with DFT [271], as well as the angle between the metal center, the center of mass of H_2, and H atom of H_2 molecule (M - H_{com} - H_{H_2}). The CO_2, and H_2 molecules interacting with open-metal centers were visualized using iRASPA [38].

The adjusted, and validated non-polarizable force field was used to study the adsorption of CO_2/H_2 mixtures in M-MOF-74 series. For mole fractions of CO_2: $y_{CO_2} = 0.1$, 0.5, the adsorption of CO_2, and H_2 was studied at 298.15 K, and 100 - 4000 kPa, and the results were discussed. The performance of M-MOF-74 in fixed-bed adsorbers was evaluated using breakthrough simulations using the RUPTURA code [291]. The combination of RUPTURA code and the RASPA software enables computation of breakthrough curves directly from GCMC simulations. The computed adsorption data of pure CO_2, and H_2 at 298.15 K, and 100 - 4000 kPa were used to fit the dual-site Langmuir-Freundlich isotherm model [292]:

$$q(p) = \sum_i q_i^{\text{sat}} \frac{b_i (\frac{p_i}{p_0})^{v_i}}{1 + b_i (\frac{p_i}{p_0})^{v_i}} \tag{5.2}$$

where $q(p)$ is absolute loading of the adsorbed phase as a function of pressure, q_i^{sat} is saturation loading, b_i is the coefficient of adsorption representing the affinity of the molecule, v_i is heterogeneity factor, p_i is the partial pressure in the gas phase in units of Pa, p_0 is the reference pressure equal to 1 Pa, and i refers to component i. The parameters of the dual-site Langmuir-Freundlich model (q_1^{sat},b_1,v_1,q_2^{sat},b_2, and v_2) for CO_2, and H_2 were used as an input for breakthrough simulations, and are listed in Table C.3 of Appendix C. The simulations of gas adsorption breakthrough curves were performed for CO_2/H_2 mixtures, where $y_{CO_2} = 0.1$, 0.2, 0.3, 0.4, 0.5, 0.9, with helium as a carrier gas. To compare the separation of CO_2/H_2 mixtures using M-MOF-74 with performance of modified activated carbon, the initial conditions were selected based on the study of Caldwell et al. [293]: temperature T=298 K, total pressure $p_T = 2.5$ MPa, packed bed void fraction $\varepsilon_B = 0.4$, interstitial gas velocity entering the packed bed $v = 0.006791$ m s^{-1}, length of packed bed adsorber

$L = 0.065$ m, axial dispersion is neglected, and isothermal conditions are assumed. The output from RUPTURA was validated by independent prediction of CO_2/H_2 mixtures using Ideal Adsorption Solution Theory (IAST) [294], followed by comparison to the previously obtained results from GCMC simulations. The breakthrough curves were analyzed depending on the metal centers, and depending on the mole fraction of CO_2.

The GCMC simulations of the adsorption of CO_2 and H_2 in M-MOF-74 were carried out with 10^4 initialization Monte Carlo (MC) cycles, and $4{\cdot}10^5$ production MC cycles. One single MC cycle includes N MC trial moves, where N is the total number of molecules at the start of the simulation. The probabilities of selecting trial moves in GCMC simulations were 25% translations, 25% rotations, 25% reinsertions, and 25% swap trial moves (exchanging molecules with the reservoir). The GCMC simulations of the CO_2/H_2 mixtures in M-MOF-74 consisted of 10^4 initialization MC cycles, and 10^5 production MC cycles. The probabilities of selecting trial moves were 16.7% translations, 16.7% rotations, 16.7% reinsertions, 16.7% identity changes (changing the identity of the selected molecule) and 33.2% swap trial moves. For more details about Monte Carlo trial moves, the reader is referred to Ref. [38, 94, 95]

5.3 — Results and Discussion

To reproduce experimental data on the adsorption of CO_2 [122], we first computed, and scaled the Coulombic interaction potentials of M-MOF-74, where M = Ni, Cu, Co, Fe, Mn, Zn. The scaled charges are compared to the initial charges computed from the 'charge-equilibration' method in Table 5.1.

The isotherms and enthalpy of CO_2 adsorption in M-MOF-74 computed with the use of new set of scaled charges at 298 K, and 10^{-1} - 10^2 kPa, are shown in Figure 5.2. By only scaling the Coulombic interaction potentials of M-MOF-74 the experimental loadings and heats of adsorption [122] were reproduced, despite starting from isotherms that deviate significantly from the experiment, see an example in Figure 5.2c. Overall, the force field agrees well with the experimental measurements, with a small deviation observed for Ni-MOF-74. The highest relative difference of 39% between the computed value of adsorption uptake in Ni-MOF-74 and literature value occurs at 3 kPa. This difference is probably due to the difficulty in describing the two-step mechanism of adsorption in the low-pressure area, wherein adsorbate molecules first adsorb at the metal centers, followed by adsorption above a triangle of oxygen atoms within the framework. The tendency in the simulated uptake and heat of CO_2 adsorption agrees with the study by Queen et al. [122]: Ni >

Table 5.1: The initial charges for M-MOF-74, where M = Ni, Cu, Co, Fe, Mn, Zn computed from the 'charge-equilibration' method of Wilmer and Snurr [247, 285], compared to the scaled charges selected based on reproduction of experimental data [122]. The chosen set of charges allows successful computation of the isotherms, and the enthalpy of CO_2 adsorption at 298 K, 10^{-1} - 10^{2} kPa. The charges for Co- and Fe-MOF-74 for CO_2 adsorption have been previously published by Luna-Triguero et al. [295]

	Ni-MOF-74		Cu-MOF-74	
Atom	$q_{\text{charge eq.}}$ /[e$^-$]	q_{scaled} /[e$^-$]	$q_{\text{charge eq.}}$ /[e$^-$]	q_{scaled} /[e$^-$]
Me	1.10769	1.55	0.923389	0.834
C1	0.431158	0.603	-0.0833878	-0.076
C2	-0.196159	-0.275	0.383558	0.345
C3	0.196702	0.275	0.17379	0.156
C4	-0.0609594	-0.086	-0.154189	-0.139
O1	-0.449624	-0.63	-0.437776	-0.394
O2	-0.581596	-0.815	-0.47853	-0.431
O3	-0.50468	-0.702	-0.408696	-0.368
H	0.0574637	0.08	0.0818392	0.073
	Co-MOF-74		Fe-MOF-74	
Atom	$q_{\text{charge eq.}}$ /[e$^-$]	q_{scaled} /[e$^-$]	$q_{\text{charge eq.}}$ /[e$^-$]	q_{scaled} /[e$^-$]
Me	1.16171	1.335	1.146450	1.226
C1	0.422607	0.485	0.332818	0.356
C2	-0.179995	-0.207	-0.138145	-0.148
C3	0.208781	0.245	0.160509	0.175
C4	-0.108009	-0.125	-0.081881	-0.088
O1	-0.472538	-0.544	-0.562089	-0.602
O2	-0.530936	-0.611	-0.410100	-0.439
O3	-0.584701	-0.673	-0.523741	-0.561
H	0.0830871	0.095	0.076157	0.081
	Mn-MOF-74		Zn-MOF-74	
Atom	$q_{\text{charge eq.}}$ /[e$^-$]	q_{scaled} /[e$^-$]	$q_{\text{charge eq.}}$ /[e$^-$]	q_{scaled} /[e$^-$]
Me	1.29091	1.161	1.213100	1.006
C1	0.409563	0.368	0.414013	0.343
C2	-0.193789	-0.175	-0.186294	-0.155
C3	0.194713	0.175	0.194483	0.161
C4	-0.0761898	-0.064	-0.099635	-0.083
O1	-0.608495	-0.548	-0.576390	-0.479
O2	-0.491698	-0.443	-0.478184	-0.393
O3	-0.579225	-0.522	-0.558839	-0.464
H	0.0542353	0.048	0.077740	0.064

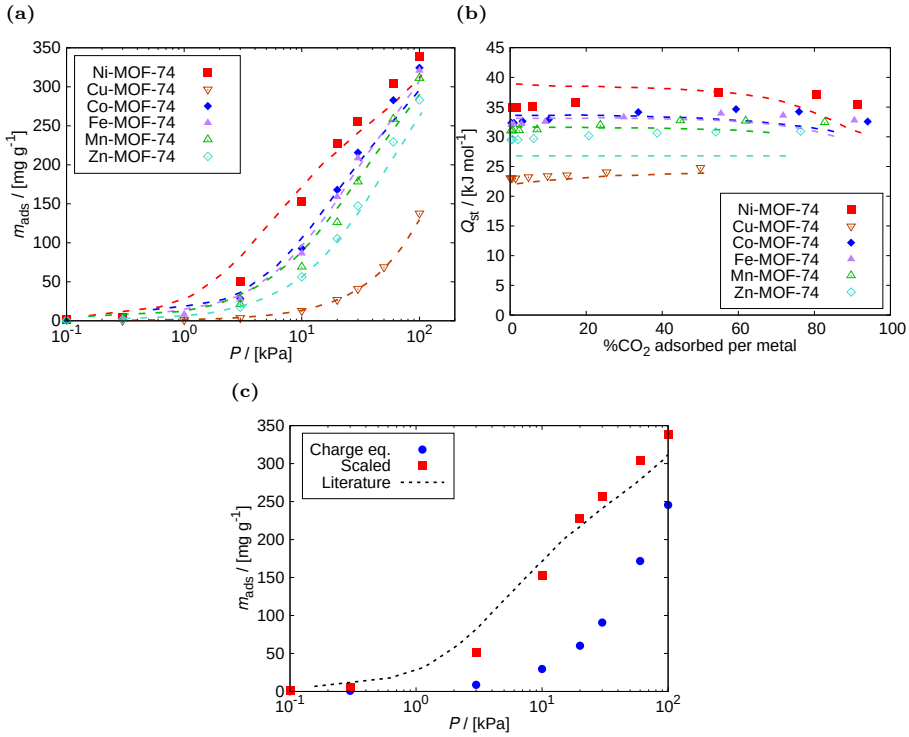

Fig. 5.2. Adsorption of CO_2 in M-MOF-74 (M = Ni, Cu, Co, Fe, Mn, Zn) computed with the use of new set of scaled charges, that enable the reproduction of experimental data [122] at 298 K, and 10^{-1} - 10^{2} kPa: (a) the adsorption isotherms, (b) the heat of adsorption, and (c) the comparison of the experimental adsorption in Ni-MOF-74 [122] to the isotherms computed using the initial charges from the 'charge-equilibration' method, and the new set of scaled charges. Adsorption results computed from modified force field are represented by data points, and the literature data by dashed lines. The force field agrees well with the experimental measurements, and the experimental trend in uptake and heat of CO_2 adsorption is reproduced.

Co > Fe > Mn > Zn > Cu. The heats of adsorption for both Co-MOF-74 and Fe-MOF-74 approach ca. 32 kJ mol^{-1} as the uptake reaches 1 CO_2 per M^{2+}, which value is close to the literature data [122], see Figure 5.2b. The heat of adsorption for Ni-MOF-74 is found to be somewhat higher, ca. 35 kJ mol^{-1}. This convergence suggests a uniform distribution of adsorption enthalpies at the secondary adsorption sites, reflecting the similarity in adsorption environments across the isostructural series.

The force field has undergone further modifications by the scaling of LJ interaction potentials between the center of mass of H_2, and the open-metal centers to reproduce experimental data on H_2 adsorption [271]. The comparison of the initial LJ interaction potentials from Lorentz–Berthelot mixing rules, and the scaled potentials is shown in Table 5.2.

The changes in the LJ potential function caused by the scaling and their consequences are shown in Figure 5.3 in the example of the adsorption of H_2 in Ni-MOF-74. To reproduce the adsorption isotherm at the low-pressure region, a deeper potential well between the center of mass of H_2 and Ni was necessary, as well as closer intermolecular distance at the energy minimum. This modification allowed the correct reproduction of adsorption at a pressure lower than 10 kPa, which was initially impossible. However, at the range between 10 kPa and 100 kPa the adsorption uptake is overestimated due to the quantum behavior of H_2 molecules at 77 K. This overestimation at cryogenic temperatures was resolved by incorporation of Feynman-Hibbs quantum correction, which affects the shape of the isotherm by reducing the adsorption capacity. The relative difference between the computed value of adsorption uptake using scaled LJ interaction potentials with Feynman-Hibbs quantum correction, and literature value at 100 kPa decreased from 13.3% to 3.6%, leading to the satisfactory reproduction of experimental data.

The isotherms, and the heat of H_2 adsorption computed from the new set of LJ potentials at 77 K, and 10^{-5} - 10^{2} kPa are shown in Figure 5.4a and b, respectively. The computed isotherms and the heats of adsorption with error bars are presented separately for each studied M-MOF-74 in Figures C.1 and C.2 of Appendix C. While the agreement with the experimental data [271] is satisfactory, larger deviations can be observed for the Co-, and Fe-based frameworks at the low-pressure region, see Figure 5.4a. To investigate the agreement of simulated isotherms with the experimental data at the low pressure regime, the Henry coefficients were compared in Table C.4 of Appendix C. The Henry coefficients for Cu-MOF-74 and Ni-MOF-74 were computed with high accuracy, showing deviations of only 1% and 8%, respectively, when compared to coefficients calculated from experimental adsorption data. The highest deviation from the experimental Henry coefficient value (84%) is observed for Fe-MOF-74. This is reflected in the disparity of the simulated isotherm shape to the experimental data, particularly in the low-pressure region, as shown in Figure C.1d of Appendix C. The highest relative difference of 60% between the computed value of adsorption uptake and literature value occurs at 0.7 kPa for Fe-MOF-74. The deviation decreases with the increase of pressure to reach a low, acceptable value of 0.7% at 10 kPa. Despite the large discrepancy in the uptake at 0.7 kPa, the corresponding enthalpy of adsorp-

Table 5.2: The initial LJ interaction potentials calculated from Lorentz–Berthelot mixing rules between the center of mass of H_2, and the open-metal centers of M-MOF-74, where M = Ni, Cu, Co, Fe, Mn, Zn, compared to the scaled potentials selected based on reproduction of experimental data [271]. The chosen LJ potentials allow successful computation of the isotherms, and the enthalpy of H_2 adsorption at 77 K, and 10^{-5} - 10^2 kPa.

Metal	$\epsilon/k_{B\,\mathrm{unscaled}}$ /[K]	$\epsilon/k_{B\,\mathrm{scaled}}$ /[K]	$\sigma_{\mathrm{unscaled}}$ /[Å]	σ_{scaled} /[Å]
Ni	16.65248	216.4823	2.7415	2.1932
Cu	9.613043	11.5357	3.036	3.036
Co	16.08752	17.6963	2.7585	2.2068
Fe	15.49488	18.5939	2.776	2.776
Mn	15.50317	13.9529	2.798	2.798
Zn	47.85447	43.069	2.7095	2.7095

tion aligns with the literature value of 8.7 kJ mol^{-1} (the relative difference of 5.8%). It can be observed in Figure C.2d of Appendix C that the heat of adsorption for Fe-MOF-74 is slightly shifted towards a higher uptake. The shift in a decrease of the computed heat of adsorption indicates that the secondary adsorption sites located directly above a triangle of oxygen atoms within the framework, start filling at ca. 0.8 mol mol^{-1}, 6 kPa, instead of experimental ca. 0.6 mol mol^{-1}, 0.7 kPa. In the simulations, molecules of H_2 and Fe centers are attracting each other too strongly causing higher occupancy of primary adsorption sites than in reality. The trend in the simulated uptake and heat of H_2 adsorption agrees with the study by Rosnes et al. [271]: Ni > Co > Fe > Zn ≈ Mn > Cu. The heats of adsorption for all M-MOF-74 frameworks approach ca. 5 kJ mol^{-1} at the secondary adsorption sites, which is in agreement with literature. As in the experiments, the two-step mechanism of adsorption is the most noticeable in case of Ni-MOF-74. The temperature transferability of the force field at cryogenic temperatures was confirmed from 77 K to 87 K, see Figure C.3 of Appendix C. In Figure 5.4c the adsorption of H_2 in M-MOF-74 at 298 K, and 10 - 4000 kPa were compared to literature data for Ni-MOF-74 [296]. The computed adsorption in Ni-MOF-74 follows the experimental isotherm, but becomes overestimated at 1500 kPa. The relative difference between computed values and literature reaches 14% at 4000 kPa. The trend in the adsorption uptake at 298 K is found to be almost identical as at 77 K: Ni > Co ≈ Fe > Zn ≈ Mn > Cu. We found the performance of the force field to be sufficient at both cryogenic and room temperatures.

The distribution of CO_2, and H_2 molecules can be analyzed inside M-MOF-74 using the average density profiles (Figure 5.5). The center of mass of the adsorbed molecules was projected onto the XY plane of anisotropic Ni-,

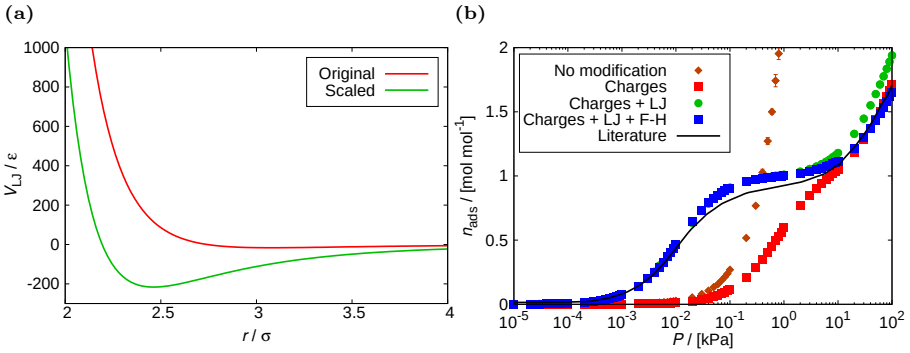

Fig. 5.3. Adsorption of H_2 in Ni-MOF-74: (a) the original and scaled LJ potential function - intermolecular potential energy as a function of the distance between the center of mass of H_2, and the open-metal center Ni, (b) the comparison of the experimental adsorption isotherm [271] to the isotherms computed from the original force field parameters using the initial charges from the 'charge-equilibration' method, the original force field parameters using the new set of scaled charges, scaled LJ potential between the center of mass of H_2 and Ni using the new set of scaled charges, and scaled LJ potential with Feynman-Hibbs quantum correction using the new set of scaled charges. The simulations were carried out at 77 K, and 10^{-5} - 10^{2} kPa. The best agreement with literature data resulted from scaled LJ potential with Feynman-Hibbs quantum correction.

and Cu-MOF-74. The average density profiles of CO_2, and H_2 in Ni-MOF-74 confirm a very high adsorption loading at the open-metal centers compared to the secondary adsorption sites. H_2 molecules are located closer to the metal centers than CO_2, due to their smaller size. The adsorbed molecules of CO_2, and H_2 in Cu-MOF-74 are more homogeneously distributed, especially in case of CO_2. The reason is in the lowest hydrogen affinity for Cu-MOF-74 among the studied structures, and the constant enthalpy resulting in the one-step mechanism of adsorption. The distribution of CO_2, and H_2 molecules inside Co-, Fe-, Mn-, Zn-MOF-74 is shown in Figures C.4, and C.5 of Appendix C, respectively.

The atomistic reference structures of Ni-MOF-74 framework that is loaded with 1.5 CO_2, and 1.5 H_2 per metal site was obtained from Baker's minimization simulations at 298 K. In Figure 5.6a, and b the adsorption of CO_2, and H_2 is visualized using iRASPA [38], respectively. The binding geometry of CO_2 molecules resembles the ball-and-stick model from the study of Queen et al. [122], showing a single channel in Fe-MOF-74 loaded with 1.5 CO_2 per Fe center. Two apparent CO_2 sites identified through high resolution neutron powder diffraction experiments exhibit the hexagon-shaped binding pattern, similarly observed here. The pattern is less explicit in case of H_2 but still

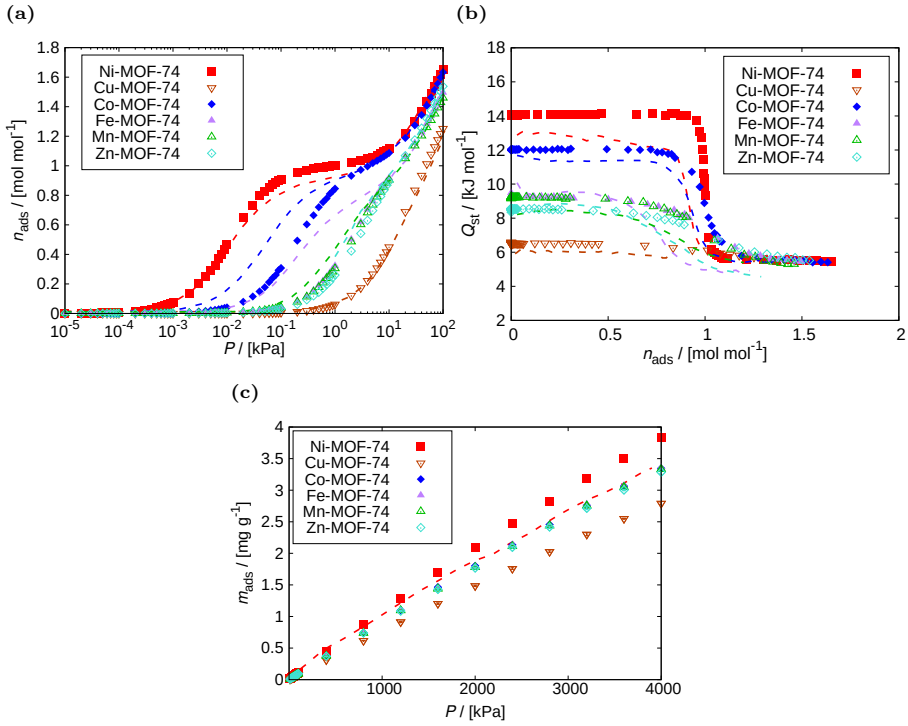

Fig. 5.4. Adsorption of H_2 in M-MOF-74 (M = Ni, Cu, Co, Fe, Mn, Zn) computed from GCMC simulations with the new set of LJ potentials, that enable the reproduction of experimental data [271]: (a) the adsorption isotherms at 77 K, and 10^{-5} - 10^{2} kPa, (b) the heat of adsorption at 77 K, and 10^{-5} - 10^{2} kPa, and (c) the adsorption isotherms at 298 K, 10 - 4000 kPa. Adsorption results computed from modified force field are represented by data points, and the literature data by dashed lines. The force field agrees well with the experimental measurements, with a slight deviation observed for Fe-MOF-74. The experimental trend in uptake and heat of H_2 adsorption is reproduced.

noticeable at the metal centers.

To examine the binding geometries in more detail, energy minimization simulations using Baker's algorithm were performed for a single molecule of the adsorbate at 298 K. The computed distances M - O_{CO_2}, and M - H_{com}, along with the angles M - H_{com} - H_{H_2} are compared with literature data [122, 124, 271, 273, 275, 297] in Table 5.3. The computed binding geometries are in a very good agreement with the reference values. The relative difference between the computed and experimental M - O_{CO_2} distances is 3 - 7%. Similarly, in the case of M - H_{com} the relative difference is 0.3 - 10%. Surprisingly, the closest result

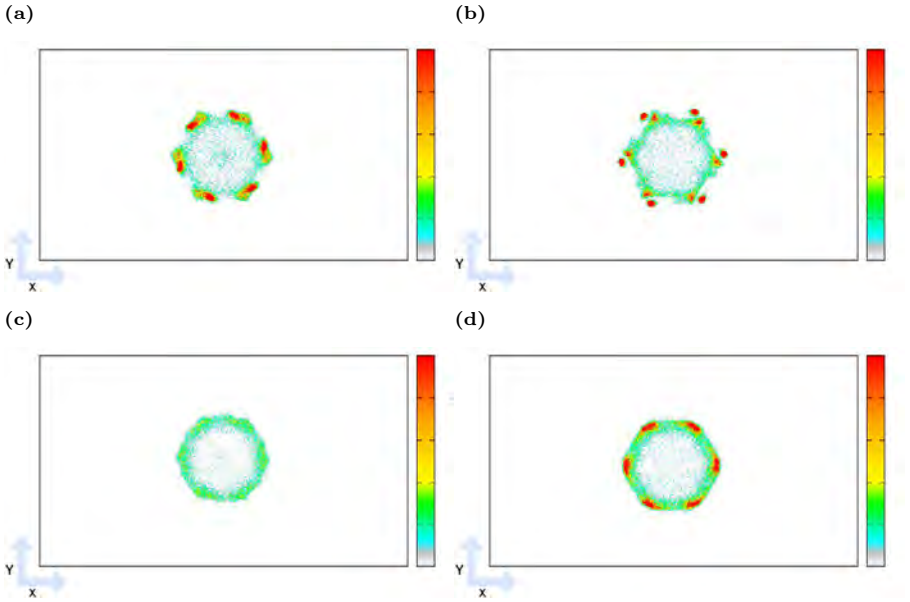

Fig. 5.5. The distribution of the CO_2, and H_2 molecules inside M-MOF-74, analyzed using density profiles from GCMC simulation: (a) the distribution of CO_2 molecules in Ni-MOF-74 at 298 K, 100 kPa, (b) the distribution of H_2 molecules in Ni-MOF-74 at 77 K, 100 kPa, (c) the distribution of CO_2 molecules in Cu-MOF-74 at 298 K, 100 kPa, (d) the distribution of H_2 molecules in Cu-MOF-74 at 77 K, 100 kPa. The center of mass of the molecules that are adsorbed was projected onto the XY plane. The color gradation of the scales relates to the most and least populated regions of the structure, which is relative in each case. The color scale is shown as a reference of the molecules loading. The preferential sites of CO_2, and H_2 molecules (colored red) in Ni-MOF-74 are at the open-metal centers. The adsorption loading of CO_2, and H_2 in Cu-MOF-74 is more homogeneously distributed, which is a reflection of the lower hydrogen affinity for Cu.

to the literature data (0.3%) was achieved for Fe-MOF-74, whose computed adsorption isotherm deviated the most from the experimental. The highest relative difference of 10.3% is between the computed and experimental Cu - H_{com} distance. In addition to neutron diffraction, Rosnes et al. [271] performed DFT computations at the PBE + D level resulting in Cu - H_{H_2} distances of 2.75 Å, and 2.66 Å that are close to our values: 2.744 Å, and 2.743 Å (the relative difference of 2.4% and 0.2%, respectively). The computed angles M - H_{com} - H_{H_2} for Co-, and Ni-MOF-74 agree with the results from DFT reported by Pham et al. [119] (83.7°and 76.9°, respectively) with the deviation of 7% and 15%, although in the case of Zn (60.8°) almost 50% of relative difference

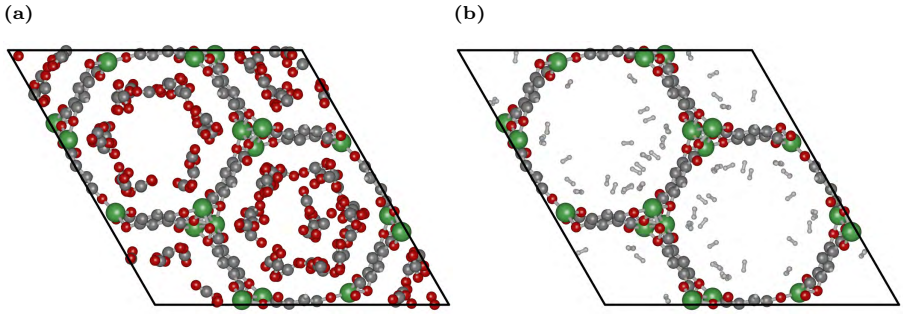

Fig. 5.6. The atomistic reference structures of Ni-MOF-74 framework obtained from Baker's minimization simulations at 298 K: (a) loaded with 1.5 CO_2 per metal site, and (b) loaded with 1.5 H_2 per metal site. The hexagon-shaped binding pattern of adsorbate molecules shown in the study of Queen et al. [122] is also displayed here, especially for CO_2 molecules. The molecules of H_2 are located mostly at the metal centers.

is observed. The CO_2, and H_2 molecules interacting with open-metal centers of Ni-MOF-74 are visualized using iRASPA [38] in Figure 5.7.

The non-polarizable force field for adsorption of CO_2, and H_2 in M-MOF-74 has been validated by reproducing the experimental data of adsorption isotherms, the heats of adsorption and binding geometries, and therefore used to predict the adsorption of CO_2/H_2 mixture. The adsorption of CO_2/H_2 mixture in M-MOF-74 at 298.15 K, and 100 - 4000 kPa is shown for CO_2 mole fraction $y_{CO_2} = 0.1$ in Figure 5.8a, and $y_{CO_2} = 0.5$ in Figure 5.8b. When CO_2 is present in the gas mixture even at the lowest studied mole fraction $y_{CO_2} = 0.1$, the adsorption of H_2 practically does not occur (it is lower than 1 mg g^{-1} of H_2). This is due to much higher CO_2 affinity for M-MOF-74 of ca. 30 kJ mol^{-1} at the secondary adsorption sites than the affinity of H_2 (ca. 6 kJ mol^{-1}). The adsorption loading decreases with mole fraction of CO_2. Compared to the adsorption of pure CO_2, its uptake from CO_2/H_2 mixture in Ni-MOF-74 at 100 kPa decreased by 1.2 times for $y_{CO_2} = 0.5$, and by 2.3 times for $y_{CO_2} = 0.1$. Similarly, the saturation loading for $y_{CO_2} = 0.1$ decreased by 1.2 times compared to $y_{CO_2} = 0.5$. The tendency in performance of M-MOF-74 has changed slightly for mixture with $y_{CO_2} = 0.5$, compared to the tendency in adsorption of pure CO_2 (Ni > Co > Fe > Mn > Zn > Cu): the adsorption uptakes in Co-, Fe-, and Mn-MOF-74 surpassed the results in Ni-MOF-74 at high pressure. In case of Co-, Mn-, and Ni-MOF-74 the adsorption loadings overlap within the error bars. The adsorption in Fe-MOF-74 is likely overestimated, due to small discrepancies between the model and the experimental adsorption isotherm of H_2 described earlier in this chapter,

Table 5.3: Binding geometry of CO_2 and H_2 molecules in M-MOF-74 obtained from Baker's minimization simulations at 298 K. The computed distances M - O_{CO_2} and M - H_{com}, together with the angles M - H_{com} - H_{H_2} are compared to the literature data [122, 124, 271, 273, 275, 297]. The computed binding distances are in very good agreement with the reference values. The relative differences between our results and experimental studies are lower than 10%. The binding distances and angles are visualized in Figure 5.7.

Binding geometry of CO_2			
Metal	M–$O_{CO_2,exp}$ [Å]	M–$O_{CO_2,DFT}$ [Å]	M–$O_{CO_2,sim}$ [Å]
Ni	2.29 [297]	2.52	2.39
Cu	2.86	2.87	2.69
Co	2.26	2.56	2.42
Fe	2.29	2.62	2.43
Mn	2.51	2.57	2.44
Zn	2.43	2.84	2.57
Binding geometry of H_2			
Metal	M–$H_{com,exp}$ [Å]	M–$H_{com,sim}$ [Å]	M–H_{com}–$H_{H_2,sim}$ [°]
Ni	2.20 [273]	2.329	88.675
Cu	3.03 [271]	2.718	89.93
Co	2.23 [273]	2.159	89.189
Fe	2.53 [275]	2.522	89.057
Mn	2.67 [271]	2.524	87.932
Zn	2.6 [124]	2.637	89.933

that might affect the adsorption of CO_2. The mole fraction of CO_2 in the gas mixture also affects the shape of Cu-MOF-74 isotherm. The increase in mole fraction of CO_2 causes saturation to be achieved in Cu-MOF-74 at lower pressure (ca. 2000 kPa), while in case of lower mole fraction of CO_2 the loading is still growing.

In Figure 5.9, the distributions of the CO_2 and H_2 molecules adsorbed from CO_2/H_2 gas mixture with CO_2 mole fraction $y_{CO_2} = 0.5$ are analyzed inside Ni- and Cu-MOF-74 at 298.15 K and 4000 kPa. The preferential sites of the CO_2 molecules adsorbed in Ni- and Cu-MOF-74 are located at the open-metal centers and in the middle of the pores. The adsorption loading of H_2 in Ni- and Cu-MOF-74 is homogeneously distributed, which reflects the lower hydrogen affinity compared to CO_2, resulting in the adsorption uptake

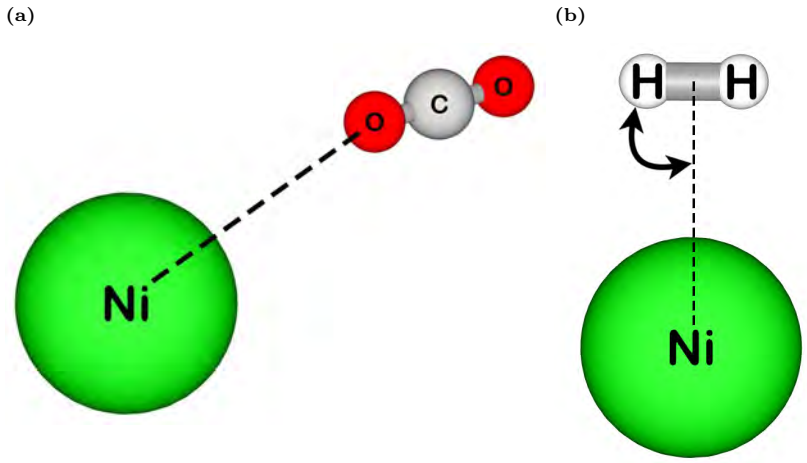

Fig. 5.7. Binding geometry of the adsorbate molecule in Ni-MOF-74 obtained from Baker's minimization simulations at 298 K: (a) CO_2, and (b) H_2. The molecules interacting with open-metal centers are visualized using iRASPA [38]. The binding distances subject to analysis in Table 5.3 (M - O_{CO_2}, and M - H_{com}) are connected by dashed lines. The angle M - H_{com} - H_{H_2} is depicted by an arc.

lower than 1 mg g^{-1} of H_2. The process of CO_2 separation from CO_2/H_2 mixtures using M-MOF-74 is promising as the molecules of H_2 do not adsorb, resulting in high purity products. The performance of M-MOF-74 was further evaluated in fixed-bed adsorbers using breakthrough simulations from RUPTURA. The breakthrough curves were computed for CO_2/H_2 mixtures, where CO_2 mole fraction y_{CO_2} = 0.1, 0.2, 0.3, 0.4, 0.5, 0.9, see Figure 5.10. The validation of output from RUPTURA by independent prediction of CO_2/H_2 mixtures from Figure 5.8 using IAST is shown in Figure C.6 of Appendix C. The prediction obtained using IAST from RUPTURA agrees well with the previously performed GCMC simulations of the CO_2/H_2 mixture, indicating the successful validation of results from RUPTURA. It is clear that the separation of CO_2 is effective, as H_2 is not being adsorbed from the gas mixture. The analysis of breakthrough curves of CO_2 obtained in Ni-, and Cu-MOF-74 (Figure 5.10a, and b) shows that the breakthrough time increases with decreasing mole fraction of CO_2 in the mixture. More adsorbate molecules flowing through a column result in faster filling of the adsorbent. Increasing the feed mole fraction of CO_2 from 0.1 to 0.9 speeds up the breakthrough time by ca. 40 min in Ni-MOF-74, and ca. 16 min in Cu-MOF-74. CO_2 eluted out

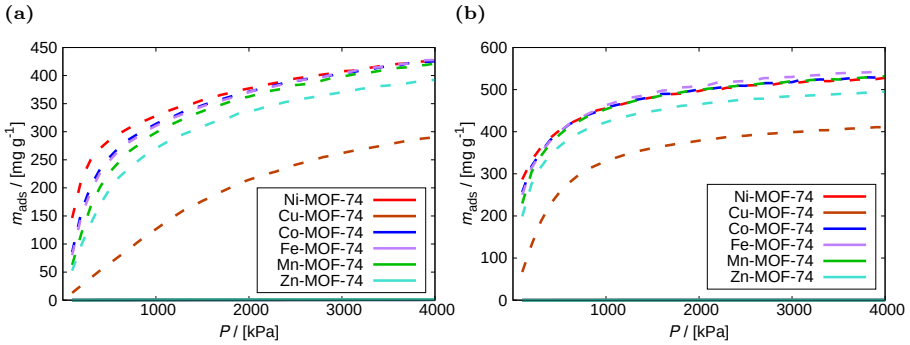

Fig. 5.8. Adsorption of CO_2/H_2 mixture in M-MOF-74 obtained from GCMC simulations at 298.15 K, and 100 - 4000 kPa for CO_2 mole fraction: (a) $y_{CO_2} = 0.1$, and (b) $y_{CO_2} = 0.5$. The adsorption isotherms of CO_2 are represented by dashed lines, and the adsorption isotherms of H_2 by solid lines. The adsorption of H_2 practically does not occur when CO_2 is present in the mixture. The adsorption loading in all studied M-MOF-74 decreases with mole fraction of CO_2.

up to 2 times later in case of Ni-MOF-74 than Cu-MOF-74. The adsorption uptake in Ni-MOF-74 is significantly higher than in Cu-MOF-74, consequently the maximum loading of column containing Ni-MOF-74 takes longer under the same conditions. The tendency in performance of all the studied M-MOF-74 is indicated in Figure 5.10c for the mixture with $y_{CO_2} = 0.5$. The time needed for CO_2 to elute out follows the same order as the uptake and the heat of CO_2 adsorption: Ni > Co > Fe > Mn > Zn > Cu, with the time difference of ca. 3 min between Ni-, and Cu-MOF-74. The breakthrough curves for Co-, Fe-, Mn-, and Zn-MOF-74, where CO_2 mole fraction in the mixture is $y_{CO_2} = 0.1$, 0.2, 0.3, 0.4, 0.5, 0.9 are shown in Figure C.7 of Appendix C. The comparison of breakthrough curves depending on the metal centers for mixtures with $y_{CO_2} = 0.1$, 0.9 is shown in Figure C.8 of Appendix C. The breakthrough time difference between Ni-, and Cu-MOF-74 is shown to decrease with increasing feed mole fraction of CO_2. At $y_{CO_2} = 0.1$ the breakthrough time difference is 24 times longer than at $y_{CO_2} = 0.9$. In the study of Caldwell et al. [293] the separation of CO_2/H_2 mixtures was performed using modified activated carbon at $y_{CO_2} = 0.1$, 0.2, 0.3, 0.4, 0.5, at the same initial conditions as specified in this study. The recorded breakthrough time was between ca. 17 min for $y_{CO_2} = 0.5$, and ca. 50 min for $y_{CO_2} = 0.1$. This is a very similar time difference as Ni-MOF-74, in which case the breakthrough time equals to ca. 12 min for $y_{CO_2} = 0.5$, and ca. 45 min for $y_{CO_2} = 0.1$. The CO_2/H_2 separation performance of Ni-MOF-74 is found to be comparable to the modified

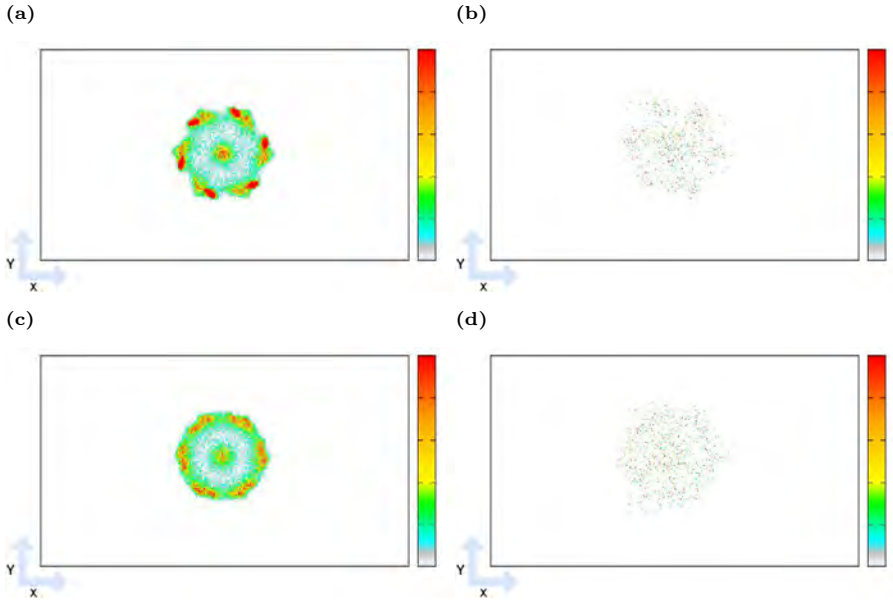

Fig. 5.9. The distribution of the CO_2, and H_2 molecules inside M-MOF-74, analyzed using density profiles from GCMC simulations of CO_2/H_2 gas mixture ($y_{CO_2} = 0.5$) at 298.15 K, 4000 kPa: (a) the distribution of CO_2 molecules in Ni-MOF-74, (b) the distribution of H_2 molecules in Ni-MOF-74, (c) the distribution of CO_2 molecules in Cu-MOF-74, (d) the distribution of H_2 molecules in Cu-MOF-74. The center of mass of the molecules that are adsorbed was projected onto the XY plane. The color gradation of the scales relates to the most and least populated regions of the structure, which is relative in each case. The color scale is shown as a reference of the molecules loading. The preferential sites of CO_2 molecules (colored red) in Ni- and Cu-MOF-74 are at the open-metal centers and in the middle of the pores. The adsorption loading of H_2 in Ni- and Cu-MOF-74 is homogeneously distributed, which is a reflection of the lower hydrogen affinity compared to CO_2, resulting in the adsorption uptake lower than 1 mg g^{-1} of H_2.

activated carbon. We feel that other factors important for Ni-MOF-74 application in PSA, such as economic analysis, resistance to moisture, and structural modifications, are beyond the scope of the present study. As MOF crystals are brittle and easily broken [298], their application in powder form leads to a high-pressure drop across the column and dust pollution. For scalable industrial applications, Ni-MOF-74 should be pressed into the pellets [299], or molded into processable shaped bodies of high porosity [300]. The molding process was described in the study of Pu et al. [300] based on Mg-MOF-74. The authors showed that the molding process rarely reduces the adsorptive

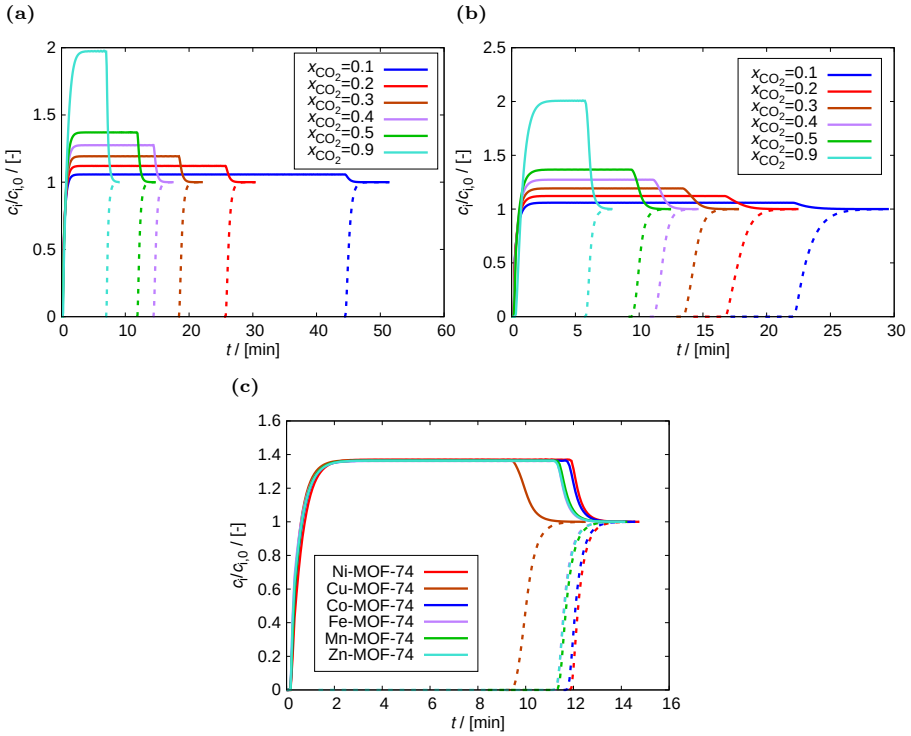

Fig. 5.10. Breakthrough curves computed from RUPTURA [291] for the separation of CO_2/H_2 mixtures in fixed-bed adsorbers using: (a) Ni-MOF-74 at CO_2 feed mole fractions of y_{CO_2} = 0.1, 0.2, 0.3, 0.4, 0.5, 0.9, (b) Cu-MOF-74 at CO_2 feed mole fractions of y_{CO_2} = 0.1, 0.2, 0.3, 0.4, 0.5, 0.9, (c) M-MOF-74, where M = Ni, Cu, Co, Fe, Mn, Zn at CO_2 feed mole fractions of y_{CO_2} = 0.5. The breakthrough curves of CO_2 are represented by dashed lines, and the breakthrough curves of H_2 by solid lines. The following dependencies are found: (1) the breakthrough time follows the same order as the uptake and the heat of CO_2 adsorption: Ni > Co > Fe > Mn > Zn > Cu, (2) the breakthrough time increases with decreasing mole fraction of CO_2 in the mixture. The initial conditions are specified as: temperature T=298 K, total pressure p_T = 2.5 MPa, packed bed void fraction ε_B = 0.4, interstitial gas velocity entering the packed bed v = 0.006791 m s^{-1}, length of packed bed adsorber L = 0.065 m, axial dispersion is neglected, and isothermal conditions are assumed.

ability. Another interesting topic explored in the literature involves modifications of M-MOF-74: the development of zeolite@metal–organic framework composites consisting of Ni-MOF-74 and zeolite-5A with a core–shell structure for efficient H_2 purification [301]. Al-Naddaf et al. [301] reported that the selectivities for separations of CO_2/H_2, CO/H_2, CH_4/H_2, and N_2/H_2 are lar-

ger than those of the bare zeolite or MOF. Due to a higher surface area, total pore volume, and formation of new mesopores at the MOF–zeolite interface, the composite showed a 20 - 30% increase in CO_2, CO, CH_4, and N_2 uptake than Ni-MOF-74 [301]. An alternative, worth exploring post-modification of Ni-MOF-74 is also amino-functionalization with ethylenediamine, successfully applied to Mg-MOF-74 in the study of Wang et al. [302] The separation performance of the studied Mg-MOF-74 membrane was found to be improved, increasing the CO_2/H_2 selectivity from 10.5 to 28 due to the enhanced adsorption of CO_2 molecules by amine groups, thereby reducing the permeance of CO_2. Further studies of Ni-MOF-74 towards its application in separation processes may be a promising subject of research in the field of CO_2 and H_2 capture.

5.4 — Conclusions

We carried out Monte Carlo simulations to adjust the non-polarizable force fields for CO_2 and H_2 adsorption in M-MOF-74, where M = Ni, Cu, Co, Fe, Mn, Zn. The model of CO_2 by Harris and Yung with LJ interactions parameters modeled by García-Sánchez et al. [176, 284] was used in this study together with the three-site charge-quadrupole model of H_2 by Darkrim and Levesque [243]. LJ parameters from the DREIDING force field were used for the atoms of the frameworks, except for metal centers, which are defined by the UFF force field. We introduced two modifications to the existing force field for CO_2, H_2, and M-MOF-74: scaling the Coulombic interaction potentials of the framework atoms of M-MOF-74, and scaling LJ interaction potentials between the center of mass of H_2 and the open-metal centers. The force field was successfully validated by reproducing experimental CO_2 and H_2 isotherms, enthalpies of adsorption, binding geometries, and showing temperature transferability of the force field from 77 K to 87 K, and 298 K. The results agree well with the experimental measurements. The Feynman-Hibbs quantum correction was found to be an important part of the force field at cryogenic temperatures, as it affects the shape of the isotherm by reducing the adsorption capacity. The two-step mechanism of adsorption was recreated, wherein adsorbate molecules first adsorb at the metal centers, followed by adsorption above a triangle of oxygen atoms within the framework. The simulated uptake and heat of adsorption for CO_2 and H_2 reproduced the tendency in performance of M-MOF-74 from the experimental data. A small deviation was observed for the adsorption of H_2 in Fe-MOF-74, however the binding distance between H_2 and the metal center was reproduced most precisely for this MOF as 2.522 Å, deviating only by 0.3% from the literature value. The

force field was applied to the adsorption of CO_2/H_2 mixtures at 298.15 K, and the prediction of breakthrough curves at 298 K. It was shown that almost no adsorption of H_2 occurs when CO_2 is present in the mixture. The breakthrough time follows the same order as the uptake and the heat of CO_2 adsorption: Ni > Co > Fe > Mn > Zn > Cu. The metal-organic frameworks M-MOF-74 have the potential in the capture of CO_2 and H_2, as well as in separation processes of CO_2/H_2 mixtures. The proposed non-polarizable force field is an alternative to the complex polarizable force fields available in the literature, that enables to fully investigate the performance of M-MOF-74 by molecular simulations. An interesting topic for future research would be the modification of the HCOOH force field to reproduce its binding geometry in M-MOF-74 obtained from DFT, to enable the application together with CO_2 and H_2 force fields. This would allow to study the process of CO_2 conversion into HCOOH, and better understanding of the effect of open-metal centers on the CO_2 hydrogenation reaction to HCOOH in confinement.

Chapter 6

The Impact of Metal Centers in the M-MOF-74 Series on Formic Acid Production

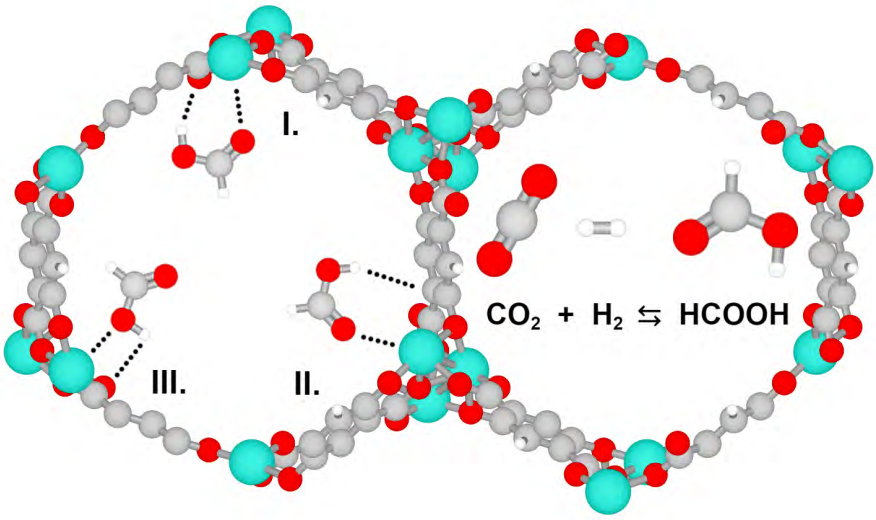

The confinement effect of porous materials on the thermodynamical equilibrium of the CO_2 hydrogenation reaction presents a cost-effective alternative to transition metal catalysts. In metal-organic frameworks, the type of metal center has a greater impact on the enhancement of formic acid production than the scale of confinement resulting from the pore size. The M-MOF-74 series enables a comprehensive study of how different metal centers affect HCOOH production, minimizing the effect of pore size. In this work, molecular simulations were used to analyze the adsorption of HCOOH and the CO_2 hydrogenation reaction in M-MOF-74, where M = Ni, Cu, Co, Fe, Mn, Zn. We combine classical simulations and Density Functional Theory calculations to gain insights into the mechanisms that govern the low coverage adsorption of HCOOH in the surrounding of the metal centers of M-MOF-74. The impact of metal centers on the HCOOH yield was assessed by Monte Carlo simulations in the grand-canonical ensemble, using gas-phase compositions of CO_2, H_2, and HCOOH at chemical equilibrium at 298.15 - 800 K, 1 - 60 bar. The performance of M-MOF-74 in HCOOH production follows the same order as the uptake and the heat of HCOOH adsorption: Ni > Co > Fe > Mn > Zn > Cu. Ni-MOF-74 increases the mole fraction of HCOOH by ca. 10^5 times compared to the gas phase at 298.15 K, 60 bar. Ni-MOF-74 has the potential to be more economically attractive for CO_2 conversion than transition metal catalysts, achieving HCOOH production at concentrations comparable to the highest formate levels reported for transition metal catalysts and offering a more valuable molecular form of the product.

This chapter is based on the following publication:

Wasik, D. O., Vicent-Luna, J. M., Rezaie, S., Luna-Triguero, A., Vlugt, T. J. H., Calero, S. The Impact of Metal Centers in the M-MOF-74 Series on Formic Acid Production. *ACS Applied Materials & Interfaces* **2024**, *16*, 45006-45019.

6.1 — Introduction

In 2023, global energy-related CO_2 emissions increased by 1.1%, reaching a new record of 37.4 billion tonnes (Gt) [22]. From 2019 to 2023, total energy-related CO_2 emissions raised by ca. 900 million tonnes (Mt), however without the adoption of clean energy technologies there emissions would have grown threefold [22]. Further advancement of sustainable energy technologies that significantly slow down emissions is an important topic for future research. An economically attractive method to reduce CO_2 emissions is the capture at the source of production and the conversion to valuable chemicals, e.g., formic acid, salicylic acid, methanol, urea, propylene, and polyols [1–4]. Due to the wide range of formic acid (HCOOH) applications, e.g., as a hydrogen carrier [7], fungicidal and bactericidal agent [5, 6], in the production of rubber [8] and the water-gas-shift reaction [9], the HCOOH global market value is forecast to increase from 1.8 billion dollars in 2023 to 2.8 billion dollars by 2033 [33]. One of the possible methods for HCOOH production that gained attention over the past few decades is the CO_2 hydrogenation reaction [18]: $CO_2 + H_2 \rightleftarrows HCOOH$. The high free energy barrier of 351.46 kJ mol^{-1} for CO_2 hydrogenation in the gas phase [19] indicates that a catalyst is needed. The most efficient transition metal-based catalytic systems for CO_2 hydrogenation involve catalysts with pincer ligands [59–61], half-sandwich catalysts with or without proton-responsive ligands [65–69], N-heterocyclic carbene ligands [62–64], and phosphine ligands [54–58]. Given the significant limitations of transition metal catalysts, such as their cost and toxicity [19], it is essential to investigate methods to improve CO_2 hydrogenation efficiency while addressing these challenges. The confinement effect of porous materials was shown to shift the thermodynamical equilibrium of several reactions [70, 210–215, 276], including CO_2 hydrogenation, resulting in an increased yield of formic acid [276]. It may be considered a cost-effective alternative to the transition metal catalysts due to: (a) the higher density of the pore phase compared to the bulk-phase, increasing yield for reactions in which there is a decrease in the total number of moles, by Le Chatelier's principle [44], (b) the selective adsorption of favored HCOOH component on the solid surfaces, promoting its enhanced formation [70]. In a molecular simulation study of Wasik et al. [276], the confinement effect of metal-organic frameworks (MOFs) was found to affect the CO_2 hydrogenation reaction, shifting the thermodynamical equilibrium towards HCOOH formation. The most significant improvement in HCOOH production was achieved with Cu-BTC at 298.15 K and 60 bar, resulting in the mole fraction of HCOOH equal to 0.0016, which is ca. 2000 times higher compared to the gas phase [276]. The final concentration of pro-

duced HCOOH (0.031 mol L^{-1} [276]) was ca. 80 times lower than the highest reported concentration obtained with the use of Wilkinson complex [55], and ca. 30 times higher than the lowest reported concentration obtained using a catalyst with N-heterocyclic carbene ligands [63]. By comparing the performance of MOFs with different pore sizes and metal centers (UiO-66, Cu-BTC, and IRMOF-1), it was found that the stronger confinement resulting from the smaller pore sizes does not ensure the enhancement in HCOOH production from the CO_2 hydrogenation reaction. Despite the smallest pore sizes within the studied MOFs, the resulting mole fraction of HCOOH in the UiO-66 framework was only ca. 200 times higher compared to the gas phase at 298.15 K, 60 bar [276]. The type of metal center in the metal-organic framework was found to be the dominant factor in HCOOH production [276]. Metal-organic frameworks offer a promising alternative or supplement to transition metal catalysts for enhancing the efficiency of CO_2 hydrogenation, as a low free energy barrier for the reaction compared to the gas phase is still needed to reach the favourable thermodynamic equilibrium in MOFs. This potential arises from several advantages: MOFs eliminate the need for expensive temperature elevation, produce a more valuable final product, which reduces the costs of downstream processing, and achieve a final concentration of HCOOH comparable to the reported concentrations of formate obtained with transition metal catalysts [276].

The M-MOF-74 series allows to explore how the type of metal center impacts the enhancement of HCOOH production while minimizing the impact of pore size. The M-MOF-74 series (where M = Ni, Cu, Co, Fe, Mn, Mg, or Zn [113–122]) is one of the most popular families of MOFs, synthesized by combining M^{2+} ions with 2,5-dioxido-1,4-benzenedicarboxylate ($dobdc^{4-}$) ligands. The presence of negatively charged ligands causes a high density of metal cations [122], accessible for sorbate molecules through large cylindrical pores with a diameter of ca. 11 Å [122]. Numerous open-metal sites increase selectivity [123] and the surface packing density of adsorbates [124]. Additionally, the open-metal sites provide reactive sites for chemical reactions, such as oxygenation [125] and size-selective Lewis acid catalysis [126]. Extensive experimental and computational studies revealed the promising performance of the M-MOF-74 series for the capture and separation of CO_2 [122, 256–260] and H_2 [113–118, 121, 270–275]. The solid adsorption using M-MOF-74 is considered an alternative to more expensive and less efficient liquid absorption [255]. In the study of Queen et al. [122], the adsorption of CO_2 in M-MOF-74 was analyzed experimentally, and computationally using Density Functional Theory (DFT) calculations. It was found that depending on the open-metal site, the affinity of CO_2 with M-MOF-74 frameworks decreases as

follows: Mg > Ni > Co > Fe > Mn > Zn > Cu [122]. The adsorption loading was obtained in the range from ca. 130 mg g^{-1} of framework for M = Cu to ca. 310 mg g^{-1} of framework for M = Mg at 100 kPa, 298 K, with the corresponding isosteric heat of adsorption from ca. 20 kJ mol^{-1} to ca. 40 kJ mol^{-1} [122]. The increase in isosteric heat of CO_2 adsorption correlated to the stronger CO_2 binding energy was found to result from a higher effective charge of the M^{2+} ion at the open-metal site where CO_2 adsorbs. This implies that electrostatic interactions are the main factor affecting CO_2 adsorption. In sharp contrast, H_2 adsorption was found to be predominantly determined by polarization interactions at low temperatures [119], resulting in a difference in affinity with M-MOF-74 compared to CO_2: Ni > Co > Mg > Fe > Zn ≈ Mn > Cu [271]. The highest adsorption uptake of H_2 is obtained for M = Ni as ca. 20 mg g^{-1} of framework at 100 kPa, 77 K [271]. The study of Wasik et al. [303] on the adsorption of CO_2/H_2 mixtures in M-MOF-74 showed that almost no adsorption of H_2 occurs (less than 1 mg g^{-1} of H_2 adsorbed) when CO_2 is present in the mixture at 298.15 K. This suggests that H_2 may be the limiting component in the CO_2 hydrogenation reaction carried out in the confinement of M-MOF-74. Considering that both adsorbates CO_2 and H_2 show different affinities for adsorption in M-MOF-74, an interesting topic for research is to examine how the type of metal center in M-MOF-74 affects the adsorption of HCOOH obtained from the CO_2 hydrogenation reaction.

Molecular simulations offer an intrinsic approach to explore confinement effects independently from catalytic effects, clarifying what is caused by confinement, and what is caused by catalysis. To the best of our knowledge, no literature data exists on force field-based molecular simulations of CO_2/H_2/HCOOH systems within the M-MOF-74 framework. In our previous work [303], we presented a non-polarizable force field for molecular simulations of CO_2 and H_2 adsorption in M-MOF-74, where M = Ni, Cu, Co, Fe, Mn, Zn, after adjusting the existing force field for CO_2, H_2, and M-MOF-74 by scaling the Coulombic interactions of M-MOF-74 atoms to reproduce experimental data on CO_2 adsorption [122], and scaling the Lennard-Jones interaction potentials between the center of mass of H_2 and the open-metal centers to reproduce experimental data on H_2 adsorption [271]. The validation of the force field was confirmed by the successful reproduction of experimental CO_2 and H_2 adsorption isotherms, heats of adsorption, binding geometries, and demonstrating temperature transferability from 77 K to 87 K, and 298 K. The advantages of a non-polarizable force field adjusted to reproduce experimental data compared to a polarizable force field are easy transferability from one component to another, low computational time, and high accuracy [303]. While polarizable force fields may have an improved description of interactions between

guest molecules and open-metal sites [277], the computational cost is high unless back-polarization is ignored [279]. A non-polarizable force field for CO_2 adsorption in M-MOF-74 was derived from DFT by Mercado et al. [280], but this approach involved adjusting not only the LJ interaction potentials of the metal site but also all interaction sites, leading to many fitting parameters and potentially lower transferability. Pham et al. [119] attempted to reproduce experimental data on H_2 adsorption in M-MOF-74 [271] by testing various models, among which only the polarizable model successfully reproduced the adsorption isotherms for all studied metal centers. For systems involving not only CO_2 and H_2 adsorption but also the hydrogenation reaction of CO_2 to HCOOH, the size and complexity of the system can affect computational time and accuracy. Developing a non-polarizable force field is beneficial for investigating the dependence of HCOOH production enhancement on the type of metal center in M-MOF-74. Additionally, non-polarizable force fields offer the advantage of transferability between different components, whereas polarizable force fields require specific development for transferability [119, 279]. In this work, molecular simulations were used to study the adsorption and production of HCOOH from the CO_2 hydrogenation reaction in M-MOF-74, where M = Ni, Cu, Co, Fe, Mn, Zn. Due to the lack of experimental data available for the adsorption of formic acid in M-MOF-74, the compatibility of the non-polarizable force field for CO_2 and H_2 adsorption in M-MOF-74 [303] with HCOOH force field [174] was evaluated by studying the binding geometries of HCOOH, using both a minimization scheme and DFT. Monte Carlo simulations in the grand-canonical ensemble (GCMC) were performed in the frameworks to compute single-component adsorption isotherms of HCOOH and the adsorption isobars of the CO_2 hydrogenation components. The effect of the type of metal center in M-MOF-74 on the CO_2 hydrogenation reaction was studied at less industrially expensive temperatures ranging from 298.15 K to 800 K and higher pressures from 1 bar to 60 bar, which allow more molecules to enter the structure.

This chapter is organized as follows: in section 6.2, we provide technical details of the molecular simulation methods, the force fields for CO_2, H_2, HCOOH, and the metal-organic frameworks. In section 6.3, we present and discuss the results. The HCOOH isotherms and heat of adsorption in M-MOF-74 are computed using GCMC simulations at 298 K, and 10^{-6} - 10 kPa. The binding geometries are simulated using Baker's minimization scheme [160] and compared to the results of DFT calculations. The adsorption isobars in M-MOF-74 frameworks are computed from GCMC simulations at 298.15 - 800 K and 1 - 60 bar, using gas-phase mole fractions of CO_2, H_2, and HCOOH at reaction equilibrium, obtained in our previous work [206]. The HCOOH

production enhancement is calculated for all systems. Depending on the metal center, the enhancement in HCOOH production decreases in the same order as its uptake and isosteric heat of adsorption: Ni > Co > Fe > Mn > Zn > Cu. The strongest guest-host interaction of HCOOH with Ni-MOF-74 causes the most significant influence on the CO_2 hydrogenation thermodynamics, enhancing HCOOH production by ca. 10^5 times compared to the gas phase at 298.15 K, 60 bar. Our findings are summarized in section 6.4.

6.2 — Methodology

The adsorption of HCOOH and the CO_2 hydrogenation reaction is studied in M-MOF-74, where M = Ni, Cu, Co, Fe, Mn, Zn using force field-based molecular simulations. Intermolecular interactions between guest-host and guest-guest molecules are modeled using Coulombic and Lennard-Jones (LJ) potentials. The Lorentz–Berthelot mixing rules [129] are used for interactions between different LJ sites, except interactions between the H_2 molecule centers of mass and open-metal centers, which are scaled and specified by an override [303]. LJ interactions are cut and shifted to zero at a 12 Å cutoff radius without tail corrections. Periodic boundary conditions are applied in all three directions. Electrostatic interactions are computed using the Ewald summation method [151], with parameters corresponding to a relative precision of 10^{-6}. The so-called 'P2' variant of the OPLS/AA force field for HCOOH [174] is applied to the HCOOH molecule model constructed and optimized at the B3LYP/6-31G(d) level of theory in a study of Wasik et al. [206] The HCOOH force field successfully reproduce the vapor-liquid equilibrium coexistence curve, saturated vapor pressures, and densities at different temperatures [206]. The non-polarizable CO_2, and H_2 force field for adsorption in M-MOF-74 was adjusted in our previous work [303] by introducing two modifications to the existing parameters for CO_2, H_2, and M-MOF-74: (1) Coulombic interactions of M-MOF-74 were scaled to reproduce experimental data on CO_2 adsorption [122] using the CO_2 model by Harris and Yung [284] combined with the LJ interaction parameters modeled by García-Sánchez et al. [176], (2) LJ interaction potentials between the center of mass of H_2 in the three-site charge-quadrupole model by Darkrim-Levesque model [243], and the open-metal centers were scaled to reproduce experimental data on H_2 adsorption [271]. The LJ parameters for the framework atoms are derived from the DREIDING force field [148], except for the metal centers, which use parameters from the UFF force field [147]. The CO_2, H_2, HCOOH, and framework models are rigid, with point charges assigned to all atoms. All framework structures are charge-neutral. All the studied M-MOF-74 crystal structures

were obtained from experimental syntheses [113–118]. The simulated systems consist of 1 × 1 × 4 trigonal unit cells to guarantee a minimum distance that exceeds twice the cutoff radius between periodic images. The LJ parameters and partial charges for all components used in this work are listed in Table C.2 of Appendix C, except for HCOOH listed in Table 4.1 of Chapter 4. For the details on the structures, Lennard-Jones and Coulombic interaction potentials for the M-MOF-74 (M = Ni, Cu, Co, Fe, Mn, Zn) frameworks, the reader is referred to the study of Wasik et al. [303]

The adsorption isotherms and the heat of HCOOH adsorption in M-MOF-74 were computed from GCMC simulations [128] at 298 K, 10^{-6} - 10 kPa, using RASPA software package [94, 95]. In the grand-canonical ensemble, the chemical potential, volume, and temperature are fixed. The RASPA software package [94] provides the uncertainties in the computed number of molecules adsorbed in a unit cell, by dividing the simulation into five blocks and calculating the standard deviation. The heat of HCOOH adsorption at finite loadings was computed using the fluctuation method [304] implemented in the RASPA software package [94]. To evaluate the resulting adsorption of HCOOH, we studied the interactions between an adsorbate molecule and the frameworks. The isosteric heat of adsorption [242] for HCOOH in M-MOF-74 was calculated for a temperature range of 298.15 - 800 K, and compared with literature data for the previously studied MOFs (UiO-66, Cu-BTC, IRMOF-1) [276]. The enthalpy of adsorption at infinite dilution representing the affinity between the molecule and the framework, is determined by Eq. 4.7.

To analyze the binding geometries of the adsorption of formic acid at infinite dilution, we performed a series of geometry optimizations of a single molecule using Baker's minimization method [160] implemented in RASPA [94, 95]. Baker's minimization method uses the eigenvalues/vectors of the Hessian matrix to efficiently and accurately locate true minima on the energy surface, ensuring the determination of equilibrium geometries with enhanced numerical stability and faster convergence [160]. Because of the asymmetric nature of formic acid, we performed 100 optimizations starting from different configurations and ranked the optimized geometries from high to low energy. The obtained equilibrium geometries of HCOOH were compared with DFT calculations. The adsorption of formic acid in M-MOF-74 has been performed using DFT and plane wave pseudo potential method (PWSCF) implemented in the Quantum Espresso package [305]. The exchange-correlation corrections has been applied using the generalized gradient approach (GGA), as formulated by Perdew, Burke and Ernzerhof (PBE) [306], including DFT-D3(BJ) dispersion corrections [307]. The kinetic energy cutoff for wavefunctions has been set to 60 Ry, while the kinetic energy cutoff for charge density and potential,

using norm-conserving pseudopotentials, has been set to 480 Ry. The unit cell of M-MOF-74 includes 54 atoms (see Figure D.1 of Appendix D) and has been fully relaxed by allowing both the ionic positions and lattice parameters to change until the convergence threshold for the total energy and forces are smaller than $1{\cdot}10^{-6}$ a.u. Due to the presence of transition metals (Co, Cu, Fe, Mn, Ni, and Zn) in M-MOF-74, the smearing method has been selected to handle the electronic occupations of the Kohn-Sham states, using a degauss value of $1.4{\cdot}10^{-2}$ Ry. Since M-MOF-74 includes atoms with magnetic properties, appropriate magnetization values have been considered depending on the transition metal. To ensure accurate results, a convergence threshold of $1{\cdot}10^{-9}$ a.u. has been selected with a mixing beta of 0.4. The Brillouin zone has been sampled using a 2 × 2 × 2 Monkhorst-Pack k-points [308]. The calculated lattice parameters resulting from the geometry optimization show a strong agreement with the previously reported literature [122, 253] (see Figure D.2 of Appendix D). To study the adsorption of formic acid in the M-MOF-74 family, we have performed a geometry relaxation of a single molecule within the previously optimized structures. In this calculation, both MOF and formic acid molecule are relaxed. Finally, the binding energy between formic acid and the surface of M-MOF-74 has been computed by:

$$E_{\mathrm{b(HCOOH)}} = E_{\mathrm{tot(M\text{-}MOF\text{-}74\ +\ HCOOH)}} - E_{\mathrm{tot(M\text{-}MOF\text{-}74)}} - E_{\mathrm{tot(HCOOH)}} \quad (6.1)$$

where $E_{\mathrm{tot(M\text{-}MOF\text{-}74\ +\ HCOOH)}}$ indicates the total energy of M-MOF-74 with HCOOH per unit cell, $E_{\mathrm{tot(M\text{-}MOF\text{-}74)}}$ denotes the total energy of M-MOF-74 per unit cell, and $E_{\mathrm{tot(HCOOH)}}$ represents the total energy of isolated formic acid molecule.

To study the thermodynamic confinement effects of M-MOF-74 on the CO_2 hydrogenation to HCOOH, the adsorption isobars were computed using GCMC simulations at 298.15 - 800 K and 1 - 60 bar. The gas-phase mole fractions of CO_2, H_2, and HCOOH at chemical equilibrium, obtained using the Monte Carlo Software Brick-CFCMC [143, 152] from Continuous Fractional Component Monte Carlo simulations [139–141] in the Reaction Ensemble [135, 136, 142] (Rx/CFC) by Wasik et al. [276], served as input data for the GCMC simulations. The chemical potential is directly derived from the fugacity, which is calculated using the fugacity coefficients from the Peng-Robinson Equation of State (PR-EoS) [157] by the RASPA software package [94, 95]. The agreement between the fugacity coefficients of CO_2, H_2, and HCOOH computed using the PR-EoS and the NIST Standard Reference Database REFPROP[239] at 298.15 - 800 K and 1 - 60 bar was found to be satisfactory, with average deviations of only 0.45% for CO_2 and 0.66% for H_2, as reported in the study of Wasik et al.[276] The initial mole fractions [276]

used in this study are listed in Table B.4 of Appendix B. The uncertainties in the computed number of molecules adsorbed in a unit cell provided by the RASPA software package [94] were used to calculate the uncertainties in the mole fractions of components Err_x, see Eqs. 4.5 and 4.6. To compare the mole fractions of HCOOH obtained from GCMC simulations in the frameworks to the gas-phase mole fractions at equivalent chemical potentials [276], the enhancement (ENH) of HCOOH production was calculated by Eq. 4.8. The final concentration of HCOOH in the adsorbed phase was calculated as:

$$c_{\mathrm{HCOOH}} = \frac{n_{\mathrm{HCOOH}}}{\xi \cdot V} \tag{6.2}$$

where n_{HCOOH} is the calculated number of moles of HCOOH adsorbed in a unit cell, ξ is the helium void fraction, and V is the volume of the unit cell.

The GCMC simulations for HCOOH adsorption in M-MOF-74 were conducted with 10^4 initial Monte Carlo (MC) cycles followed by 10^6 production MC cycles. Each MC cycle consists of N trial moves, where N is the total number of molecules at the beginning of the simulation. The probabilities assigned to different trial moves in these GCMC simulations were 25% for translations, 25% for rotations, 25% for reinsertions, and 25% for swap trial moves (exchanging molecules with the reservoir). For the GCMC simulations of the CO_2 hydrogenation reaction to HCOOH, 10^4 equilibration MC cycles, and $4{\cdot}10^5$ production MC cycles were used. The probabilities for these trial moves were 16.7% translations, 16.7% rotations, 16.7% reinsertions, 16.7% identity changes (changing the identity of a selected molecule), and 33.2% swap trial moves. For further details on Monte Carlo trial moves, see Refs. [38, 94, 95].

6.3 — Results and Discussion

To investigate the adsorption of HCOOH in M-MOF-74 (M = Ni, Cu, Co, Fe, Mn, Zn), we first computed the isotherms and heats of adsorption for all the studied frameworks at 298 K, and 10^{-6} - 10 kPa, see Figure 6.1a and b. At low pressures, a significant variation in HCOOH adsorption characteristics is observed, indicating that the open-metal sites have a dominant influence on the adsorption process. The HCOOH molecules start to fill the Ni-MOF-74 structure at the lowest pressure, ca. 10^{-5} kPa with the corresponding heat of adsorption ca. 80 kJ mol^{-1}. Cu-MOF-74 starts to fill at the highest pressure, ca. $4{\cdot}10^{-2}$ kPa with the corresponding heat of adsorption ca. 40 kJ mol^{-1}, followed by rapid nucleation of adsorbate molecules. The trend in the simulated uptake and heat of HCOOH adsorption depends on the open-metal site as follows: Ni > Co > Fe > Mn > Zn > Cu. The same trend is found for the adsorption of CO_2 in M-MOF-74, which suggests that HCOOH adsorption is

also predominantly influenced by the electrostatic interactions dependent on the effective charge of the M^{2+} ion at the open-metal site. The two-step mechanism of adsorption, wherein the adsorbate molecules first adsorb at the metal centers, followed by adsorption above a triangle of oxygen atoms within the framework, is present in the adsorption isotherms of Ni-, Co-, Fe-, and Mn-MOF-74 frameworks. The primary adsorption sites fill until ca. 1 molecule of HCOOH per metal center, resulting in a sudden decrease in the heat of adsorption when the secondary sites start filling. While the binding affinities at the primary adsorption sites differ within the M-MOF-74 series, the isotherms converge as the metal centers become saturated at higher pressures due to the isostructural properties of the frameworks. As pressures of 1 kPa, the capacities of the Ni-, Co-, Fe-, Mn-, and Zn-MOF-74 frameworks become highly comparable, each accommodating ca. 2 molecules of HCOOH per metal center. The dependence of HCOOH affinity in M-MOF-74 on a temperature was investigated in the range from 298.15 K to 800 K and compared with literature data for different MOFs [276]. In Figure 6.1c, the isosteric heat of adsorption for HCOOH is shown, which is a measure of the change in enthalpy when adsorbate molecules are adsorbed from the gas phase (higher energy state) to the adsorbed phase (lower energy state), causing the release of heat. The energy state of HCOOH on the adsorbent surface increases with temperature, leading to weaker interactions between the framework and adsorbate. The isosteric heat of adsorption corresponds to the values obtained from GCMC simulations of adsorption at low pressure, where the adsorption loading is very low. The affinity of HCOOH in MOFs decrease with the isosteric heat of adsorption in the following order: Ni-MOF-74 > Co-MOF-74 > Fe-MOF-74 > Mn-MOF-74 > Zn-MOF-74 > Cu-BTC > Cu-MOF-74 > UiO-66 > IRMOF-1. The strongest isosteric heat of adsorption was found for Ni-MOF-74, resulting in the isosteric heat of adsorption ca. 75 kJ mol^{-1} at 298.15 K. The obtained value is 1.6 times higher than the isosteric heat of adsorption in Cu-BTC (ca. 45 mol^{-1}), the best-performing MOF for CO_2 hydrogenation reaction from our previous study [276]. This indicates that Ni-MOF-74 can be expected to be a more promising candidate for CO_2 hydrogenation application, than Cu-BTC which was found to enhance HCOOH production ca. 2000 times compared to the gas phase [276].

The distribution of HCOOH molecules was analyzed inside M-MOF-74 using the average density profiles and shown for Ni-, and Cu-MOF-74 in Figure 6.2. The center of mass of the adsorbed molecules was projected onto the XY plane of anisotropic frameworks. The average density profiles of HCOOH in Ni-MOF-74 confirm that the open-metal centers are primary adsorption sites, where molecules adsorb at low pressures. As the adsorption proceeds at

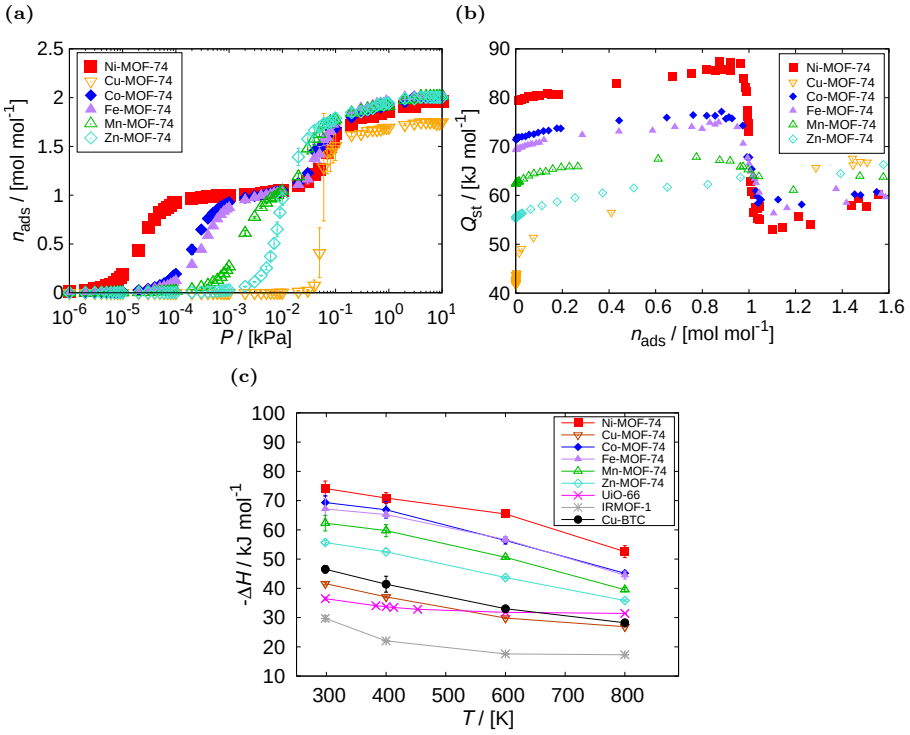

Fig. 6.1. Adsorption of HCOOH in M-MOF-74 (M = Ni, Cu, Co, Fe, Mn, Zn) computed from GCMC simulations: (a) the adsorption isotherms at 298 K, and 10^{-6} - 10 kPa, (b) the corresponding heat of adsorption at 298 K, and 10^{-6} - 10 kPa, and (c) the isosteric heat of adsorption at 298.15 - 800 K. The units of adsorption loading [mol mol^{-1}] refer to the number of HCOOH molecules adsorbed per metal center. The trend in the simulated uptake and heat of HCOOH adsorption depends on the open-metal site as follows: Ni > Co > Fe > Mn > Zn > Cu.

higher pressures, the molecules also adsorb above a triangle of oxygen atoms within the framework. A very high adsorption loading is observed at the open-metal centers compared to the secondary adsorption sites. The adsorbed molecules of HCOOH in Cu-MOF-74 are more homogeneously distributed, due to the lowest affinity for Cu-MOF-74 among the studied structures and the lack of a two-step mechanism of adsorption. The distribution of HCOOH molecules inside Co-, Fe-, Mn-, and Zn-MOF-74 is shown in Figure D.3 of Appendix D.

The guest-guest interaction energies were analyzed and shown in Fig-

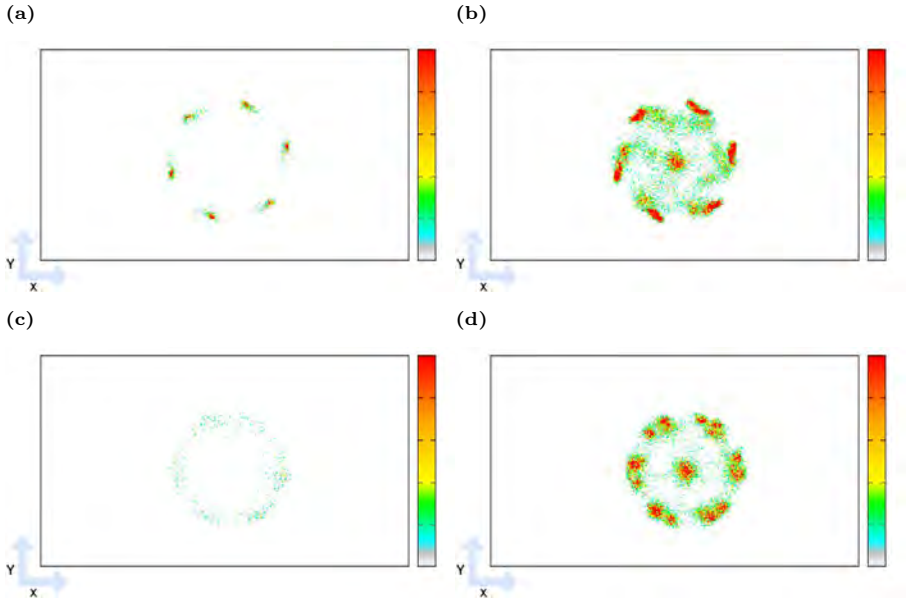

Fig. 6.2. The distribution of the HCOOH molecules inside M-MOF-74, analyzed using density profiles from GCMC simulation: (a) Ni-MOF-74 at 298 K, 10^{-5} kPa, (b) Ni-MOF-74 at 298 K, 10 kPa, (c) Cu-MOF-74 at 298 K, $4{\cdot}10^{-2}$ kPa, (d) Cu-MOF-74 at 298 K, 10 kPa. The center of mass of the molecules that are adsorbed was projected onto the XY plane. The color gradation of the scales relates to the most and least populated regions of the structure, which is relative in each case. The color scale is shown as a reference for the molecule loading. The preferential sites of HCOOH molecules (colored red) in Ni-MOF-74 are at the open-metal centers. The adsorption loading of HCOOH in Cu-MOF-74 is more homogeneously distributed, which is a reflection of the lower affinity for Cu.

ure 6.3a as a function of the pressure. The increase in guest-guest interaction energies with pressure indicates that the adsorption mechanism at the secondary adsorption sites is driven by the nucleation of polar HCOOH molecules via hydrogen bond interactions. The largest jump in the guest-guest interaction energy is observed for Cu-MOF-74 which reflects the rapid nucleation of adsorbate molecules shown in adsorption isotherm at the pressure range from $4{\cdot}10^{-2}$ kPa to 10^{-1} kPa. At the saturation pressure of 10 kPa, the guest-guest interaction energies for all the studied MOFs are close to the enthalpy of vaporization for HCOOH, which is reported as ca. 20.1 kJ mol^{-1} at 298.15 K [186] or 29.6 kJ mol^{-1} at 303 K [188]. The energy contribution from the interaction between HCOOH and the adsorbents is shown in Figure 6.3b. The affinity between the adsorbate and the framework increases with the guest-

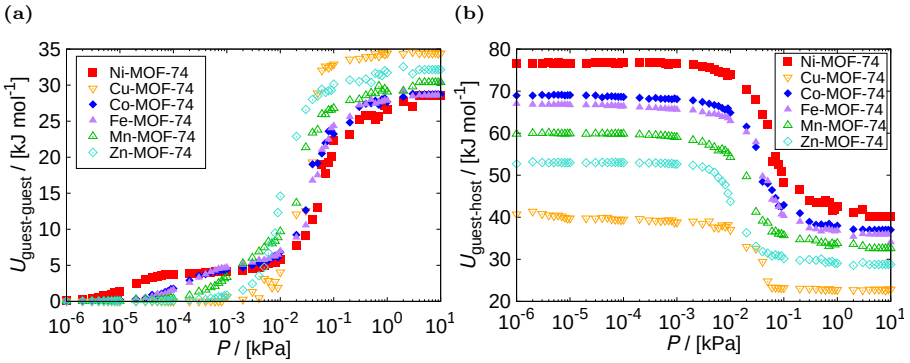

Fig. 6.3. Interaction energies of HCOOH in M-MOF-74 (M = Ni, Cu, Co, Fe, Mn, Zn) computed from GCMC simulations at 298 K, and 10^{-6} - 10 kPa: (a) guest-guest interaction energies, (b) guest-host interaction energies. The increase in guest-guest interaction energies with pressure indicates that the adsorption mechanism at the secondary adsorption sites is driven by the nucleation of HCOOH molecules through hydrogen bond interactions. As the adsorption loading increases in the frameworks, guest-host interaction energies decrease as the preferential adsorption sites fill up, and guest-guest interactions become more important.

host interaction energy. As the loading increases with pressure, guest-host interactions weaken due to the preferential adsorption sites filling up, and guest-guest interactions becoming more significant. The guest-host interactions at a low-pressure regime correspond to the isosteric heat of adsorption in infinite dilution.

The binding geometries of the HCOOH adsorption were analyzed using Baker's minimization method [160] and ranked from high to low energy to find the favorable configurations. To provide a clear depiction of the atomic positions within the frameworks and the HCOOH molecule, a schematic representation of Ni-MOF-74 is shown in Figure 6.4 together with the HCOOH model. The three primary binding geometries of HCOOH found in the surroundings of the metal centers are shown in Figure 6.5. In the three situations, one of the oxygen atoms of HCOOH and the hydrogen atom of the hydroxyl (OH) group strongly interact with the metal center and a negatively charged atom close to it. Configuration I is the most stable, followed by configurations II and III. In configuration I, the electronegative O_{fa2} atom of HCOOH molecules points to the metal while the H_{fa2} aligns to one of the oxygen atoms in the metal cluster (Oa). Unlike the other two oxygen atoms (Ob and Oc) of M-MOF-74 that are connected to two metal atoms, the Oa oxygen atom is connected to a single metal atom and to a carbon atom (Ca). As a result, it can act as a hydrogen bond acceptor, while the OH group of HCOOH

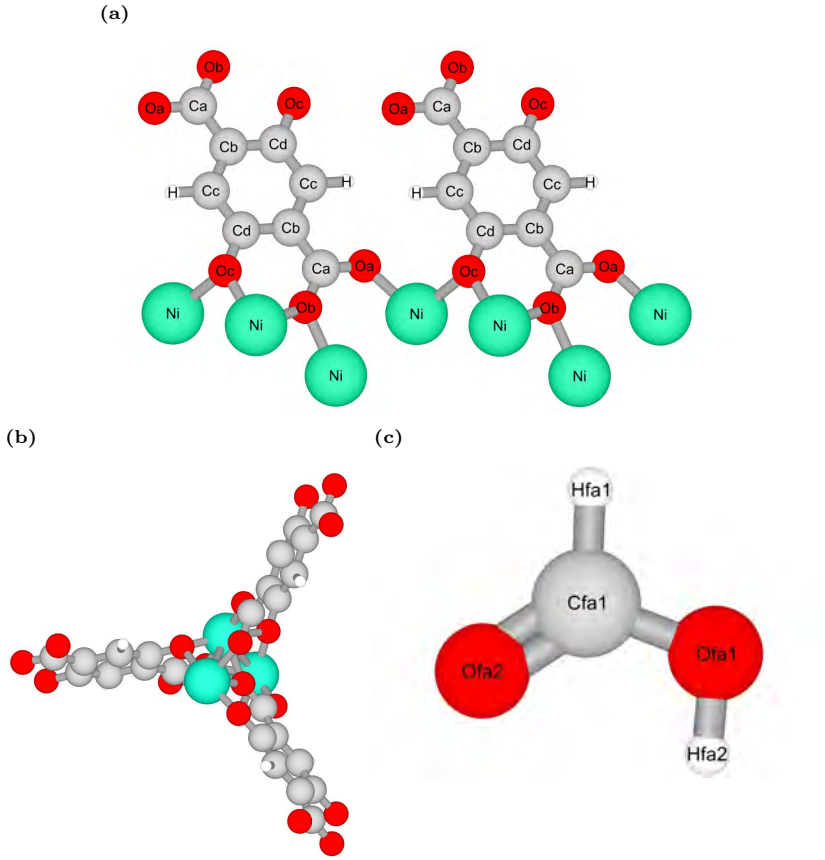

Fig. 6.4. Schematic representation visualized using iRASPA [38] of: (a) the labels and positions of different types of atoms in the M-MOF-74 frameworks for the example of Ni-MOF-74, (b) an atomistic reference structure of MOF-74 framework, and (c) HCOOH model with the atoms labeled.

is a hydrogen bond donor group. Because of this combined interaction, the configuration I shows the highest binding energy compared to the other two configurations. The orientation of the molecule in this configuration is driven by the electrostatic field lines within the cavities of these MOFs, which go from the positively charged metal sites to the electronegative Oa atoms [295], see Figure D.4 of Appendix D. Similarly to configuration I, in configuration II, the electronegative O_{fa2} atom of HCOOH points to the metal, but in this case,

the OH group points to the Cb carbon atom of the aromatic ligand, which has a negative charge. In the less favorable configuration (configuration III), the OH group of HCOOH is nearest to the metal center, while the O_{fa2} atom points to the center of the cage. In this configuration, the OH group is placed in a parallel configuration concerning the M-Oa bond of the metal cluster. To provide a better understanding of the HCOOH binding configurations, the Coulombic potentials for M-MOF-74 were normalized with respect to the partial charge of the metal center, see Table D.1 of Appendix D. The calculated relative charges exhibit a high degree of similarity among the different atom types identified across all frameworks. Normalization reveals that in the most stable configuration I, H_{fa2} aligns with the available hydrogen bond acceptor Oa of the strongest electronegativity (relative charge of -0.40). In the following configuration II, H_{fa2} points to the next in order of electronegativity Cb carbon atom (-0.15). The analysis suggests that the electronegativity of the ligand atom significantly affects the binding configuration of HCOOH. Specifically, together with the open metal sites, atoms with stronger electronegativity are identified as the primary sites for HCOOH adsorption.

The binding geometries and the M-O_{fa2} distances of the most stable configuration I of HCOOH in M-MOF-74 obtained from force field-based molecular simulations were compared with the DFT (PBE-D3(BJ)) results in Figure 6.6. The distances between O_{fa2} atom of HCOOH molecule and the metal center obtained from both methods differ by no more than 0.1 Å for all the studied frameworks, except Zn-MOF-74. The slightly higher discrepancy of ca. 0.2 Å between the distances computed from force field-based molecular simulations and DFT could result from the highest reactivity of Zn metal center [309], which is not accounted for in the classical force field. Within the M-MOF-74 family, Zn-MOF-74 was found to exhibit the highest catalytic activity towards several reactions, e.g. water dissociation [310], CO_2 cycloaddition reaction with epoxides [311, 312], and HCOOH synthesis via CO hydration [313]. The obtained binding distances in all the frameworks range from approximately 2.15 Å to 2.5 Å. The closest configuration of HCOOH to the metal center is found in Ni-MOF-74 according to force field-based molecular simulations, and in Co-MOF-74 based on DFT. The farthest configuration is found in Cu-MOF-74 according to both methods. The binding energies of the most stable configuration I of HCOOH in M-MOF-74 obtained from force field-based molecular simulations and the DFT (PBE-D3(BJ)) calculations are shown in Figure D.5 of Appendix D. The binding energies vary between the methods but follow a similar general trend across the different metal centers. Both computational methods indicate that Cu-MOF-74 has the weakest binding affinity, while Ni-MOF-74 shows the strongest binding affinity. It is worth mention-

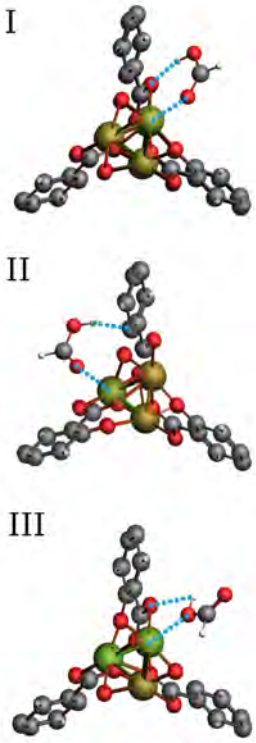

Fig. 6.5. The primary binding geometries of the HCOOH adsorption in M-MOF-74 (M = Co, Cu, Fe, Mn, Ni, and Zn) obtained using Baker's minimization method [160]. In the most stable configuration I, the O_{fa2} atom of HCOOH molecule points to the metal center while the H_{fa2} aligns to the Oa atoms in the metal cluster. In configuration II, the O_{fa2} atom of HCOOH points to the metal and the H_{fa2} points to the Cb carbon atom of the aromatic ligand. In the least favorable configuration (configuration III), the OH group of HCOOH is placed in a parallel configuration concerning the M-Oa bond of the metal cluster, while the O_{fa2} atom points to the center of the cage.

ing that the binding geometries of HCOOH calculated with the classical force field were obtained using rigid frameworks, while in the DFT calculations, the molecule and framework atoms, as well as the system volume were allowed to relax. Despite these different approaches that could substantially affect the binding geometries and energies, Figure 6.6 and Figure D.5 of Appendix D show a reasonable agreement between DFT calculations and classical simulations. The relative difference between the two methods is 3% (or 1.6%

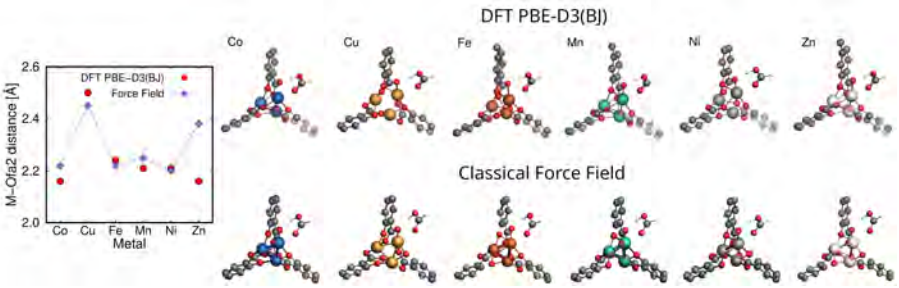

Fig. 6.6. Binding geometries of the most stable configuration I of HCOOH in M-MOF-74 (M = Co, Cu, Fe, Mn, Ni, and Zn) obtained from force field-based molecular simulations compared to the DFT (PBE-D3(BJ)) results. The resulting distances between O_{fa2} atom of HCOOH molecule and the metal center are plotted for all the framework types. The optimized geometries of HCOOH calculated by DFT (top) are visualized with the geometries computed from the force field-based simulations (bottom) for comparison. The general trend of distances is similar across both methods, except Zn-MOF-74 due to its highest reactivity. The lines connecting the symbols are used to guide the eye.

excluding highly reactive Zn-MOF-74) for binding geometries and 18% for binding energies. This confirms the validity of the force field to describe the complex interactions between HCOOH and M-MOF-74, and no adjustments of the existing force field for HCOOH are needed. In cases where the binding geometries would show high deviations between the two computational methods, the adjustment of the force field by scaling the Lennard-Jones interaction potentials and/or the Coulombic potentials is necessary. The binding distance between the metal center of the MOF and the atoms of the adsorbate molecule can be modified by applying a scaling factor to σ (the distance at which the intermolecular potential between the two particles is zero). To modify the binding energy of the adsorbate in MOF, ϵ (the depth of the potential well) and/or partial charges q should be adjusted by applying a scaling factor.

The process of CO_2 hydrogenation to HCOOH using M-MOF-74 is promising as the molecules of HCOOH are found to interact strongly with the frameworks, especially with Ni-MOF-74, resulting in high adsorption loadings. The mole fractions obtained from GCMC simulations for M-MOF-74 frameworks are provided in Tables D.2 – D.7 of Appendix D. Figure D.9 of Appendix D shows a comparison of HCOOH mole fractions obtained in M-MOF-74 and the literature data for Cu-BTC, UiO-66, and IRMOF-1 [276] at 298.15 - 800 K and 60 bar. The increase in pressure raises the concentration of HCOOH molecules, driving more molecules into the M-MOF-74 structure, filling its pores, and ensuring the system reaches a new equilibrium state with

higher adsorbate loading by Le Chatelier's principle [44]. The mole fractions of HCOOH decrease with increasing temperature due to weakening guest-host interactions. The optimal conditions for all the systems, resulting in the highest mole fraction of HCOOH, are found at 298.15 K and 60 bar. The enhancement in HCOOH production due to the confinement within M-MOF-74 was calculated and compared with the literature data for Cu-BTC, UiO-66, and IRMOF-1 [276] at 298.15 - 800 K and 60 bar, see Figure 6.7. The performance of M-MOF-74 in the production of HCOOH in confinement follows the same order as the uptake and the heat of HCOOH adsorption: Ni > Co > Fe > Mn > Zn > Cu. The application of Ni-MOF-74 framework resulted in the highest enhancement of HCOOH production. The obtained mole fraction of HCOOH reaches ca. 0.1 at 298.15 K, which is ca. 10^5 times higher compared to the gas phase. There is a significant difference in the enhancement of HCOOH production between Ni-MOF-74 and the second best-performing framework Co-MOF-74, which application results in x_{HCOOH} = 33,000 times higher than in the gas phase. The enhancement in HCOOH production using Ni-MOF-74 is ca. 60 times higher than the enhancement achieved with Cu-BTC in our previous work (mole fraction of HCOOH obtained with Cu-BTC was ca. 2000 times higher compared to the gas phase) [276]. Interestingly, the confinement effect of Cu-MOF-74 was found to be ca. 7 times weaker than that of Cu-BTC, resulting in the mole fraction of HCOOH ca. 300 times higher compared to the gas phase.

To assess what has the largest impact on HCOOH production using MOFs with the same type of metal centers, radial distribution functions were computed for Cu-MOF-74 and Cu-BTC at 298.15 K, see Figure D.7 of Appendix D. While ca. 6 molecules are present in Cu-BTC within the preferential distance to the metal centers of 2.4 Å [276], in Cu-MOF-74 only ca. 1.5 adsorbed molecules of HCOOH are within the distance of 2.54 Å to the metal centers. This difference in intensity is due to the higher charge on the metal center in Cu-BTC compared to Cu-MOF-74. Another reason for the higher affinity of HCOOH in Cu-BTC than Cu-MOF-74 is the presence of different types of ligands in the structures. By comparing the intensity of HCOOH adsorption in configuration pointing to the most electronegative ligand atom of the framework, it was found that the stronger electronegativity of the oxygen atom in Cu-BTC leads to a higher intensity of HCOOH adsorption oriented towards this atom (H_{fa2}-O1) that in Cu-MOF-74 where the oxygen atom is less electronegative (H_{fa2}-Oa). The affinity with the framework also affects the formation of hydrogen bonds between HCOOH molecules. The HCOOH nucleation and dimerization are slightly more intense in Cu-MOF-74 than in Cu-BTC due to weaker interactions with the framework.

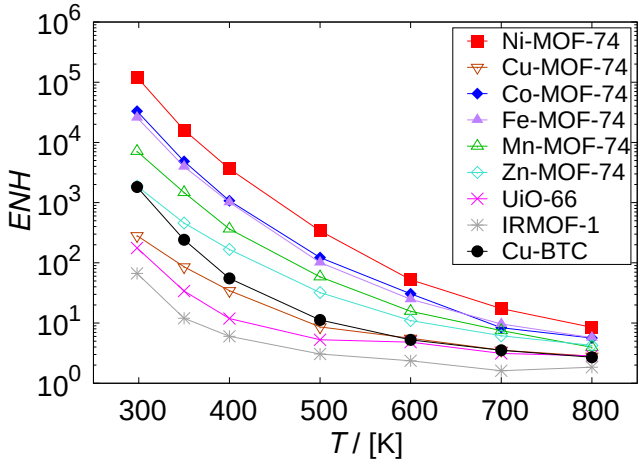

Fig. 6.7. Enhancement (*ENH*, Eq. 4.8) in the production of HCOOH obtained from GCMC simulations in M-MOF-74 frameworks at 298.15 - 800 K and 60 bar, compared with the literature data for Cu-BTC, UiO-66, and IRMOF-1 [276]. The enhancement in HCOOH production decreases with increasing temperature due to the weakening of guest-host interactions. The performance of M-MOF-74 in the production of HCOOH in confinement follows the same order as the uptake and the heat of HCOOH adsorption: Ni > Co > Fe > Mn > Zn > Cu. The enhancement in the HCOOH production is the highest in the Ni-MOF-74 framework at 298.15 K, resulting in the mole fraction of HCOOH being ca. 10^5 times higher compared to the gas phase.

Radial distribution functions simulated for 50 molecules of HCOOH, corresponding to the adsorption loading of ca. 1 molecule of HCOOH per metal center are compared for Ni-, Co-, Fe-, Mn-, Zn-, and Cu-MOF-74 at 298 K in Figure 6.8. The presence of three primary binding geometries of HCOOH found in the surroundings of the metal centers is confirmed. The distance between the double bonded O_{fa2} atom and the metal center (configuration I) range from 2.22 Å for Ni-MOF-74 to 2.54 Å for Cu-MOF-74. The binding distances and the corresponding adsorption intensities decrease in M-MOF-74 in the following order: Ni > Co ≈ Fe > Zn > Mn > Cu. In Cu-MOF-74, which has the weakest affinity with HCOOH, configuration III is found to outperform configuration II in terms of stability. Radial distribution functions for the interactions between HCOOH in the M-MOF-74 series are shown in Figure D.8 of Appendix D. The intensity of hydrogen bond formation increases with decreasing affinity of HCOOH with the framework: Cu-MOF-74 ≈ Zn-MOF-74 > Mn-MOF-74 > Fe-MOF-74 > Co-MOF-74 > Ni-MOF-74. In Zn-, and Cu-MOF-74, the HCOOH dimerization is found to be prevalent over the

hydrogen bonds-driven nucleation.

The mole fractions of CO_2 and H_2 obtained from the GCMC simulations of the CO_2 hydrogenation reaction are shown in Figure D.9 of Appendix D. The mole fractions of adsorbed CO_2 are significantly higher than the mole fraction of H_2 at all the studied conditions, showing similarity to the adsorption isotherms of CO_2/H_2 mixtures in M-MOF-74, studied by Wasik et al. [303]. The mole fractions of CO_2 decrease with increasing temperature, except for Ni-, Co-, and Fe-MOF-74 at the temperature range 298.15 - 350 K, where the mole fraction of CO_2 slightly increases. The increase is caused by the large decrease in HCOOH production, affecting mole fractions of the other components. The number of adsorbed CO_2 molecules decreases throughout the range of studied temperatures. The mole fractions of H_2 increase with temperature, inversely related to the mole fractions of CO_2 and HCOOH. The highest mole fractions of H_2 and the lowest mole fractions of CO_2 and HCOOH are observed for Cu-MOF-74, indicating that HCOOH production is more influenced by the type of metal center than by the quantity of the limiting reagent. The affinity of CO_2, H_2 and HCOOH with M-MOF-74 was compared in Figure 6.9. For all the studied frameworks, the isosteric heat of adsorption of HCOOH was significantly higher (from ca. 74 kJ mol^{-1} in Ni-MOF-74 to ca. 42 kJ mol^{-1} in Cu-MOF-74) than the other components of CO_2 hydrogenation reaction, followed by CO_2 (from 34 kJ mol^{-1} in Ni-MOF-74 to 23 kJ mol^{-1} in Cu-MOF-74), and H_2 (from 7 kJ mol^{-1} in Ni-MOF-74 to 6 kJ mol^{-1} in Cu-MOF-74). This high difference in affinity leads to the selective adsorption of favored HCOOH component, causing its enhanced formation in the CO_2 hydrogenation reaction. The isosteric heat of adsorption for CO_2 decreases in the same order as the isosteric heat of adsorption for HCOOH depending on the type of metal center in M-MOF-74: Ni > Co > Fe > Mn > Zn > Cu. The isosteric heat of adsorption for H_2 is similar in all the frameworks with a slight advantage for Ni-MOF-74.

In Table 6.1, the HCOOH production from CO_2 hydrogenation using M-MOF-74 at 298.15 K and 60 bar was compared with previously studied MOF Cu-BTC [276], and the most [55] as well as the least effective [63] transition metal catalysts. The types of catalysts were selected based on the resulting concentration of the CO_2 hydrogenation product (c_{HCOOH}, Eq. 6.2). The final concentration of HCOOH obtained from the Ni-MOF-74 confinement (c_{HCOOH} = 2.20 mol L^{-1}) is only 1.14 times lower than the highest reported concentration obtained with the use of the Wilkinson complex [55], and 2200 times higher than the lowest reported concentration obtained using a catalyst with N-heterocyclic carbene ligands [63]. This is a significant improvement compared to our previous work [276], where the application of the best per-

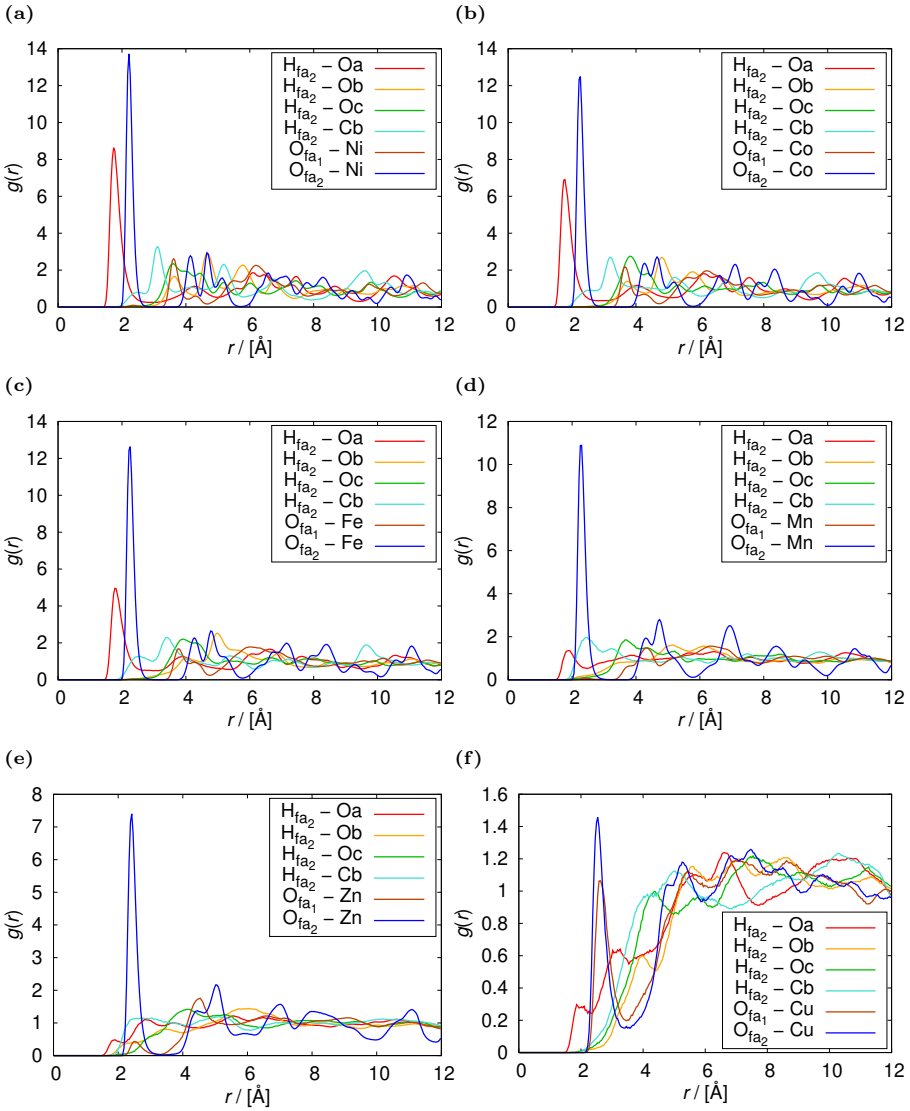

Fig. 6.8. Radial distribution functions simulated for 50 molecules of HCOOH at 298 K in: (a) Ni-MOF-74, (b) Co-MOF-74, (c) Fe-MOF-74, (d) Mn-MOF-74, (e) Zn-MOF-74, and (f) Cu-MOF-74. The presence of three primary binding geometries of HCOOH found in the surroundings of the metal centers is confirmed. In Cu-MOF-74, which has the weakest affinity with HCOOH, configuration III is found to outperform configuration II in terms of stability. The simulation was performed using the RASPA software package [94, 95].

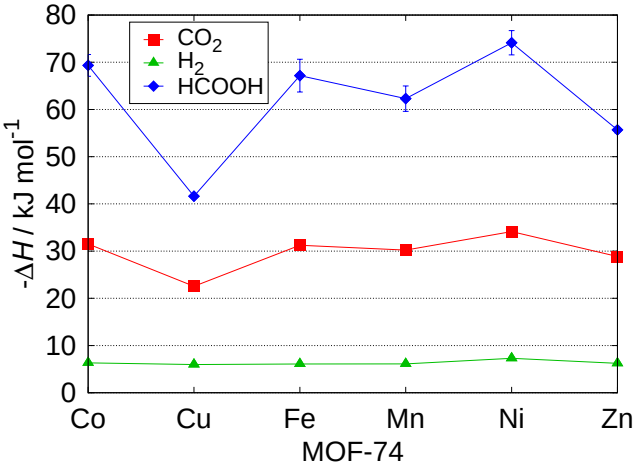

Fig. 6.9. Isosteric heat of adsorption of CO_2, H_2 and HCOOH at 298.15 K in M-MOF-74. The isosteric heat of adsorption of HCOOH is significantly higher than the other components of CO_2 hydrogenation reaction in all the studied frameworks, leading to the selective adsorption of favored HCOOH component. The isosteric heat of adsorption for H_2 is similar in all the frameworks with a slight advantage for Ni-MOF-74. The lines connecting the symbols are used to guide the eye.

forming MOF Cu-BTC resulted in the concentration of HCOOH ca. 80 times lower than the Wilkinson complex. Notably, the HCOOH concentration obtained using Cu-BTC is ca. 6 times higher than Cu-MOF-74 despite the same type of metal center, reflecting the importance of higher partial charge of the metal cation. Considering the resulting concentration of HCOOH from the confinement of Ni-MOF-74 close to the highest concentration of the formate product obtained with the Wilkinson complex, and a more valuable molecular form of the product, the application of Ni-MOF-74 has the potential to be an economically more attractive method of CO_2 conversion than transition metal catalysts. The costs of formate downstream processing methods including separation, concentration, and acidification of formate solutions can be avoided [17]. The cost reduction for the conversion and concentration of 10 wt% formate to 85 wt% formic acid is estimated at $380/ton of FA in an economic analysis performed by Ramdin et al. [17]. Further studies of Ni-MOF-74 towards its ligands functionalization and the analysis of other Ni-based MOFs may be promising research subjects in HCOOH production.

Table 6.1: HCOOH production from CO_2 hydrogenation using M-MOF-74 at 298.15 K and 60 bar, compared to Cu-BTC [276], and the most [55] as well as the least [63] effective transition metal catalysts. The highest final concentration of HCOOH (c_{HCOOH}, Eq. 6.2) obtained from the Ni-MOF-74 confinement is only 1.14 times lower than the highest reported concentration obtained with the use of the Wilkinson complex [55], and 2200 times higher than the lowest reported concentration obtained using a catalyst with N-heterocyclic carbene ligands [63].

Catalyst	**Conditions**	**Product**	**Concentration / [mol L^{-1}]**	**Reference**
Wilkinson complex $RhCl(PPh_3)_3$ + 3 PPh_3	298.15 K, p_{CO_2} = 40 bar, p_{H_2} = 20 bar, 20h	HCOOH	2.50	[55]
none	Ni-MOF-74 confinement, 298.15 K, 60 bar	HCOOH	2.20	this work
none	Co-MOF-74 confinement, 298.15 K, 60 bar	HCOOH	0.59	this work
none	Fe-MOF-74 confinement, 298.15 K, 60 bar	HCOOH	0.46	this work
none	Mn-MOF-74 confinement, 298.15 K, 60 bar	HCOOH	0.12	this work
none	Zn-MOF-74 confinement, 298.15 K, 60 bar	HCOOH	0.032	this work
none	Cu-BTC confinement, 298.15 K, 60 bar	HCOOH	0.031	[276]

none	Cu-MOF-74 confinement, 298.15 K, 60 bar	HCOOH	0.005	this work
(η^6-arene)Ru(bis-NHC) complex no. 1	353.15 K, 40 bar, 1h	formate	0.001	[63]

6.4 — Conclusions

We carried out Monte Carlo and DFT simulations to study the performance of M-MOF-74, where M = Ni, Cu, Co, Fe, Mn, Zn, for the adsorption and production process of formic acid. The non-polarizable CO_2, and H_2 force field for adsorption in M-MOF-74 [303] was evaluated for compatibility with a variant of the OPLS/AA force field for HCOOH [174]. The loading and heat of HCOOH adsorption were found to depend on the metal center as follows: Ni > Co > Fe > Mn > Zn > Cu, which suggests that HCOOH adsorption is predominantly influenced by the electrostatic interactions dependent on the effective charge of the M^{2+} ion at the open-metal site. The two-step mechanism of adsorption, wherein HCOOH molecules preferably adsorb at the metal centers, followed by adsorption above a triangle of oxygen atoms within the framework, was present in the adsorption isotherms of Ni-, Co-, Fe-, and Mn-MOF-74 frameworks. The three primary binding geometries of HCOOH adsorption in M-MOF-4 were found in the surroundings of the metal centers using Baker's minimization method. The binding geometries and energies of the most stable configuration computed from force field-based simulations agree with DFT calculations. The effect of the type of metal centers on the yield of HCOOH from the CO_2 hydrogenation reaction carried out in confinement was analyzed in M-MOF-74, and compared with the literature data for Cu-BTC and transition metal catalysts. The adsorption isobars of the studied systems were computed with Monte Carlo simulations in the grand-canonical ensemble, and the enhancement in HCOOH production was calculated. The performance of M-MOF-74 in the production of HCOOH in confinement was shown to follow the same order as the uptake and the heat of HCOOH adsorption. The application of the Ni-MOF-74 framework results in the highest enhancement in HCOOH production. The obtained mole fraction of HCOOH equals ca. 0.1 at 298.15 K, 60 bar, which is ca. 10^5 times higher compared to the gas phase. The final concentration of HCOOH resulting from the Ni-MOF-74 confinement

(c_{HCOOH} = 2.20 mol L^{-1}) is only 1.14 times lower than the highest reported concentration obtained with the use of the Wilkinson complex, and 2200 times higher than the lowest reported concentration obtained using a catalyst with N-heterocyclic carbene ligands. This is a major improvement compared to our previous work, where the application of the best performing MOF Cu-BTC resulted in ca. 2000 times higher HCOOH mole fraction compared to the gas phase, and the final concentration of HCOOH ca. 80 times lower than obtained with the Wilkinson complex. The metal-organic framework Ni-MOF-74 has comparable performance to the most effective transition metal catalyst and an additional advantage of a more valuable molecular form of the product. An economic and carbon emission analysis should be carried out to fully investigate the potential of Ni-MOF-74 as a useful alternative to transition metal catalysts. An interesting topic for future research is the study of ligands functionalization and the review of other Ni-based MOFs that may be promising in the HCOOH production from the CO_2 hydrogenation reaction.

Chapter 7

Multiscale Modelling of Dimerization Thermodynamics of Formic Acid

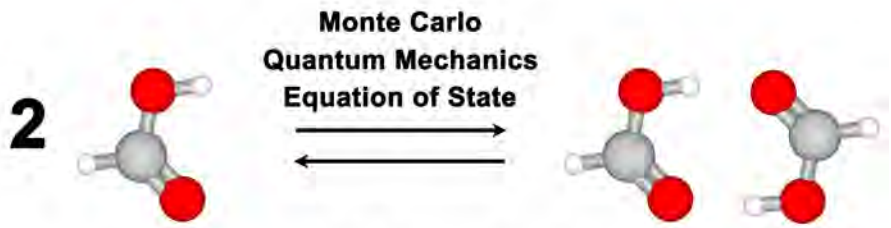

$$K_{\mathrm{d}}, \Delta_{\mathrm{d}}H, \Delta_{\mathrm{vap}}H, P_{\mathrm{sat}}, \rho_{\mathrm{liq}}$$
$$\rho_{\mathrm{vap}}, s, P\text{-}\{x, y\}, T\text{-}\{x, y\}$$

Heat pumps, which recycle waste heat, are a promising technology for reducing CO_2 emissions. Efficiently using low-grade waste heat remains challenging due to the limitations of standard heat exchangers and the need for more effective working fluids. This work introduces a multi-scale methodology that combines force field-based Monte Carlo simulations, quantum mechanics, and equations of state to explore the potential of formic acid as a new reactive fluid in thermodynamic cycles. Formic acid exhibits dimerization behavior, forming cyclic dimers in the gas phase, which can enhance the thermodynamic efficiency of heat recovery systems. The dimerization reaction of formic acid is crucial because it integrates chemical energy into thermodynamic processes, potentially improving the performance of heat pumps and other energy systems. The study implements umbrella sampling in Monte Carlo simulations to compute the thermodynamic properties of HCOOH dimerization, including equilibrium constants, enthalpy, and entropy. Results from two different methods to study dimer formation, namely the dimer counter method and the potential of mean force method, show strong agreement with the enthalpy of dimerization of -60.46 kJ mol^{-1} and -62.91 kJ mol^{-1}, and entropy of -137.36 J $mol^{-1}K^{-1}$ and -146.98 J $mol^{-1}K^{-1}$, respectively. A very good agreement of the Monte Carlo results with Quantum Mechanics and experimental data validates the accuracy of the simulations. For phase equilibrium properties, the Peng-Robinson equation of state, coupled with advanced mixing rules, was applied and compared to Monte Carlo simulations in the Gibbs ensemble. This approach enabled the determination of the Global Phase Equilibrium of the system, vaporization enthalpy, phase composition, vapor and liquid densities of the coexisting phases, and entropy as a function of temperature. The agreement between the thermodynamic model and Monte Carlo simulations confirms the reliability of the methodology in capturing the phase behavior of the system. The findings demonstrate a promising approach for discovering and characterizing new reactive fluids, contributing to more efficient and sustainable energy technologies.

This chapter is based on the following publication:
Wasik, D. O., Lasala, S., Herbinet, O., Vlugt, T. J. H., Calero, S. Multiscale Modelling of Dimerization Thermodynamics of Formic Acid (submitted **2024**).

7.1 — Introduction

The reduction of greenhouse gas emissions has become urgent as the European Climate Law requires the European Union economy and society to achieve climate neutrality by 2050 [20]. The global energy-related CO_2 emissions were estimated at 37.4 billion tonnes (Gt) in 2023 [22], which indicates a need for further advancements in sustainable energy technologies. The total energy-related emissions would have increased three times more than the actual increase of ca. 900 Mt between 2019 and 2023, if not for the application of five key clean energy technologies: heat pumps, solar photovoltaics, electric cars, wind power, and nuclear power [22]. Heat pump technology which operates on a thermodynamic cycle that absorbs heat from a source, upgrades, and transfers it to a sink using compression work, has the potential for waste heat recovery towards the decarbonization of EU industry [314–317]. The most promising sectors for heat pump application are non-metallic minerals, non-ferrous metals, paper, and food, while chemical industry show much lower potential due to the predominant need for high-temperature heat, where heat pumps are less efficient [315]. To reduce carbon emissions and utilization of non-renewable energy sources, heat pumps are being explored as an alternative to heating technologies based on fossil fuels. Heat pumps supplied only ca. 7% of the global building heating demand in 2021 [318]. According to the International Energy Agency (IEA), to achieve net zero emissions by 2050, the number of installed heat pumps must increase from the current 180 million to 600 million by 2030 [318]. Several countries, including Canada and the United States, encourage residents to adopt heat pump technologies for their space and water heating needs through, i.a. subsidies [318]. The analysis of Kosmadakis et al. [315] showed that the total potential of industrial heat pumps in the EU is 28.37 TWh/year which corresponds to 1.5% of the total heat consumption. The waste heat required to be recovered and upgraded by the heat pump to cover this consumption is approximately 21 TWh/year, representing 7% of the total waste heat potential in EU industries. Despite being a significant energy resource, waste heat is currently insufficiently utilized. Forman et al. [319] reported that around 72% of the world's primary energy supply is lost through exhaust/effluents (52%) and other losses (20%). The electricity generation sector accounts for the largest portion of this heat loss at 39%, with 88% of it being extremely low-grade heat (below 373 K).

Although harnessing waste heat is appealing, the low-temperature difference between the heat source and the working fluid hinders effective heat transfer in standard heat exchangers, affecting the efficiency [320]. While many heat transfer enhancement solutions exist, these are generally designed

for medium-to-high temperature ranges (>500 K) [321], with limited options for low-temperature applications [322]. Heat recovery techniques are broadly classified into two categories: active methods, which involve mechanical or electrical systems requiring external energy inputs, and passive methods, which utilize natural processes or simple design features without external energy inputs. Passive techniques are considered more competitive than active methods for recovering very low-grade heat (below 373 K) cost-effectively. Therefore, there is significant motivation to re-evaluate a potentially cost-effective yet under-explored passive method: heat transfer intensification through gas dissociation [320]. Currently, reactive working fluids that undergo endothermic dissociation reactions when heated or compressed and exothermic recombination when cooled, instantly progressing towards chemical equilibrium, are investigated as an alternative to inert working fluids in thermodynamic cycles, due to their higher energy-efficiency potential [314, 323–325]. As the temperature and pressure change during various unit operations, e.g. turbines, heat exchangers, pumps, and compressors, the fluid can undergo spontaneous, rapid, and reversible chemical reactions. These reactions incorporate chemical energy into the thermodynamic processes, significantly influencing the efficiency of the thermodynamic cycle and the design of components such as turbines [326]. Several studies have shown that the thermodynamic efficiency of supercritical (Brayton) and subcritical (Rankine) cycles using reactive working fluids, particularly N_2O_4, is higher than that of cycles using specific inert fluids such as water, ammonia, helium, or CO_2 [326–329]. The main disadvantages of Brayton cycles with ideal gas working fluids are the substantial compression work relative to the net output, and the highly sensitive performance to the efficiency of the turbomachinery and pressure losses [330]. In studies that consider fictive reactive fluids to examine how reaction stoichiometry, enthalpy, and entropy affect the performance of Brayton power cycles and heat pumps compared to pure fluids, it was shown that reactive working fluids can improve power plant efficiency by up to 30% [323] and more than double the coefficient of performance of heat pumps based on a gaseous inversed Brayton cycle [314]. The general reaction for fictive reactive fluids is:

$$A_n \rightleftharpoons \left(\frac{n}{m}\right) A_m \tag{7.1}$$

where n, and m specify the number of atoms of the two molecules.

Recent theoretical studies are focusing on the use and characterization of reactive fluids, including N_2O_4/NO_2, $Al_2Cl_6/AlCl_3$, and $Al_2Br_6/AlBr_3$ [326], to enhance the performance of unit operations and thermodynamic cycles. Among these, N_2O_4 is the most thoroughly studied, with its thermodynamic

properties being determined through equations of state [324, 331–335], direct numerical simulation [320], Monte Carlo simulations [324, 336], and Quantum Mechanics [324]. In the study of Zhang et al. [320] it was shown that the N_2O_4/NO_2 chemical reaction can enhance the heat transfer coefficient by up to 600% compared to non-reactive fluids. Despite this potential, the broader adoption of reactive working fluids in thermodynamic cycles is limited by the lack of similarly reversible fast chemical reactions, aside from N_2O_4. Addressing this challenge, the European Research Council funded project REACHER [337, 338] that aims to discover new working fluids, characterize their thermodynamic and kinetic properties, optimize thermodynamic cycle architectures, and validate performance calculations through experimental micro-power plant testing.

Formic acid (HCOOH) reacting system has the potential as a new reactive fluid in thermodynamic cycles due to its strong dimerization behavior [339]. Formic acid is the simplest carboxylic acid, serving as a prototypical molecule and one of the most stable neutral complexes, with a dimerization energy of ca. 63 kJ mol^{-1} [340]. Formic acid is a significant product in the chemical industry, with a production capacity reaching 800,000 tons annually as of 2017 [18, 32]. The global market value of HCOOH is projected to grow from 1.8 billion dollars in 2023 to 2.8 billion dollars by 2033 [33]. Producing HCOOH offers an economically viable method for reducing CO_2 emissions through direct capture at the production source and subsequent conversion [4]. In 2021, HCOOH was utilized in various industries, including animal feed and grass silage (27%), leather tanning (22%), pharmaceuticals and food chemicals (14%), textiles (9%), natural rubber (7%), drilling fluids (4%), and other applications (17%) [8, 31]. The predominant method for HCOOH production involves methanol carbonylation, resulting in a formate ester that is subsequently hydrolyzed to HCOOH [8, 34–36]. Alternative methods for HCOOH production include the electrochemical reduction of carbon dioxide in aqueous electrolyte solutions [12–15, 17, 46, 206] and the hydrogenation of CO_2 [18, 19, 276, 341].

The formation of cyclic HCOOH dimers that occurs in the gas phase is significant to the human metabolism [342] and applications, e.g. the oxidation of unsaturated hydrocarbons [343] and atmospheric chemistry [344]. The graphical representation of the formic acid dimerization equilibrium is shown in Figure 7.1. The dimerization of formic acid (HCOOH) has been extensively studied both theoretically and experimentally [167, 169, 339, 340, 345–348]. In this chapter, we focus on the thermodynamic properties essential for the design of heat pumps using reactive fluids like HCOOH, including vapor pressure, vaporization enthalpy, phase composition, and the densities of coexisting vapor and liquid phases. These properties, influenced by dimerization

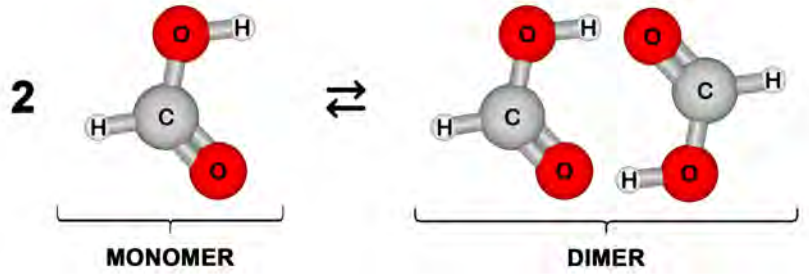

Fig. 7.1. Graphical representation of the formic acid dimerization equilibrium, given by a reaction: $2HCOOH \rightleftharpoons (HCOOH)_2$

behavior, directly affect the heat transfer and energy storage capabilities of HCOOH, enhancing its potential as a working fluid in various industrial and engineering processes [339]. While HCOOH remains stable at room temperature, it exhibits thermal instability and decomposes when subjected to heat [28]. Despite extensive studies, there are still gaps in experimental data, particularly at varying temperature and pressure conditions, which makes the prediction of entropy and phase behavior challenging. Given the complex nature of HCOOH and the limited availability of experimental data, molecular simulations provide an alternative for determining these thermodynamic properties. Slavchov et al. [339] proposed a model to describe the temperature dependence of vapor pressure and heat of vaporization of associated liquids containing dimers and linear associates in the gas phase. The analytic generalization of the Clausius-Clapeyron equation resulted in an enthalpy of dimerization of -58.5 kJ mol^{-1} for formic acid. In a Monte Carlo simulation study by Turner et al. [345], the enthalpy of dimerization for formic acid in a carbon dioxide solvent was predicted to be -50.3 kJ mol^{-1} in the gas phase. In a study by Chao and Zwolinski [28], several experimental values of the HCOOH dimerization enthalpy were reviewed. The average enthalpy of dimerization obtained from P-V-T methods is ca. -59 kJ mol^{-1}, while the average obtained from spectroscopic methods is ca. -57 kJ mol^{-1}. The chemicophysical properties of formic acid are influenced by its ability to form various types of hydrogen bonds (H-bonds) [167]. A formic acid molecule can act as a hydrogen acceptor via its two oxygen atoms and as a hydrogen donor through its hydroxy and

formyl hydrogen atoms [167]. Consequently, four types of H-bonds are theoretically possible: O-H$\cdots$Oc, O-H$\cdots$Oh, C-H$\cdots$Oc, and C-H$\cdots$Oh, where Oc and Oh represent the carbonyl- and hydroxy oxygen atoms, respectively. This variety leads to different structural forms despite the molecular simplicity [167]. A recent ab-initio study by Brinkmann [348] describes formic acid dimerization as a stepwise process. The study found that the acyclic dimer, which is thermodynamically less stable, converts to the global minimum, a cyclic structure with two O-H$\cdots$O=C hydrogen bonds. This cyclic dimer has a direct dissociation energy of 67.4 kJ mol^{-1} and is 26.4 kJ mol^{-1} more stable than the acyclic dimer [348]. Farfan et al. [346] used DFT to determine the equilibrium geometries of various formic acid dimer combinations (cis + cis, cis + trans, and trans + trans). These authors identified 21 distinct minima within a 69.0 kJ mol^{-1} energy window on the potential energy surface for formic acid dimers.

In the gas phase, the dimer is more stable by ca. 58.6 kJ mol^{-1} compared to the monomer [349]. The population of the cyclic H-bonded dimer configuration, dominant in the gas phase, is estimated to be around 23% [168, 169], with approximately 95% of the vapor existing in the dimerized form at room temperature and normal pressure leading to non-ideal gas behavior [8]. Unlike most carboxylic acids, which retain dimeric structures in their crystalline form, formic acid exhibits an infinite "polymeric" crystal structure [350, 351] - H-bonded chains with alternating O-H$\cdots$O and C-H$\cdots$O bonds [167, 352, 353]. Additionally, at high pressure, crystalline formic acid can adopt a cis molecular structure, differing from the trans structure found under normal conditions (where "trans" and "cis" refer to the positions of the hydrogen atoms) [167, 354]. The liquid structure of formic acid is complex and consists of a hydrogen-bonded network with various chain-like structures, differing from both the gas and crystalline forms [163, 167, 355–357]. Small clusters with O-H$\cdots$O bonds are held together by weaker C-H$\cdots$O bonds, forming large branched structures, as suggested by recent first-principles and classical molecular dynamics simulations [167, 168]. In addition to polymeric chains and cyclic dimers, an acyclic "open" dimer or a mixture of these species have been proposed as the main components of liquid formic acid [347]. The structure and dynamics of liquid formic acid related to H-bonding have been investigated using reverse Monte Carlo simulations by Jedlovszky et al. [355] Jedlovszky, Turi et al. performed Monte Carlo [163, 358] and molecular dynamics (MD) [194] simulations using a potential model based on the ab-initio potential energy surface of formic acid dimers [358]. Hermida Ramón and Ríos [342] developed a polarizable force field for trans-formic acid for MD simulations in the liquid phase.

In this chapter, a multi-scale methodology, including force field-based Monte Carlo simulations, Quantum Mechanics, and equations of state is proposed to model the thermodynamic properties of a formic acid reacting system to explore its potential as a new reactive fluid in thermodynamic cycles. This chapter is organized as follows: in section 7.2, we provide technical details of the computational and mathematical methods. The methodologies for conducting two types of umbrella sampling Monte Carlo (MC) simulations—the dimer counter method and the potential of mean force method—are described, along with the thermodynamic modelling of the formic acid reactive mixture. In section 7.3, we present and discuss the results. The thermodynamic properties are computed from Monte Carlo simulations and compared to Quantum Mechanics calculations. The dimer counter and PMF methods showed strong agreement, resulting in the enthalpies of HCOOH dimerization of ca. -60.46 kJ mol^{-1} and ca. -62.91 kJ mol^{-1}, respectively. The QM-calculated enthalpy of dimerization is -60.48 kJ mol^{-1}, deviating by 0.02% from the dimer counter method and 4% from the PMF method. The QM and umbrella sampling MC simulations demonstrate high accuracy in reproducing the experimental thermodynamic properties of HCOOH dimerization. The Global Phase Equilibrium of the system, vaporization enthalpy, phase composition, vapor and liquid densities of the coexisting phases, and entropy as a function of temperature were obtained from the thermodynamic model and compared with Monte Carlo simulations in the Gibbs ensemble. The MC simulations agree well with the model, confirming the accuracy of the simulations in capturing the phase behavior of the system. Our findings are summarized in section 7.4.

7.2 — Methodology

7.2.1 – Monte Carlo Simulations

The dimerization of formic acid in thermodynamic equilibrium is simulated using the Monte Carlo (MC) Software Brick-CFCMC [143, 152], an open-source molecular simulation code for the calculation of phase and reaction equilibria using state-of-the-art force field-based MC simulations in different ensembles, such as the *NVT*, *NPT*, grand-canonical, reaction, and the Gibbs ensemble [152]. To sample the dimerization reaction, it is crucial to explore all possible distances between the two molecules of formic acid in the Monte Carlo simulation in the canonical ensemble. Due to the strong interaction between the two monomers through hydrogen bonds, once a dimer forms, it tends to persist in each simulation cycle without dissociating. This phenomenon leads to a simulation dominated by dimers, resulting in an insufficient sampling of monomers at various distances, which hinders the accurate sampling of

thermodynamic averages, such as the equilibrium constant and enthalpy of dimerization. To address this issue, we implement umbrella sampling to Brick-CFCMC, a technique that biases the sampling process to include a range of distances between the two molecules. By applying this method, we can obtain a more comprehensive representation of the system, enabling precise calculation of equilibrium properties.

In a Monte Carlo simulation in the canonical ensemble, ensemble averages are computed by sampling configurations with a probability proportional to the Boltzmann factor ($e^{-\beta U(r^N)}$) as follows [359]:

$$\langle A \rangle = \frac{\int \mathrm{d}r^N A(r^N) \exp\left[-\beta U(r^N)\right]}{\int \mathrm{d}r^N \exp\left[-\beta U(r^N)\right]} \tag{7.2}$$

where $\beta = \frac{1}{k_B T}$, and $U(r^N)$ is the potential energy of a configuration. The conventional Metropolis acceptance rule for a trial move is given by [128, 359]:

$$\mathrm{acc}(\mathrm{old} \to \mathrm{new}) = \min\left(1, \exp\left[-\beta \cdot (U_{\mathrm{new}} - U_{\mathrm{old}})\right]\right) \tag{7.3}$$

where U_{old} is the potential energy of the current configuration, and U_{new} is the potential energy of the new configuration. In the umbrella sampling method, a simulation is performed in an ensemble π, in which a weight function $W(d(r^N))$ is added to the partition function, and the configurations are sampled with a probability proportional to [359]:

$$\pi(r^N, d) = \exp\left[-\beta U(r^N) + W(d(r^N))\right] \tag{7.4}$$

where $W(d(r^N)$ is a weight function (or biasing function) of the configuration that depends on the distance between the centers of two molecules d. The new acceptance rule for translation trial moves is given by:

$$\mathrm{acc}(\mathrm{old} \to \mathrm{new}) = \min\left(1, \exp\left[W_{\mathrm{new}}(d_{\mathrm{new}}) - W_{\mathrm{old}}(d_{\mathrm{old}}) - \beta \cdot (U_{\mathrm{new}} - U_{\mathrm{old}})\right]\right) \tag{7.5}$$

where d_{old} and d_{new} are the old and new distances between dimers, respectively. The ensemble average $\langle A \rangle$ in the canonical ensemble can be computed by [360]:

$$\langle A \rangle = \frac{\langle A \exp[-W] \rangle_\pi}{\langle \exp[-W] \rangle_\pi} \tag{7.6}$$

where $\langle \dots \rangle_\pi$ is an ensemble average in the ensemble π (Eq. 7.4). This assumes that a single coordinate (distance) is sufficient to describe dimerization.

To sample all possible distances between the two molecules, a histogram of $W(d)$ must be obtained. This ensures that all distances are accommodated in

simulation bins. Initially, $W(d)$ is set to zero. During a short simulation, the following iterative rule is applied:

$$W(d) \rightarrow W(d) - \frac{1}{2}\ln(\mathrm{Hist}(d)) \tag{7.7}$$

where $\mathrm{Hist}(d)$ is the histogram count of observations for a given distance d between the centers of two molecules. The procedure involves a series of short simulations, where the updated $W(d)$ from each simulation is used as the input for the next. The process continues until the resulting histogram of $W(d)$ becomes sufficiently flat, ensuring that all distances in the simulation box are adequately sampled. The final function $W(d)$ is then used in a longer simulation of the dimerization reaction. From this simulation, the equilibrium constants of dimerization can be obtained using two routes: the dimer counter method and the potential of mean force (PMF) method.

The dimer counter method uses geometric criteria from a study by Turner et al. [345] to identify whether the configuration consists of one dimer or two monomers of formic acid:

$$0.20\,\mathrm{nm} \leq d_{\mathrm{Ofa2}\cdots\mathrm{Ofa1}} \leq 0.34\,\mathrm{nm} \tag{7.8}$$

$$0.14\,\mathrm{nm} \leq d_{\mathrm{Ofa2}\cdots\mathrm{Hfa2}} \leq 0.24\,\mathrm{nm} \tag{7.9}$$

The schematic representation of the geometric criteria for HCOOH dimer with the atoms labeled is visualized in Figure 7.2. The number of monomers (N_{monomer}) and dimers (N_{dimer}) are computed using the probabilities of observing two monomers (p) or one dimer ($1-p$):

$$N_{\mathrm{monomer}} = 2p \tag{7.10}$$

$$N_{\mathrm{dimer}} = 1 - p \tag{7.11}$$

The equilibrium constant K is defined as:

$$K = \frac{\frac{P_{\mathrm{dimer}}}{P_0}}{\left(\frac{P_{\mathrm{monomer}}}{P_0}\right)^2} = \frac{\frac{N_{\mathrm{dimer}}\cdot RT}{P_0\cdot V}}{\left(\frac{N_{\mathrm{monomer}}\cdot RT}{P_0\cdot V}\right)^2} = \frac{N_{\mathrm{dimer}}}{N_{\mathrm{monomer}}^2}\cdot\frac{P_0\cdot V}{RT} \tag{7.12}$$

where P_0 is the reference pressure (1 bar), V is the volume of the simulation box, R is the universal gas constant, and T is the temperature in the studied range from 250 K to 300 K. Substituting N_{monomer} and N_{dimer} from Eqs. 7.10 and 7.11 into Eq. 7.12, the equilibrium constant is given as:

$$K = \frac{(1-p)}{(2p)^2}\cdot\frac{P_0\cdot V}{RT} \tag{7.13}$$

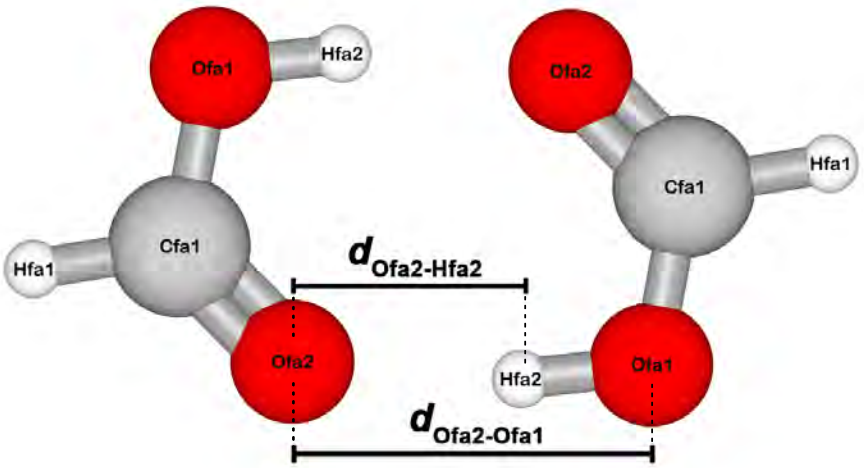

Fig. 7.2. Graphical representation of the geometric criteria for the HCOOH dimer [345] with the atoms labeled.

The enthalpy of dimerization is determined using the Van't Hoff equation [286]:

$$\frac{\mathrm{d}\ln K}{\mathrm{d}\left(\frac{1}{T}\right)} = -\frac{\Delta_{\mathrm{d}} H}{R} \tag{7.14}$$

The second approach for computing the equilibrium constants of HCOOH dimerization involves the potential of mean force (PMF). Umbrella sampling is used for computing the PMF, which allows to understand the energy changes involved in the association/dissociation processes of noncovalent ligand–receptor pairs [361]. This method is particularly useful because it can be applied to a wide range of systems, from small molecular systems [362, 363] to complex biological systems [361, 364, 365]. By computing the free energy along the dissociation pathway, the PMF provides thermodynamic details for molecular recognition. The PMF is obtained from umbrella sampling simulations using:

$$PMF = -\ln\left(\frac{\mathrm{Hist}(d)\cdot\exp(-W(d))}{\mathrm{Norm}_2\cdot V_{\mathrm{bin}}}\right) \tag{7.15}$$

where $\mathrm{Hist}(d)$ is the histogram count of observations for a given distance bin d, $W(d)$ is the weight function for the distance bin d, Norm_2 is a normalization

factor for Hist(d), and V_{bin} is the volume of the bin in the distance histogram, accounting for the spacing between discrete bins.

The change in Helmholtz free energy ΔF is calculated by integrating the PMF over the distance d, from an initial distance d_0 of ca. 2.6 Å to ca. 4.6 Å using:

$$\Delta F = RT \cdot \int_{d_0}^{d} PMF(d')\mathrm{d}d' \tag{7.16}$$

Substituting the enthalpy and Helmholtz free energy change from Eqs. 7.17 and 7.18 into Eq. 7.19, the change in Gibbs free energy ΔG was determined:

$$\Delta H = \Delta U + \Delta PV \tag{7.17}$$

$$\Delta F = \Delta U - T\Delta S \tag{7.18}$$

$$\Delta G = \Delta H - T\Delta S = \Delta U + \Delta PV - T\Delta S = \Delta F + \Delta PV = \Delta F + RT\Delta n \tag{7.19}$$

where $\Delta n = 1$ (representing the dissociation of a dimer). The equilibrium constant K is obtained from Eq. 7.20, and is used to calculate the enthalpy of dimerization from the Van't Hoff equation (Eq. 7.14).

$$K = \exp\left[-\frac{\Delta G}{RT}\right] \tag{7.20}$$

The molar entropy for HCOOH dimerization was calculated at 298.15 K for both the dimer counter method and the PMF method by:

$$\Delta_{\mathrm{d}} S = \frac{\Delta_{\mathrm{d}} H - \Delta G}{298.15[\mathrm{K}]} \tag{7.21}$$

The composition of the vapor and liquid phases at saturation conditions is computed using the Gibbs Ensemble method at constant total volume, combined with the CFC method [143]. This ensemble consists of two simulation boxes that can exchange molecules. In the Gibbs ensemble, thermodynamic equilibrium of dimerization is achieved without the need for umbrella sampling, as both the formation of dimers and their subsequent dissociation into monomers are observed due to molecule exchanges between simulation boxes. Initially, each simulation box contains 200 molecules, and both boxes are identical in terms of the number of molecules and volume. Phase equilibrium densities are simulated for a temperature range of 335 K to 560 K. The mole fractions of monomers in each phase are computed using the implemented monomer counter based on the inverse dimer geometric criterion (where pairs of molecules that do not meet the dimer criterion defined in Eqs. 7.8

and 7.9, are considered monomers). For the temperature range from 335 K to 460 K, additional *NPT* simulations of the gas phase were performed using densities obtained from Gibbs Ensemble simulations. This approach was used to determine the mole fractions of HCOOH monomers in the gas phase with higher accuracy. Saturated vapor pressures are estimated by assuming an ideal gas phase [182], using Eq. 3.10. The P-$\{x,y\}$ and T-$\{x,y\}$ diagrams are obtained and compared with results from the Equation of State. The enthalpy of vaporization can be calculated using the following equation for a non-ideal gas [366]:

$$\Delta_{\text{vap}}H = (U_{\text{vap}} \cdot R + P_{\text{sat}}V_m) - \left(U_{\text{liq}} \cdot R + P_{\text{sat}}V_m\right) \tag{7.22}$$

where U_{vap} and U_{liq} represent the potential energies of the vapor and liquid phases, respectively, R is the gas constant, P_{sat} is the saturation pressure, and V_m is the molar volume. The entropy of the liquid and vapor phases was calculated from [367]:

$$s_i = \frac{U_i - \mu N_i + k_{\text{B}} T \ln P_{\text{sat}}}{T} \tag{7.23}$$

where U_i is the potential energy of the vapor or liquid phase, μ_i is the chemical potential of the vapor or liquid phase, N_i is the number of molecules in the vapor or liquid phase, k_{B} is the Boltzmann constant, T is the temperature, and P_{sat} is the pressure at saturation.

The dimerization of HCOOH is studied using the 'P2' variant of the OPLS/AA force field for HCOOH [174]. This force field is applied to the HCOOH molecule model, which was constructed and optimized at the B3LYP/6-31G(d) level of theory in a study of Wasik et al. [206], see Chapter 3 of this thesis. The HCOOH model is rigid, with point charges assigned to all atoms. The LJ parameters and partial charges for HCOOH used in this work are listed in Table 4.1 of Chapter 4. The geometry of the HCOOH molecule is presented in Table A.1 of Appendix A. The HCOOH force field has been validated by successful reproduction of the vapor-liquid equilibrium coexistence curve, saturated vapor pressures, and densities at various temperatures [206]. Additionally, the force field was used in our previous studies on the adsorption of HCOOH in M-MOF-74 [341], as well as the CO_2 hydrogenation reaction to HCOOH in UiO-66, Cu-BTC, IRMOF-1 [276], and M-MOF-74 [341], where it was applied together with the non-polarizable CO_2 and H_2 force fields [303]. The presence of dimers was confirmed in the gas phase of pure HCOOH and HCOOH/H_2O/NaCl simulations using the HCOOH force field, leading to non-ideal gas behavior and an inaccurate description of the HCOOH/H_2O azeotrope [206].

In all MC simulations, intermolecular interactions are modeled using Coulombic and Lennard-Jones (LJ) potentials. The Lorentz–Berthelot mixing rules [129] are applied for interactions between different LJ sites. The cutoff radius for intermolecular interactions is set to 10 Å, with interactions truncated and analytic tail corrections applied. Periodic boundary conditions are applied in all three directions. Electrostatic interactions are computed using the Ewald summation method [151], with the number of k-vectors in each direction ($K_{\max}$) set to 8, and the damping parameter (α) set to 0.32 $Å^{-1}$. The Ewald summation parameters correspond to a relative precision of 10^{-6}.

The weight functions $W(d)$ for HCOOH dimerization equilibrium are obtained from a series of ten short consecutive umbrella sampling simulations for each temperature within the range of 250 K to 300 K. These simulations involve 2 molecules of HCOOH in a simulation box with a length of 80 Å. Each simulation comprises $2 \cdot 10^2$ initialization MC cycles, $2 \cdot 10^5$ equilibration MC cycles, and 10^6 production MC cycles. A single MC cycle consists of N MC trial moves, where N is the total number of molecules at the start of the simulation. The final weight functions are used as input for extended umbrella sampling simulations of 2 molecules of HCOOH in a simulation box of the same size and at the corresponding temperatures to compute equilibrium constants. These simulations involve $2 \cdot 10^3$ initialization MC cycles, 10^6 equilibration MC cycles, and 10^8 production MC cycles. The probabilities for selecting trial moves were 50% for translations and 50% for rotations. The Gibbs Ensemble simulations are performed with $2 \cdot 10^3$ initialization MC cycles, $2 \cdot 10^5$ equilibration MC cycles, and 10^6 production MC cycles. The probabilities for selecting trial moves in these simulations were 28.57% for translations, 28.57% for rotations, 14.29% for λ changes, and 28.57% for CFC hybrid trial moves, which combine swap and identity changes [143]. To calculate the standard deviations of the computed values, all sets of simulations were conducted five times, starting from independent configurations and using different random number seeds. Random initial configurations were generated using the algorithms provided in Brick-CFCMC [143, 152].

7.2.2 – Thermodynamic Modelling of Formic Acid Formation

One of the successful tentative approaches used in the modelling of the thermodynamic properties of carboxylic acids is based on the representation of these systems as reactive mixtures [368, 369]. It is possible to model the breaking (dissociation) and formation (association) of hydrogen bonds between, respectively, dimers and monomers, as a chemical reaction effect (see Fig. 7.1).

The theoretical model which has been applied in this work to characterize the formic acid system is similar to the one that has recently been used to

represent the reactive $N_2O_4 \rightleftharpoons 2NO_2$ mixture [324], where the use of a cubic equation of state has already proven its successful application. This model is summarised below. For more details, the reader is referred to the description by Lasala et al. [324].

The equation of state which has been selected is the cubic Peng-Robinson equation of state (Eq. 7.24), coupled with advanced mixing rules, EoS+$a_{res}^{E,\gamma}$ (Eq. 7.25) [370].

$$P\left(T, v, \boldsymbol{z}\right) = \frac{RT}{v - b_m} - \frac{a_m}{v(v + b_m) + b_m(v - b_m)} \tag{7.24}$$

where T is the temperature, R is the universal gas constant, v is the molar volume, $\boldsymbol{z}$ is the vector of the molar composition, and a_m and b_m are the mixing energy and covolume parameters calculated as follows:

$$\begin{cases} b_m = \sum_{i=1}^{NC} z_i b_i \\ \frac{a_m}{b_m} = \sum_{i=1}^{NC} z_i \frac{a_i}{b_i} + \frac{a_{\text{res}}^{E,\gamma}}{\Lambda_{\text{EoS}}} \end{cases} \tag{7.25}$$

where EoS+$a_{\text{res}}^{E,\gamma}$ is the residual part of an excess Helmholtz energy model calculated from an activity coefficient (γ) model, Λ_{EoS} is a numerical parameter being a function of the considered equation of state, the pure component energy and co-volume parameters, i.e. a_i and b_i, respectively, are calculated using the standard PR-78 equation of state [371] as a function of the critical temperature, critical pressure and acentric factor of the two components of the mixture (the monomer and the dimer of formic acid). The composition $\boldsymbol{z}$ is a result of the chemical equilibrium condition, the zero-Gibbs energy condition:

$$\Delta_R G(T, P, \boldsymbol{z}) = 0 \tag{7.26}$$

In this work, the athermal version of Eq. 7.25 has been considered, i.e. the residual excess Helmholtz energy is null ($a_{\text{res}}^{E,\gamma} = 0$). This choice is motivated by the fact that the strong physical interactions related to hydrogen bonds are modelled here as chemical interactions instead of physical association effects.

To calculate the thermodynamic – phase equilibrium and energetic – properties of the reactive system formed by monomers and dimers of, for example, formic acid with a cubic equation of state, it is necessary to determine some basic properties for the single molecules forming the mixtures: the monomeric and the dimeric form of, in this case, formic acid. These basic properties are the ideal gas thermochemical properties (standard enthalpy of formation, standard absolute entropy) and some thermophysical ones (the ideal gas heat

capacity, critical temperature, critical pressure, and acentric factor). To calculate these properties, we have performed Quantum Mechanics (QM) calculations to determine the ideal gas properties, and then an optimization step aimed to fit the critical coordinates of the two pure components in order to match the experimental vaporization enthalpy and saturation pressures of the reactive mixture. Since the reactive system is at chemical equilibrium, it is not possible to experimentally determine the critical parameters of both the monomer and the dimer.

Quantum mechanics calculations were performed at the CBS-QB3 level of theory, with the Gaussian09 software [171], to obtain the lowest energy conformer. A post-processing of the results has been performed with GPOP [372] to derive thermodynamic properties. The results of these calculations are shown in Table 7.2 where the expression for the ideal gas isobaric specific heat capacity is given by:

$$c_{P,i}^{ig}(T) = c_0 + c_1 \left(\frac{c_2/T}{\sinh(c_2/T)} \right)^2 + c_3 \left(\frac{c_4/T}{\cosh(c_4/T)} \right)^2 \tag{7.27}$$

We have then optimised the critical temperature, T_{c1} and T_{c2}, and the critical pressure, P_{c1} and P_{c2}, of the monomer (subscript 1) and of the dimer (subscript 2) by minimising the following objective function:

$$\begin{aligned} \min_{\substack{Tc_1, Tc_2 \\ Pc_1, Pc_2}} F = & \frac{1}{n_{\Delta_{\text{vap}}H^{\text{exp}}}} \sum_{i=1}^{n_{\Delta_{\text{vap}}H^{\text{exp}}}} \left(\frac{\Delta_{\text{vap}}H^{\text{calc}} - \Delta_{\text{vap}}H^{\text{exp}}}{\Delta_{\text{vap}}H^{\text{exp}}} \right)^2 \\ & + \frac{1}{n_{P_{\text{VLE}}^{\text{exp}}}} \sum_{i=1}^{n_{P_{\text{VLE}}^{\text{exp}}}} \left(\frac{P_{\text{VLE}}^{\text{calc}} - P_{\text{VLE}}^{\text{exp}}}{P_{\text{calc}}^{\text{exp}}} \right)^2 + \left(\frac{T_c^{\text{calc}} - T_c^{\text{exp}}}{T_c^{\text{exp}}} \right)^2 + \left(\frac{P_c^{\text{calc}} - P_c^{\text{exp}}}{P_c^{\text{exp}}} \right)^2 \end{aligned} \tag{7.28}$$

The experimental data used for this optimization are the ones reported for formic acid by the DIPPR database [373] (79 points for P_{VLE} and 23 points for $\Delta_{\text{vap}}H$, see Tables E.1 and E.2 of Appendix E, respectively) and the ones obtained in this study. It is worth highlighting that the available data are quite dispersed and cover, for the vapor-liquid equilibrium pressure, a quite limited temperature range (up to 400 K). At a first but acceptably accurate approach, the acentric factor of dimers can be considered to be double the acentric factor of monomers. In this study, the acentric factor has been considered to be equal to 0.1 for the monomer of formic acid and equal to 0.2 for its dimeric form.

7.3 — Results and Discussion

To investigate the dimerization of HCOOH at thermodynamic equilibrium, we first computed the weight functions $W(d)$ and the observed probability distributions $p(d)$ (normalized Hist(d)) of the distance between the centers of two HCOOH molecules from the umbrella sampling MC simulations at 250 - 300 K. Figure 7.3 shows examples of $W(d)$ and $p(d)$ computed at 250 K. In Figure 7.3a and b, the initial weight function (resulting from the first short consecutive umbrella sampling simulation) and the corresponding probability distribution of the distance between the centers of two HCOOH molecules are shown, respectively. In the initial $W(d)$, the distances longer than ca. 4.6 Å are not sampled as the corresponding probability distribution $p(d)$ is close to 0. The distances from ca. 2.9 Å to 4.6 Å, corresponding to dimer formation, are sampled with a very high probability. Since monomers are not sampled in the simulation, the equilibrium of HCOOH dimerization cannot be reproduced. In Figure 7.3c and d, the final weight function (resulting from the last short consecutive umbrella sampling simulation) and the corresponding observed probability distribution of the distance between the centers of two HCOOH molecules are shown, respectively. The distances are sampled starting from ca. 2.6 Å, which is the shortest distance between two HCOOH molecules possible due to intermolecular interactions. The distance range between two HCOOH molecules considered a dimer (2.6 - 4.6 Å) is sampled with a slightly higher probability than longer distances assigned to monomers (longer than 4.6 Å) by ca. 0.06. Due to the small difference between the probabilities of sampling dimers and monomers, the final weight function $W(d)$ was selected as the input for the extended umbrella sampling simulation of two HCOOH molecules at the corresponding temperature to determine the thermodynamic properties of HCOOH dimerization. The procedure used to compute $W(d)$ at 250 K was applied consistently for simulations performed at 260, 270, 290, and 300 K.

The equilibrium constants of HCOOH dimerization were computed from both routes of umbrella sampling MC simulations: dimer counter and potential of mean force. To obtain the equilibrium constants from the PMF method, it is necessary to calculate the change in Helmholtz free energy and subsequently the Gibbs free energy, see Eq. 7.20. The Helmholtz free energy change ΔF is calculated using Eq. 7.16 by integrating the PMF over the distance d, from an initial distance d_0 of ca. 2.6 Å to ca. 4.6 Å where two molecules are considered dimers according to the probability distribution $p(d)$ of the distance between the centers of two HCOOH molecules computed using the geometrical criteria [345] (Eqs. 7.8 and 7.9). The example of PMF as a function of the distance between the centers of two HCOOH molecules is shown in Figure 7.4.

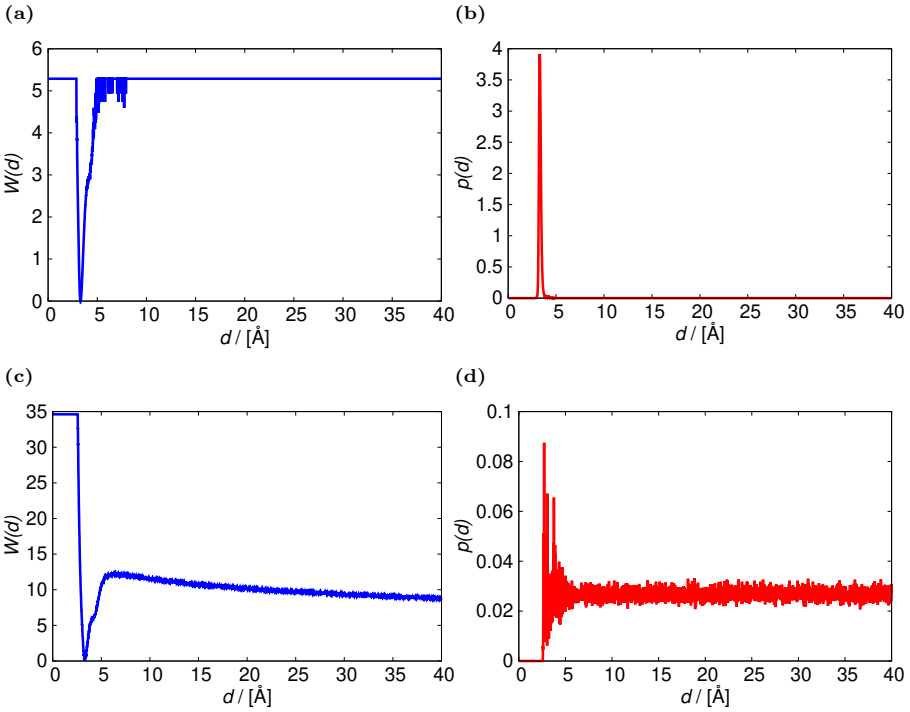

Fig. 7.3. Weight function $W(d)$ in units of $k_\mathrm{B}T$ and probability distribution $p(d)$ of the distance between the centers of two HCOOH molecules simulated at 250 K: (a) the weight function resulting from the first of a series of ten short umbrella sampling MC simulations, (b) the probability distribution of the observed distance between two molecules resulting from the first of a series of ten short umbrella sampling MC simulations, (c) the weight function resulting from the tenth of a series of ten short umbrella sampling MC simulations, (d) the probability distribution of the distance between two molecules resulting from the tenth of a series of ten short umbrella sampling MC simulations. The probabilities for the distance distribution sum up to 100.

The logarithms of the equilibrium constants for HCOOH dimerization computed using the dimer counter method and the potential of mean force (PMF) method are compared in Figure 7.5. The changes in Gibbs free energy and equilibrium constants used to obtain the Arrhenius plots are listed in Table E.3 in Appendix E. The values of $\ln K$ from both methods show close agreement, with an average deviation of ca. 2%. Compared to literature data from the study by Chao and Zwolinski [28] based on the statistical thermodynamic method, the values of $\ln K$ from the dimer counter and PMF methods are shifted by

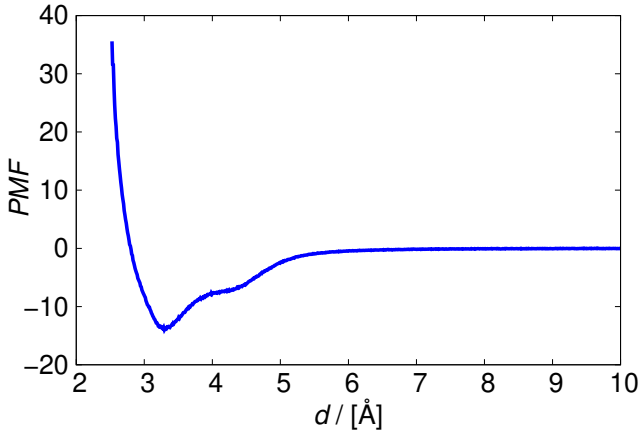

Fig. 7.4. Potential of mean force (PMF) in units of $k_{\mathrm{B}}T$ from an umbrella sampling MC simulation of two HCOOH molecules at 250 K as a function of the distance between the centers of two HCOOH molecules d. The value of Helmholtz free energy change ΔF calculated for this example by integrating the PMF over the distance d, from an initial distance d_0 of ca. 2.6 Å to ca. 4.6 Å, is -28.33 kJ mol^{-1}.

approximately 2 units, which slightly affects the slopes of the linear trendlines and consequently the enthalpy of dimerization. Compared to the computational study of formic acid dimerization in a carbon dioxide solvent by Turner et al. [345], the values of $\ln K$ from both methods are shifted by approximately 4 units. The enthalpies of HCOOH dimerization, derived from the slopes of the linear trendlines in the Arrhenius plots ($-\Delta_{\mathrm{d}}H/R$), are provided in Table 7.1. The $\Delta_{\mathrm{d}}H$ values differ by only 4% between the dimer counter and PMF methods, resulting in -60.46 kJ mol^{-1} and -62.91 kJ mol^{-1}, respectively. The difference between the molar entropy of dimerization between the two routes is slightly higher at 7%. The deviation between the enthalpy of dimerization from Monte Carlo simulations and the study by Chao and Zwolinski [28] is only ca. 3%. The deviation between the enthalpy of dimerization from Monte Carlo simulations and the computational study by Turner et al. [345] is more significant, at an average of 23%. In the study of formic acid dimerization by Turner et al. [345], carbon dioxide is present in the simulated system as a solvent, and a different HCOOH force field is used (from the study of Jedlovszky and Turi [358]). Due to these differences, umbrella sampling MC simulations show better agreement with experimental data of pure formic acid than the computations of Turner et al. [345] The dimerization enthalpies obtained from the dimer counter and PMF methods deviate by ca. 4% from P-V-T methods and

by ca. 9% from spectroscopic methods. The dimer counter method shows a smaller deviation than PMF, with an average difference of 5% from both experimental methods, while PMF results in a 9% difference. In sharp contrast, $\Delta_d H$ from the study of Turner et al. [345] deviate by ca. 15% from *P-V-T* methods and by ca. 11% from spectroscopic methods. These results indicate that the umbrella sampling MC simulations used in our work provide an accurate reproduction of the enthalpy of HCOOH dimerization. The thermodynamical properties computed from MC simulations were also compared to the Quantum Mechanics calculations. The results of the Quantum Mechanics calculations are reported in Table 7.2. The enthalpy of monomer formation at 298.15 K calculated from QM (-379.07 kJ mol^{-1}) is in excellent agreement with the literature data reported by Chao and Zwolinski [28] (-378.57 kJ mol^{-1}), resulting in 0.1% difference. Similarly, the calculated enthalpy of dimer formation at 298.15 K (-818.617 kJ mol^{-1}) deviates by only 0.3% from the literature value of -820.94 kJ mol^{-1} [28]. The entropies of monomer and dimer formation at 298.15 K obtained from QM are 254 J $mol^{-1}K^{-1}$ and 370 J $mol^{-1}K^{-1}$, respectively. This results in 2% of deviation from the reported entropy of monomer formation (248.88 J $mol^{-1}K^{-1}$) [28] and 11% from the reported entropy of dimer formation (332.67 J $mol^{-1}K^{-1}$) [28].

The logarithms of the equilibrium constants for HCOOH dimerization from QM calculations were compared to the dimer counter method and the PMF method in Figure 7.5. Compared to MC methods, the $\ln K$ values from QM are shifted by approximately 0.16 units and result in the enthalpy of dimerization equal to -60.48 kJ mol^{-1}, deviating from the dimer counter method by 0.02% and from PMF by 4% (Table 7.1). The values of $\Delta_d H$ calculated from QM differs similarly from the experimental data [28] as the MC simulations, resulting in an average deviation of 5% from *P-V-T* methods and spectroscopic methods, and the deviation of 5% from the calculated using the enthalpies of monomer and dimer formation at 298.15 K [28]. The molar entropy of dimerization calculated from QM (-138 J $mol^{-1}K^{-1}$) differs by an average of 3% from both MC methods and is in good agreement with the value calculated based on the entropies of monomer and dimer formation at 298.15 K (-165.09 J $mol^{-1}K^{-1}$) [28] with a difference of 16%.

The QM and umbrella sampling MC simulations used in this study have demonstrated a high degree of accuracy in reproducing the experimental thermodynamic properties of HCOOH dimerization. Our results show that the dimer counter and PMF methods are in excellent agreement. Notably, the dimer counter method provides a more precise match with experimental data compared to the PMF method.

The results of the Quantum Mechanics calculations (Table 7.2) and the op-

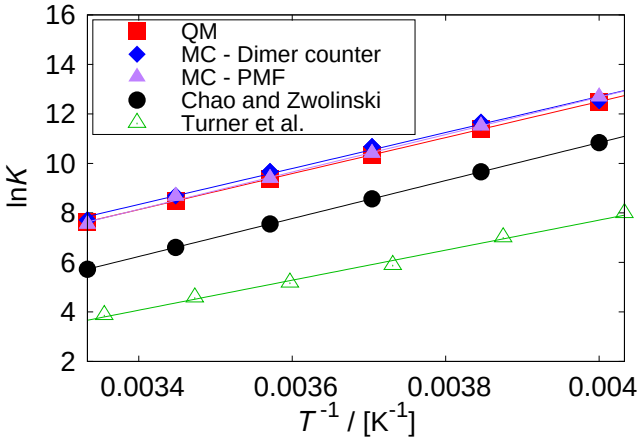

Fig. 7.5. Arrhenius plot for HCOOH dimerization at 250 - 300 K computed from Quantum Mechanics and both routes of umbrella sampling MC simulations: dimer counter and potential of mean force. The logarithms of the equilibrium constants are compared with literature data from a study by Chao and Zwolinski [28] using a statistical thermodynamic method, as well as the computational study by Turner et al. [345] The enthalpies of dimerization are calculated from slopes of the linear trendlines. The error bars are smaller than the size of the symbols.

Table 7.1: Enthalpy and entropy of dimerization computed from Quantum Mechanics and both routes of umbrella sampling MC simulations: dimer counter and potential of mean force. The subscripts show uncertainties computed as the standard deviation from five independent simulations. The computed results are compared with literature data [28, 345].

Method	$\Delta_\mathrm{d}H$ /[kJ/mol]	$\Delta_\mathrm{d}S$ /[J/mol/K]
MC - Dimer counter	$-60.46_{0.45}$	$-137.36_{1.76}$
MC - PMF	$-62.91_{0.64}$	$-146.98_{2.27}$
QM	-60.48	-138
Chao and Zwolinski [28]	-63.81	-165.09
Turner et al. [345]	-50.3	
P-V-T [28]	-59.12	
Spectroscopy [28]	-56.57	

timization procedure (Table 7.3) have enabled plotting the Global Phase Equilibrium Diagram of the system (Fig. 7.6), the vaporization enthalpy (Fig. 7.7), and the non-isothermal but unique phase diagram showing the molar composition of the liquid phase (x_1) and of the vapor phase (y_1) as a function of the

Table 7.2: Results of QM calculations for the monomer and dimer of HCOOH, including the enthalpy and entropy of monomer and dimer formation at 298.15 K, as well as the expression for the ideal gas isobaric specific heat capacity (Eq. 7.27).

Compound	$\Delta_f H_i^{\circ,298.15\text{K}}$ /[kJ/mol]	$\Delta_f S_i^{\circ,298.15\text{K}}$ /[J/mol/K]	c_0 /[J/kmol/K]	c_1 /[J/kmol/K]
HCOOH	-379.07	254	36322.4	46443.9
$(HCOOH)_2$	-818.617	370	77376.5	97286.3

Compound	c_2 /[K]	c_3 /[J/kmol/K]	c_4 /[K]
HCOOH	724.28	41856.3	2168.01
$(HCOOH)_2$	712.16	92502.6	1979.58

Table 7.3: Results of the optimization procedure for the monomer and the dimer of HCOOH.

Compound	T_c/[K]	P_c/[bar]	Acentric Factor
HCOOH	350	40	0.1
$(HCOOH)_2$	633	38	0.2

pressure (and thus of the temperature) of this mono-variant system (Fig. 7.8). Additionally, the vapor and liquid densities of the coexisting phases of the reactive HCOOH mixture, as a function of temperature (Fig. 7.9) was calculated, as well as T-s diagram (Fig. 7.10). More details on the methodology are provided in Lasala et al. [324] The results of Monte Carlo simulations in the Gibbs ensemble are shown in Table E.4 in Appendix E.

Figure 7.6 shows the Global Phase Equilibrium Diagram that highlights the complex behavior of the monomer and dimer forms of formic acid, as well as the critical phenomena that arise from the interactions. The results of thermodynamic model calculations are compared to MC simulations in the Gibbs ensemble and the experimental data [373]. The figure features the saturation pressure of the monomer of formic acid, the saturation pressure of the dimer of formic acid, the reactive mixture vapor-liquid equilibrium pressure curve, and the locus of the critical points of the inert mixtures formed by monomers and dimers. As temperature increases from 281.5 K (which is the melting point of formic acid [186]) to a critical value of 350 K, the saturation pressure of the formic acid monomer also rises, reflecting the typical behavior of a pure substance where higher temperatures require higher pressures to maintain the substance in a liquid state. The curve starts at a low-pressure value of ca.

10 bar and gradually increases with temperature to a critical pressure of ca. 40 bar. The curve of the saturation pressure of the HCOOH dimer lies below the monomer saturation pressure curve, indicating that the dimer has a lower vapor pressure compared to the monomer at the same temperature. This is consistent with the fact that dimers, being larger and having stronger intermolecular forces, are less volatile than monomers. The curve also shows an upward trend as temperature increases from 281.5 K to a critical value of 633 K, where the critical pressure is as high as 38 bar. The vapor-liquid equilibrium pressure of the reactive mixture includes contributions from both monomers and dimers. This curve lies between the monomer and dimer saturation pressure curves, reflecting the combined effects of both species in the equilibrium. As temperature rises from 281.5 K to ca. 570 K, the equilibrium pressure also increases up to ca. 65 bar, determined by the ongoing reaction between monomers and dimers. The results are compared with vapor-liquid equilibrium pressures computed using MC simulations and experimental data [373], showing reasonable agreement across the examined conditions and confirming the thermodynamic model prediction. The locus of the critical points for the inert mixture of monomers and dimers shows a parabolic shape, peaking at ca. 490 K and ca. 80 bar, and then declining. This behavior is characteristic of critical phenomena for systems of type I according to the classification of Van Konynenburg and Scott [374–376].

The vaporization enthalpy calculated from the thermodynamic model is compared to MC simulations in the Gibbs ensemble and the experimental data [373] in Figure 7.7. In the temperature region from 281.5 K to 500 K, the vaporization enthalpy is relatively high (ca. 450 kJ mol^{-1}), as indicated by both the experimental data and the thermodynamic model. The curve remains almost flat or slightly increases with temperature. This suggests that the amount of heat required to vaporize the substance does not change significantly with temperature in this range. The MC simulations show a significant deviation in this region, predicting higher values of vaporization enthalpy than observed experimentally and by the model. In the high-temperature region, particularly above 500 K, the curve shows a sharp decline in the vaporization enthalpy. This indicates that the heat required to vaporize the mixture becomes significantly less as the temperature approaches the critical temperature of the mixture, where the liquid and vapor phases become indistinguishable. This behavior is typical as the thermal energy of the system increases, making it easier for molecules to escape the liquid phase. The experimental data and the thermodynamic model start to converge with the MC simulations in this temperature range, suggesting a better agreement between theoretical and experimental observations. All three data sets - experimental, thermodynamic

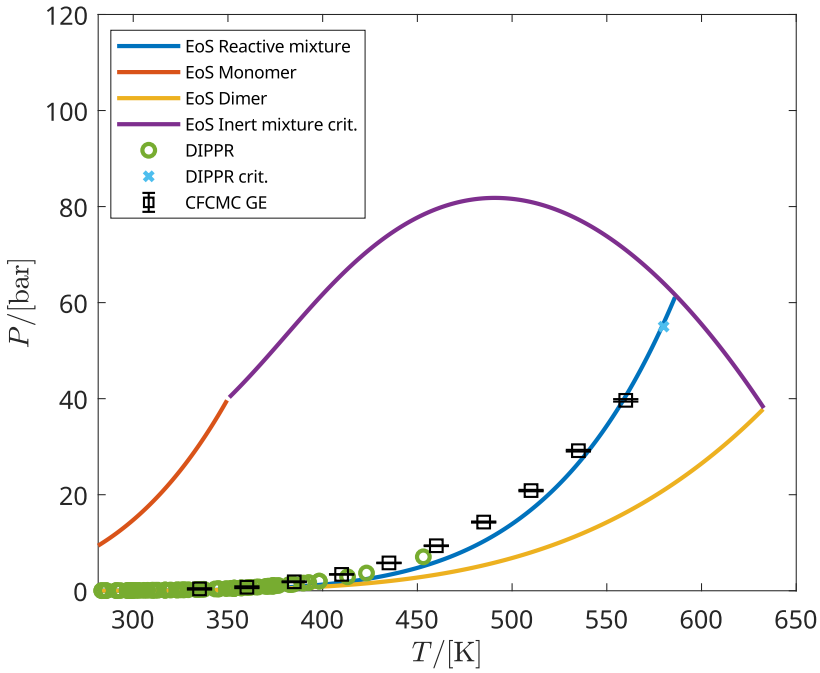

Fig. 7.6. Global Phase Equilibrium Diagram, showing the saturation pressure of the monomer of formic acid (orange curve), the saturation pressure of the dimer of formic acid (yellow curve), the reactive mixture vapor-liquid equilibrium pressure curve (blue curve), and the locus of the critical points of the inert mixtures formed by monomers and dimers (violet curve), calculated with the thermodynamic model. The green points represent experimental vapor-liquid equilibrium pressures [373] while the blue cross represents the experimental critical coordinate of the equilibrium mixture. The black points represent vapor-liquid equilibrium pressures computed from MC simulations in the Gibbs ensemble. Vapor-liquid equilibrium properties of HCOOH computed from MC simulations in the Gibbs ensemble are listed in Table E.4.

model, and MC simulations - show this sharp decrease, which is consistent with the behavior expected near the critical point.

Figure 7.8a shows a non-isothermal phase diagram for a reactive formic acid mixture at chemical equilibrium, with the pressure P as a function of the mole fractions x_1 and y_1, representing the HCOOH monomers in the liquid and vapor phases, respectively. The phase behavior calculated from the thermodynamic model is compared with the results from MC simulations in the Gibbs

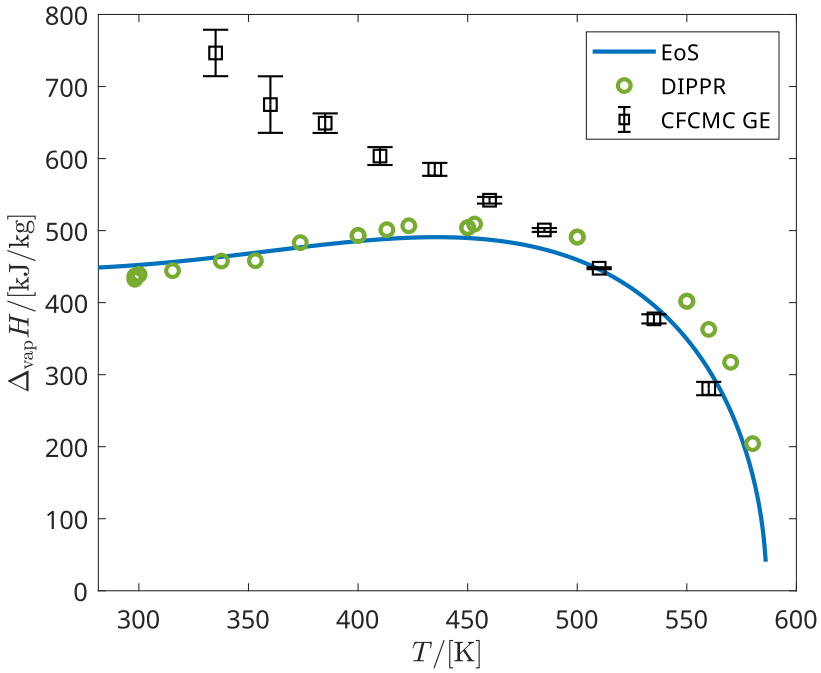

Fig. 7.7. Vaporization enthalpy as a function of temperature of the reactive mixture at chemical equilibrium. The blue line represents calculations from the thermodynamic model, while the green points represent the experimental data [373]. The black points represent the results of MC simulations in the Gibbs ensemble.

ensemble. In the liquid phase, the mole fraction of the monomers increases rapidly from $x_1 = 0$ to ca. 0.35 with pressure up to ca. 65 bar, which suggests that more monomers are retained in the liquid phase, reducing the tendency to vaporize. The results of MC simulations align closely with the thermodynamic model curve, showing the accurate reproduction of the behavior of the liquid phase. This agreement indicates that the force field used in the simulations is well-suited for modelling the liquid-phase behavior of HCOOH monomers. The vapor-phase curve behaves differently, initially increasing more slowly at low pressures and low mole fractions. It eventually reaches a maximum mole fraction of ca. 0.5, where the curve bends and begins to decrease. This behavior is characteristic of a vapor phase where, beyond a certain pressure, further increases lead to the condensation of monomers, thereby reducing the

mole fraction in the vapor. The MC simulation data for the vapor phase also match the thermodynamic model curve, particularly in the higher pressure range of 20 - 40 bar. At pressures lower than 20 bar, there is a slight deviation between the simulation data points and the model curve, but the overall trend is consistent. This slight discrepancy at lower pressures could be due to the limitations in the MC simulations, such as the challenge of accurately capturing the complex phase behavior in reactive mixtures at chemical equilibrium. The phase diagram shows that the thermodynamic model is successful in describing the non-isothermal phase behavior of the HCOOH mixture, with the liquid and vapor phase curves exhibiting expected behaviors as pressure varies. The MC simulations agree well with the model across most of the pressure and mole fraction range, confirming the validity of the simulations in capturing the phase behavior of the system. The phase compositions are also presented as a function of temperature in Figure 7.8b, where the trends in the mole fraction of HCOOH monomers exhibit similar patterns.

Figure 7.9 shows vapor and liquid densities of the coexisting phases of the reactive HCOOH mixture, as a function of temperature calculated from the thermodynamic model, compared to MC simulation in the Gibbs ensemble. The vapor phase density, starting from very low densities and increasing as the temperature approaches the critical point, is in good agreement with MC simulations and closely matches the experimental data, especially at lower densities. However, the liquid phase density of the thermodynamic model is underestimated by ca. 400 kg m^{-3} at 335 K but still follows the general trend. As temperature increases, the liquid phase curve calculated from the thermodynamic model slowly converges to MC simulation and experimental data. While the MC simulations agree well with experimental data, effectively capturing the experimental liquid phase behavior up to the critical point, there is still potential for improving the thermodynamic model for formic acid, particularly in accurately reproducing the liquid phase density. The low accuracy of cubic equations of state in reproducing the liquid phase density is well known. Nevertheless, an improvement in modelling liquid densities could be achieved with the inclusion of a volume-translation term in the cubic equation of state [377].

Figure 7.10 shows T-s diagram of the reactive HCOOH mixture at chemical equilibrium, calculated with the thermodynamic model and compared to MC simulations in the Gibbs ensemble. The liquid phase has a relatively low entropy compared to the vapor phase at the same temperature, with the highest difference at 281.5 K (ca. 2.9 kJ $mol^{-1}K^{-1}$ and ca. 4.5 kJ $mol^{-1}K^{-1}$ for liquid and vapor phases, respectively). This difference is due to the structured nature of the liquid phase, where molecules are more ordered compared to the

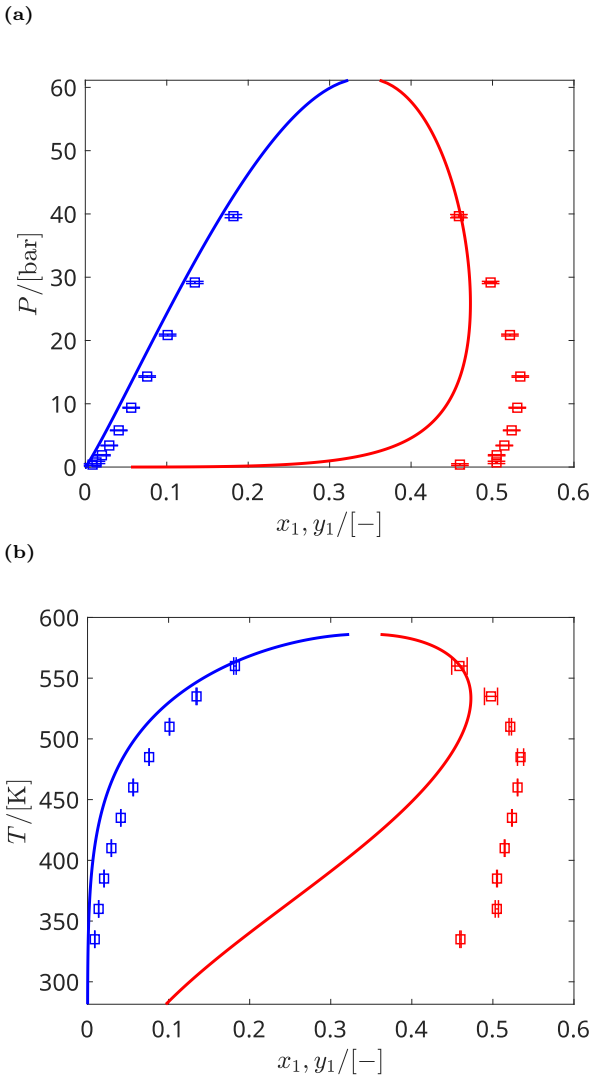

Fig. 7.8. Phase diagrams of the reactive HCOOH mixture at chemical equilibrium: (a) non-isothermal P-$\{x,y\}$, and (b) T-$\{x,y\}$. The curves represent the mole fraction of HCOOH monomer in the liquid phase (blue curve) and in the vapor phase (red curve), calculated with the thermodynamic model. The points represent the mole fraction of HCOOH monomer in the liquid phase (blue points) and the vapor phase (red points), resulting from MC simulations in the Gibbs ensemble.

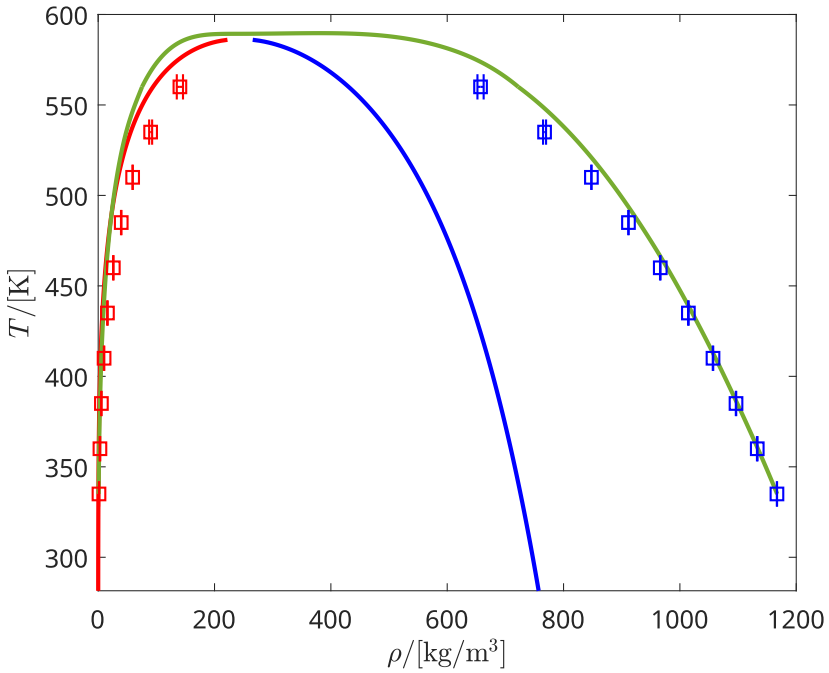

Fig. 7.9. Vapor and liquid densities of the coexisting phases of the reactive HCOOH mixture at chemical equilibrium, as a function of temperature. The curves represent the liquid phase density (blue curve) and the vapor phase density (red curve), calculated with the thermodynamic model. The points represent the liquid phase density (blue points) and the vapor phase density (red points), resulting from MC simulations in the Gibbs ensemble. The green curve represents experimental data [373].

vapor phase, which is more disordered and has higher entropy. In the vapor phase, temperature increases significantly from 281.5 K to 500 K while entropy changes relatively little (from ca. 4.5 kJ $\text{mol}^{-1}\text{K}^{-1}$ to 4.7 kJ $\text{mol}^{-1}\text{K}^{-1}$). In this phase, adding heat energy leads to a large increase in temperature without a corresponding large increase in entropy due to a low heat capacity. In the vapor phase, the molecules are already highly disordered and have many degrees of freedom (movement, rotation, etc.). Thus, additional heat primarily increases the temperature, rather than further increasing entropy significantly. In sharp contrast, in the liquid phase temperature increases more steadily from 281.5 K to ca. 580 K with an increase in entropy from ca. 2.9 kJ $\text{mol}^{-1}\text{K}^{-1}$

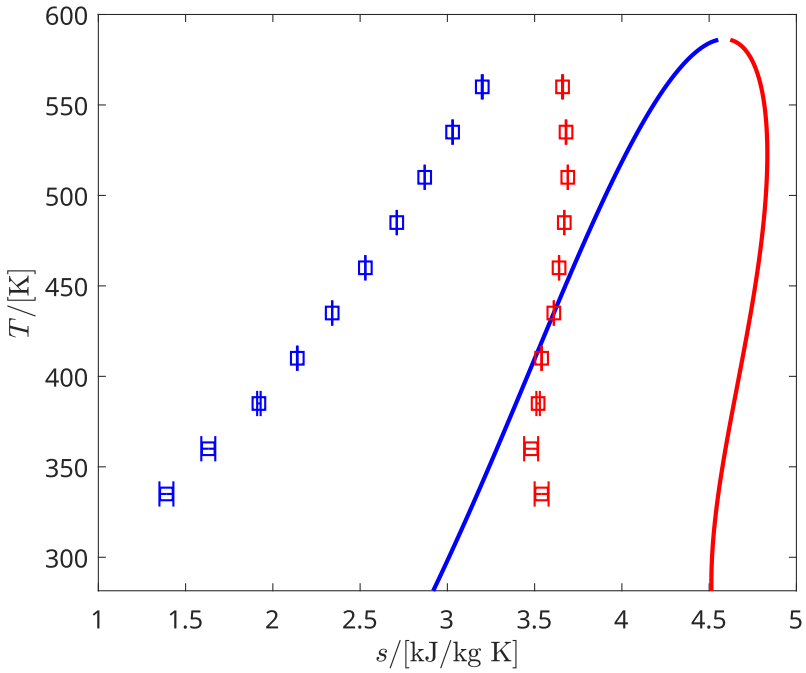

Fig. 7.10. T-s diagram of the reactive HCOOH mixture at chemical equilibrium, calculated with the thermodynamic model. The blue curve represents the liquid phase, where temperature increases gradually with entropy. The red curve represents the vapor phase, where temperature increases significantly while entropy changes relatively little due to a low heat capacity. The points represent the entropy of the liquid phase (blue points) and the vapor phase (red points), resulting from MC simulations in the Gibbs ensemble.

to ca. 4.5 kJ $\text{mol}^{-1}\text{K}^{-1}$. This gradual change reflects a higher heat capacity of the liquid phase and a more ordered structure compared to the gas phase. The results of MC simulations in the Gibbs ensemble are in good agreement with the thermodynamic model, reproducing the trend in entropy of the liquid and vapor phases. The values of entropy of the liquid and vapor phase are shifted from the thermodynamic model by ca. 1.5 kJ $\text{mol}^{-1}\text{K}^{-1}$ and ca. 1 kJ $\text{mol}^{-1}\text{K}^{-1}$, respectively. The close alignment between the thermodynamic model and MC simulations confirms the accuracy of the multi-scale methodology in capturing the behavior of both phases for a wide range of temperatures.

7.4 — Conclusions

This work introduces a multi-scale methodology that integrates force field-based Monte Carlo simulations, Quantum Mechanics, and equations of state to characterize the thermodynamics of the formic acid dimerization reaction. This approach explores the potential application of formic acid as a new reactive fluid in thermodynamic cycles, particularly in the design of heat pumps. Accurate knowledge of thermodynamic properties is crucial for optimizing heat transfer and energy efficiency in these systems. To compute thermodynamic properties, such as the equilibrium constants, enthalpy, and entropy of dimerization, umbrella sampling was implemented in Monte Carlo simulations. This technique biases the sampling process to include a range of distances between the two molecules. The logarithms of the equilibrium constants for HCOOH dimerization were computed at 250 - 300 K using both the dimer counter and the potential of mean force methods. Both methods showed strong agreement, with an average deviation of only 1.8%. The enthalpies of HCOOH dimerization derived from the Arrhenius plots were -60.46 kJ mol^{-1} and -62.91 kJ mol^{-1} for the dimer counter and PMF methods, respectively. The molar entropy of dimerization computed from the dimer counter method is -137.36 J $mol^{-1}K^{-1}$, while from the PMF method, it is -146.98 J $mol^{-1}K^{-1}$. The results of Monte Carlo simulations were compared to Quantum Mechanics calculations. The QM-calculated enthalpy of dimerization is -60.48 kJ mol^{-1}, deviating by 0.02% from the dimer counter method and 4% from the PMF method. The QM-calculated molar entropy of dimerization is -138 J $mol^{-1}K^{-1}$, differing by an average of 3% from both MC methods. The QM and umbrella sampling MC simulations employed in this study demonstrated high accuracy in reproducing the experimental thermodynamic properties of HCOOH dimerization, with the dimer counter method providing the most precise match with experimental data. To calculate the thermodynamic phase equilibrium properties, the cubic Peng-Robinson equation of state, coupled with an athermal version of advanced mixing rules, was applied. Ideal gas properties, which cannot be experimentally measured, were determined using Quantum Mechanics calculations. These properties are necessary for an optimization step aimed at fitting the critical coordinates of the two pure components to match the experimental vaporization enthalpy and saturation pressures of the reactive mixture. The Global Phase Equilibrium of the system, vaporization enthalpy, phase composition, vapor and liquid densities of the coexisting phases as a function of temperature, and entropy as a function of temperature were obtained from the thermodynamic model and compared with Monte Carlo simulations in the Gibbs ensemble. Overall, the MC sim-

ulations agree well with the model, especially for saturation pressure and the non-isothermal phase diagram of the HCOOH mixture, confirming the validity of the simulations in capturing the phase behavior of the system. These results are directly relevant to the design of heat pumps using formic acid as a working fluid, where precise control over thermodynamic properties is essential for optimizing performance. However, it is important to note that this study does not consider the kinetics of the dimerization reaction, which could influence the performance of heat pumps. Future work could incorporate reaction kinetics into the simulations, potentially through kinetic Monte Carlo or Molecular Dynamics simulations, to provide a more comprehensive understanding of the system behavior. To conclude, the presented methodology has proven effective in accurately determining the chemical equilibrium properties of $2\mathrm{HCOOH} \rightleftharpoons (\mathrm{HCOOH})_2$. It could be adapted to preliminarily predict the thermodynamic properties of other similar reactive systems, such as other carboxylic acids, thereby broadening its applicability in the design of heat pumps and other thermodynamic devices. It is important to note that our rigid HCOOH force field was not optimized or fitted to the dimerization reaction. As a first step, the Monte Carlo simulation only considers monomers and dimers. A more realistic description would include trimers and more complex structures.

Chapter 8

Conclusions and Outlook

The first part of this thesis, comprising the dependence of the carbon dioxide solubility in aqueous formic acid solutions with electrolytes on the composition and the sodium chloride concentration is presented in Chapter 3. The main conclusions in this regard are:

- The Continuous Fractional Component Monte Carlo approach using the probability distribution of the scaling factor $[p(\lambda)]$ is precise enough to compute excess chemical potentials, resulting in μ^{ex} that differed from thermodynamic integration by less than 0.5%.
- Validation of the selected variant of the OPLS/AA force field for HCOOH was performed by comparing the density, vapor-liquid equilibrium, and vapor pressure with experimental values, demonstrating a high accuracy of the model.
- The salting-out effect of NaCl on CO_2 solubility is observed, which is economically and ecologically unfavorable as it decreases the product yield as well as results in less CO_2 being reduced and removed from the environment.
- HCOOH production could be an alternative method to CO_2 pressure elevation for adjusting solubility, due to the observed increase in CO_2 solubility with higher HCOOH fractions in the solution.

The effect of confinement on the CO_2 hydrogenation reaction is studied in the second part of this thesis, as presented in Chapter 4. The main conclusions are:

- The metal-organic framework confinement increases the HCOOH production, due to the higher density of the pore phase compared to the gas phase and the selective adsorption of HCOOH as a favored component, by Le Chatelier's principle.

- The mole fractions of HCOOH increase with pressure and decrease with increasing temperature, resulting in the most efficient conditions for the HCOOH production in the confinement at 298.15 K and 60 bar.
- The prevailing factor in the enhancement of HCOOH production in CO_2 hydrogenation reaction is the type of metal center in the metal-organic framework. The production of HCOOH in the UiO-66 framework characterized by the smallest pore size for all studied MOFs is ca. 200 times higher compared to the gas phase, while in Cu-BTC the HCOOH production is ca. 2000 times higher compared to the gas phase.
- The metal-organic framework Cu-BTC shows promise as an effective alternative or complement to transition metal catalysts for enhancing CO_2 hydrogenation efficiency due to the elimination of the need for costly temperature elevation, the production of a more valuable final product that reduces the cost of downstream processing, and achieving final HCOOH concentrations comparable to those obtained with transition metal catalysts.

The third part of this thesis, proposing a non-polarizable CO_2 and H_2 force field for adsorption in M-MOF-74 (M = Ni, Cu, Co, Fe, Mn, Zn) is presented in Chapter 5. The main conclusions are:

- The Feynman-Hibbs quantum correction plays a crucial role in the force field of H_2 at cryogenic temperatures, as it influences the isotherm shape by lowering the adsorption capacity.
- The breakthrough curves are predicted for the separation of CO_2/H_2 mixtures at 298 K, resulting in the breakthrough time following the same order as the uptake and the heat of CO_2 adsorption: Ni > Co > Fe > Mn > Zn > Cu.
- The metal-organic frameworks M-MOF-74 have the potential in the capture of CO_2 and H_2, as well as in separation processes of CO_2/H_2 mixtures.
- The proposed non-polarizable CO_2 and H_2 force field for adsorption in M-MOF-74 is an alternative to the complex polarizable force fields available in the literature, that would enable to study of the process of CO_2 conversion into HCOOH, and a better understanding of the effect of open-metal centers on the CO_2 hydrogenation reaction to HCOOH in confinement.

The effect of the type of metal center in M-MOF-74 (M = Ni, Cu, Co, Fe, Mn, Zn) on the CO_2 hydrogenation reaction to HCOOH is investigated in the

fourth part of this thesis, as presented in Chapter 6. The main conclusions are:

- The loading and heat of HCOOH adsorption depend on the metal center as follows: Ni > Co > Fe > Mn > Zn > Cu, suggesting that HCOOH adsorption is predominantly influenced by the electrostatic interactions dependent on the effective charge of the M^{2+} ion at the open-metal site.
- The two-step adsorption mechanism of HCOOH is found in Ni-, Co-, Fe-, and Mn-MOF-74: primary adsorption at metal centers followed by adsorption above oxygen atoms inside the framework.
- The three primary binding geometries of HCOOH adsorption in M-MOF-4 are in the surroundings of the metal centers. The binding geometries and energies of the most stable configuration computed from force field-based simulations agree with DFT calculations.
- The performance of M-MOF-74 in the production of HCOOH in confinement follows the same order as the uptake and the heat of HCOOH adsorption.
- The highest enhancement in HCOOH production results from the application of the Ni-MOF-74 framework. The obtained mole fraction of HCOOH is ca. 10^5 times higher compared to the gas phase.
- Ni-MOF-74 has comparable performance to the most effective transition metal catalyst and an additional advantage of a more valuable molecular form of the product.

The multi-scale methodology including force field-based Monte Carlo simulations, quantum mechanics, and equations of state is introduced to investigate the thermodynamics of formic acid dimerization in the fifth part of this thesis, as presented in Chapter 7. The main conclusions are:

- The multi-scale methodology integrating force field-based Monte Carlo simulations, Quantum Mechanics, and equations of state has proven effective in accurately characterizing the thermodynamics of the formic acid dimerization reaction. The method could be adapted to preliminarily predict the thermodynamic properties of other similar reactive systems, such as other carboxylic acids.
- The umbrella sampling method was necessary implementation to Monte Carlo simulations to compute thermodynamic properties of formic acid dimerization such as equilibrium constants, enthalpy, and entropy of dimerization.
- Both methods for studying dimer formation, the dimer counter and the potential of mean force computation, showed good agreement, resulting

in the enthalpies of HCOOH dimerization of -60.46 kJ mol^{-1} and -62.91 kJ mol^{-1}, respectively. The molar entropy of dimerization computed from the dimer counter method is -137 J $mol^{-1}K^{-1}$, while from the potential of mean force method it is -147 J $mol^{-1}K^{-1}$.

- Comparison of Monte Carlo simulations with Quantum Mechanics calculations showed that the QM-calculated enthalpy of dimerization of -60.48 kJ mol^{-1} deviates only by 0.02% from the dimer counter method and 4% from the PMF method. The QM-calculated molar entropy of dimerization is -138 J $mol^{-1}K^{-1}$, differing by an average of 3% from both MC methods. The dimer counter method provided the most precise match with experimental data.
- The global phase equilibrium of the system, vaporization enthalpy, phase composition, vapor and liquid densities of the coexisting phases as a function of temperature, and entropy as a function of temperature obtained from the thermodynamic model are in good agreement with Monte Carlo simulations in the Gibbs ensemble.
- The methodology for formic acid dimerization simulation is effective for accurately determining chemical equilibrium properties and can be adapted for predicting thermodynamic properties of other reactive systems, such as different carboxylic acids.

In this thesis, molecular simulation is used to explore and propose alternative approaches for improving two conventional methods of formic acid production: (1) electrochemical reduction of CO_2 in aqueous electrolyte solutions, and (2) the CO_2 hydrogenation reaction. Molecular simulation has demonstrated its ability to supplement experimental data in the field of formic acid production. Beyond enabling predictions for the "confinement effect" of porous materials on the thermodynamic equilibrium of the CO_2 hydrogenation reaction independently from the "catalytic effect", a task difficult experimentally, it provides insights into the microscopic mechanisms that govern the adsorption behaviors within the investigated porous materials.

Building on the findings, several promising avenues for future research emerge. For electrochemical reduction of CO_2 studies, investigating other chemicals that may enhance solubility and conversion efficiency of CO_2 without decreasing the ionic conductivity of electrolyte solutions is crucial. For the CO_2 hydrogenation reaction carried out in confinement, a comprehensive economic and carbon emission analysis of Ni-MOF-74 compared to traditional catalysts is essential to fully assess its potential. Furthermore, exploring ligand functionalization and other Ni-based MOFs could reveal new opportunities for optimizing HCOOH production from CO_2 hydrogenation.

An essential consideration for HCOOH production in MOFs is ensuring that the reaction free energy barrier is sufficiently low to allow the chemical equilibrium to be favorable. Without a low enough energy barrier, the reaction will not proceed efficiently. To address this, several strategies can be employed:

1. **Catalyst Optimization**: Improving the catalytic properties of the active sites within the MOFs may significantly lower the reaction energy barrier. This includes designing active sites that provide better stabilization of transition states and intermediates. For example, incorporating highly active metal sites such as Ru or Pd into the MOF structure can enhance catalytic activity. Computational techniques, such as DFT, can be used to screen and identify MOF structures with optimal catalytic properties.

2. **Ligand Functionalization**: Modifying the ligands within MOFs can tune the electronic properties of the active sites, thereby lowering the reaction energy barrier. For instance, functionalizing the ligands with electron-donating groups such as amines may enhance the stabilization of reaction intermediates. Similarly, introducing electron-withdrawing groups can adjust the electronic environment to favor specific reaction pathways.

3. **Bimetallic Catalysts**: Incorporating a second metal into the MOF structure can create synergistic effects that enhance catalytic performance. An example is the combination of Ni and Fe in bimetallic catalysts, which has been shown to lower the activation energy for CO_2 hydrogenation. Bimetallic catalysts can provide a combination of electronic and geometric properties that lower the reaction energy barrier more effectively than single-metal catalysts.

4. **Support Materials**: Using support materials that enhance the dispersion of active sites can improve the accessibility of reactants to the catalytic sites, thereby lowering the overall energy barrier. For example, incorporating carbon-based supports, such as graphene, can increase the surface area and improve the distribution of active sites within the MOF. Support materials can also modify the electronic environment of the active sites, further enhancing catalytic performance.

5. **Reaction Conditions**: Optimizing reaction conditions such as temperature, pressure, and solvent can also play a crucial role in lowering the reaction energy barrier. For instance, conducting the reaction at

elevated pressures can increase the reaction rate and lower the energy barrier. Additionally, using solvents that stabilize reaction intermediates can improve the overall efficiency of the process.

6. **Computational Modelling**: Advanced computational modelling can predict the reaction pathways and identify the key steps where the energy barriers are highest. By understanding these steps, targeted modifications to the MOF structure and composition can be made to lower these barriers. For example, simulations can reveal the most effective sites for catalyst placement or the optimal configuration of ligands to stabilize intermediates.

These strategies for lowering the reaction energy barrier are essential for making the CO_2 hydrogenation process viable in MOFs. By implementing these approaches, we can significantly enhance the efficiency of HCOOH production and contribute to advancing CO_2 reduction technologies, thereby improving the sustainability and efficiency of chemical processes.

Appendix A

Appendix A corresponds to Chapter 3 of this thesis.

- The derivation of the equation for computing activity coefficients;
- Details on the calculation of HCOOH monomer and dimer partial pressures in the gas phase;
- Information about the HCOOH models and force field parameters;
- Compositions and average box lengths of all studied systems;
- Excess chemical potentials for HCOOH and H_2O obtained from the probability distribution of the scaling factor $p(\lambda)$ as well as thermodynamic integration;
- Activity coefficients and densities for HCOOH and H_2O;
- Gibbs-Duhem integration test for four studied HCOOH/H_2O force fields as a function of the HCOOH mole fraction;
- Simulated HCOOH pressures in the gas phase;
- HCOOH dimer and monomer partial pressures in the gas phase.

1. ACTIVITY COEFFICIENTS

The chemical potential of component i in a mixture with respect to the ideal gas reference state is described by [179, 378]:

$$\mu_i = \overset{\circ}{\mu_i} + RT \ \ln \frac{\langle \rho_i \rangle}{\rho_0} + \mu_i^{\text{ex}} = \overset{\circ}{\mu_i} + RT \ \ln \frac{\langle \rho_i \rangle}{\rho_0} - RT \ \ln \frac{p\left(\lambda_i = 1\right)}{p\left(\lambda_i = 0\right)} \tag{A.1}$$

where $\overset{\circ}{\mu_i}$ is the reference state of the chemical potential of component i, which depends on temperature but not on the pressure, $\langle \rho_i \rangle$ is the average number density of i, ρ_0 is the reference number density of the pure solvent ($\rho_{0,\text{HCOOH}} = 1.5 \cdot 10^{28}$ m^{-3}, and $\rho_{0,\text{H}_2\text{O}} = 3.3 \cdot 10^{28}$ m^{-3}), μ_i^{ex} is the excess chemical potential of i, $p(\lambda_i = 1)$ and $p(\lambda_i = 0)$ are the probabilities of the scaling factor λ_i taking the value 1 and 0, respectively. The chemical potential of component i in a mixture for a liquid-based reference state is expressed by [378]:

$$\mu_i = \mu_i^* + k_{\text{B}} T \ \ln \left(\gamma_i x_i\right) \tag{A.2}$$

where γ_i is the activity coefficients of component i and x_i is a mole fraction of component i. Combining Equations (A.1) and (A.2), the reference chemical

potential μ_i^* is obtained for a pure component:

$$\mu_i^* = \mu_i^\circ + k_B T \ \ln \frac{\langle \rho_i \rangle}{\rho_0} + \mu_{0i}^{ex} \tag{A.3}$$

where μ_i^* is the reference state of the chemical potential of component i, which depends on temperature and pressure, μ_{0i}^{ex} is the excess chemical potential of i with respect to the ideal gas. Combining Equations (A.2) and (A.3) and neglecting the pressure-dependence of μ_i^*, the chemical potential of component i is:

$$\mu_i = \mu_i^\circ + k_B T \ \ln \frac{\langle \rho_i \rangle}{\rho_0} + \mu_{0i}^{ex} + k_B T \ \ln (\gamma_i x_i) \tag{A.4}$$

The activity coefficient is obtained by combining Equations (A.1) and (A.4):

$$k_B T \ \ln \frac{\langle \rho_i \rangle}{\langle \rho_{0i} \rangle} + \mu_i^{ex} - \mu_{0i}^{ex} = k_B T \ \ln (\gamma_i x_i) \tag{A.5}$$

$$\gamma_i = \frac{\langle \rho_i \rangle}{x_i \cdot \langle \rho_{i0} \rangle} \cdot \exp \left[\frac{\mu_i^{ex} - \mu_{i0}^{ex}}{k_B T} \right] \tag{A.6}$$

The same result was obtained by Sadowski et al. [179]

2. HCOOH DIMER AND MONOMER PARTIAL PRESSURE IN THE GAS PHASE

HCOOH monomer and dimer partial pressures in the gas phase are calculated by [156]:

$$\frac{P_{M2}}{P^0} = \left(\frac{P_M}{P^0} \right)^2 \exp \left[\frac{2\mu_M^{ex} - \mu_{M2}^{ex}}{RT} \right] \tag{A.7}$$

$$y_{M2} = 1 - y_M = \frac{P_{M2}}{P} = 1 - \frac{P_M}{P} \tag{A.8}$$

Combining Equations (A.7) and (A.8), a quadratic equation is obtained:

$$\frac{1 - y_M}{y_M^2} = \exp \left[\frac{2\mu_M^{ex} - \mu_{M2}^{ex}}{RT} \right] \cdot \frac{P}{P^0} \tag{A.9}$$

where y_{M2} is the HCOOH dimer vapor mole fraction, y_M is the HCOOH monomer vapor mole fraction, R is the ideal gas constant, T is temperature, P is the HCOOH partial pressure in the gas phase, P^0 is the standard pressure (100 000 Pa) and μ_{M2}^{ex} and μ_M^{ex} are the excess chemical potentials of a dimer and monomer with respect to the ideal gas state, equal to -716.59 kJ mol^{-1} and -351 kJ mol^{-1}, respectively [28]. All results for the HCOOH/H_2O system without the addition of NaCl are shown in Table A.12.

Table A.1: Geometry for the HCOOH model optimized using Gaussian09 [171] at the B3LYP/6-31G(d) level of theory.

Atom	x/**[Å]**	y/**[Å]**	z/**[Å]**
C_{fa1}	0.133025	0.400057	0
O_{fa1}	-1.120802	-0.091884	0
O_{fa2}	1.139287	-0.262302	0
H_{fa1}	0.093278	1.498951	0
H_{fa2}	-1.039312	-1.065806	0

Table A.2: Interaction parameters for the formic acid FF-0 force field [174]. Lennard-Jones interactions between different atoms are computed using the Lorentz-Berthelot mixing rules [129]. It is important to note that there are exceptions/overrides to the use of the LB mixing rules. For some atom pairs, a minimum distance between two atoms ($R_{\min}$) is specified. For distances smaller than $R_{\min}$ the interaction energy is ∞.

Atom	σ /[Å]	ϵ/k_B /[K]	q /[e$^-$]
C_{fa1}	3.75	52.7999	0.52
O_{fa1}	3	85.51419	-0.53
O_{fa2}	2.96	105.72007	-0.44
H_{fa1}	2.42	7.57721	0
H_{fa2}	1	1	0.45
	override		
Atom pair	σ /[Å]	ϵ/k_B /[K]	$R_{\min}$ /[Å]
O_{fa2} - H_{fa2}	1.98	10.28202651	1.4

Table A.3: Interaction parameters for the formic acid FF-1 force field [174]. It is important to note that there are exceptions/overrides to the use of the LB mixing rules. For some atom pairs, a minimum distance between two atoms ($R_{\min}$) is specified. For distances smaller than $R_{\min}$ the interaction energy is ∞.

Atom	σ /[Å]	ϵ/k_B /[K]	q /[e$^-$]
C_{fa1}	3.64	43.29832	0.5148
O_{fa1}	2.91	69.39759	-0.5247
O_{fa2}	2.87	86.47637	-0.4356
H_{fa1}	2.35	6.13393	0
H_{fa2}	1	1	0.4455
	override		
Atom pair	σ /[Å]	ϵ/k_B /[K]	$R_{\min}$ /[Å]
O_{fa2} - H_{fa2}	1.935	9.299	1.4

Table A.4: Interaction parameters for the formic acid FF-2 force field [174], water SPC/E [175], CO_2 [176] and NaCl [177] force fields. It is important to note that there are exceptions/overrides to the use of the LB mixing rules. For some atom pairs, a minimum distance between two atoms ($R_{\min}$) is specified. For distances smaller than $R_{\min}$ the interaction energy is ∞.

Atom	σ /[Å]	ϵ/k_B /[K]	q /[e$^-$]
C_{fa1}	3.67	49.6728	0.52
O_{fa1}	2.94	80.46271	-0.53
O_{fa2}	2.9	99.34559	-0.44
H_{fa1}	2.37	7.09611	0
H_{fa2}	1	1	0.45
O_{SPCE}	3.166	78.17706	-0.8476
H_{SPCE}	0	0	0.4238
O_{CO_2}	3.017	85.671	-0.3256
C_{CO_2}	2.742	29.93	0.6512
Na	2.159	177.457	1
Cl	4.83	6.434	-1
	overrides		
Atom pair	σ /[Å]	ϵ/k_B /[K]	$R_{\min}$ /[Å]
O_{CO_2} - O_{SPCE}	3.058	79.14	1.529
C_{CO_2} - O_{SPCE}	3.052	53.04	1.527
O_{fa2} - H_{fa2}	1.95	9.967	1.4

Table A.5: Interaction parameters for the formic acid FF-3 force field [172].

Atom	σ /[Å]	ϵ/k_B /[K]	q /[e$^-$]
C_{fa1}	3.2335	59.993	0
O_{fa1}	3.1496	85.053	-0.31574
O_{fa2}	2.9953	96.696	-0.42186
H_{fa1}	0	0	0.29364
H_{fa2}	0	0	0.44396

Table A.6: Compositions and average box volumes of all 7 systems simulated for the Gibbs-Duhem integration test. The HCOOH FF-2 force field [174] and water SPC/E force field [175] were used.

x_{HCOOH}	N_{HCOOH}	N_{H_2O}	$V_{box}/[Å^3]$
0	0	400	12053.37
0.1	40	360	13391.47
0.3	120	280	16324.03
0.5	200	200	19186.16
0.7	280	120	21981.36
0.9	360	40	24690.59
1	400	0	26031.60

Table A.7: Compositions and average box volumes for all 28 systems simulated for the computation of Henry coefficients of CO_2. HCOOH pseudo-mole fractions were used, which are defined by: $x_{\mathrm{HCOOH}} = \frac{N_{\mathrm{HCOOH}}}{N_{\mathrm{HCOOH}}+N_{\mathrm{H_2O}}}$. For each HCOOH pseudo-mole fraction, four concentrations of NaCl are considered: 0, 0.25, 0.5, 0.75 mol NaCl per kilogram of solvent (H_2O + HCOOH).

x_{HCOOH}	N_{HCOOH}	$N_{\mathrm{H_2O}}$	N_{NaCl}	$V_{\mathrm{box}}/[\mathrm{Å}^3]$
0	0	400	0	12115.11
	0	400	2	12147.29
	0	400	4	12206.27
	0	400	5	12223.00
0.1	40	360	0	13471.09
	40	360	2	13513.98
	40	360	4	13582.70
	40	360	6	13633.51
0.3	120	280	0	16378.56
	120	280	3	16472.98
	120	280	5	16536.55
	120	280	8	16654.32
0.5	200	200	0	19271.93
	200	200	3	19371.17
	200	200	6	19467.67
	200	200	10	19605.28
0.7	280	120	0	22040.87
	280	120	4	22171.52
	280	120	8	22347.01
	280	120	11	22477.45
0.9	360	40	0	24752.86
	360	40	4	24916.40
	360	40	9	25141.52
	360	40	13	25345.05
1	400	0	0	26100.08
	400	0	5	26279.19
	400	0	9	26538.52
	400	0	14	26779.70

Table A.8: Average values of the excess chemical potentials for HCOOH and H_2O obtained from (1) the probability distribution $p(\lambda)$, and (2) thermodynamic integration. The HCOOH FF-2 force field [174] and water SPC/E force field [175] were used. $T = 298$ K and $P = 1$ bar. The values are listed depending on HCOOH mole fraction in the system. The subscripts show uncertainties computed as the standard deviation. The values of the excess chemical potential are in units of kJ mol^{-1}.

Compound		x_{HCOOH}						
	Route	0	0.1	0.3	0.5	0.7	0.9	1
HCOOH	$p(\lambda)$	$-23.3_{0.3}$	$-24.4_{0.3}$	$-26.0_{0.3}$	$-26.1_{0.2}$	$-26.0_{0.2}$	$-25.6_{0.2}$	$-25.63_{0.08}$
	$\langle\frac{\partial U}{\partial\lambda}\rangle$	$-23.2_{0.2}$	$-24.5_{0.1}$	$-26.1_{0.1}$	$-26.1_{0.1}$	$-25.9_{0.1}$	$-25.55_{0.04}$	$-25.4_{0.1}$
	Route	0	0.1	0.3	0.5	0.7	0.9	1
H_2O	$p(\lambda)$	$-29.7_{0.2}$	$-29.21_{0.08}$	$-28.4_{0.2}$	$-27.6_{0.2}$	$-27.3_{0.3}$	$-26.8_{0.2}$	$-26.7_{1.7}$
	$\langle\frac{\partial U}{\partial\lambda}\rangle$	$-29.7_{0.1}$	$-29.30_{0.08}$	$-28.22_{0.09}$	$-27.2_{0.2}$	$-27.2_{0.1}$	$-27.0_{0.2}$	$-26.8_{0.3}$

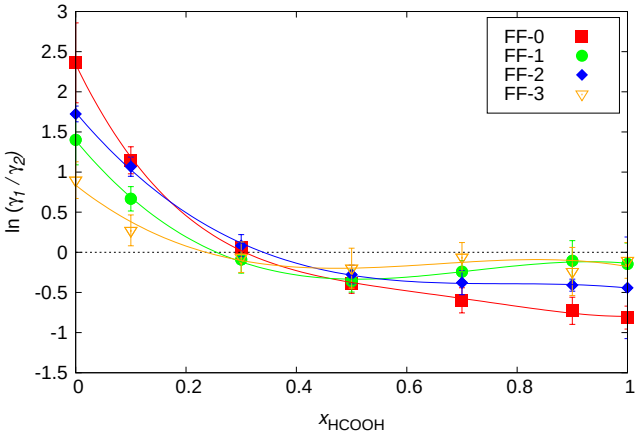

Fig. A.1. Gibbs-Duhem integration test for the four studied HCOOH/H_2O force fields FF-0 (Table A.2) [174], FF-1 (Table A.3) [174], FF-2 (Table A.4) [174] and FF-3 (Table A.5) [172] as a function of the mole fraction of HCOOH. The symbols represent data points for $\ln\left(\frac{\gamma_1}{\gamma_2}\right)$ obtained from the simulations for $x_{\mathrm{HCOOH}} = 0, 0.1, 0.3, 0.5, 0.7, 0.9, 1$. The lines connecting the symbols are cubic polynomials (for FF-1, FF-2, FF-3) and quartic polynomial (for FF-0). The 101 data points for $\ln\left(\frac{\gamma_1}{\gamma_2}\right)$ in a range $x_{\mathrm{HCOOH}} \in [0, 1]$ were obtained by interpolating the computed values with the use of polynomials. All the studied force fields resulted in the Gibbs-Duhem integral equals to zero within the error bars. The results for the Gibbs-Duhem integration test were as follows:

- FF-0: -0.08 ± 0.10,
- FF-1: -0.01 ± 0.13,
- FF-2: 0.03 ± 0.11,
- FF-3: -0.02 ± 0.16.

The uncertainties of the Gibbs-Duhem integrals were calculated using error propagation rules, see Eqs. 3.7-3.9 of Chapter 3.

Table A.9: Average values of activity coefficients for HCOOH and H_2O, computed based on the values of μ^{ex} of HCOOH and H_2O from the probability distribution of λ. The HCOOH FF-0, FF-1, FF-2 and FF-3 force fields [172, 174] and water SPC/E force field [175] were used. $T = 298$ K and $P = 1$ bar. The listed values depend on the compound mole fraction in the system. The subscripts show uncertainties computed as the standard deviation obtained from 5 independent simulations. The activity coefficients at the limit $x_i = 0$ are calculated for 1 theoretical molecule of compound i in the system.

	FF-0		**FF-1**	
x_i	γ_{HCOOH}	γ_{H_2O}	γ_{HCOOH}	γ_{H_2O}
0	11.9_{6}	$2.3_{0.3}$	4.3_{1}	$1.2_{0.4}$
0.1	$3.6_{0.3}$	$1.9_{0.2}$	$2.1_{0.3}$	$1.1_{0.2}$
0.3	$1.4_{0.2}$	$1.8_{0.2}$	$1.1_{0.2}$	$1.3_{0.2}$
0.5	$1.2_{0.1}$	$1.71_{0.05}$	$0.9_{0.1}$	$1.3_{0.1}$
0.7	$1.0_{0.1}$	$1.3_{0.1}$	$1.01_{0.09}$	$1.2_{0.1}$
0.9	$0.9_{0.1}$	$1.11_{0.09}$	$1.00_{0.09}$	$1.1_{0.1}$
1	1	1	1	1
	FF-2		**FF-3**	
x_i	γ_{HCOOH}	γ_{H_2O}	γ_{HCOOH}	γ_{H_2O}
0	$5.6_{0.5}$	$1.8_{0.9}$	$2.3_{0.6}$	$1.1_{0.2}$
0.1	$3.2_{0.5}$	$1.6_{0.1}$	$1.3_{0.1}$	$1.2_{0.1}$
0.3	$1.4_{0.1}$	$1.5_{0.2}$	$1.1_{0.2}$	$1.1_{0.1}$
0.5	$1.1_{0.1}$	$1.5_{0.2}$	$0.9_{0.1}$	$1.2_{0.1}$
0.7	$1.01_{0.04}$	$1.3_{0.2}$	$1.1_{0.1}$	$1.1_{0.1}$
0.9	$1.1_{0.1}$	$1.11_{0.07}$	$1.0_{0.3}$	$1.0_{0.1}$
1	1	1	1	1

Table A.10: Average number densities in units of mol m^{-3} for HCOOH and H_2O, computed from the probability distribution of λ route of CFCMC simulations. The HCOOH FF-0, FF-1, FF-2 and FF-3 force fields [172, 174] and water SPC/E force field [175] were used. $T = 298$ K and $P = 1$ bar. The listed values depend on the compound mole fraction in the system. The subscripts show uncertainties computed as the standard deviation obtained from 5 independent simulations. The densities at the limit $x_i = 0$ are calculated for 1 theoretical molecule of the compound i in the system.

	FF-0		**FF-1**	
x_i	ρ_{HCOOH}	$\rho_{\mathrm{H_2O}}$	ρ_{HCOOH}	$\rho_{\mathrm{H_2O}}$
0	$137.9_{0.2}$	$61.47_{0.01}$	$137.8_{0.1}$	$62.97_{0.04}$
0.1	$4919.3_{9.8}$	$2595.8_{1.8}$	$4959.8_{8.1}$	$2660.8_{3.4}$
0.3	$11998.1_{7.7}$	8785.9_{10}	12185.0_{19}	$8990.8_{5.3}$
0.5	16877.9_{17}	16876.2_{17}	17196.5_{28}	17194.8_{28}
0.7	20502.5_{24}	27992.7_{18}	20980.5_{12}	28428.9_{44}
0.9	23364.6_{16}	44269.3_{88}	23949.6_{31}	44633.8_{73}
1	$24595.9_{5.5}$	55157.8_{63}	25196.7_{16}	55147.5_{58}
	FF-2		**FF-3**	
x_i	ρ_{HCOOH}	$\rho_{\mathrm{H_2O}}$	ρ_{HCOOH}	$\rho_{\mathrm{H_2O}}$
0	$137.7_{0.2}$	$63.78_{0.02}$	$137.7_{0.2}$	$72.7_{0.1}$
0.1	$4961.2_{8.2}$	$2690.4_{2.5}$	$5067.2_{7.7}$	$3045.5_{2.1}$
0.3	12209.9_{20}	$9066.3_{3.1}$	13034.3_{17}	$10142.9_{4.5}$
0.5	17313.8_{16}	17312.1_{16}	19003.7_{11}	19001.8_{11}
0.7	$21156.7_{7.1}$	28486.9_{48}	23669.2_{11}	30410.3_{39}
0.9	24216.5_{23}	44646.8_{73}	27412.0_{19}	45600.3_{69}
1	$25520.7_{9.8}$	55114.5_{91}	29086.5_{22}	55091.9_{61}

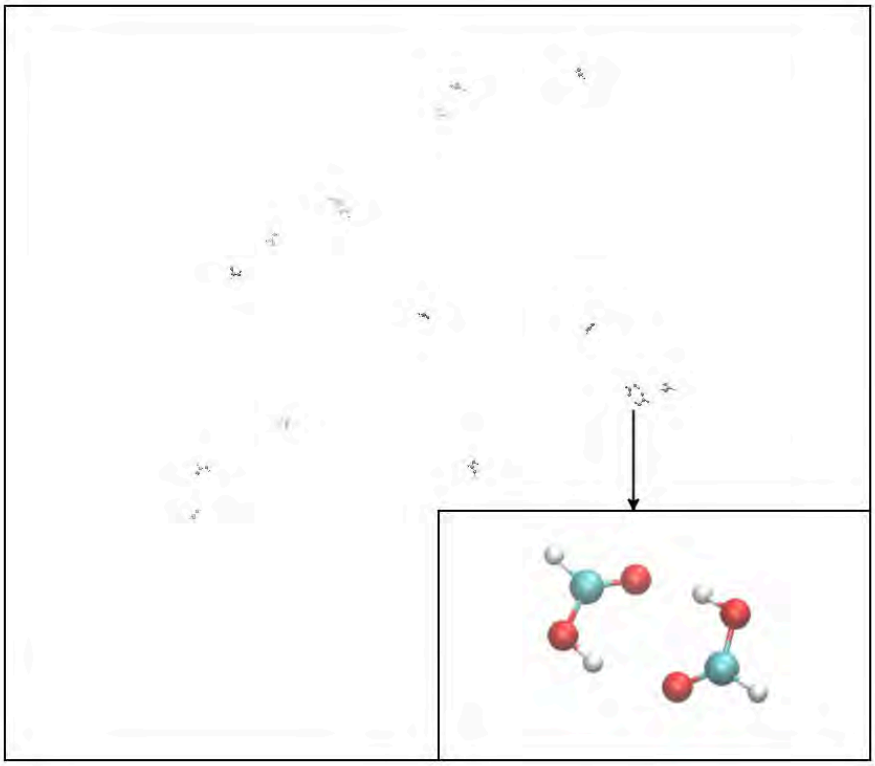

Fig. A.2. Visualization of a pure HCOOH system configuration in the gas phase at $T = 360$ K, $P = 0.7$ bar, using the VMD software [379]. The HCOOH FF-2 force field [174] was used. The presence of dimers was confirmed and visualized within all the HCOOH molecules present in the gas phase. A typical example of a dimer is highlighted in red, and its enlarged image is shown in the lower right corner.

Table A.11: Comparison of the saturated vapor pressures of pure HCOOH (computed from series of NPT simulations of the vapor phase and calculated using the liquid phase properties from Gibbs Ensemble simulations) with experimental values [172], as a function of temperature. The HCOOH FF-2 force field [174] and water SPC/E force field [175] were used. The subscripts show uncertainties computed as the standard deviation obtained from five independent Gibbs Ensemble simulations. The uncertainties of the pure HCOOH vapor pressures computed from a series of NPT simulations ($P_{\mathrm{HCOOH,sim}}$) and calculated using Eq. 10, are close to zero due to the small number of molecules in the vapor phase.

T/[K]	$P_{\mathrm{HCOOH,sim}}$/[MPa]	$P_{\mathrm{HCOOH,calc}}$/[MPa]	$P_{\mathrm{HCOOH,exp}}$/[MPa]
335	$0.019_{0.003}$	$0.037_{0.022}$	0.027
360	$0.057_{0.013}$	$0.077_{0.03}$	0.066
385	$0.220_{0.02}$	$0.176_{0.031}$	0.140
410	$0.443_{0.024}$	$0.343_{0.008}$	0.269
435	$0.694_{0.09}$	$0.573_{0.013}$	0.480
460	$1.232_{0.124}$	$0.947_{0.02}$	0.803
485	$1.720_{0.06}$	$1.431_{0.014}$	1.275
510	$2.819_{0.313}$	$2.086_{0.01}$	1.937
535	$3.381_{0.205}$	$2.922_{0.023}$	2.839
560	$4.872_{0.189}$	$3.988_{0.036}$	4.036

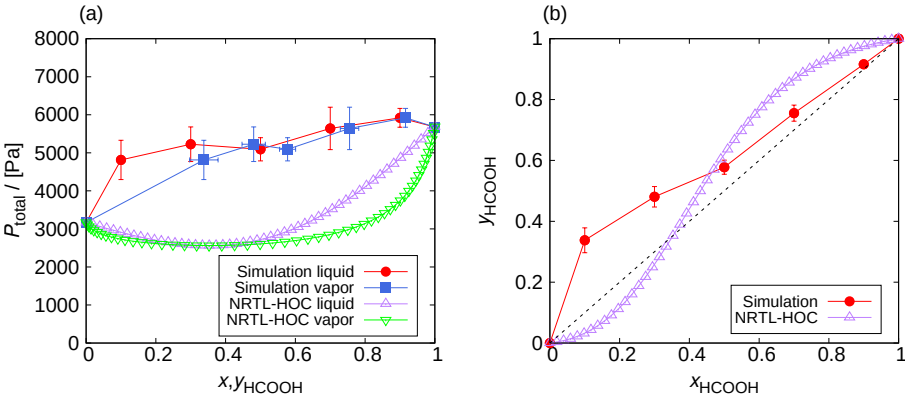

Fig. A.3. The azeotropic behavior of the $HCOOH/H_2O$ system without addition of NaCl: (a) total pressure of the vapor (P_{H_2O} + P_{HCOOH}) as a function of the mole fractions of HCOOH in the vapor and liquid, (b) mole fraction of HCOOH in the liquid phase as a function of vapor mole fraction. The lines connecting the symbols are used to guide the eye. The simulated $HCOOH/H_2O$ systems show a low-boiling azeotrope behavior in sharp contrast to the high-boiling azeotrope obtained from NRTL-HOC calculations [17]. The uncertainties were computed as the standard deviation from five independent simulations.

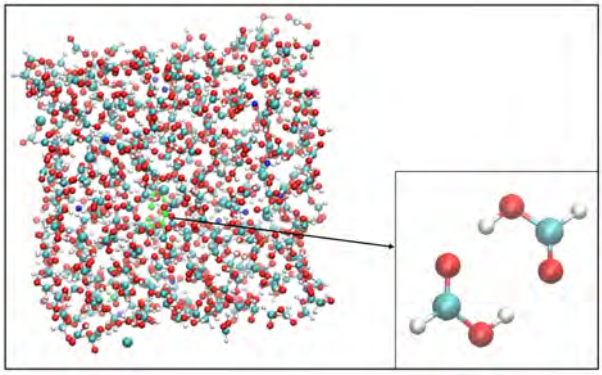

Fig. A.4. Visualization of a HCOOH/H_2O/CO_2/NaCl system configuration at $T = 298$ K, $P = 1$ bar, using the VMD software [379]. The pseudo-mole fraction of HCOOH in the system was $x_{HCOOH} = 1$ and the concentration of NaCl added was 0.75 mol NaCl per kilogram of solvent (HCOOH + H_2O). The HCOOH FF-2 force field [174], water SPC/E force field [175], CO_2 force field [176] and NaCl [177] force field were used. The presence of dimers was confirmed in the gas phase. A typical example of a dimer is highlighted in green, and its enlarged image is shown in the lower right corner.

Table A.12: The HCOOH dimer and monomer partial pressures in the gas phase calculated for the HCOOH/H_2O system without the addition of NaCl. The HCOOH FF-2 force field [174], water SPC/E force field [175] and CO_2 force field [176] were used. The subscripts show uncertainties computed using error propagation rules. The calculated dimer partial pressures of the vapor are found to be approximately 2 - 4 times higher than monomer partial pressures, confirming that the non-ideal dimer formation behavior is the reason, why the studied model does not reproduce vapor pressures and azeotropic behavior more precisely than the order of magnitude.

x_{HCOOH}	P_{HCOOH}/[Pa]	P_{M2}/[Pa]	P_M/[Pa]
0.1	$1615.7_{196.3}$	$1070.9_{8.9}$	$544.8_{8.9}$
0.3	$2510.4_{304.8}$	$1803.5_{11.6}$	$706.9_{11.6}$
0.5	$2946.6_{284.6}$	$2171.0_{8.1}$	$775.6_{8.1}$
0.7	$4271.5_{543.6}$	$3313.3_{17.3}$	$958.2_{17.3}$
0.9	$5422.1_{236.5}$	$4327.1_{2.3}$	$1095.0_{2.3}$
1	5678.2	4554.7	1123.5

Appendix B

Appendix B corresponds to Chapter 4 of this thesis.

- Information about the ideal-gas partition functions of CO_2, H_2, and HCOOH at 298.15 - 800 K;
- The validation of ideal-gas partition functions - the equilibrium composition of syngas obtained by co-feeding HCOOH to the steam reforming of methane reaction at 1 bar, H_2O:CH_4 = 1 and HCOOH:H_2O = 0.5;
- Geometries for the CO_2, H_2, and HCOOH models;
- Cell parameters for UiO-66, Cu-BTC, and IRMOF-1;
- Mole fractions of CO_2, H_2, and HCOOH obtained from Continuous Fractional Component Monte Carlo simulations in the Reaction Ensemble at 298.15 - 800 K, and 1 - 60 bar;
- Fugacity coefficients of CO_2, H_2, and HCOOH computed using the Peng-Robinson equation of state at 298.15 - 800 K, and 1 - 60 bar;
- Mole fractions of CO_2, H_2, and HCOOH obtained from grand-canonical Monte Carlo simulations at 298.15 - 800 K, and 1 - 60 bar;
- Enthalpy of adsorption at infinite dilution of CO_2, H_2, and HCOOH in Cu-BTC, and IRMOF-1;
- Radial distribution functions for HCOOH and metal centers in UiO-66, Cu-BTC, and IRMOF-1.

Table B.1: Ideal-gas partition functions for CO_2, H_2 and HCOOH at 298.15 - 800 K. The values were calculated based on the vibrational and rotational experimental data from the NIST database [232–236]. Λ_i is the thermal wavelength. For the details about the computation of ideal gas partition functions, the reader is referred to the book by McQuarrie et al. [156].

	CO_2	H_2	HCOOH
T/[K]	$\ln(q/\Lambda^3)$	$\ln(q/\Lambda^3)$	$\ln(q/\Lambda^3)$
298.15	655.94	175.86	825.14
350	560.90	150.44	705.67
400	492.66	132.22	619.89
500	397.26	106.79	500.00
600	333.81	89.92	420.29
700	288.60	77.93	363.52
800	254.78	68.99	321.08

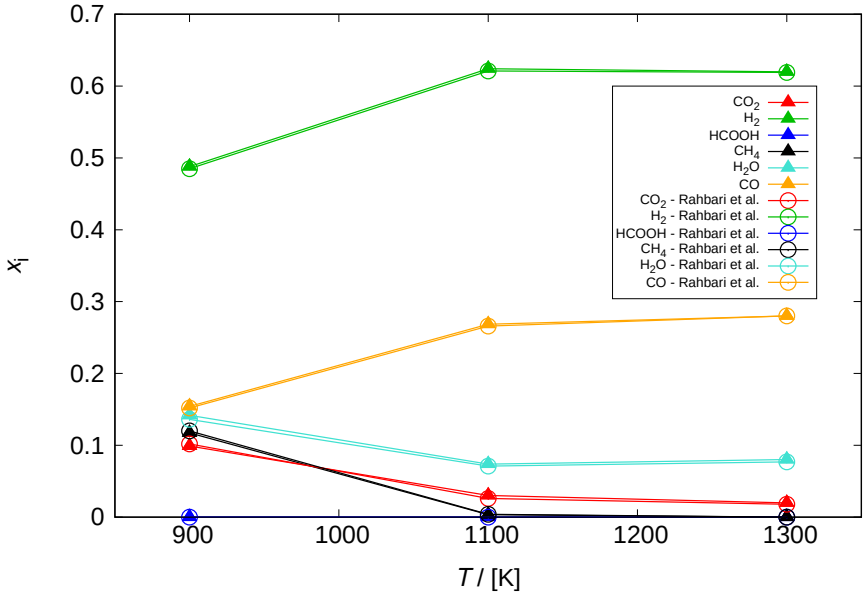

Fig. B.1. Equilibrium composition of syngas as a function of temperature obtained by co-feeding HCOOH to the steam reforming of methane reaction [41] at 1 bar, H_2O:CH_4 = 1 and HCOOH:H_2O = 0.5. The simulated reactions are:

$$CH_4 + H_2O \rightleftarrows CO + 3H_2$$

$$CO_2 + H_2 \rightleftarrows HCOOH \rightleftarrows H_2O + CO$$

The lines connecting the symbols are used to guide the eye. The mole fractions of H_2, CO, CH_4, H_2O, CO_2, and HCOOH are computed from Rx/CFC simulations [142], using ideal-gas partition functions from Table B.1. Ideal gas behavior was assumed. The obtained mole fractions were compared to the equilibrium composition of syngas from the study of Rahbari et al. [41]. The uncertainties of the computed mole fractions were calculated as the standard deviations from five independent simulations, performed using Brick-CFCMC [143, 152]. The resulting mole fractions differ from the literature by ca. 4%, meaning that the validation was successful.

Table B.2: Geometries of the CO_2 [176], and H_2 [243].

Atom	x/[Å]	y/[Å]	z/[Å]
O_{CO_2}	0	0	1.149
C_{CO_2}	0	0	0
O_{CO_2}	0	0	-1.149
H_{H_2}	0	0	0.37
H_{com}	0	0	0
H_{H_2}	0	0	-0.37

Table B.3: Cell parameters for UiO-66 [238], Cu-BTC [109] and IRMOF-1 [81].

MOF	a/[Å]	b/[Å]	c/[Å]	α/[°]	β/[°]	γ/[°]	V/[Å^3]
UiO-66	41.4008	41.4008	41.4008	90	90	90	70962.1
Cu-BTC	26.343	26.343	26.343	90	90	90	18280.8
IRMOF-1	25.832	25.832	25.832	90	90	90	17237.5

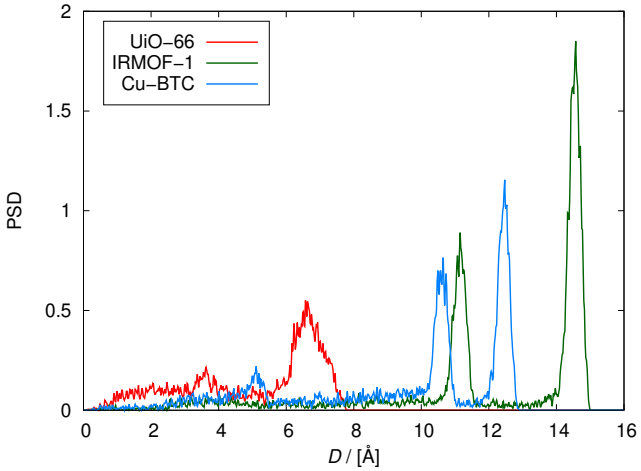

Fig. B.2. Pore size distribution of UiO-66, Cu-BTC, and IRMOF-1 frameworks, computed using the RASPA software package [94, 95] at 298.15 K. There are two types of micropores with a diameter at 3.5 Å and 7 Å present in the UiO-66. Cu-BTC is characterized by larger micropores with diameters at 5, 11, and 13 Å. The diameters of micropores in IRMOF-1 are at 11 Å and 15 Å.

Table B.4: Mole fractions of CO_2, H_2, and HCOOH obtained from Continuous Fractional Component Monte Carlo simulations [139–141] in the Reaction Ensemble [135, 136, 142] in the bulk-phase at 298.15 - 800 K and 1 - 60 bar. The initial compositions of the systems consist of equal numbers of CO_2 and H_2 molecules (200) according to the stoichiometry of the CO_2 hydrogenation reaction:

$$CO_2 + H_2 \rightleftarrows HCOOH$$

The subscripts show uncertainties computed using error propagation rules, see Eqs. 4.5 and 4.6.

P/[bar]	T/[K]	x_{CO_2,H_2}	x_{HCOOH} / 10^{-6}
1	298.15	$0.49999999_{1\cdot10^{-8}}$	$0.017_{0.008}$
	400	$0.49999998_{2\cdot10^{-8}}$	$0.04_{0.01}$
	500	$0.49999995_{2\cdot10^{-8}}$	$0.10_{0.02}$
	600	$0.49999993_{3\cdot10^{-8}}$	$0.14_{0.02}$
	700	$0.49999991_{4\cdot10^{-8}}$	$0.17_{0.03}$
	800	$0.49999991_{4\cdot10^{-8}}$	$0.18_{0.03}$
5	298.15	$0.49999996_{4\cdot10^{-8}}$	$0.08_{0.03}$
	400	$0.49999988_{3\cdot10^{-8}}$	$0.24_{0.02}$
	500	$0.49999979_{9\cdot10^{-8}}$	$0.42_{0.07}$
	600	$0.49999966_{7\cdot10^{-8}}$	$0.68_{0.05}$
	700	$0.4999996_{1\cdot10^{-7}}$	$0.8_{0.1}$
	800	$0.49999950_{9\cdot10^{-8}}$	$1.00_{0.07}$
10	298.15	$0.49999994_{3\cdot10^{-8}}$	$0.13_{0.03}$
	400	$0.49999977_{3\cdot10^{-8}}$	$0.46_{0.02}$
	500	$0.49999956_{4\cdot10^{-8}}$	$0.88_{0.03}$
	600	$0.49999935_{8\cdot10^{-8}}$	$1.30_{0.06}$
	700	$0.4999992_{1\cdot10^{-7}}$	$1.6_{0.1}$
	800	$0.4999990_{1\cdot10^{-7}}$	$1.92_{0.09}$
15	298.15	$0.49999988_{4\cdot10^{-8}}$	$0.24_{0.03}$
	400	$0.49999967_{6\cdot10^{-8}}$	$0.66_{0.05}$
	500	$0.4999994_{1\cdot10^{-7}}$	$1.3_{0.1}$
	600	$0.4999991_{2\cdot10^{-7}}$	$1.9_{0.1}$
	700	$0.4999988_{1\cdot10^{-7}}$	$2.4_{0.1}$
	800	$0.4999986_{2\cdot10^{-7}}$	$2.7_{0.1}$
20	298.15	$0.49999987_{4\cdot10^{-8}}$	$0.25_{0.03}$
	400	$0.49999952_{3\cdot10^{-8}}$	$0.96_{0.03}$
	500	$0.49999916_{7\cdot10^{-8}}$	$1.68_{0.06}$
	600	$0.4999988_{2\cdot10^{-7}}$	$2.5_{0.1}$
	700	$0.4999984_{1\cdot10^{-7}}$	$3.2_{0.1}$
	800	$0.4999981_{3\cdot10^{-7}}$	$3.8_{0.2}$

25	298.15	$0.49999983_{7\cdot10^{-8}}$	$0.35_{0.05}$
	400	$0.4999995_{1\cdot10^{-7}}$	$1.0_{0.1}$
	500	$0.4999989_{2\cdot10^{-7}}$	$2.1_{0.1}$
	600	$0.4999984_{2\cdot10^{-7}}$	$3.1_{0.1}$
	700	$0.4999980_{1\cdot10^{-7}}$	$3.93_{0.09}$
	800	$0.4999977_{1\cdot10^{-7}}$	$4.7_{0.1}$
30	298.15	$0.49999984_{5\cdot10^{-8}}$	$0.33_{0.04}$
	400	$0.4999993_{1\cdot10^{-7}}$	$1.38_{0.08}$
	500	$0.4999987_{2\cdot10^{-7}}$	$2.5_{0.1}$
	600	$0.4999981_{2\cdot10^{-7}}$	$3.8_{0.2}$
	700	$0.4999976_{2\cdot10^{-7}}$	$4.8_{0.2}$
	800	$0.4999973_{2\cdot10^{-7}}$	$5.5_{0.2}$
40	298.15	$0.49999972_{8\cdot10^{-8}}$	$0.56_{0.06}$
	350	$0.4999995_{2\cdot10^{-7}}$	$1.1_{0.1}$
	400	$0.49999909_{8\cdot10^{-8}}$	$1.82_{0.06}$
	500	$0.4999983_{2\cdot10^{-7}}$	$3.4_{0.2}$
	600	$0.4999976_{2\cdot10^{-7}}$	$4.7_{0.1}$
	700	$0.4999969_{2\cdot10^{-7}}$	$6.2_{0.2}$
	800	$0.4999964_{3\cdot10^{-7}}$	$7.2_{0.2}$
50	298.15	$0.4999996_{3\cdot10^{-7}}$	$0.8_{0.2}$
	350	$0.4999993_{2\cdot10^{-7}}$	$1.3_{0.2}$
	400	$0.4999989_{1\cdot10^{-7}}$	$2.10_{0.09}$
	500	$0.4999980_{1\cdot10^{-7}}$	$4.1_{0.1}$
	600	$0.4999970_{3\cdot10^{-7}}$	$6.0_{0.2}$
	700	$0.4999962_{3\cdot10^{-7}}$	$7.6_{0.2}$
	800	$0.4999954_{3\cdot10^{-7}}$	$9.1_{0.3}$
60	298.15	$0.4999996_{1\cdot10^{-7}}$	$0.9_{0.1}$
	350	$0.49999920_{9\cdot10^{-8}}$	$1.61_{0.07}$
	400	$0.4999987_{2\cdot10^{-7}}$	$2.6_{0.1}$
	500	$0.4999975_{2\cdot10^{-7}}$	$4.9_{0.2}$
	600	$0.49999650_{7\cdot10^{-8}}$	$7.01_{0.06}$
	700	$0.4999954_{3\cdot10^{-7}}$	$9.3_{0.2}$
	800	$0.4999946_{3\cdot10^{-7}}$	$10.9_{0.2}$

Table B.5: Fugacity coefficients of CO_2, H_2, and HCOOH computed using the Peng-Robinson equation of state [157] at 298.15 - 800 K and 1 - 60 bar. The fugacity coefficients obtained from the NIST Standard Reference Database REFPROP [239] were listed for comparison.

P/[bar]	T/[K]	φ_{CO_2}	φ_{H_2}	φ_{HCOOH}	$\varphi_{REFPROP,CO_2}$	$\varphi_{REFPROP,H_2}$
1	298.15	0.995	1.001	0.983	0.996	1.003
	400	0.998	1.001	0.993	0.999	1.001
	500	0.999	1.000	0.997	0.999	1.001
	600	1.000	1.000	0.998	1.000	1.001
	700	1.000	1.000	0.999	1.000	1.000
	800	1.000	1.000	1.000	1.000	1.000
5	298.15	0.978	1.006	0.919	0.981	1.008
	400	0.992	1.003	0.965	0.993	1.005
	500	0.997	1.002	0.984	0.997	1.004
	600	0.999	1.002	0.992	0.999	1.003
	700	1.000	1.001	0.997	1.000	1.002
	800	1.001	1.001	0.999	1.001	1.002
10	298.15	0.956	1.013	0.845	0.961	1.017
	400	0.983	1.007	0.932	0.986	1.010
	500	0.994	1.005	0.968	0.994	1.007
	600	0.998	1.003	0.985	0.999	1.005
	700	1.000	1.003	0.993	1.001	1.004
	800	1.001	1.002	0.998	1.002	1.004
15	298.15	0.934	1.019	0.776	0.943	1.026
	400	0.975	1.010	0.900	0.979	1.015
	500	0.991	1.007	0.952	0.992	1.010
	600	0.997	1.005	0.977	0.998	1.008
	700	1.001	1.004	0.990	1.001	1.006
	800	1.002	1.003	0.997	1.002	1.005
20	298.15	0.914	1.026	0.713	0.924	1.035
	400	0.967	1.014	0.869	0.972	1.020
	500	0.988	1.009	0.937	0.989	1.014
	600	0.997	1.007	0.970	0.997	1.011
	700	1.001	1.005	0.987	1.001	1.009
	800	1.003	1.005	0.997	1.003	1.007
25	298.15	0.893	1.033	0.655	0.906	1.044
	400	0.960	1.017	0.840	0.965	1.025
	500	0.985	1.011	0.922	0.987	1.017
	600	0.996	1.008	0.962	0.996	1.013
	700	1.001	1.007	0.984	1.001	1.011

	800	1.004	1.006	0.996	1.004	1.009
30	298.15	0.873	1.040	0.602	0.888	1.053
	400	0.952	1.021	0.812	0.958	1.030
	500	0.982	1.014	0.908	0.984	1.021
	600	0.995	1.010	0.955	0.996	1.016
	700	1.001	1.008	0.981	1.002	1.013
	800	1.004	1.007	0.995	1.005	1.011
40	298.15	0.835	1.054	0.508	0.854	1.072
	350	0.900	1.037	0.658	0.912	1.051
	400	0.937	1.028	0.759	0.945	1.040
	500	0.976	1.018	0.880	0.979	1.028
	600	0.993	1.013	0.942	0.995	1.021
	700	1.002	1.011	0.975	1.002	1.017
	800	1.006	1.009	0.994	1.007	1.014
50	298.15	0.798	1.069	0.429	0.821	1.091
	350	0.877	1.047	0.594	0.892	1.065
	400	0.922	1.035	0.711	0.932	1.050
	500	0.970	1.023	0.854	0.974	1.035
	600	0.992	1.017	0.929	0.993	1.027
	700	1.002	1.013	0.970	1.003	1.021
	800	1.008	1.011	0.993	1.008	1.018
60	298.15	0.764	1.085	0.363	0.789	1.112
	350	0.855	1.057	0.538	0.872	1.078
	400	0.908	1.042	0.666	0.919	1.061
	500	0.965	1.027	0.829	0.969	1.042
	600	0.991	1.020	0.916	0.992	1.032
	700	1.003	1.016	0.964	1.004	1.026
	800	1.009	1.014	0.992	1.010	1.021

Table B.6: Mole fractions of CO_2, H_2, and HCOOH obtained from grand-canonical Monte Carlo ensemble simulations in the UiO-66 framework at 298.15 - 800 K and 1 - 60 bar. The mole fractions of CO_2, H_2, and HCOOH at reaction equilibrium obtained from the Continuous Fractional Component Monte Carlo simulations in the Reaction Ensemble were used in the GCMC simulations as input. The subscripts show uncertainties computed using error propagation rules.

P/[bar]	T/[K]	x_{CO_2}	x_{H_2}	x_{HCOOH} / 10^{-6}
1	298.15	$0.994_{0.006}$	$0.0058_{0.0004}$	$2.2_{2.9}$
	400	$0.967_{0.015}$	$0.033_{0.002}$	$0.03_{0.06}$
	500	$0.919_{0.017}$	$0.081_{0.003}$	$0.9_{2.6}$
	600	$0.857_{0.015}$	$0.143_{0.004}$	0_{0}
	700	$0.795_{0.011}$	$0.205_{0.006}$	0_{0}
	800	$0.745_{0.022}$	$0.255_{0.012}$	15.0_{42}
5	298.15	$0.994_{0.004}$	$0.0063_{0.0001}$	$14.7_{4.6}$
	400	$0.963_{0.008}$	$0.0368_{0.0004}$	$1.8_{1.9}$
	500	$0.915_{0.011}$	$0.085_{0.001}$	$1.2_{3.3}$
	600	$0.857_{0.012}$	$0.143_{0.003}$	$0.2_{0.6}$
	700	$0.798_{0.018}$	$0.202_{0.003}$	$4.7_{7.4}$
	800	$0.742_{0.011}$	$0.258_{0.004}$	6.1_{12}
10	298.15	$0.994_{0.006}$	$0.0062_{0.0002}$	23.5_{11}
	400	$0.961_{0.007}$	$0.039_{0.001}$	$7.7_{6.4}$
	500	$0.913_{0.006}$	$0.087_{0.001}$	$11.4_{8.8}$
	600	$0.854_{0.009}$	$0.146_{0.002}$	11.0_{13}
	700	$0.796_{0.006}$	$0.204_{0.002}$	$7.2_{6.5}$
	800	$0.742_{0.010}$	$0.258_{0.003}$	$6.2_{9.4}$
15	298.15	$0.993_{0.002}$	$0.0066_{0.0001}$	57.2_{10}
	400	$0.959_{0.007}$	$0.0411_{0.0002}$	$8.3_{6.8}$
	500	$0.910_{0.005}$	$0.090_{0.001}$	$10.0_{8.4}$
	600	$0.851_{0.007}$	$0.149_{0.002}$	$9.2_{8.3}$
	700	$0.794_{0.005}$	$0.206_{0.002}$	9.3_{11}
	800	$0.740_{0.007}$	$0.260_{0.004}$	$2.9_{3.8}$
20	298.15	$0.993_{0.004}$	$0.0071_{0.0002}$	75.8_{64}
	400	$0.957_{0.003}$	$0.0433_{0.0002}$	$8.7_{5.0}$
	500	$0.907_{0.007}$	$0.093_{0.001}$	$12.6_{9.8}$
	600	$0.850_{0.007}$	$0.150_{0.001}$	$9.4_{5.1}$
	700	$0.792_{0.005}$	$0.208_{0.002}$	$11.0_{6.4}$
	800	$0.738_{0.009}$	$0.262_{0.004}$	$14.3_{6.8}$
25	298.15	$0.992_{0.002}$	$0.00751_{0.00004}$	79.1_{27}
	400	$0.956_{0.005}$	$0.044_{0.001}$	$15.4_{8.6}$
	500	$0.905_{0.002}$	$0.095_{0.001}$	$12.8_{8.7}$

	600	$0.847_{0.008}$	$0.153_{0.002}$	$12.2_{7.4}$
	700	$0.790_{0.009}$	$0.210_{0.002}$	$11.3_{5.8}$
	800	$0.738_{0.005}$	$0.262_{0.002}$	12.7_{14}
30	298.15	$0.992_{0.003}$	$0.0080_{0.0005}$	63.7_{43}
	400	$0.954_{0.004}$	$0.0460_{0.0005}$	$19.2_{6.1}$
	500	$0.903_{0.005}$	$0.097_{0.001}$	$16.0_{4.0}$
	600	$0.846_{0.004}$	$0.154_{0.001}$	18.8_{11}
	700	$0.788_{0.007}$	$0.212_{0.003}$	$13.5_{4.8}$
	800	$0.737_{0.008}$	$0.263_{0.003}$	$19.1_{3.8}$
40	298.15	$0.991_{0.004}$	$0.0091_{0.0002}$	156.0_{24}
	350	$0.975_{0.004}$	$0.025_{0.001}$	36.5_{17}
	400	$0.951_{0.004}$	$0.0485_{0.0003}$	$19.8_{7.0}$
	500	$0.898_{0.005}$	$0.102_{0.001}$	$15.7_{6.6}$
	600	$0.842_{0.003}$	$0.158_{0.001}$	$20.2_{8.1}$
	700	$0.787_{0.008}$	$0.213_{0.003}$	$22.6_{4.0}$
	800	$0.734_{0.007}$	$0.266_{0.003}$	$19.6_{4.1}$
50	298.15	$0.990_{0.003}$	$0.010_{0.001}$	162.3_{59}
	350	$0.974_{0.006}$	$0.026_{0.001}$	44.5_{17}
	400	$0.949_{0.005}$	$0.0510_{0.0004}$	$24.4_{7.1}$
	500	$0.895_{0.004}$	$0.1053_{0.0005}$	$20.2_{5.3}$
	600	$0.838_{0.003}$	$0.162_{0.001}$	28.2_{10}
	700	$0.783_{0.007}$	$0.217_{0.002}$	$27.8_{6.5}$
	800	$0.732_{0.002}$	$0.268_{0.002}$	$27.2_{7.1}$
60	298.15	$0.989_{0.003}$	$0.011_{0.001}$	152.2_{61}
	350	$0.973_{0.003}$	$0.0270_{0.0002}$	54.8_{13}
	400	$0.947_{0.002}$	$0.053_{0.001}$	$31.2_{9.0}$
	500	$0.891_{0.003}$	$0.109_{0.001}$	$25.9_{7.4}$
	600	$0.835_{0.003}$	$0.165_{0.001}$	33.8_{16}
	700	$0.780_{0.004}$	$0.220_{0.001}$	$29.1_{3.6}$
	800	$0.730_{0.004}$	$0.270_{0.002}$	$31.0_{7.1}$

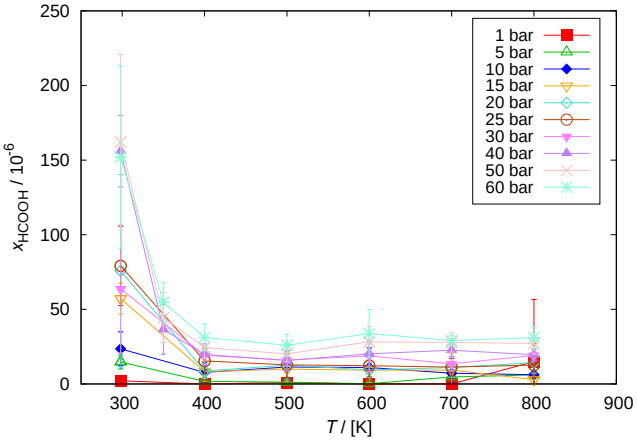

Fig. B.3. HCOOH mole fractions computed from GCMC simulations in UiO-66 framework. The mole fractions of HCOOH computed from the Rx/CFC simulations are used as an input for GCMC ensemble. The simulations were carried out at 298.15 - 800 K and 1 - 60 bar. The mole fractions of HCOOH increase with pressure and decrease with the increasing temperature.

Table B.7: The energy of adsorption at infinite dilution of the guest H_2 molecules (ΔU) inside the host-frameworks UiO-66, Cu-BTC, and IRMOF-1 at 298.15 - 800 K, calculated from Eq. 4.7. The adsorption energy of hydrogen decreases (in absolute value) with increasing temperature. The linear behavior of the heat of adsorption (ΔH) at increasing temperature results from the fact that the increment of RT is larger than the reduction of ΔU. The subscripts show uncertainties computed by the RASPA software package [94, 95].

MOF	T/[K]	ΔU/[kJ mol^{-1}]	ΔH/[kJ mol^{-1}]
UiO-66	298.15	$-4.653_{0.005}$	$-7.132_{0.005}$
	400	$-4.340_{0.007}$	$-7.666_{0.007}$
	600	$-3.87_{0.01}$	$-8.86_{0.01}$
	800	$-3.465_{0.005}$	$-10.117_{0.005}$
Cu-BTC	298.15	$-3.52_{0.01}$	$-6.00_{0.01}$
	400	$-3.12_{0.01}$	$-6.44_{0.01}$
	600	$-2.698_{0.006}$	$-7.687_{0.006}$
	800	$-2.432_{0.009}$	$-9.084_{0.009}$
IRMOF-1	298.15	$-2.176_{0.002}$	$-4.655_{0.002}$
	400	$-1.995_{0.003}$	$-5.321_{0.003}$
	600	$-1.777_{0.005}$	$-6.766_{0.005}$
	800	$-1.625_{0.004}$	$-8.277_{0.004}$

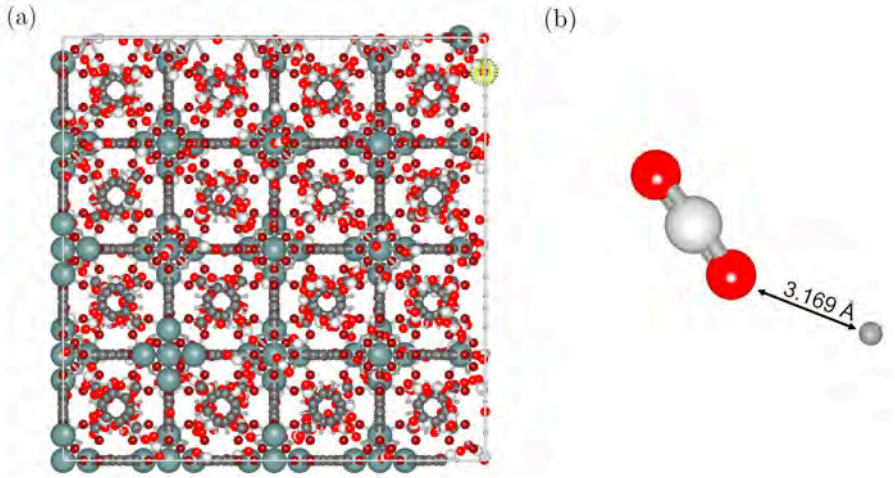

Fig. B.4. Visualization of: (a) CO_2, H_2 and HCOOH molecules adsorbed in the UiO-66 unit cell at $T = 298.15$ K, $P = 60$ bar. The CO_2 molecule interacting with an H atom of the framework is highlighted using a yellow circle, (b) close-up of the CO_2 molecule interacting with the H atom of the UiO-66 framework at $T = 298.15$ K, $P = 60$ bar. The distance between O atom of the CO_2 molecule and the H atom of the framework is 3.169 Å. Hydrogen bond formation between O atom of the CO_2 molecule and the H atom of the framework is possible, as the distance between donor and acceptor atoms is defined in the literature as 2.7 - 3.3 Å [380]. The visualization is created using iRASPA [38].

Table B.8: Mole fractions of CO_2, H_2, and HCOOH obtained from grand-canonical Monte Carlo ensemble simulations in the Cu-BTC framework at 298.15 - 800 K and 1 - 60 bar. The mole fractions of CO_2, H_2, and HCOOH at reaction equilibrium obtained from the Continuous Fractional Component Monte Carlo simulations in the Reaction Ensemble were used in the GCMC simulations as input. The subscripts show uncertainties computed using error propagation rules.

P/[bar]	T/[K]	x_{CO_2}	x_{H_2}	x_{HCOOH} / 10^{-6}
1	298.15	$0.987_{0.010}$	$0.0130_{0.0004}$	$11.4_{9.4}$
	400	$0.937_{0.021}$	$0.063_{0.002}$	$0.3_{0.3}$
	500	$0.862_{0.007}$	$0.138_{0.002}$	$1.2_{1.4}$
	600	$0.788_{0.007}$	$0.212_{0.003}$	0_{0}
	700	$0.727_{0.004}$	$0.273_{0.001}$	0_{0}
	800	$0.680_{0.004}$	$0.320_{0.001}$	0_{0}
5	298.15	$0.989_{0.005}$	$0.0110_{0.0001}$	$122.7_{9.6}$
	400	$0.935_{0.002}$	$0.0655_{0.0005}$	$8.4_{2.3}$
	500	$0.860_{0.004}$	$0.140_{0.001}$	$7.5_{4.7}$
	600	$0.787_{0.003}$	$0.213_{0.001}$	$8.4_{3.5}$
	700	$0.728_{0.003}$	$0.272_{0.001}$	$1.4_{1.9}$
	800	$0.681_{0.002}$	$0.319_{0.002}$	$0.2_{0.4}$
10	298.15	$0.992_{0.001}$	$0.0078_{0.0001}$	343.5_{23}
	400	$0.932_{0.002}$	$0.0675_{0.0004}$	$22.2_{4.8}$
	500	$0.859_{0.002}$	$0.1415_{0.0004}$	$12.9_{3.7}$
	600	$0.786_{0.003}$	$0.214_{0.001}$	$5.3_{2.3}$
	700	$0.727_{0.002}$	$0.273_{0.001}$	$7.3_{3.4}$
	800	$0.681_{0.002}$	$0.319_{0.001}$	$7.1_{2.9}$
15	298.15	$0.992_{0.002}$	$0.0070_{0.0001}$	650.6_{50}
	400	$0.932_{0.004}$	$0.068_{0.001}$	48.8_{15}
	500	$0.858_{0.001}$	$0.142_{0.001}$	$15.6_{5.8}$
	600	$0.786_{0.002}$	$0.2137_{0.0005}$	$9.8_{3.0}$
	700	$0.727_{0.002}$	$0.273_{0.001}$	$8.7_{2.3}$
	800	$0.680_{0.002}$	$0.320_{0.001}$	$5.4_{2.6}$
20	298.15	$0.992_{0.003}$	$0.0070_{0.0001}$	622.5_{34}
	400	$0.932_{0.002}$	$0.0675_{0.0002}$	$47.6_{4.7}$
	500	$0.857_{0.001}$	$0.1432_{0.0004}$	$21.3_{2.1}$
	600	$0.785_{0.003}$	$0.215_{0.001}$	$14.6_{7.0}$
	700	$0.727_{0.001}$	$0.2734_{0.0002}$	$11.9_{3.1}$
	800	$0.680_{0.002}$	$0.320_{0.001}$	$10.5_{1.6}$
25	298.15	$0.992_{0.003}$	$0.0070_{0.0001}$	885.0_{210}
	400	$0.933_{0.004}$	$0.0668_{0.0004}$	$50.0_{7.0}$
	500	$0.856_{0.002}$	$0.1444_{0.0005}$	$22.1_{4.5}$

	600	$0.785_{0.001}$	$0.215_{0.001}$	$18.5_{1.6}$
	700	$0.726_{0.001}$	$0.274_{0.001}$	$16.4_{2.4}$
	800	$0.680_{0.001}$	$0.320_{0.001}$	$12.4_{1.2}$
30	298.15	$0.992_{0.001}$	$0.00723_{0.00004}$	801.2_{78}
	400	$0.934_{0.004}$	$0.0663_{0.0003}$	62.7_{13}
	500	$0.855_{0.002}$	$0.1449_{0.0003}$	$28.0_{2.8}$
	600	$0.784_{0.002}$	$0.216_{0.001}$	$20.4_{3.0}$
	700	$0.726_{0.002}$	$0.274_{0.001}$	$18.1_{2.4}$
	800	$0.680_{0.001}$	$0.320_{0.001}$	$12.9_{2.7}$
40	298.15	$0.991_{0.001}$	$0.0079_{0.0001}$	1343.2_{89}
	350	$0.972_{0.001}$	$0.0275_{0.0001}$	$290.4_{6.4}$
	400	$0.935_{0.002}$	$0.0650_{0.0004}$	95.5_{14}
	500	$0.854_{0.002}$	$0.1457_{0.0005}$	$44.8_{4.7}$
	600	$0.783_{0.001}$	$0.2168_{0.0005}$	$22.9_{2.7}$
	700	$0.725_{0.001}$	$0.2747_{0.0004}$	$21.9_{1.1}$
	800	$0.680_{0.002}$	$0.320_{0.001}$	$18.4_{1.4}$
50	298.15	$0.990_{0.001}$	$0.0086_{0.0001}$	1623.7_{89}
	350	$0.972_{0.001}$	$0.0277_{0.0004}$	331.8_{32}
	400	$0.936_{0.002}$	$0.0643_{0.0002}$	$119.5_{6.4}$
	500	$0.854_{0.001}$	$0.1463_{0.0002}$	$48.5_{3.9}$
	600	$0.782_{0.003}$	$0.218_{0.001}$	$34.1_{5.3}$
	700	$0.724_{0.002}$	$0.2758_{0.0005}$	$27.7_{1.8}$
	800	$0.679_{0.001}$	$0.3211_{0.0004}$	$24.1_{2.4}$
60	298.15	$0.989_{0.001}$	$0.0092_{0.0003}$	1569.2_{51}
	350	$0.972_{0.001}$	$0.0279_{0.0002}$	389.1_{22}
	400	$0.936_{0.002}$	$0.0640_{0.0002}$	$145.2_{6.6}$
	500	$0.853_{0.002}$	$0.1470_{0.0003}$	$55.2_{3.5}$
	600	$0.781_{0.002}$	$0.2190_{0.0004}$	$36.9_{3.5}$
	700	$0.723_{0.001}$	$0.2767_{0.0003}$	$32.8_{4.9}$
	800	$0.678_{0.001}$	$0.322_{0.001}$	$29.4_{1.5}$

Table B.9: Mole fractions of CO_2, H_2, and HCOOH obtained from grand-canonical Monte Carlo ensemble simulations in the IRMOF-1 framework at 298.15 - 800 K and 1 - 60 bar. The mole fractions of CO_2, H_2, and HCOOH at reaction equilibrium obtained from the Continuous Fractional Component Monte Carlo simulations in the Reaction Ensemble were used in the GCMC simulations as input. The subscripts show uncertainties computed using error propagation rules.

P/[bar]	T/[K]	x_{CO_2}	x_{H_2}	x_{HCOOH} / 10^{-6}
1	298.15	$0.925_{0.006}$	$0.0746_{0.0004}$	$0.1_{0.1}$
	400	$0.823_{0.001}$	$0.177_{0.001}$	0_{0}
	500	$0.743_{0.004}$	$0.257_{0.002}$	0_{0}
	600	$0.688_{0.004}$	$0.312_{0.002}$	0_{0}
	700	$0.648_{0.004}$	$0.352_{0.003}$	0_{0}
	800	$0.618_{0.002}$	$0.382_{0.002}$	0_{0}
5	298.15	$0.932_{0.002}$	$0.0680_{0.0005}$	$3.7_{4.1}$
	400	$0.825_{0.003}$	$0.175_{0.001}$	$1.9_{2.5}$
	500	$0.744_{0.003}$	$0.256_{0.001}$	$1.2_{1.3}$
	600	$0.688_{0.001}$	$0.312_{0.001}$	$1.5_{1.9}$
	700	$0.647_{0.002}$	$0.353_{0.001}$	$0.9_{1.3}$
	800	$0.617_{0.002}$	$0.383_{0.002}$	$0.9_{1.8}$
10	298.15	$0.942_{0.003}$	$0.0577_{0.0005}$	$4.8_{2.1}$
	400	$0.827_{0.003}$	$0.1734_{0.0005}$	$1.9_{1.4}$
	500	$0.745_{0.002}$	$0.255_{0.001}$	$2.8_{1.3}$
	600	$0.688_{0.002}$	$0.312_{0.001}$	$3.5_{1.4}$
	700	$0.647_{0.001}$	$0.353_{0.001}$	$2.1_{1.9}$
	800	$0.617_{0.002}$	$0.383_{0.001}$	$3.5_{1.8}$
15	298.15	$0.954_{0.002}$	$0.0460_{0.0003}$	$10.2_{2.8}$
	400	$0.828_{0.002}$	$0.1716_{0.0004}$	$3.1_{0.7}$
	500	$0.745_{0.002}$	$0.255_{0.001}$	$4.0_{0.8}$
	600	$0.688_{0.001}$	$0.312_{0.001}$	$4.3_{1.1}$
	700	$0.647_{0.001}$	$0.353_{0.001}$	$4.2_{2.4}$
	800	$0.617_{0.002}$	$0.383_{0.001}$	$5.1_{1.4}$
20	298.15	$0.965_{0.004}$	$0.0354_{0.0002}$	$11.2_{2.9}$
	400	$0.830_{0.002}$	$0.170_{0.001}$	$4.6_{1.2}$
	500	$0.745_{0.002}$	$0.255_{0.001}$	$3.6_{1.1}$
	600	$0.687_{0.002}$	$0.313_{0.001}$	$5.0_{1.7}$
	700	$0.646_{0.002}$	$0.354_{0.001}$	$6.8_{1.2}$
	800	$0.616_{0.001}$	$0.384_{0.001}$	$6.0_{1.1}$
25	298.15	$0.972_{0.003}$	$0.0285_{0.0001}$	$21.6_{7.3}$
	400	$0.831_{0.002}$	$0.1690_{0.0004}$	$5.4_{1.3}$
	500	$0.746_{0.001}$	$0.2544_{0.0005}$	$6.3_{1.7}$

	600	$0.687_{0.001}$	$0.313_{0.001}$	$7.8_{1.5}$
	700	$0.646_{0.001}$	$0.354_{0.001}$	$8.2_{2.4}$
	800	$0.617_{0.001}$	$0.3834_{0.0005}$	$6.9_{1.8}$
30	298.15	$0.975_{0.001}$	$0.0248_{0.0001}$	$23.5_{8.0}$
	400	$0.833_{0.003}$	$0.167_{0.001}$	$7.0_{1.2}$
	500	$0.746_{0.002}$	$0.254_{0.001}$	$9.2_{1.4}$
	600	$0.687_{0.001}$	$0.3127_{0.0004}$	$7.8_{0.6}$
	700	$0.647_{0.001}$	$0.353_{0.001}$	$7.1_{2.7}$
	800	$0.617_{0.001}$	$0.383_{0.001}$	$9.0_{2.9}$
40	298.15	$0.978_{0.001}$	$0.0224_{0.0002}$	47.9_{12}
	350	$0.902_{0.001}$	$0.0976_{0.0002}$	$12.4_{2.3}$
	400	$0.836_{0.001}$	$0.1639_{0.0003}$	$10.7_{3.0}$
	500	$0.746_{0.001}$	$0.254_{0.001}$	$8.9_{1.2}$
	600	$0.687_{0.001}$	$0.313_{0.001}$	$10.0_{2.1}$
	700	$0.646_{0.001}$	$0.354_{0.001}$	$12.1_{1.7}$
	800	$0.616_{0.001}$	$0.384_{0.001}$	$11.6_{2.9}$
50	298.15	$0.978_{0.001}$	$0.0217_{0.0001}$	64.8_{21}
	350	$0.908_{0.001}$	$0.0918_{0.0003}$	$16.3_{2.6}$
	400	$0.839_{0.001}$	$0.1614_{0.0004}$	$12.5_{1.8}$
	500	$0.746_{0.002}$	$0.254_{0.001}$	$11.6_{1.8}$
	600	$0.687_{0.001}$	$0.313_{0.001}$	$14.0_{1.5}$
	700	$0.646_{0.001}$	$0.354_{0.001}$	$15.3_{2.2}$
	800	$0.616_{0.001}$	$0.384_{0.001}$	$15.1_{1.9}$
60	298.15	$0.978_{0.001}$	$0.0221_{0.0002}$	$57.5_{7.7}$
	350	$0.913_{0.002}$	$0.0871_{0.0003}$	$19.3_{3.0}$
	400	$0.842_{0.001}$	$0.1585_{0.0003}$	$15.8_{2.9}$
	500	$0.746_{0.001}$	$0.2538_{0.0003}$	$15.0_{1.7}$
	600	$0.686_{0.001}$	$0.314_{0.001}$	$16.5_{2.7}$
	700	$0.645_{0.002}$	$0.355_{0.001}$	$15.0_{1.0}$
	800	$0.615_{0.001}$	$0.385_{0.001}$	$20.1_{3.3}$

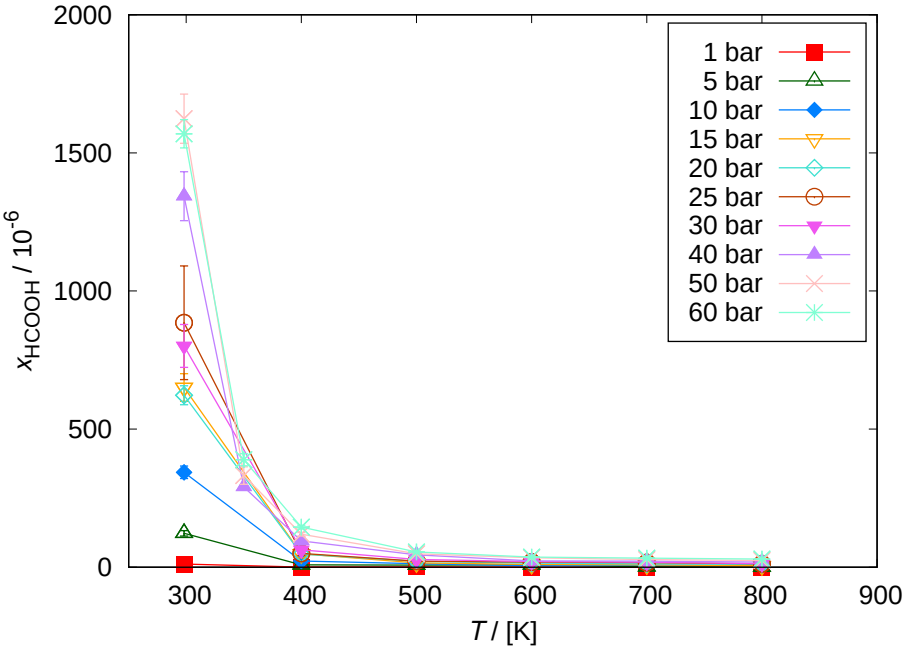

Fig. B.5. HCOOH mole fractions computed from GCMC simulations in Cu-BTC framework. The mole fractions of HCOOH computed from the Rx/CFC simulations are used as an input for GCMC ensemble. The simulations were carried out at 298.15 - 800 K and 1 - 60 bar. The mole fractions of HCOOH increase with pressure and decrease with the increasing temperature.

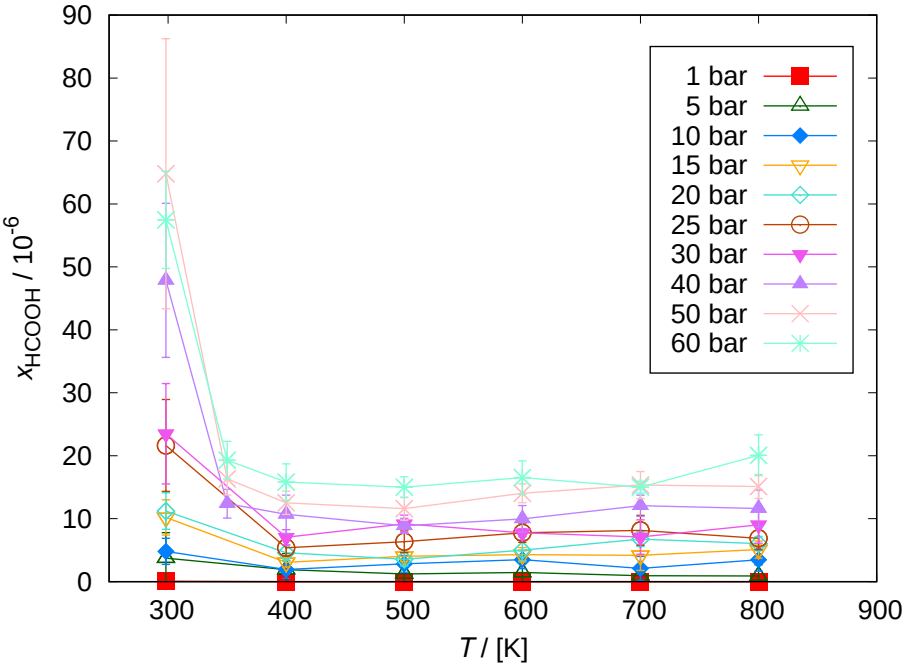

Fig. B.6. HCOOH mole fractions computed from GCMC simulations in IRMOF-1 framework. The mole fractions of HCOOH computed from the Rx/CFC simulations are used as an input for GCMC ensemble. The simulations were carried out at 298.15 - 800 K and 1 - 60 bar. The mole fractions of HCOOH increase with pressure and decrease with the increasing temperature.

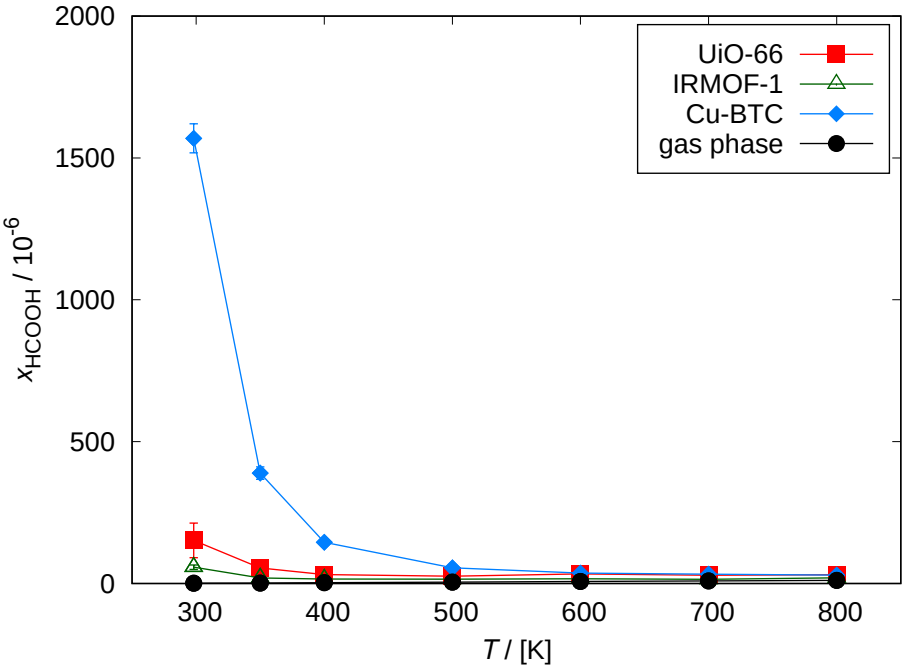

Fig. B.7. HCOOH mole fractions computed from the Rx/CFC simulations in the gas phase compared to the HCOOH mole fractions computed from GCMC simulations in UiO-66, Cu-BTC and IRMOF-1 at 298.15 - 800 K and 60 bar. The mole fractions of HCOOH computed from the Rx/CFC simulations are used as an input for GCMC ensemble. The mole fractions of HCOOH decrease with the increasing temperature. The highest HCOOH production resulted from the effect of the Cu-BTC confinement at the lowest temperature (298.15 K) with the mole fraction equal to 0.0016.

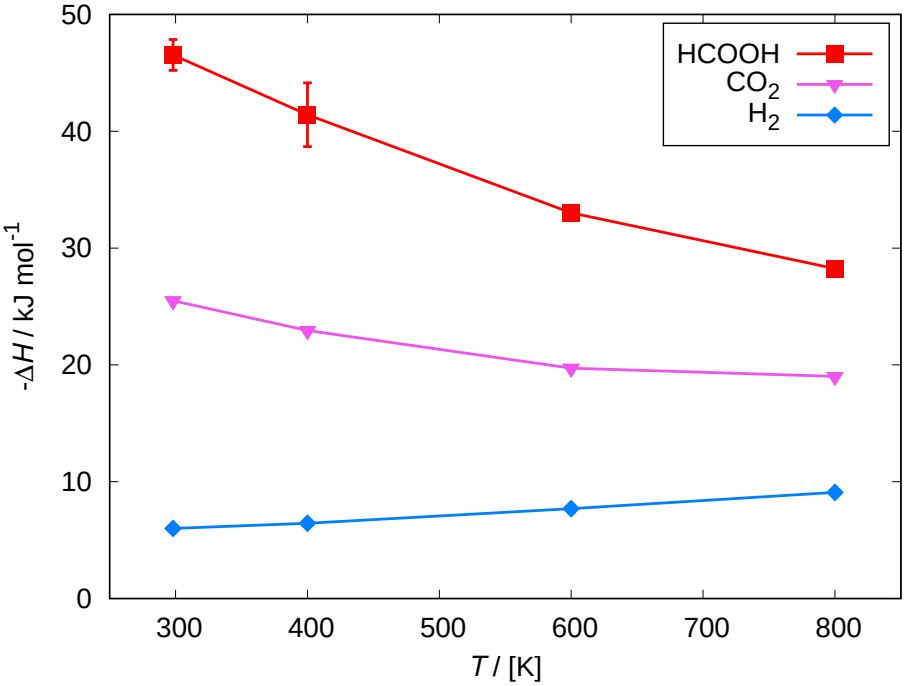

Fig. B.8. Isosteric heat of adsorption of CO_2, H_2 and HCOOH at 298.15 - 800 K in Cu-BTC. The isosteric heat of adsorption of HCOOH decreases with increasing temperature. The energy state of HCOOH on the adsorbent surface increases, leading to weaker interactions between the framework and adsorbate. The increase of temperature causes the decrease in the enthalpy of adsorption of CO_2. The opposite effect is for H_2, which enthalpy of adsorption increases with temperature. The error bars are smaller than the size of the symbols.

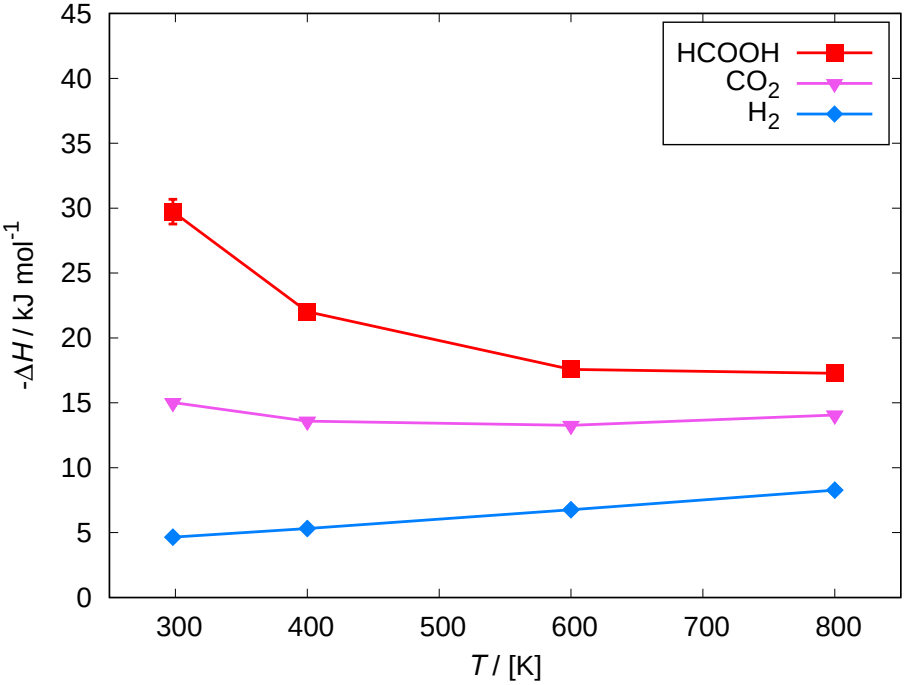

Fig. B.9. Isosteric heat of adsorption of CO_2, H_2 and HCOOH at 298.15 - 800 K in IRMOF-1. The isosteric heat of adsorption of HCOOH decreases with increasing temperature. The energy state of HCOOH on the adsorbent surface increases, leading to weaker interactions between the framework and adsorbate. The increase of temperature causes the decrease in the enthalpy of adsorption of CO_2 in the temperature range from 298.15 to 600 K. The enthalpy of adsorption of CO_2 increases with temperature in the range from 600 to 800 K. The enthalpy of adsorption of H_2 increases with temperature. The error bars are smaller than the size of the symbols.

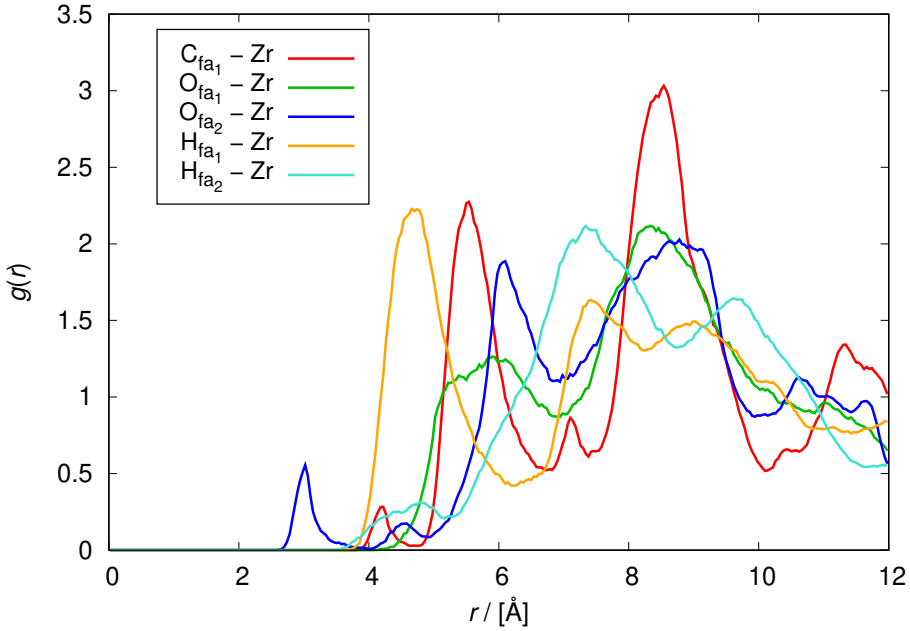

Fig. B.10. Radial distribution functions for HCOOH and the zirconium metal center in UiO-66 at 298.15 K. The preferential orientation of HCOOH molecule with respect to the metal center is by a double bonded O_{fa2} atom, within a distance of 3 Å. The simulation was performed using the RASPA software package [94, 95].

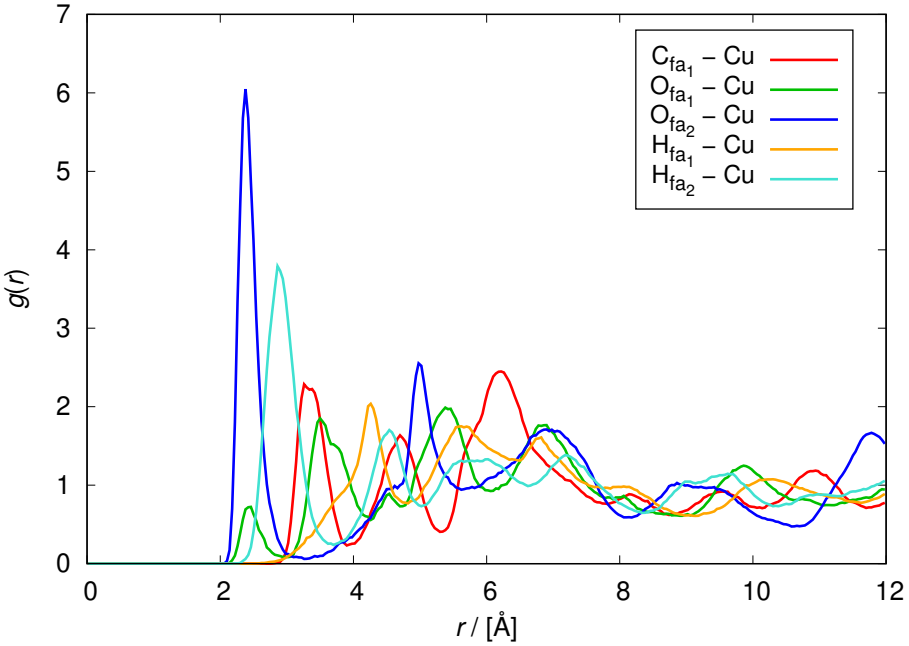

Fig. B.11. Radial distribution functions for HCOOH and the copper metal center in Cu-BTC at 298.15 K. The preferential orientation of HCOOH molecule with respect to the metal center is by a double bonded O_{fa2} atom, within a distance of 2.4 Å. The simulation was performed using the RASPA software package [94, 95].

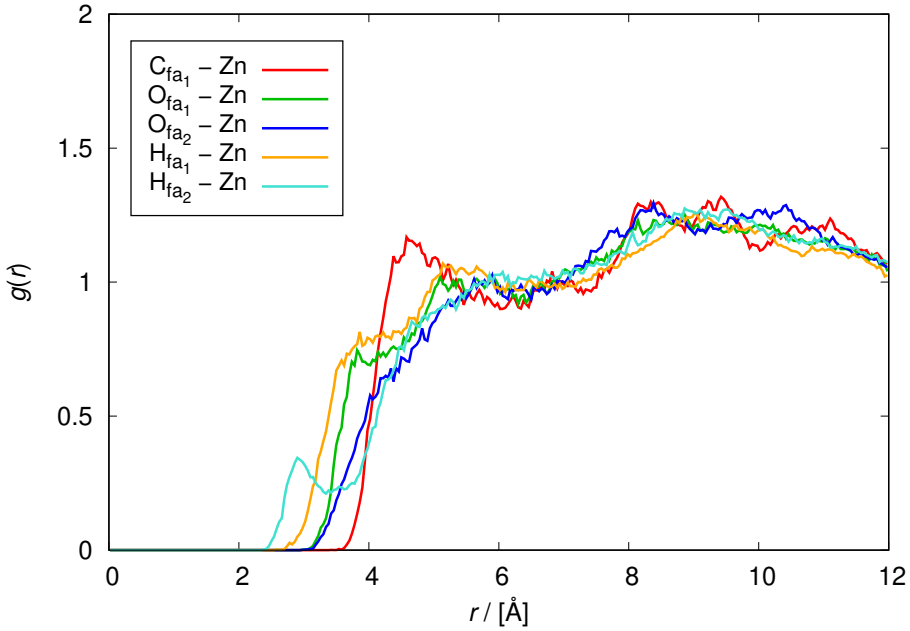

Fig. B.12. Radial distribution functions for HCOOH and the zinc metal center in IRMOF-1 at 298.15 K. The preferential orientation of HCOOH molecule with respect to the metal center is by an oxygen-bonded H_{fa2} atom, within a distance of 2.9 Å. The simulation was performed using the RASPA software package [94, 95].

Appendix C

Appendix C corresponds to Chapter 5 of this thesis.

- Cell parameters for M-MOF-74 (M = Ni, Cu, Co, Fe, Mn, Zn);
- Lennard-Jones and Coulombic interaction potentials for CO_2, H_2 and M-MOF-74 frameworks;
- Parameters of the dual-site Langmuir-Freundlich model for CO_2 and H_2, obtained from RUPTURA;
- Adsorption isotherms of H_2 in M-MOF-74 (M = Ni, Cu, Co, Fe, Mn, Zn), and the corresponding enthalpy of adsorption obtained from grand-canonical Monte Carlo simulations at 77 K and 10^{-5} - 10^{2} kPa;
- Henry coefficients computed from the adjusted force field using Widom's test particle insertions at 77 K, compared to the coefficients calculated from the slope of experimental isotherms in the linear region at low pressures;
- Adsorption isotherms of H_2 in M-MOF-74 (M = Ni, Cu, Co, Fe, Mn, Zn) obtained from grand-canonical Monte Carlo simulations at 87 K and 10^{-5} - 10^{2} kPa;
- Distribution of the CO_2, and H_2 molecules inside M-MOF-74 (M = Co, Fe, Mn, Zn) analyzed using density profiles from grand-canonical Monte Carlo simulations at 298 K, 100 kPa;
- Comparison of breakthrough curves of CO_2/H_2 mixtures at y_{CO_2} = 0.1, 0.2, 0.3, 0.4, 0.5, 0.9 for M-MOF-74, where M = Co, Fe, Mn, Zn;
- Comparison of breakthrough curves of CO_2/H_2 mixtures in M-MOF-74 (M = Ni, Cu, Co, Fe, Mn, Zn) for y_{CO_2} = 0.1, 0.9;
- Prediction of adsorption of CO_2/H_2 mixtures at y_{CO_2} = 0.5 in M-MOF-74 (M = Ni, Cu, Co, Fe, Mn, Zn) using Ideal Adsorption Solution Theory;
- Detailed information on the M-MOF-74 (M = Ni, Cu, Co, Fe, Mn, Zn) structures in the form of cif files.

Table C.1: Cell parameters for M-MOF-74 (M = Ni, Cu, Co, Fe, Mn, Zn) obtained from experimental synthesis [113–118].

MOF-74	a/[Å]	b/[Å]	c/[Å]	α/[°]	β/[°]	γ/[°]	V/[Å^3]
Ni	25.7856	25.7856	6.7701	90	90	120	15593.4
Cu	25.9972	25.9972	6.2587	90	90	120	14653
Co	25.885	25.885	6.8058	90	90	120	15796.7
Fe	26.1627	26.1627	6.8422	90	90	120	16223.8
Mn	25.7824	25.7824	6.9126	90	90	120	15917.6
Zn	25.9322	25.9322	6.8365	90	90	120	15925.9

Table C.2: Lennard-Jones and Coulombic interaction potentials for M-MOF-74 (M = Ni, Cu, Co, Fe, Mn, Zn) frameworks [147, 148], CO_2 [176, 284], and H_2 [243]. It is important to note that there is an exception/override to the use of the Lorentz-Berthelot mixing rules [129] for H_{com}–Me interactions. The listed charges for M-MOF-74 atoms were obtained by scaling initial charges computed using the 'charge-equilibration' method of Wilmer and Snurr [247, 285] by a factor within the range of 0.5 - 1.5. The set of charges leading to the closest results to the experimental uptakes and the enthalpies of CO_2 adsorption [122] was selected for further study as a part of the final force field. All the frameworks and molecules are charge-neutral. The schematic representation of M-MOF-74 series with the atoms labelled is visualized in Figure 5.1 of Chapter 5. The charges for Co- and Fe-MOF-74 for CO_2 adsorption have been previously published by Luna-Triguero et al. [295]

Atom	ϵ/k_B /[K]	σ /[Å]	q /[e$^-$]
O_{CO_2}	85.671	3.017	-0.3256
C_{CO_2}	29.93	2.742	0.6512
H_{com}	36.7	2.958	-0.936
H_{H_2}	0	0	0.468
Ni-MOF-74			
Ni	7.556	2.525	1.55
C1	47.86	3.473	0.603
C2	47.86	3.473	-0.275
C3	47.86	3.473	0.275
C4	47.86	3.473	-0.086
O1	48.19	3.0331	-0.63
O2	48.19	3.0331	-0.815
O3	48.19	3.0331	-0.702
H	7.65	2.8464	0.08

	Cu-MOF-74		
Cu	2.518	3.114	0.834
C1	47.86	3.473	-0.076
C2	47.86	3.473	0.345
C3	47.86	3.473	0.156
C4	47.86	3.473	-0.139
O1	48.19	3.0331	-0.394
O2	48.19	3.0331	-0.431
O3	48.19	3.0331	-0.368
H	7.65	2.8464	0.073
	Co-MOF-74		
Co	7.052	2.559	1.335
C1	47.86	3.473	0.485
C2	47.86	3.473	-0.207
C3	47.86	3.473	0.245
C4	47.86	3.473	-0.125
O1	48.19	3.0331	-0.544
O2	48.19	3.0331	-0.611
O3	48.19	3.0331	-0.673
H	7.65	2.8464	0.095
	Fe-MOF-74		
Fe	6.542	2.594	1.226
C1	47.86	3.473	0.356
C2	47.86	3.473	-0.148
C3	47.86	3.473	0.175
C4	47.86	3.473	-0.088
O1	48.19	3.0331	-0.602
O2	48.19	3.0331	-0.439
O3	48.19	3.0331	-0.561
H	7.65	2.8464	0.081
	Mn-MOF-74		
Mn	6.549	2.638	1.161
C1	47.86	3.473	0.368
C2	47.86	3.473	-0.175
C3	47.86	3.473	0.175
C4	47.86	3.473	-0.064
O1	48.19	3.0331	-0.548
O2	48.19	3.0331	-0.443
O3	48.19	3.0331	-0.522

H	7.65	2.8464	0.048
	Zn-MOF-74		
Zn	62.3992	2.461	1.006
C1	47.86	3.473	0.343
C2	47.86	3.473	-0.155
C3	47.86	3.473	0.161
C4	47.86	3.473	-0.083
O1	48.19	3.0331	-0.479
O2	48.19	3.0331	-0.393
O3	48.19	3.0331	-0.464
H	7.65	2.8464	0.064
	overrides		
H_{com} - Ni	216.4823	2.1932	
H_{com} - Cu	11.5357	3.036	
H_{com} - Co	17.6963	2.2068	
H_{com} - Fe	18.5939	2.776	
H_{com} - Mn	13.9529	2.798	
H_{com} - Zn	43.069	2.7095	

Table C.3: Parameters of the dual-site Langmuir-Freundlich model [292] obtained from fitting on adsorption isotherms data of pure CO_2 and H_2 in M-MOF-74 (M = Ni, Cu, Co, Fe, Mn, Zn) frameworks, computed using the RASPA software package [94, 95]. The fitting was performed by RUPTURA [291] and the resulted model parameters were used as an input for breakthrough simulations. The functional form of the dual-site Langmuir-Freundlich isotherm model [292] is expressed as:

$$q(p) = \sum_i q_i^{\text{sat}} \frac{b_i (\frac{p_i}{p_0})^{v_i}}{1 + b_i (\frac{p_i}{p_0})^{v_i}} \tag{C.1}$$

where $q(p)$ is absolute loading of the adsorbed phase as a function of pressure, q_i^{sat} is saturation loading, b_i is the coefficient of adsorption representing the affinity of the molecule, v_i is heterogeneity factor, p_i is the partial pressure in the gas phase in units of Pa, p_0 is the reference pressure equal to 1 Pa, and i refers to component i.

MOF-74	adsorbate	q_1^{sat} [mol (kg framework)$^{-1}$]	b_1 [-]	v_1 [-]	q_2^{sat} [mol (kg framework)$^{-1}$]	b_2 [-]	v_2 [-]
Ni	CO_2	12.0936	0.228134	0.0938348	7.10943	$2.13 \cdot 10^{-5}$	0.891086
	H_2	2	$1.36 \cdot 10^{-12}$	1.76051	1.99999	$7.58 \cdot 10^{-8}$	1.09375
Cu	CO_2	8.04687	0.00780695	0.336492	5.46875	$2.41 \cdot 10^{-10}$	1.79974
	H_2	2.19767	$2.18 \cdot 10^{-11}$	1.60905	1.57042	0.000166379	0.475571
Co	CO_2	4.3995	0.0557628	0.321359	9.41687	$9.63 \cdot 10^{-5}$	0.783058
	H_2	1.94147	$1.58 \cdot 10^{-8}$	1.17914	1.79365	$3.30 \cdot 10^{-10}$	1.39858
Fe	CO_2	15.4219	0.0043923	0.468742	0.124994	$4.34 \cdot 10^{-10}$	1.73161
	H_2	2	$4.48 \cdot 10^{-10}$	1.39075	1.12567	$2.94 \cdot 10^{-10}$	1.49625
Mn	CO_2	11.75	0.0031686	0.524252	2.12503	$3.54 \cdot 10^{-10}$	1.72654
	H_2	2	$5.80 \cdot 10^{-11}$	1.54346	1.5	$4.59 \cdot 10^{-7}$	0.941039
Zn	CO_2	5.82052	$1.06 \cdot 10^{-5}$	0.939475	6.65485	0.00131705	0.628489
	H_2	1.31477	$4.17 \cdot 10^{-10}$	1.47217	1.96875	$2.56 \cdot 10^{-10}$	1.40625

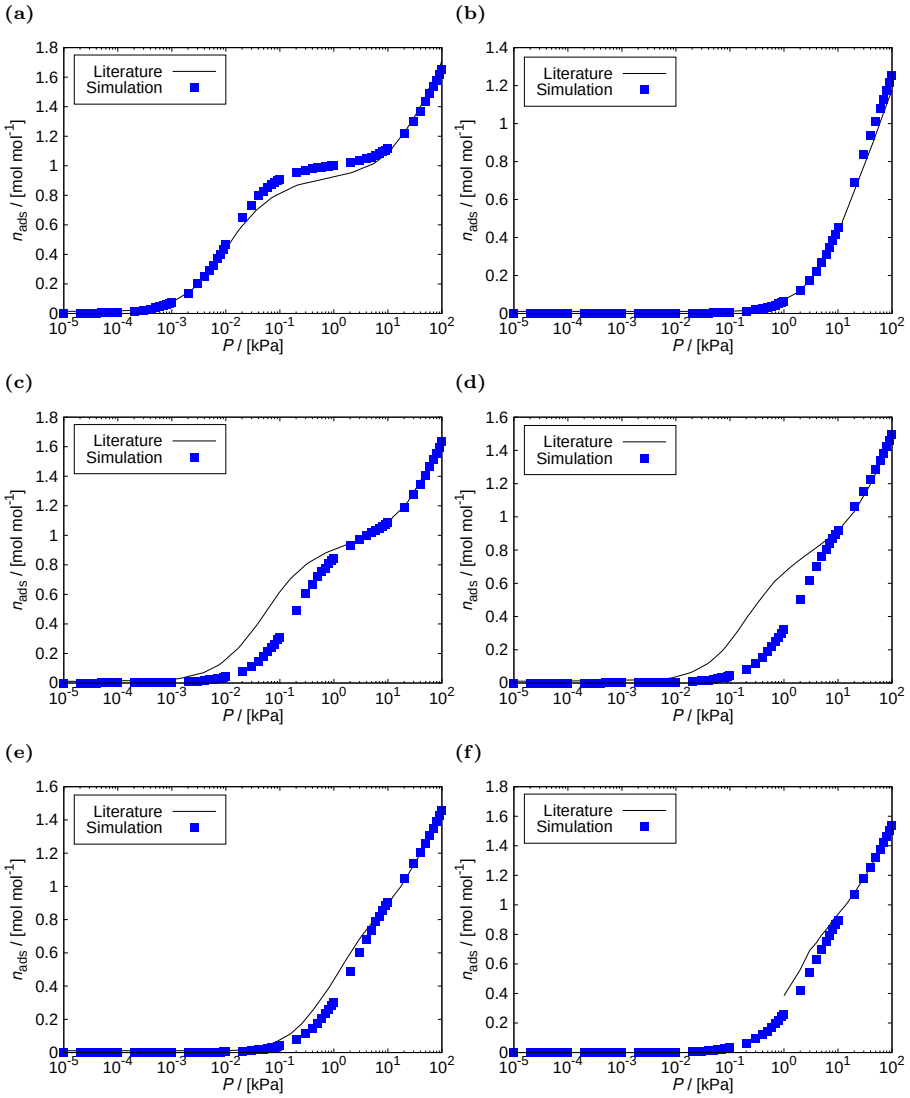

Fig. C.1. Adsorption isotherms of H_2 computed from GCMC simulations using the RASPA software package [94, 95] at 77 K, and 10^{-5} - 10^{2} kPa in: (a) Ni-MOF-74, (b) Cu-MOF-74, (c) Co-MOF-74, (d) Fe-MOF-74, (e) Mn-MOF-74, and (f) Zn-MOF-74. The adsorption results computed from the adjusted force field are represented by blue data points, and the experimental data from literature [271] by solid black lines. The error bars are smaller than the size of the symbols. The force field agrees well with the experimental values, exhibiting considerable deviation only for Fe-MOF-74 at low pressure range.

Table C.4: Henry coefficients for adsorption of H_2 in M-MOF-74 (M = Co, Fe, Mn, Zn) computed from the adjusted force field using Widom's test particle insertions [128] at 77 K, and calculated from the slope of experimental isotherms [271] in the linear region at low pressures by [286]:

$$q = K_{\mathrm{H}} \cdot P \tag{C.2}$$

where q is the adsorption loading of H_2 in M-MOF-74, K_{H} is the Henry coefficient, and P is the pressure. The experimental adsorption data for Zn-MOF-74 is not available at the Henry regime. The Henry coefficients for Cu-MOF-74 and Ni-MOF-74 were computed with high accuracy, showing deviations of only 1% and 8%, respectively, when compared to coefficients calculated from experimental adsorption data. The highest deviation of 84% from the experimental Henry coefficient is observed for Fe-MOF-74. This is clearly reflected in the disparity of the simulated isotherm shape to the experimental data, particularly in the low-pressure region, as illustrated in Fig. C.1d.

MOF-74	$K_{\mathrm{H,sim}}$ [mol kg^{-1} Pa^{-1}]	$K_{\mathrm{H,exp}}$ [mol kg^{-1} Pa^{-1}]
Ni	$0.50_{0.03}$	0.46
Cu	$0.000403_{3\cdot10^{-6}}$	0.0004
Co	$0.03_{0.01}$	0.0205
Fe	$0.0029_{2\cdot10^{-4}}$	0.0183
Mn	$0.00275_{9\cdot10^{-5}}$	0.0043
Zn	$0.00200_{4\cdot10^{-5}}$	-

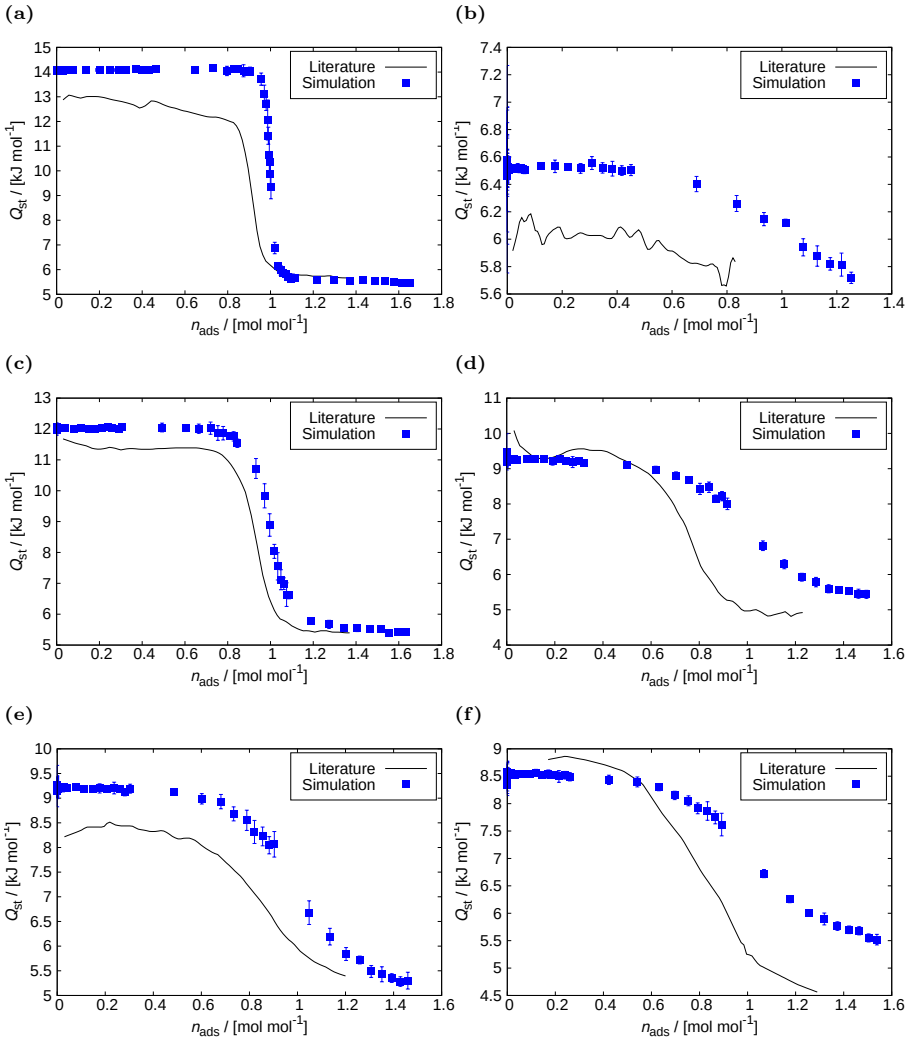

Fig. C.2. Heat of adsorption of H_2 computed from GCMC simulations using the RASPA software package [94, 95] at 77 K, and 10^{-5} - 10^{2} kPa in: (a) Ni-MOF-74, (b) Cu-MOF-74, (c) Co-MOF-74, (d) Fe-MOF-74, (e) Mn-MOF-74, and (f) Zn-MOF-74. The heat of adsorption results computed from the adjusted force field are represented by blue data points, and the experimental data from literature [271] by solid black lines. The force field agrees well with the experimental values, with a slight shift towards a higher uptake observed for Fe-MOF-74.

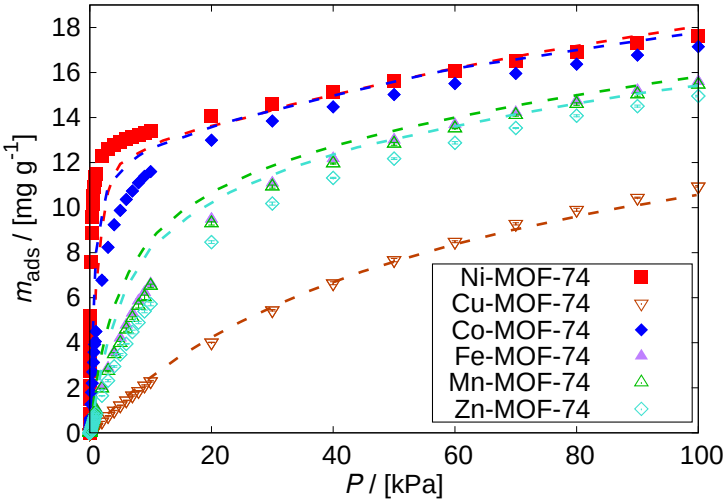

Fig. C.3. Adsorption isotherms of H_2 computed from GCMC simulations using the RASPA software package [94, 95] at 87 K, and 10^{-5} - 10^{2} kPa in M-MOF-74 (M = Ni, Cu, Co, Fe, Mn, Zn). The adsorption results computed from the adjusted force field are represented by data points, and the experimental data [121, 269, 271] by dashed lines with corresponding colors. The error bars are smaller than the size of the symbols. The simulations reproduce the experimental values, showing the temperature transferability of the force field from 77 K to 87 K.

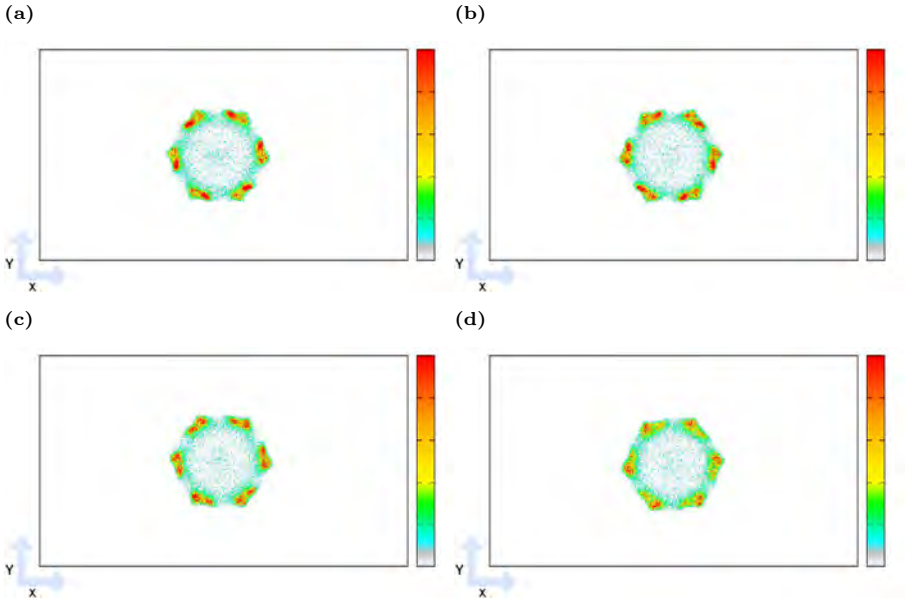

Fig. C.4. The distribution of the CO_2 molecules analyzed using density profiles from GCMC simulations at 298 K, 100 kPa in: (a) Co-MOF-74, (b) Fe-MOF-74, (c) Mn-MOF-74, (d) Zn-MOF-74. The center of mass of the molecules that are adsorbed was projected onto the XY plane. The color gradation of the scales relates to the most and least populated regions of the structure, which is relative in each case. The color scale is shown as a reference of the loading. The preferential sites of CO_2 (colored red) in all M-MOF-74 are at the open-metal centers.

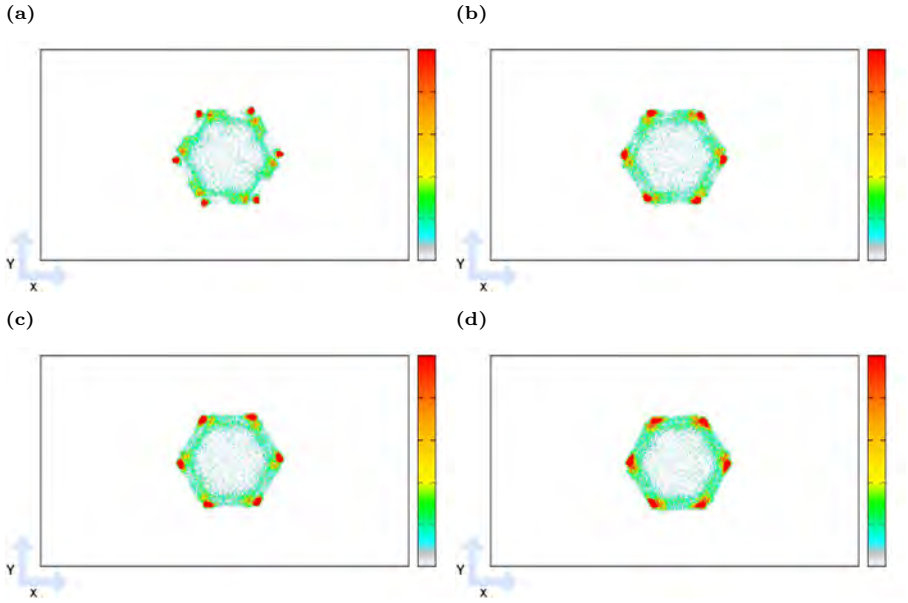

Fig. C.5. The distribution of the H_2 molecules analyzed using density profiles from GCMC simulations at 77 K, 100 kPa in: (a) Co-MOF-74, (b) Fe-MOF-74, (c) Mn-MOF-74, (d) Zn-MOF-74. The center of mass of the molecules that are adsorbed was projected onto the XY plane. The color gradation of the scales relates to the most and least populated regions of the structure, which is relative in each case. The color scale is shown as a reference of the molecules loading. The preferential sites of H_2 (colored red) in all M-MOF-74 are at the open-metal centers.

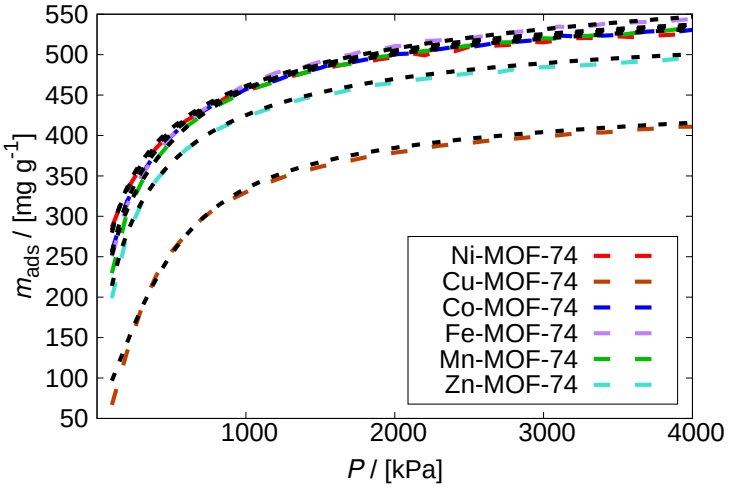

Fig. C.6. The prediction of CO_2/H_2 gas mixture adsorption using IAST [294] obtained from RUPTURA [291] for $y_{CO_2} = 0.5$ in M-MOF-74 (M = Ni, Cu, Co, Fe, Mn, Zn) at 298.15 K, and 100 - 4000 kPa, compared to the GCMC simulations from RASPA [94, 95]. The adsorption loading for CO_2 computed from GCMC simulations of the binary mixture is represented by data points, and the IAST prediction by black, dashed lines. The loading for H_2 was omitted as it is lower than 1 mg g^{-1} of H_2 in all the M-MOF-74 frameworks. The results obtained from IAST mixture prediction using RUPTURA agree well with the multicomponent GCMC simulations, meaning that the validation of the breakthrough curves was successful.

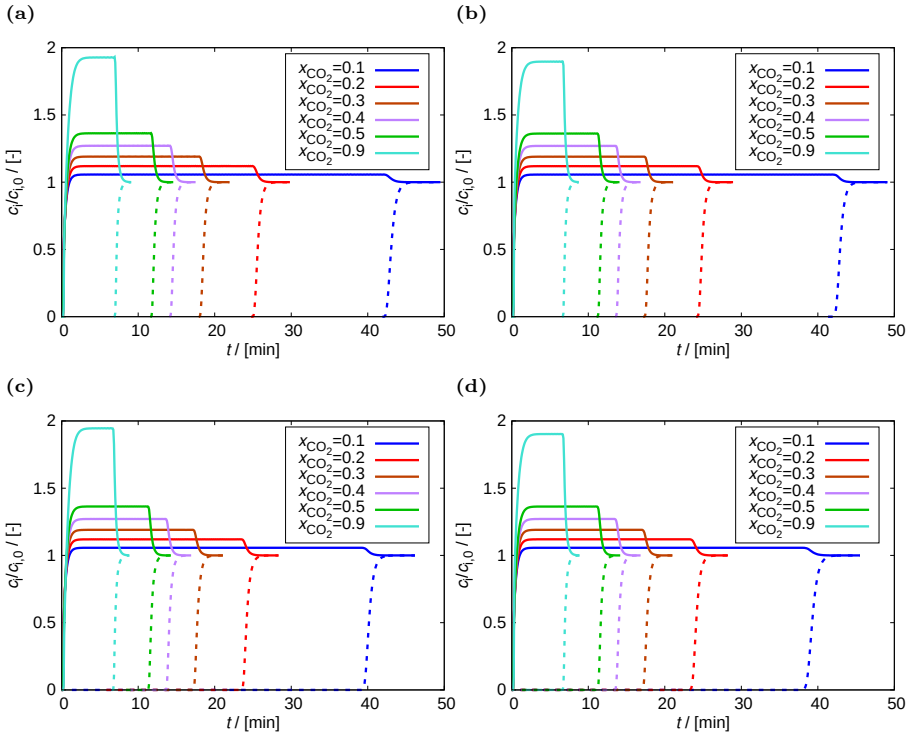

Fig. C.7. Breakthrough curves computed from RUPTURA [291] for the separation of CO_2/H_2 mixtures in fixed-bed adsorbers at CO_2 feed mole fractions of y_{CO_2} = 0.1, 0.2, 0.3, 0.4, 0.5, 0.9, using: (a) Co-MOF-74, (b) Fe-MOF-74, (c) Mn-MOF-74, (d) Zn-MOF-74. The breakthrough curves of CO_2 are represented by dashed lines, and the breakthrough curves of H_2 by solid lines. The initial conditions are specified as: temperature T=298 K, total pressure p_T = 2.5 MPa, packed bed void fraction ε_B = 0.4, interstitial gas velocity entering the packed bed v = 0.006791 m s^{-1}, length of packed bed adsorber L = 0.065 m, axial dispersion is neglected, and isothermal conditions are assumed.

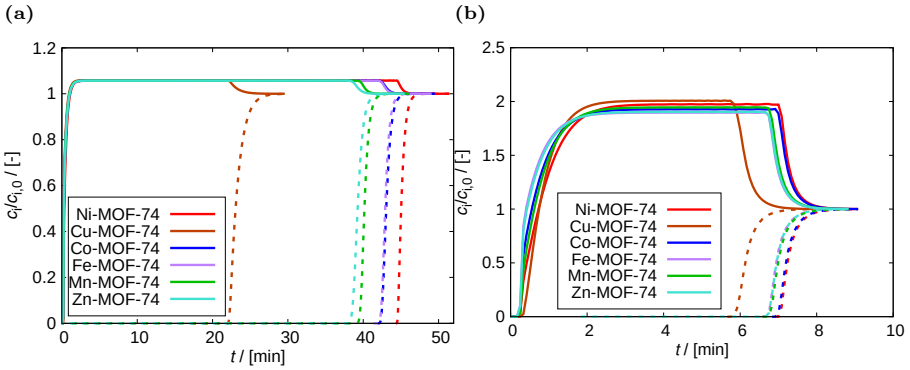

Fig. C.8. Breakthrough curves computed from RUPTURA [291] for the separation of CO_2/H_2 mixtures in fixed-bed adsorbers using M-MOF-74 (M = Ni, Cu, Co, Fe, Mn, Zn) at CO_2 feed mole fractions of: (a) $y_{CO_2} = 0.1$, (b) $y_{CO_2} = 0.9$. The breakthrough curves of CO_2 are represented by dashed lines, and the breakthrough curves of H_2 by solid lines. The initial conditions are specified as: temperature T=298 K, total pressure $p_T = 2.5$ MPa, packed bed void fraction $\varepsilon_B = 0.4$, interstitial gas velocity entering the packed bed $v = 0.006791$ m s^{-1}, length of packed bed adsorber $L = 0.065$ m, axial dispersion is neglected, and isothermal conditions are assumed.

- Detailed information on the Ni-MOF-74 structure in the form of cif file.

```
data_Ni-MOF-74-cCO2
_audit_creation_method RASPA-1.0
_audit_creation_date 2019-12-13
_audit_author_name 'Jose Manuel Vicent-Luna'
_cell_length_a    25.7856
_cell_length_b    25.7856
_cell_length_c    6.7701
_cell_angle_alpha 90
_cell_angle_beta  90
_cell_angle_gamma 120
_cell_volume      15593.4
_symmetry_cell_setting          trigonal
_symmetry_space_group_name_Hall '-R 3'
_symmetry_space_group_name_H-M  'R -3'
_symmetry_Int_Tables_number     148
loop_
_symmetry_equiv_pos_as_xyz
 'x,y,z'
 '-y,x-y,z'
```

```
 '-x+y,-x,z'
 '-x,-y,-z'
 'y,-x+y,-z'
 'x-y,x,-z'
 'x+2/3,y+1/3,z+1/3'
 '-y+2/3,x-y+1/3,z+1/3'
 '-x+y+2/3,-x+1/3,z+1/3'
 '-x+2/3,-y+1/3,-z+1/3'
 'y+2/3,-x+y+1/3,-z+1/3'
 'x-y+2/3,x+1/3,-z+1/3'
 'x+1/3,y+2/3,z+2/3'
 '-y+1/3,x-y+2/3,z+2/3'
 '-x+y+1/3,-x+2/3,z+2/3'
 '-x+1/3,-y+2/3,-z+2/3'
 'y+1/3,-x+y+2/3,-z+2/3'
 'x-y+1/3,x+2/3,-z+2/3'
loop_
_atom_site_label
_atom_site_type_symbol
_atom_site_fract_x
_atom_site_fract_y
_atom_site_fract_z
_atom_site_charge
Ni       Ni     0.018170     0.713530     0.188130     1.55
C1       C      0.260070     0.914730     0.085340     0.603
C2       C      0.212570     0.875030     0.960330    -0.275
C3       C      0.123270     0.775530     0.910330     0.275
C4       C      0.168170     0.816730     0.035340    -0.086
O1       O      0.262870     0.899130     0.265340    -0.63
O2       O      0.300270     0.964230     0.020330    -0.815
O3       O      0.082870     0.721130     0.979330    -0.702
H        H      0.170670     0.804330     0.193330     0.08
```

- Detailed information on the Cu-MOF-74 structure in the form of cif file.

```
data_Cu-MOF-74-cCO2
_audit_creation_method RASPA-1.0
_audit_creation_date 2019-12-13
_audit_author_name 'Jose Manuel Vicent-Luna'
_cell_length_a    25.9972
```

```
_cell_length_b    25.9972
_cell_length_c    6.2587
_cell_angle_alpha 90
_cell_angle_beta  90
_cell_angle_gamma 120
_cell_volume      14653
_symmetry_cell_setting          trigonal
_symmetry_space_group_name_Hall '-R 3'
_symmetry_space_group_name_H-M  'R -3'
_symmetry_Int_Tables_number     148
loop_
_symmetry_equiv_pos_as_xyz
 'x,y,z'
 '-y,x-y,z'
 '-x+y,-x,z'
 '-x,-y,-z'
 'y,-x+y,-z'
 'x-y,x,-z'
 'x+2/3,y+1/3,z+1/3'
 '-y+2/3,x-y+1/3,z+1/3'
 '-x+y+2/3,-x+1/3,z+1/3'
 '-x+2/3,-y+1/3,-z+1/3'
 'y+2/3,-x+y+1/3,-z+1/3'
 'x-y+2/3,x+1/3,-z+1/3'
 'x+1/3,y+2/3,z+2/3'
 '-y+1/3,x-y+2/3,z+2/3'
 '-x+y+1/3,-x+2/3,z+2/3'
 '-x+1/3,-y+2/3,-z+2/3'
 'y+1/3,-x+y+2/3,-z+2/3'
 'x-y+1/3,x+2/3,-z+2/3'
loop_
_atom_site_label
_atom_site_type_symbol
_atom_site_fract_x
_atom_site_fract_y
_atom_site_fract_z
_atom_site_charge
Cu       Cu     0.290950     0.015230     0.346670     0.834
C1       C      0.169800     0.816900     0.538500    -0.076
C2       C      0.257700     0.913900     0.625600     0.345
```

```
C3       C      0.209600     0.890500     0.255200     0.156
C4       C      0.212100     0.872700     0.466900    -0.139
O1       O      0.250190     0.943270     0.168700    -0.394
O2       O      0.284800     0.969230     0.598900    -0.431
O3       O      0.266220     0.890810     0.789000    -0.368
H        H      0.172500     0.806100     0.681200     0.073
```

- Detailed information on the Co-MOF-74 structure in the form of cif file.

```
data_Co-MOF-74-cCO2
_audit_creation_method RASPA-1.0
_audit_creation_date 2019-12-13
_audit_author_name 'Jose Manuel Vicent-Luna'
_cell_length_a    25.885
_cell_length_b    25.885
_cell_length_c    6.8058
_cell_angle_alpha 90
_cell_angle_beta  90
_cell_angle_gamma 120
_cell_volume      15796.7
_symmetry_cell_setting          trigonal
_symmetry_space_group_name_Hall '-R 3'
_symmetry_space_group_name_H-M  'R -3'
_symmetry_Int_Tables_number     148
loop_
_symmetry_equiv_pos_as_xyz
 'x,y,z'
 '-y,x-y,z'
 '-x+y,-x,z'
 '-x,-y,-z'
 'y,-x+y,-z'
 'x-y,x,-z'
 'x+2/3,y+1/3,z+1/3'
 '-y+2/3,x-y+1/3,z+1/3'
 '-x+y+2/3,-x+1/3,z+1/3'
 '-x+2/3,-y+1/3,-z+1/3'
 'y+2/3,-x+y+1/3,-z+1/3'
 'x-y+2/3,x+1/3,-z+1/3'
 'x+1/3,y+2/3,z+2/3'
 '-y+1/3,x-y+2/3,z+2/3'
```

```
 '-x+y+1/3,-x+2/3,z+2/3'
 '-x+1/3,-y+2/3,-z+2/3'
 'y+1/3,-x+y+2/3,-z+2/3'
 'x-y+1/3,x+2/3,-z+2/3'
loop_
_atom_site_label
_atom_site_type_symbol
_atom_site_fract_x
_atom_site_fract_y
_atom_site_fract_z
_atom_site_charge
Co       Co     0.048500     0.362110     0.975420     1.335
C1       C      0.086900     0.347400     0.594700     0.485
C2       C      0.126400     0.339400     0.453700    -0.207
C3       C      0.011100     0.455300     0.923700     0.245
C4       C      0.016900     0.501800     0.808190    -0.125
O1       O      0.104200     0.365300     0.766600    -0.544
O2       O      0.022100     0.414400     0.838700    -0.611
O3       O      0.329130     0.032570     0.865760    -0.673
H        H      0.028400     0.503700     0.677800     0.095
```

- Detailed information on the Fe-MOF-74 structure in the form of cif file.

```
data_Fe-MOF-74-cCO2
_audit_creation_method RASPA-1.0
_audit_creation_date 2019-12-13
_audit_author_name 'Jose Manuel Vicent-Luna'
_cell_length_a    26.1627
_cell_length_b    26.1627
_cell_length_c    6.8422
_cell_angle_alpha 90
_cell_angle_beta  90
_cell_angle_gamma 120
_cell_volume      16223.8
_symmetry_cell_setting          trigonal
_symmetry_space_group_name_Hall '-R 3'
_symmetry_space_group_name_H-M  'R -3'
_symmetry_Int_Tables_number     148
loop_
_symmetry_equiv_pos_as_xyz
```

```
 'x,y,z'
 '-y,x-y,z'
 '-x+y,-x,z'
 '-x,-y,-z'
 'y,-x+y,-z'
 'x-y,x,-z'
 'x+2/3,y+1/3,z+1/3'
 '-y+2/3,x-y+1/3,z+1/3'
 '-x+y+2/3,-x+1/3,z+1/3'
 '-x+2/3,-y+1/3,-z+1/3'
 'y+2/3,-x+y+1/3,-z+1/3'
 'x-y+2/3,x+1/3,-z+1/3'
 'x+1/3,y+2/3,z+2/3'
 '-y+1/3,x-y+2/3,z+2/3'
 '-x+y+1/3,-x+2/3,z+2/3'
 '-x+1/3,-y+2/3,-z+2/3'
 'y+1/3,-x+y+2/3,-z+2/3'
 'x-y+1/3,x+2/3,-z+2/3'
loop_
_atom_site_label
_atom_site_type_symbol
_atom_site_fract_x
_atom_site_fract_y
_atom_site_fract_z
_atom_site_charge
Fe       Fe     0.382300     0.350970     0.139570     1.226
C1       C      0.317610     0.245000     0.427190     0.356
C2       C      0.330280     0.205750     0.293830    -0.148
C3       C      0.343180     0.222470     0.089460     0.175
C4       C      0.352650     0.180570     0.965880    -0.088
O1       O      0.327500     0.294890     0.363950    -0.602
O2       O      0.297710     0.219750     0.598130    -0.439
O3       O      0.356720     0.274650     0.004040    -0.561
H        H      0.361740     0.190690     0.834200     0.081
```

- Detailed information on the Mn-MOF-74 structure in the form of cif file.

```
data_Mn-MOF-74-cCO2
_audit_creation_method RASPA-1.0
_audit_creation_date 2019-12-13
```

```
_audit_author_name 'Jose Manuel Vicent-Luna'
_cell_length_a    25.7824
_cell_length_b    25.7824
_cell_length_c    6.9126
_cell_angle_alpha 90
_cell_angle_beta  90
_cell_angle_gamma 120
_cell_volume      15917.6
_symmetry_cell_setting          trigonal
_symmetry_space_group_name_Hall '-R 3'
_symmetry_space_group_name_H-M  'R -3'
_symmetry_Int_Tables_number     148
loop_
_symmetry_equiv_pos_as_xyz
 'x,y,z'
 '-y,x-y,z'
 '-x+y,-x,z'
 '-x,-y,-z'
 'y,-x+y,-z'
 'x-y,x,-z'
 'x+2/3,y+1/3,z+1/3'
 '-y+2/3,x-y+1/3,z+1/3'
 '-x+y+2/3,-x+1/3,z+1/3'
 '-x+2/3,-y+1/3,-z+1/3'
 'y+2/3,-x+y+1/3,-z+1/3'
 'x-y+2/3,x+1/3,-z+1/3'
 'x+1/3,y+2/3,z+2/3'
 '-y+1/3,x-y+2/3,z+2/3'
 '-x+y+1/3,-x+2/3,z+2/3'
 '-x+1/3,-y+2/3,-z+2/3'
 'y+1/3,-x+y+2/3,-z+2/3'
 'x-y+1/3,x+2/3,-z+2/3'
loop_
_atom_site_label
_atom_site_type_symbol
_atom_site_fract_x
_atom_site_fract_y
_atom_site_fract_z
_atom_site_charge
Mn       Mn     0.639720     0.690220     0.484690     1.161
```

```
C1       C      0.926810     0.244410     0.427820     0.368
C2       C      0.879080     0.206580     0.291510    -0.175
C3       C      0.210810     0.890160     0.763230     0.175
C4       C      0.165210     0.849500     0.643290    -0.064
O1       O      0.970970     0.293680     0.363200    -0.548
O2       O      0.924140     0.227920     0.602680    -0.443
O3       O      0.250820     0.943470     0.687320    -0.522
H        H      0.164180     0.862120     0.492850     0.048
```

- Detailed information on the Zn-MOF-74 structure in the form of cif file.

```
data_Zn-MOF-74-cCO2
_audit_creation_method RASPA-1.0
_audit_creation_date 2019-12-13
_audit_author_name 'Jose Manuel Vicent-Luna'
_cell_length_a    25.9322
_cell_length_b    25.9322
_cell_length_c    6.8365
_cell_angle_alpha 90
_cell_angle_beta  90
_cell_angle_gamma 120
_cell_volume      15925.9
_symmetry_cell_setting          trigonal
_symmetry_space_group_name_Hall '-R 3'
_symmetry_space_group_name_H-M  'R -3'
_symmetry_Int_Tables_number     148
loop_
_symmetry_equiv_pos_as_xyz
 'x,y,z'
 '-y,x-y,z'
 '-x+y,-x,z'
 '-x,-y,-z'
 'y,-x+y,-z'
 'x-y,x,-z'
 'x+2/3,y+1/3,z+1/3'
 '-y+2/3,x-y+1/3,z+1/3'
 '-x+y+2/3,-x+1/3,z+1/3'
 '-x+2/3,-y+1/3,-z+1/3'
 'y+2/3,-x+y+1/3,-z+1/3'
 'x-y+2/3,x+1/3,-z+1/3'
```

```
 'x+1/3,y+2/3,z+2/3'
 '-y+1/3,x-y+2/3,z+2/3'
 '-x+y+1/3,-x+2/3,z+2/3'
 '-x+1/3,-y+2/3,-z+2/3'
 'y+1/3,-x+y+2/3,-z+2/3'
 'x-y+1/3,x+2/3,-z+2/3'
loop_
_atom_site_label
_atom_site_type_symbol
_atom_site_fract_x
_atom_site_fract_y
_atom_site_fract_z
_atom_site_charge
Zn       Zn     0.280080     0.982240     0.687100     1.006
C1       C      0.350670     0.087270     0.411730     0.343
C2       C      0.339610     0.125890     0.548730    -0.155
C3       C      0.322980     0.111220     0.747630     0.161
C4       C      0.317830     0.153290     0.859230    -0.083
O1       O      0.345470     0.039270     0.476730    -0.479
O2       O      0.365000     0.104470     0.237730    -0.393
O3       O      0.311450     0.059840     0.834040    -0.464
H        H      0.307470     0.144730     0.993330     0.064
```

Appendix D

Appendix D corresponds to Chapter 6 of this thesis.

- Lennard-Jones and Coulombic interactions for CO_2, H_2, and HCOOH;
- Schematic representation of M-MOF-74 (M = Ni, Cu, Co, Fe, Mn, Zn) structures and the HCOOH model for DFT;
- Lattice parameters for M-MOF-74 (M = Ni, Cu, Co, Fe, Mn, Zn) unit cells resulting from the geometry optimization from DFT;
- Initial gas-phase mole fractions of CO_2, H_2, and HCOOH used as an input for grand-canonical Monte Carlo simulations at 298.15 - 800 K, and 1 - 60 bar;
- Distribution of the HCOOH molecules inside M-MOF-74 (M = Co, Fe, Mn, Zn) analyzed using density profiles from grand-canonical Monte Carlo simulations at 298 K, 10 kPa;
- Binding energies of the most stable configuration of HCOOH in M-MOF-74 (M = Ni, Cu, Co, Fe, Mn, Zn) obtained from force field-based molecular simulations and DFT;
- Mole fractions of CO_2, H_2, and HCOOH obtained from grand-canonical Monte Carlo simulations in M-MOF-74 (M = Ni, Cu, Co, Fe, Mn, Zn) at 298.15 - 800 K, and 1 - 60 bar;
- Radial distribution functions for HCOOH in M-MOF-74 (M = Ni, Cu, Co, Fe, Mn, Zn).

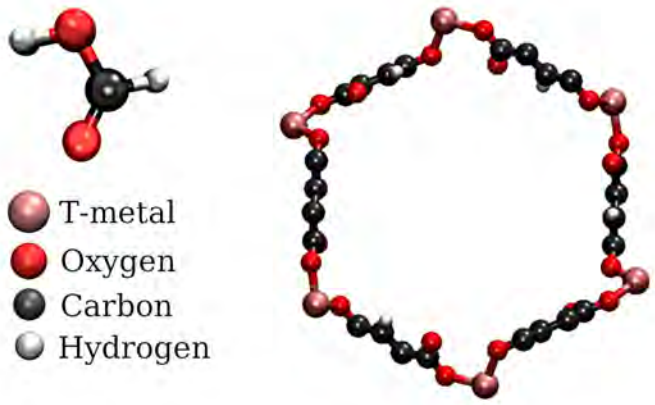

Fig. D.1. Schematic representation of: (a) a HCOOH molecule, and (b) M-MOF-74 unit cell (T-Metals: Co, Cu, Fe, Mn, Ni, and Zn), used in Density Functional Theory calculations.

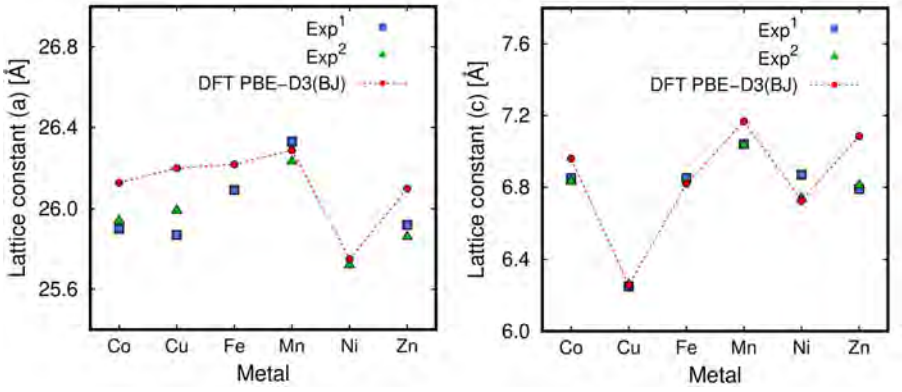

Fig. D.2. Lattice parameters resulting from the geometry optimization calculated from Density Functional Theory using the M-MOF-74 unit cell (M = Co, Cu, Fe, Mn, Ni, and Zn) shown in Figure D.1 of Appendix D. The calculated values show a strong agreement with the literature data [122, 253].

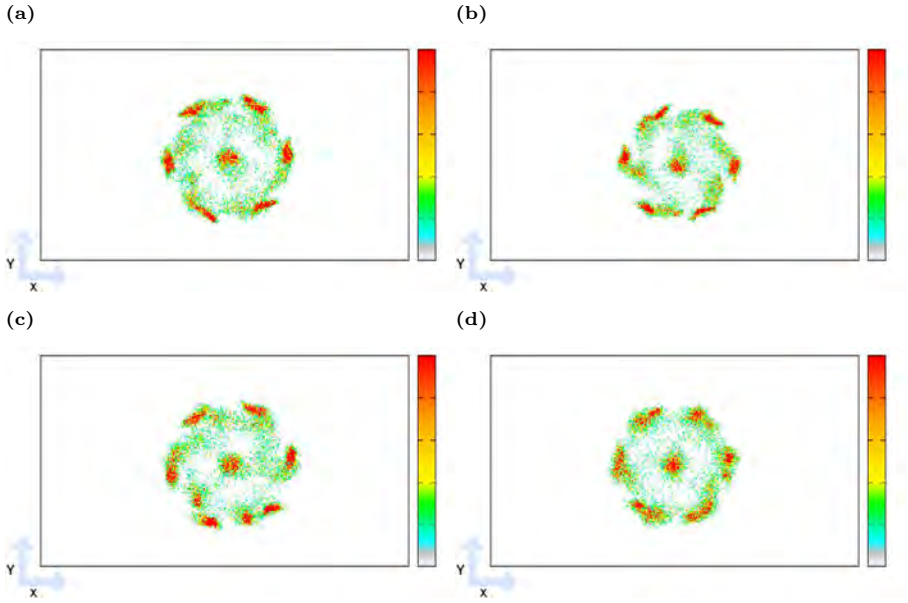

Fig. D.3. Distribution of the HCOOH molecules analyzed using density profiles from GCMC simulations at 298 K, 10 kPa in: (a) Co-MOF-74, (b) Fe-MOF-74, (c) Mn-MOF-74, (d) Zn-MOF-74. The center of mass of the molecules that are adsorbed was projected onto the XY plane. The color gradation of the scales relates to the most and least populated regions of the structure, which is relative in each case. The color scale is shown as a reference for the loading. The preferential sites of HCOOH (colored red) in all structures are at the open-metal centers.

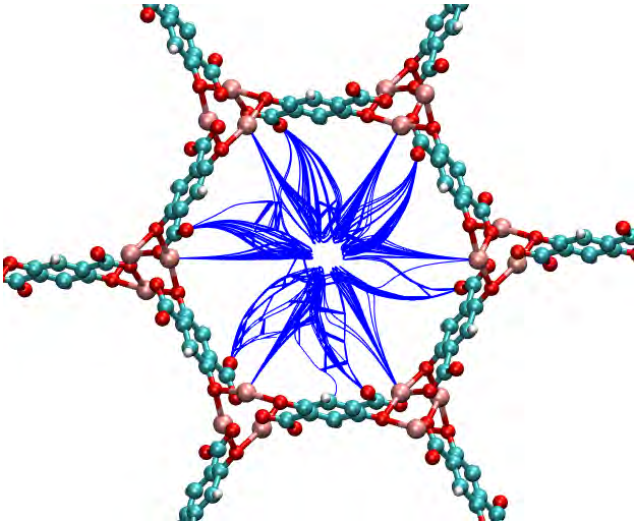

Fig. D.4. Electrostatic field lines within the cavities of M-MOF-74 (M = Co, Cu, Fe, Mn, Ni, and Zn) from the positively charged metal sites to the electronegative Oa atoms. For details about calculation the reader is referred to the study by Luna-Triguero et al. [295].

Table D.1: Normalized Coulombic charges for M-MOF-74 (M = Ni, Cu, Co, Fe, Mn, Zn) with respect to the partial charge of the metal center. The charges used for analysis are from Chapter 5. The calculated relative charges show high similarity for each type of atom identified in all the frameworks. The subscripts show the deviation in the average partial charges of the atom types through the M-MOF-74 series.

Atom	Co	Cu	Fe	Mn	Ni	Zn	Average normalized charge
Me	1	1	1	1	1	1	1
Ca	0.363	0.414	0.290	0.317	0.389	0.341	$0.35_{0.04}$
Cb	-0.155	-0.167	-0.121	-0.151	-0.177	-0.154	$-0.15_{0.02}$
Cc	-0.094	-0.091	-0.072	-0.055	-0.055	-0.083	$-0.07_{0.02}$
Cd	0.184	0.187	0.143	0.151	0.177	0.160	$0.17_{0.02}$
Oa	-0.407	-0.441	-0.358	-0.382	-0.406	-0.391	$-0.40_{0.03}$
Ob	-0.504	-0.517	-0.491	-0.472	-0.526	-0.476	$-0.50_{0.02}$
Oc	-0.458	-0.472	-0.458	-0.450	-0.453	-0.461	$-0.459_{0.007}$
H	0.071	0.088	0.066	0.041	0.052	0.064	$0.06_{0.01}$

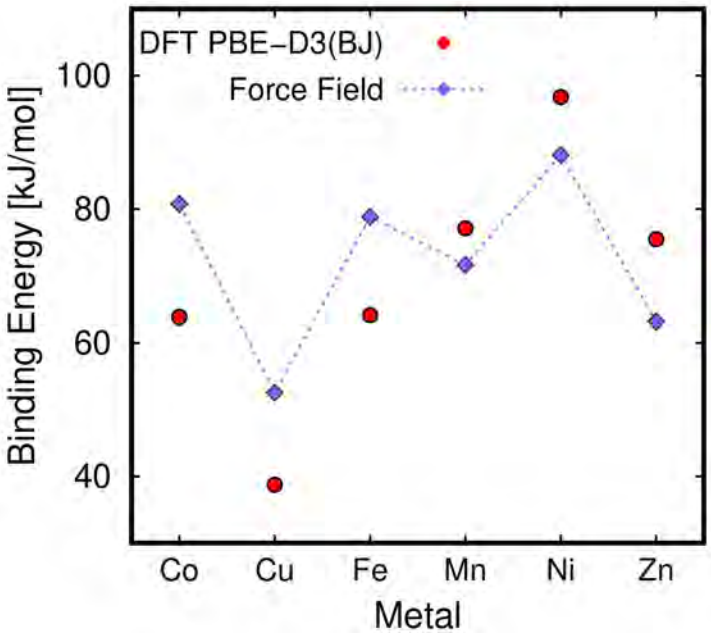

Fig. D.5. Absolute values of binding energies of the most stable configuration of HCOOH in M-MOF-74 (M = Co, Cu, Fe, Mn, Ni, and Zn) obtained from force field-based molecular simulations compared to the DFT (PBE-D3(BJ)) results. The binding energies vary between the selected methods but follow a similar general trend across the different metals. Both computational methods indicate that Cu-MOF-74 has the weakest binding affinity, while Ni-MOF-74 shows the strongest binding affinity. The binding energy in Cu-MOF-74 is ca. 40 kJ mol^{-1} for DFT, while it is significantly higher (ca. 50 kJ mol^{-1}) for force field simulations. The force field-based simulations show a binding energy of HCOOH in Ni-MOF-74 ca. 90 kJ mol^{-1}, whereas DFT shows a higher value, close to ca. 100 kJ mol^{-1}. The relative difference between the two methods is 18%. The lines connecting the symbols are used to guide the eye.

Table D.2: Mole fractions of CO_2, H_2, and HCOOH obtained using Monte Carlo simulations in the grand-canonical ensemble in the Ni-MOF-74 framework at 298.15 - 800 K and 1 - 60 bar. The mole fractions of CO_2, H_2, and HCOOH at reaction equilibrium obtained from the Continuous Fractional Component Monte Carlo simulations in the Reaction Ensemble [276] were used in the GCMC simulations as input. The subscripts show uncertainties computed using error propagation rules.

P/[bar]	T/[K]	x_{CO_2}	x_{H_2}	x_{HCOOH} / 10^{-6}
1	298.15	$0.988_{0.008}$	$0.0017_{0.0001}$	9875.5_{1100}
	400	$0.981_{0.19}$	$0.019_{0.004}$	78.8_{93}
	500	$0.928_{0.058}$	$0.072_{0.005}$	$3.1_{5.7}$
	600	$0.852_{0.038}$	$0.148_{0.012}$	$1.7_{3.1}$
	700	$0.791_{0.020}$	$0.209_{0.005}$	$4.1_{11.3}$
	800	$0.740_{0.031}$	$0.260_{0.011}$	0_{0}
5	298.15	$0.964_{0.014}$	$0.0031_{0.0002}$	32487.4_{6600}
	400	$0.979_{0.018}$	$0.019_{0.001}$	1288.7_{370}
	500	$0.925_{0.039}$	$0.075_{0.004}$	123.0_{82}
	600	$0.855_{0.021}$	$0.145_{0.003}$	39.9_{35}
	700	$0.792_{0.021}$	$0.208_{0.004}$	12.2_{17}
	800	$0.737_{0.012}$	$0.263_{0.005}$	0_{0}
10	298.15	$0.958_{0.011}$	$0.0033_{0.0002}$	38650.0_{5400}
	400	$0.979_{0.016}$	$0.0195_{0.0005}$	1984.1_{830}
	500	$0.925_{0.033}$	$0.074_{0.002}$	399.5_{190}
	600	$0.856_{0.024}$	$0.144_{0.005}$	87.5_{110}
	700	$0.790_{0.007}$	$0.210_{0.003}$	32.4_{24}
	800	$0.738_{0.005}$	$0.262_{0.003}$	$12.8_{9.8}$
15	298.15	$0.931_{0.011}$	$0.004_{0.001}$	64600.9_{5700}
	400	$0.977_{0.007}$	$0.020_{0.001}$	3191.7_{630}
	500	$0.926_{0.018}$	$0.074_{0.002}$	360.0_{100}
	600	$0.856_{0.008}$	$0.144_{0.002}$	129.9_{41}
	700	$0.789_{0.014}$	$0.210_{0.004}$	23.4_{25}
	800	$0.738_{0.006}$	$0.262_{0.002}$	21.2_{20}
20	298.15	$0.941_{0.019}$	$0.0040_{0.0002}$	54877.4_{11000}
	400	$0.975_{0.007}$	$0.0200_{0.0004}$	4678.6_{380}
	500	$0.925_{0.023}$	$0.075_{0.002}$	460.3_{280}
	600	$0.857_{0.017}$	$0.143_{0.002}$	139.5_{56}
	700	$0.790_{0.011}$	$0.210_{0.002}$	48.4_{19}
	800	$0.738_{0.007}$	$0.262_{0.003}$	33.2_{26}
25	298.15	$0.925_{0.009}$	$0.0042_{0.0004}$	71231.6_{4700}
	400	$0.975_{0.006}$	$0.0207_{0.0003}$	3926.0_{700}
	500	$0.926_{0.024}$	$0.073_{0.002}$	524.5_{56}

	600	0.855 $_{0.014}$	0.145 $_{0.002}$	201.9 $_{73}$
	700	0.791 $_{0.004}$	0.209 $_{0.002}$	63.0 $_{23}$
	800	0.739 $_{0.006}$	0.261 $_{0.003}$	30.0 $_{9.2}$
30	298.15	0.934 $_{0.014}$	0.0048 $_{0.0005}$	61063.8 $_{10000}$
	400	0.973 $_{0.007}$	0.022 $_{0.001}$	5543.2 $_{580}$
	500	0.927 $_{0.017}$	0.072 $_{0.002}$	831.1 $_{180}$
	600	0.855 $_{0.019}$	0.144 $_{0.003}$	170.1 $_{39}$
	700	0.790 $_{0.011}$	0.210 $_{0.003}$	67.2 $_{30}$
	800	0.738 $_{0.007}$	0.262 $_{0.003}$	54.4 $_{15}$
40	298.15	0.899 $_{0.025}$	0.0048 $_{0.0003}$	95858.1 $_{14000}$
	350	0.968 $_{0.007}$	0.012 $_{0.001}$	20183.1 $_{850}$
	400	0.970 $_{0.005}$	0.023 $_{0.001}$	6950.5 $_{770}$
	500	0.926 $_{0.010}$	0.073 $_{0.002}$	1158.7 $_{320}$
	600	0.856 $_{0.015}$	0.143 $_{0.003}$	246.1 $_{110}$
	700	0.791 $_{0.009}$	0.209 $_{0.002}$	101.7 $_{22}$
	800	0.736 $_{0.006}$	0.264 $_{0.003}$	54.2 $_{11}$
50	298.15	0.879 $_{0.028}$	0.0053 $_{0.0003}$	115594.3 $_{16000}$
	350	0.963 $_{0.008}$	0.013 $_{0.001}$	23487.9 $_{3200}$
	400	0.968 $_{0.005}$	0.024 $_{0.001}$	7704.2 $_{600}$
	500	0.926 $_{0.009}$	0.073 $_{0.001}$	1254.6 $_{190}$
	600	0.854 $_{0.010}$	0.146 $_{0.002}$	315.3 $_{130}$
	700	0.789 $_{0.013}$	0.210 $_{0.003}$	112.9 $_{31}$
	800	0.737 $_{0.003}$	0.263 $_{0.002}$	71.5 $_{23}$
60	298.15	0.889 $_{0.034}$	0.006 $_{0.001}$	104742.3 $_{18000}$
	350	0.960 $_{0.002}$	0.0141 $_{0.0002}$	25871.3 $_{780}$
	400	0.965 $_{0.004}$	0.025 $_{0.002}$	9561.3 $_{1000}$
	500	0.925 $_{0.008}$	0.074 $_{0.003}$	1663.0 $_{230}$
	600	0.856 $_{0.012}$	0.144 $_{0.002}$	367.4 $_{73}$
	700	0.790 $_{0.009}$	0.210 $_{0.003}$	161.3 $_{60}$
	800	0.736 $_{0.005}$	0.264 $_{0.002}$	92.2 $_{15}$

Table D.3: Mole fractions of CO_2, H_2, and HCOOH obtained using Monte Carlo simulations in the grand-canonical ensemble in the Cu-MOF-74 framework at 298.15 - 800 K and 1 - 60 bar. The mole fractions of CO_2, H_2, and HCOOH at reaction equilibrium obtained from the Continuous Fractional Component Monte Carlo simulations in the Reaction Ensemble [276] were used in the GCMC simulations as input. The subscripts show uncertainties computed using error propagation rules.

P/[bar]	T/[K]	x_{CO_2}	x_{H_2}	x_{HCOOH} / 10^{-6}
1	298.15	$0.990_{0.018}$	$0.0100_{0.0003}$	20.0_{37}
	400	$0.943_{0.038}$	$0.057_{0.005}$	0_{0}
	500	$0.872_{0.013}$	$0.128_{0.007}$	0_{0}
	600	$0.812_{0.024}$	$0.188_{0.006}$	0_{0}
	700	$0.755_{0.011}$	$0.245_{0.009}$	9.6_{27}
	800	$0.712_{0.018}$	$0.288_{0.007}$	0_{0}
5	298.15	$0.993_{0.004}$	$0.0065_{0.0004}$	37.8_{30}
	400	$0.942_{0.016}$	$0.058_{0.001}$	30.2_{59}
	500	$0.874_{0.006}$	$0.126_{0.003}$	$0.8_{1.3}$
	600	$0.808_{0.008}$	$0.192_{0.005}$	$4.4_{5.4}$
	700	$0.758_{0.009}$	$0.242_{0.003}$	0_{0}
	800	$0.713_{0.008}$	$0.287_{0.003}$	0_{0}
10	298.15	$0.994_{0.007}$	$0.0058_{0.0005}$	77.8_{48}
	400	$0.945_{0.011}$	$0.0549_{0.0007}$	18.7_{16}
	500	$0.876_{0.008}$	$0.124_{0.002}$	$5.7_{6.5}$
	600	$0.811_{0.004}$	$0.189_{0.001}$	$5.1_{8.7}$
	700	$0.755_{0.004}$	$0.245_{0.004}$	$5.8_{7.0}$
	800	$0.713_{0.007}$	$0.287_{0.003}$	7.7_{14}
15	298.15	$0.994_{0.008}$	$0.0059_{0.0007}$	74.3_{60}
	400	$0.948_{0.002}$	$0.052_{0.001}$	19.7_{20}
	500	$0.876_{0.006}$	$0.124_{0.002}$	12.1_{14}
	600	$0.811_{0.004}$	$0.189_{0.002}$	$4.7_{5.8}$
	700	$0.756_{0.008}$	$0.244_{0.002}$	14.5_{14}
	800	$0.712_{0.008}$	$0.288_{0.004}$	$5.4_{6.7}$
20	298.15	$0.994_{0.006}$	$0.0059_{0.0003}$	101.7_{24}
	400	$0.949_{0.007}$	$0.0508_{0.0007}$	33.6_{19}
	500	$0.876_{0.006}$	$0.124_{0.001}$	16.6_{12}
	600	$0.810_{0.009}$	$0.190_{0.002}$	16.1_{12}
	700	$0.756_{0.003}$	$0.2443_{0.0008}$	$7.2_{3.9}$
	800	$0.712_{0.005}$	$0.288_{0.003}$	$5.8_{7.6}$
25	298.15	$0.994_{0.004}$	$0.0061_{0.0005}$	181.4_{55}
	400	$0.951_{0.011}$	$0.0489_{0.0006}$	29.0_{15}
	500	$0.877_{0.009}$	$0.123_{0.001}$	$16.2_{8.9}$

	600	0.811 $_{0.004}$	0.189 $_{0.001}$	10.8 $_{6.4}$
	700	0.756 $_{0.008}$	0.244 $_{0.002}$	16.5 $_{12}$
	800	0.712 $_{0.004}$	0.288 $_{0.002}$	15.5 $_{19}$
30	298.15	0.993 $_{0.003}$	0.0066 $_{0.0002}$	149.7 $_{71}$
	400	0.951 $_{0.006}$	0.0487 $_{0.0003}$	40.6 $_{9.1}$
	500	0.878 $_{0.002}$	0.1223 $_{0.0009}$	26.6 $_{13}$
	600	0.811 $_{0.002}$	0.189 $_{0.001}$	18.2 $_{10}$
	700	0.755 $_{0.007}$	0.245 $_{0.003}$	21.3 $_{11}$
	800	0.711 $_{0.003}$	0.289 $_{0.003}$	18.6 $_{21}$
40	298.15	0.993 $_{0.009}$	0.007 $_{0.002}$	255.5 $_{190}$
	350	0.979 $_{0.003}$	0.0212 $_{0.0002}$	94.9 $_{36}$
	400	0.953 $_{0.008}$	0.0473 $_{0.0008}$	65.7 $_{23}$
	500	0.878 $_{0.006}$	0.1220 $_{0.0007}$	29.9 $_{6.4}$
	600	0.810 $_{0.004}$	0.190 $_{0.002}$	30.8 $_{9.0}$
	700	0.755 $_{0.005}$	0.245 $_{0.002}$	16.0 $_{6.2}$
	800	0.711 $_{0.005}$	0.289 $_{0.002}$	17.8 $_{3.3}$
50	298.15	0.992 $_{0.003}$	0.0077 $_{0.0004}$	275.3 $_{66}$
	350	0.978 $_{0.004}$	0.0221 $_{0.0003}$	106.2 $_{60}$
	400	0.953 $_{0.003}$	0.0474 $_{0.0006}$	64.0 $_{18}$
	500	0.879 $_{0.003}$	0.121 $_{0.002}$	39.6 $_{18}$
	600	0.810 $_{0.003}$	0.190 $_{0.001}$	41.0 $_{20}$
	700	0.755 $_{0.006}$	0.245 $_{0.002}$	28.3 $_{10}$
	800	0.711 $_{0.005}$	0.289 $_{0.002}$	19.8 $_{10}$
60	298.15	0.992 $_{0.005}$	0.0082 $_{0.0006}$	244.1 $_{170}$
	350	0.977 $_{0.005}$	0.0225 $_{0.0006}$	138.1 $_{39}$
	400	0.952 $_{0.005}$	0.0479 $_{0.0003}$	90.8 $_{35}$
	500	0.879 $_{0.004}$	0.121 $_{0.001}$	42.2 $_{11}$
	600	0.810 $_{0.005}$	0.190 $_{0.001}$	39.2 $_{16}$
	700	0.754 $_{0.006}$	0.246 $_{0.002}$	32.9 $_{10}$
	800	0.710 $_{0.004}$	0.290 $_{0.001}$	30.6 $_{11}$

Table D.4: Mole fractions of CO_2, H_2, and HCOOH obtained using Monte Carlo simulations in the grand-canonical ensemble in the Co-MOF-74 framework at 298.15 - 800 K and 1 - 60 bar. The mole fractions of CO_2, H_2, and HCOOH at reaction equilibrium obtained from the Continuous Fractional Component Monte Carlo simulations in the Reaction Ensemble [276] were used in the GCMC simulations as input. The subscripts show uncertainties computed using error propagation rules.

P/[bar]	T/[K]	x_{CO_2}	x_{H_2}	x_{HCOOH} / 10^{-6}
1	298.15	$0.996_{0.010}$	$0.0021_{0.0001}$	2365.8_{550}
	400	$0.974_{0.059}$	$0.026_{0.002}$	41.6_{53}
	500	$0.922_{0.037}$	$0.078_{0.004}$	18.5_{50}
	600	$0.848_{0.028}$	$0.152_{0.007}$	59.0_{160}
	700	$0.790_{0.021}$	$0.210_{0.010}$	0_{0}
	800	$0.736_{0.021}$	$0.264_{0.006}$	0_{0}
5	298.15	$0.990_{0.006}$	$0.0032_{0.0001}$	6848.9_{720}
	400	$0.975_{0.047}$	$0.024_{0.003}$	369.2_{320}
	500	$0.919_{0.036}$	$0.081_{0.004}$	61.6_{140}
	600	$0.849_{0.019}$	$0.151_{0.005}$	9.1_{10}
	700	$0.790_{0.009}$	$0.210_{0.003}$	5.3_{10}
	800	$0.737_{0.006}$	$0.263_{0.004}$	8.4_{11}
10	298.15	$0.988_{0.004}$	$0.0035_{0.0003}$	8536.9_{920}
	400	$0.976_{0.022}$	$0.024_{0.001}$	764.0_{460}
	500	$0.919_{0.023}$	$0.081_{0.004}$	120.4_{85}
	600	$0.851_{0.011}$	$0.149_{0.001}$	35.1_{23}
	700	$0.789_{0.009}$	$0.211_{0.003}$	20.6_{31}
	800	$0.739_{0.007}$	$0.261_{0.003}$	7.7_{11}
15	298.15	$0.982_{0.007}$	$0.0039_{0.0005}$	14087.9_{1600}
	400	$0.976_{0.013}$	$0.0227_{0.0009}$	848.5_{350}
	500	$0.920_{0.036}$	$0.080_{0.003}$	198.2_{145}
	600	$0.850_{0.019}$	$0.150_{0.003}$	69.3_{67}
	700	$0.790_{0.007}$	$0.210_{0.002}$	$19.6_{9.5}$
	800	$0.739_{0.005}$	$0.261_{0.003}$	$18.8_{9.9}$
20	298.15	$0.981_{0.006}$	$0.0038_{0.0002}$	14991.3_{3500}
	400	$0.975_{0.007}$	$0.0238_{0.0008}$	1180.3_{220}
	500	$0.920_{0.013}$	$0.080_{0.001}$	198.9_{52}
	600	$0.854_{0.015}$	$0.146_{0.004}$	95.4_{100}
	700	$0.789_{0.004}$	$0.211_{0.002}$	23.8_{18}
	800	$0.738_{0.008}$	$0.262_{0.003}$	23.8_{16}
25	298.15	$0.980_{0.007}$	$0.0042_{0.0002}$	16296.5_{2400}
	400	$0.975_{0.007}$	$0.0237_{0.0005}$	1399.9_{250}
	500	$0.919_{0.013}$	$0.081_{0.003}$	317.0_{64}

	600	0.851 $_{0.012}$	0.149 $_{0.002}$	66.5 $_{15}$
	700	0.790 $_{0.017}$	0.210 $_{0.003}$	41.9 $_{16}$
	800	0.739 $_{0.007}$	0.261 $_{0.002}$	22.3 $_{7.2}$
30	298.15	0.977 $_{0.004}$	0.0045 $_{0.0001}$	18294.1 $_{1200}$
	400	0.974 $_{0.007}$	0.0240 $_{0.0004}$	1835.4 $_{280}$
	500	0.920 $_{0.009}$	0.080 $_{0.002}$	321.2 $_{150}$
	600	0.851 $_{0.007}$	0.149 $_{0.001}$	93.8 $_{39}$
	700	0.788 $_{0.004}$	0.212 $_{0.002}$	38.8 $_{11}$
	800	0.737 $_{0.005}$	0.263 $_{0.002}$	26.6 $_{9.2}$
40	298.15	0.968 $_{0.018}$	0.004 $_{0.001}$	28068.9 $_{6700}$
	350	0.982 $_{0.003}$	0.0123 $_{0.0005}$	6143.9 $_{690}$
	400	0.973 $_{0.003}$	0.0252 $_{0.0008}$	2093.9 $_{340}$
	500	0.921 $_{0.009}$	0.0789 $_{0.0009}$	416.3 $_{82}$
	600	0.850 $_{0.006}$	0.149 $_{0.001}$	137.3 $_{41}$
	700	0.789 $_{0.009}$	0.211 $_{0.002}$	64.5 $_{28}$
	800	0.738 $_{0.004}$	0.262 $_{0.001}$	33.6 $_{12}$
50	298.15	0.963 $_{0.009}$	0.0053 $_{0.0002}$	31646.6 $_{3000}$
	350	0.980 $_{0.005}$	0.0140 $_{0.0009}$	5933.9 $_{330}$
	400	0.971 $_{0.011}$	0.0262 $_{0.0004}$	2366.1 $_{320}$
	500	0.920 $_{0.008}$	0.0798 $_{0.0008}$	521.2 $_{130}$
	600	0.851 $_{0.009}$	0.149 $_{0.002}$	166.9 $_{26}$
	700	0.788 $_{0.005}$	0.212 $_{0.002}$	76.1 $_{13}$
	800	0.737 $_{0.006}$	0.263 $_{0.002}$	46.9 $_{9.0}$
60	298.15	0.966 $_{0.003}$	0.0057 $_{0.0004}$	28489.5 $_{2200}$
	350	0.978 $_{0.003}$	0.0142 $_{0.0002}$	7797.5 $_{640}$
	400	0.970 $_{0.006}$	0.0275 $_{0.0005}$	2823.2 $_{220}$
	500	0.920 $_{0.007}$	0.079 $_{0.001}$	601.1 $_{59}$
	600	0.850 $_{0.008}$	0.149 $_{0.002}$	214.7 $_{42}$
	700	0.787 $_{0.007}$	0.213 $_{0.002}$	77.7 $_{9.5}$
	800	0.737 $_{0.004}$	0.263 $_{0.001}$	61.3 $_{17}$

Table D.5: Mole fractions of CO_2, H_2, and HCOOH obtained using Monte Carlo simulations in the grand-canonical ensemble in the Fe-MOF-74 framework at 298.15 - 800 K and 1 - 60 bar. The mole fractions of CO_2, H_2, and HCOOH at reaction equilibrium obtained from the Continuous Fractional Component Monte Carlo simulations in the Reaction Ensemble [276] were used in the GCMC simulations as input. The subscripts show uncertainties computed using error propagation rules.

P/[bar]	T/[K]	x_{CO_2}	x_{H_2}	x_{HCOOH} / 10^{-6}
1	298.15	$0.996_{0.012}$	$0.0023_{0.0003}$	1595.0_{310}
	400	$0.972_{0.027}$	$0.028_{0.004}$	17.3_{36}
	500	$0.913_{0.032}$	$0.087_{0.003}$	$0.9_{1.7}$
	600	$0.844_{0.011}$	$0.156_{0.005}$	0_{0}
	700	$0.782_{0.033}$	$0.218_{0.010}$	0_{0}
	800	$0.729_{0.025}$	$0.271_{0.009}$	0_{0}
5	298.15	$0.991_{0.008}$	$0.0035_{0.0004}$	5511.9_{680}
	400	$0.973_{0.019}$	$0.0262_{0.0008}$	346.4_{140}
	500	$0.913_{0.028}$	$0.087_{0.005}$	41.3_{67}
	600	$0.845_{0.008}$	$0.155_{0.002}$	16.2_{22}
	700	$0.784_{0.013}$	$0.216_{0.006}$	18.3_{40}
	800	$0.730_{0.004}$	$0.270_{0.004}$	0_{0}
10	298.15	$0.989_{0.007}$	$0.0039_{0.0006}$	7503.4_{1900}
	400	$0.974_{0.027}$	$0.0258_{0.0009}$	662.6_{260}
	500	$0.914_{0.021}$	$0.086_{0.002}$	156.3_{110}
	600	$0.843_{0.016}$	$0.157_{0.003}$	34.8_{18}
	700	$0.782_{0.010}$	$0.218_{0.003}$	$18.6_{7.2}$
	800	$0.731_{0.013}$	$0.269_{0.004}$	$4.0_{7.7}$
15	298.15	$0.984_{0.008}$	$0.0038_{0.0003}$	12339.0_{1400}
	400	$0.974_{0.015}$	$0.0252_{0.0007}$	934.2_{220}
	500	$0.914_{0.031}$	$0.085_{0.003}$	186.5_{40}
	600	$0.845_{0.018}$	$0.155_{0.003}$	39.1_{18}
	700	$0.781_{0.008}$	$0.219_{0.002}$	19.2_{20}
	800	$0.730_{0.003}$	$0.270_{0.002}$	12.0_{18}
20	298.15	$0.983_{0.004}$	$0.0042_{0.0004}$	12733.8_{1300}
	400	$0.973_{0.004}$	$0.0260_{0.0005}$	1190.3_{86}
	500	$0.915_{0.005}$	$0.085_{0.001}$	200.5_{59}
	600	$0.844_{0.009}$	$0.156_{0.002}$	63.7_{29}
	700	$0.782_{0.005}$	$0.217_{0.002}$	35.5_{24}
	800	$0.731_{0.004}$	$0.269_{0.004}$	$13.7_{6.4}$
25	298.15	$0.981_{0.005}$	$0.0045_{0.0004}$	14375.7_{3000}
	400	$0.973_{0.006}$	$0.0258_{0.0005}$	1180.3_{150}
	500	$0.915_{0.011}$	$0.085_{0.001}$	229.4_{36}

	600	0.845 $_{0.009}$	0.155 $_{0.002}$	58.9 $_{9.5}$
	700	0.781 $_{0.008}$	0.219 $_{0.002}$	34.9 $_{14}$
	800	0.731 $_{0.007}$	0.269 $_{0.002}$	24.3 $_{11}$
30	298.15	0.981 $_{0.007}$	0.0048 $_{0.0005}$	14334.3 $_{1600}$
	400	0.972 $_{0.004}$	0.0267 $_{0.0006}$	1658.1 $_{510}$
	500	0.915 $_{0.018}$	0.084 $_{0.002}$	263.8 $_{99}$
	600	0.844 $_{0.012}$	0.156 $_{0.002}$	98.4 $_{28}$
	700	0.782 $_{0.005}$	0.218 $_{0.002}$	44.9 $_{9.8}$
	800	0.731 $_{0.006}$	0.269 $_{0.002}$	25.4 $_{18}$
40	298.15	0.976 $_{0.006}$	0.0054 $_{0.0003}$	18536.2 $_{3400}$
	350	0.981 $_{0.003}$	0.0135 $_{0.0005}$	5500.7 $_{640}$
	400	0.971 $_{0.004}$	0.0273 $_{0.0006}$	1877.4 $_{170}$
	500	0.914 $_{0.015}$	0.085 $_{0.001}$	425.3 $_{130}$
	600	0.844 $_{0.008}$	0.155 $_{0.002}$	129.3 $_{50}$
	700	0.780 $_{0.011}$	0.220 $_{0.003}$	51.8 $_{15}$
	800	0.731 $_{0.007}$	0.269 $_{0.002}$	37.8 $_{9.5}$
50	298.15	0.972 $_{0.005}$	0.0058 $_{0.0002}$	22638.2 $_{3600}$
	350	0.979 $_{0.005}$	0.0146 $_{0.0003}$	6342.0 $_{460}$
	400	0.969 $_{0.005}$	0.0284 $_{0.0003}$	2126.2 $_{96}$
	500	0.915 $_{0.010}$	0.084 $_{0.002}$	496.2 $_{130}$
	600	0.843 $_{0.006}$	0.157 $_{0.002}$	159.7 $_{42}$
	700	0.781 $_{0.004}$	0.219 $_{0.003}$	70.2 $_{9.4}$
	800	0.730 $_{0.006}$	0.270 $_{0.002}$	47.8 $_{19}$
60	298.15	0.971 $_{0.005}$	0.0067 $_{0.0006}$	22258.6 $_{2300}$
	350	0.978 $_{0.004}$	0.0153 $_{0.0004}$	6373.0 $_{230}$
	400	0.968 $_{0.004}$	0.0295 $_{0.0006}$	2668.8 $_{340}$
	500	0.916 $_{0.010}$	0.084 $_{0.001}$	495.6 $_{55}$
	600	0.843 $_{0.004}$	0.157 $_{0.001}$	174.1 $_{28}$
	700	0.781 $_{0.005}$	0.219 $_{0.002}$	89.6 $_{14}$
	800	0.729 $_{0.002}$	0.271 $_{0.001}$	62.1 $_{8.9}$

Table D.6: Mole fractions of CO_2, H_2, and HCOOH obtained using Monte Carlo simulations in the grand-canonical ensemble in the Mn-MOF-74 framework at 298.15 - 800 K and 1 - 60 bar. The mole fractions of CO_2, H_2, and HCOOH at reaction equilibrium obtained from the Continuous Fractional Component Monte Carlo simulations in the Reaction Ensemble [276] were used in the GCMC simulations as input. The subscripts show uncertainties computed using error propagation rules.

P/[bar]	T/[K]	x_{CO_2}	x_{H_2}	x_{HCOOH} / 10^{-6}
1	298.15	$0.997_{0.015}$	$0.0025_{0.0004}$	420.7_{180}
	400	$0.968_{0.021}$	$0.032_{0.004}$	17.8_{46}
	500	$0.910_{0.041}$	$0.090_{0.008}$	5.4_{12}
	600	$0.843_{0.022}$	$0.157_{0.004}$	0_{0}
	700	$0.781_{0.033}$	$0.219_{0.010}$	0_{0}
	800	$0.729_{0.006}$	$0.271_{0.009}$	0_{0}
5	298.15	$0.995_{0.004}$	$0.0035_{0.0001}$	1396.2_{250}
	400	$0.972_{0.026}$	$0.028_{0.004}$	58.2_{74}
	500	$0.909_{0.015}$	$0.091_{0.002}$	13.3_{10}
	600	$0.841_{0.009}$	$0.159_{0.002}$	13.5_{15}
	700	$0.780_{0.015}$	$0.220_{0.005}$	10.6_{27}
	800	$0.731_{0.010}$	$0.269_{0.003}$	8.7_{20}
10	298.15	$0.994_{0.009}$	$0.0037_{0.0004}$	1823.0_{610}
	400	$0.972_{0.013}$	$0.0281_{0.0009}$	220.4_{110}
	500	$0.911_{0.015}$	$0.089_{0.002}$	48.0_{32}
	600	$0.841_{0.013}$	$0.158_{0.002}$	19.7_{13}
	700	$0.780_{0.005}$	$0.220_{0.002}$	11.5_{13}
	800	$0.733_{0.010}$	$0.267_{0.003}$	8.8_{18}
15	298.15	$0.993_{0.008}$	$0.0036_{0.0006}$	3488.4_{460}
	400	$0.972_{0.014}$	$0.028_{0.001}$	393.1_{87}
	500	$0.910_{0.012}$	$0.090_{0.001}$	52.2_{29}
	600	$0.841_{0.009}$	$0.159_{0.002}$	21.5_{11}
	700	$0.781_{0.011}$	$0.219_{0.003}$	19.2_{23}
	800	$0.729_{0.005}$	$0.271_{0.002}$	$14.7_{7.5}$
20	298.15	$0.993_{0.006}$	$0.0044_{0.0006}$	2739.3_{1200}
	400	$0.972_{0.010}$	$0.0276_{0.0004}$	493.1_{71}
	500	$0.911_{0.009}$	$0.089_{0.002}$	91.5_{31}
	600	$0.841_{0.005}$	$0.159_{0.002}$	46.3_{25}
	700	$0.779_{0.005}$	$0.221_{0.002}$	$17.8_{5.8}$
	800	$0.731_{0.004}$	$0.269_{0.001}$	14.6_{16}
25	298.15	$0.992_{0.006}$	$0.0043_{0.0005}$	3931.5_{1100}
	400	$0.971_{0.017}$	$0.029_{0.002}$	511.4_{260}
	500	$0.911_{0.008}$	$0.089_{0.001}$	170.2_{77}

	600	$0.841_{0.008}$	$0.159_{0.001}$	58.0_{14}
	700	$0.779_{0.005}$	$0.221_{0.002}$	37.2_{12}
	800	$0.730_{0.005}$	$0.270_{0.002}$	$19.0_{8.6}$
30	298.15	$0.992_{0.005}$	$0.0046_{0.0004}$	3313.9_{420}
	400	$0.972_{0.013}$	$0.027_{0.002}$	511.7_{194}
	500	$0.912_{0.009}$	$0.088_{0.002}$	150.7_{64}
	600	$0.840_{0.009}$	$0.160_{0.002}$	54.5_{18}
	700	$0.779_{0.006}$	$0.220_{0.001}$	$28.5_{5.5}$
	800	$0.729_{0.006}$	$0.271_{0.003}$	$30.0_{8.6}$
40	298.15	$0.990_{0.006}$	$0.0051_{0.0004}$	5294.1_{520}
	350	$0.985_{0.004}$	$0.0136_{0.0005}$	1728.2_{280}
	400	$0.970_{0.008}$	$0.0289_{0.0004}$	874.0_{170}
	500	$0.911_{0.014}$	$0.089_{0.001}$	193.3_{41}
	600	$0.841_{0.009}$	$0.159_{0.002}$	77.6_{22}
	700	$0.778_{0.006}$	$0.222_{0.001}$	46.8_{15}
	800	$0.730_{0.004}$	$0.270_{0.003}$	26.3_{19}
50	298.15	$0.988_{0.007}$	$0.0050_{0.0004}$	6761.3_{1800}
	350	$0.984_{0.004}$	$0.0145_{0.0008}$	1951.9_{310}
	400	$0.970_{0.005}$	$0.0295_{0.0004}$	910.8_{130}
	500	$0.912_{0.003}$	$0.0879_{0.0008}$	257.6_{45}
	600	$0.840_{0.008}$	$0.160_{0.001}$	90.0_{19}
	700	$0.779_{0.008}$	$0.221_{0.002}$	57.1_{12}
	800	$0.730_{0.004}$	$0.270_{0.002}$	37.2_{13}
60	298.15	$0.987_{0.003}$	$0.0064_{0.0003}$	6127.1_{590}
	350	$0.982_{0.003}$	$0.0156_{0.0005}$	2367.8_{100}
	400	$0.969_{0.004}$	$0.0305_{0.0007}$	961.0_{150}
	500	$0.911_{0.005}$	$0.0886_{0.0004}$	286.7_{40}
	600	$0.840_{0.005}$	$0.160_{0.002}$	110.0_{18}
	700	$0.778_{0.005}$	$0.222_{0.002}$	69.7_{20}
	800	$0.729_{0.004}$	$0.271_{0.002}$	$43.0_{9.8}$

Table D.7: Mole fractions of CO_2, H_2, and HCOOH obtained using Monte Carlo simulations in the grand-canonical ensemble in the Zn-MOF-74 framework at 298.15 - 800 K and 1 - 60 bar. The mole fractions of CO_2, H_2, and HCOOH at reaction equilibrium obtained from the Continuous Fractional Component Monte Carlo simulations in the Reaction Ensemble [276] were used in the GCMC simulations as input. The subscripts show uncertainties computed using error propagation rules.

P/[bar]	T/[K]	x_{CO_2}	x_{H_2}	x_{HCOOH} / 10^{-6}
1	298.15	$0.997_{0.023}$	$0.0031_{0.0004}$	77.9_{70}
	400	$0.969_{0.054}$	$0.031_{0.004}$	$0.0_{0.0}$
	500	$0.912_{0.030}$	$0.088_{0.003}$	$0.1_{0.3}$
	600	$0.843_{0.020}$	$0.157_{0.007}$	0_{0}
	700	$0.786_{0.015}$	$0.214_{0.007}$	0_{0}
	800	$0.735_{0.010}$	$0.265_{0.008}$	0_{0}
5	298.15	$0.996_{0.003}$	$0.0036_{0.0002}$	289.3_{36}
	400	$0.970_{0.021}$	$0.030_{0.001}$	75.7_{65}
	500	$0.911_{0.018}$	$0.089_{0.003}$	16.8_{16}
	600	$0.846_{0.005}$	$0.154_{0.001}$	$4.2_{4.8}$
	700	$0.787_{0.007}$	$0.213_{0.002}$	$7.8_{9.2}$
	800	$0.737_{0.009}$	$0.263_{0.003}$	0_{0}
10	298.15	$0.996_{0.002}$	$0.0036_{0.0003}$	349.9_{100}
	400	$0.971_{0.004}$	$0.0291_{0.0007}$	92.6_{60}
	500	$0.913_{0.006}$	$0.087_{0.001}$	21.4_{13}
	600	$0.847_{0.017}$	$0.153_{0.003}$	15.6_{22}
	700	$0.786_{0.005}$	$0.214_{0.002}$	$7.6_{2.9}$
	800	$0.738_{0.007}$	$0.262_{0.002}$	$4.2_{5.5}$
15	298.15	$0.995_{0.005}$	$0.0041_{0.0004}$	702.7_{270}
	400	$0.971_{0.011}$	$0.0284_{0.0007}$	102.3_{20}
	500	$0.912_{0.011}$	$0.088_{0.001}$	39.5_{32}
	600	$0.845_{0.010}$	$0.155_{0.002}$	19.2_{17}
	700	$0.786_{0.006}$	$0.214_{0.002}$	14.5_{12}
	800	$0.737_{0.003}$	$0.263_{0.002}$	9.9_{14}
20	298.15	$0.995_{0.004}$	$0.0044_{0.0003}$	783.8_{200}
	400	$0.971_{0.009}$	$0.0284_{0.0008}$	159.1_{30}
	500	$0.912_{0.014}$	$0.088_{0.001}$	44.0_{17}
	600	$0.846_{0.005}$	$0.154_{0.002}$	35.0_{27}
	700	$0.786_{0.009}$	$0.214_{0.002}$	18.3_{14}
	800	$0.737_{0.005}$	$0.263_{0.002}$	10.4_{12}
25	298.15	$0.994_{0.004}$	$0.0045_{0.0001}$	990.3_{160}
	400	$0.971_{0.009}$	$0.0283_{0.0004}$	171.6_{53}
	500	$0.912_{0.013}$	$0.087_{0.001}$	77.8_{35}

	600	$0.845_{0.004}$	$0.155_{0.002}$	32.6_{27}
	700	$0.786_{0.008}$	$0.214_{0.002}$	20.3_{13}
	800	$0.737_{0.006}$	$0.263_{0.003}$	30.8_{20}
30	298.15	$0.994_{0.004}$	$0.0048_{0.0001}$	821.8_{270}
	400	$0.971_{0.007}$	$0.029_{0.001}$	253.4_{34}
	500	$0.913_{0.007}$	$0.086_{0.001}$	88.9_{44}
	600	$0.846_{0.007}$	$0.154_{0.001}$	38.1_{21}
	700	$0.786_{0.004}$	$0.2136_{0.0008}$	29.5_{15}
	800	$0.738_{0.006}$	$0.262_{0.002}$	14.8_{13}
40	298.15	$0.993_{0.003}$	$0.0055_{0.0004}$	1231.4_{400}
	350	$0.985_{0.003}$	$0.0140_{0.0009}$	549.5_{95}
	400	$0.971_{0.004}$	$0.0291_{0.0003}$	310.5_{43}
	500	$0.914_{0.009}$	$0.0861_{0.0007}$	$90.4_{9.5}$
	600	$0.846_{0.004}$	$0.1544_{0.0009}$	51.1_{22}
	700	$0.785_{0.004}$	$0.215_{0.001}$	34.4_{21}
	800	$0.737_{0.004}$	$0.2633_{0.0009}$	32.0_{11}
50	298.15	$0.993_{0.002}$	$0.0058_{0.0001}$	1474.1_{220}
	350	$0.984_{0.002}$	$0.0149_{0.0003}$	648.1_{120}
	400	$0.970_{0.004}$	$0.030_{0.001}$	347.0_{96}
	500	$0.913_{0.002}$	$0.0867_{0.0006}$	135.7_{13}
	600	$0.845_{0.005}$	$0.1546_{0.0008}$	71.9_{12}
	700	$0.785_{0.003}$	$0.215_{0.001}$	61.4_{15}
	800	$0.736_{0.003}$	$0.264_{0.001}$	30.9_{11}
60	298.15	$0.992_{0.006}$	$0.0065_{0.0004}$	1621.5_{770}
	350	$0.984_{0.007}$	$0.0151_{0.0008}$	736.2_{310}
	400	$0.968_{0.004}$	$0.0315_{0.0001}$	438.8_{68}
	500	$0.913_{0.013}$	$0.087_{0.001}$	157.3_{54}
	600	$0.845_{0.002}$	$0.1549_{0.0009}$	77.2_{17}
	700	$0.784_{0.007}$	$0.216_{0.002}$	57.0_{12}
	800	$0.736_{0.004}$	$0.264_{0.002}$	$46.3_{5.6}$

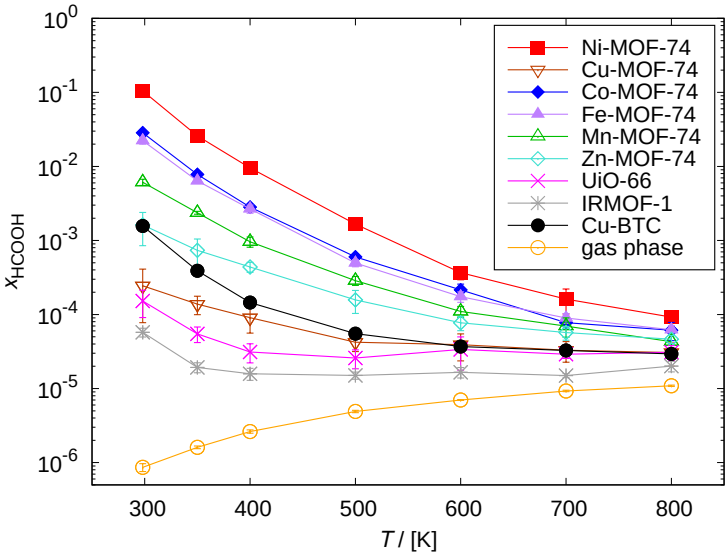

Fig. D.6. HCOOH mole fractions computed from Monte Carlo simulations in the grand-canonical ensemble in M-MOF-74 compared to the literature data for UiO-66, Cu-BTC, IRMOF-1, and the gas phase [276] at 298.15 - 800 K and 60 bar. The mole fractions of HCOOH computed from the Rx/CFC simulations in the study by Wasik et al. [276] are used as an input for the GCMC ensemble. The HCOOH mole fractions decrease with the increasing temperature. The highest HCOOH production resulted from the effect of confinement in Ni-MOF-74 at 298.15 K with a mole fraction equal to ca. 0.1.

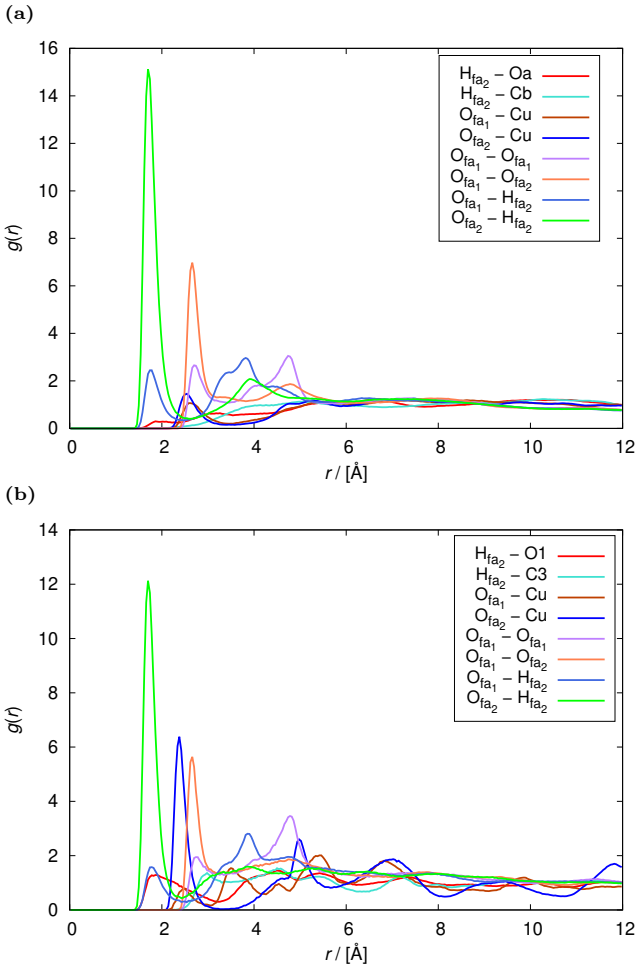

Fig. D.7. Radial distribution functions for 50 molecules of HCOOH in MOFs at 298 K: (a) Cu-MOF-74, and (b) Cu-BTC. While ca. 6 molecules are present in Cu-BTC within the preferential distance to the metal centers of 2.4 Å [276], in Cu-MOF-74 only ca. 1.5 adsorbed molecules of HCOOH are within the distance of 2.54 Å to the metal centers. This difference in intensity is due to the higher charge on the metal center in Cu-BTC compared to Cu-MOF-74. The same effect is observed for the most electronegative ligand atom of the frameworks. The stronger electronegativity of the oxygen atom in Cu-BTC leads to a higher intensity of HCOOH adsorption oriented towards this atom (H_{fa2}-O1) that in Cu-MOF-74 (H_{fa2}-Oa). The formation of hydrogen bonds between HCOOH molecules is slightly more intense in Cu-MOF-74 than in Cu-BTC due to weaker interactions with the framework. The simulations were performed using the RASPA software package [94, 95].

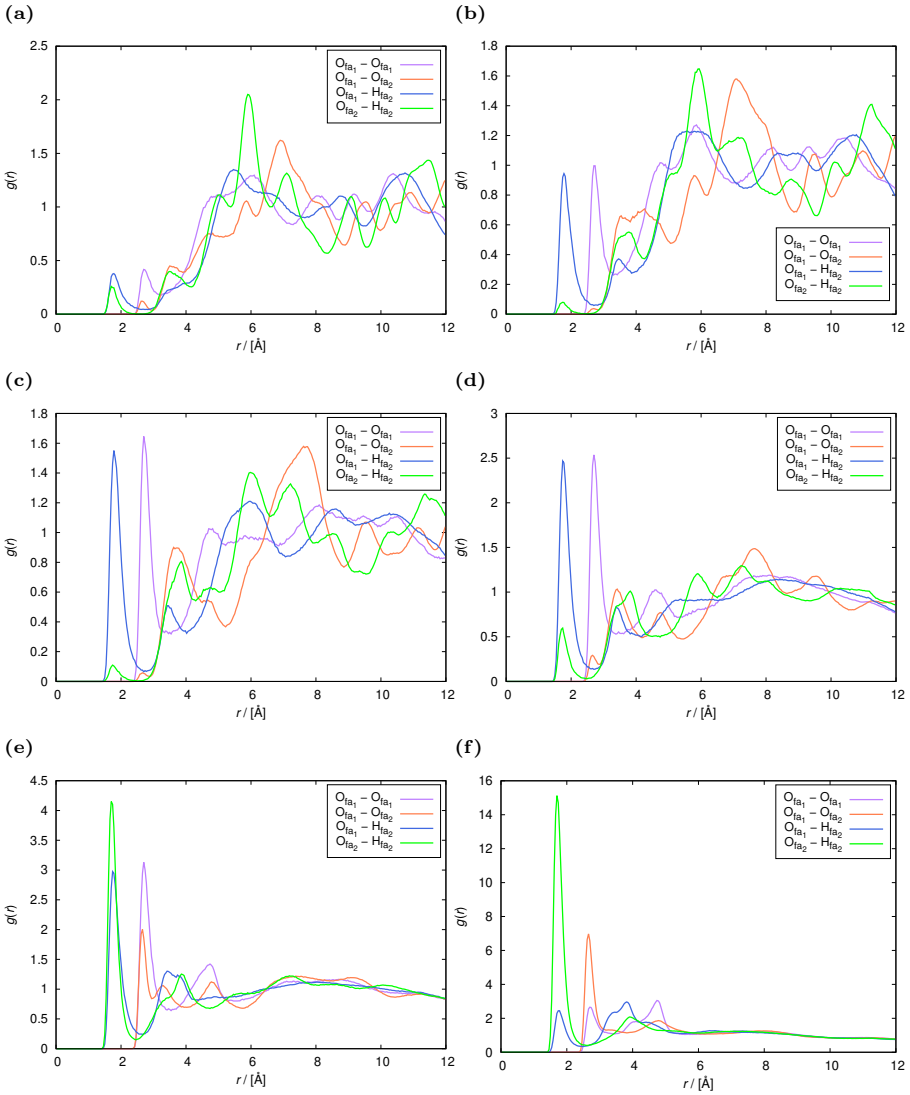

Fig. D.8. Radial distribution functions simulated for 50 molecules of HCOOH at 298 K in: (a) Ni-MOF-74, (b) Co-MOF-74, (c) Fe-MOF-74, (d) Mn-MOF-74, (e) Zn-MOF-74, and (f) Cu-MOF-74. The intensity of hydrogen bond formation increase with decreasing affinity of HCOOH with the framework. In Zn-, and Cu-MOF-74, the HCOOH dimerization is found to be prevalent over the hydrogen bonds-driven nucleation. The simulations were performed using the RASPA software package [94, 95].

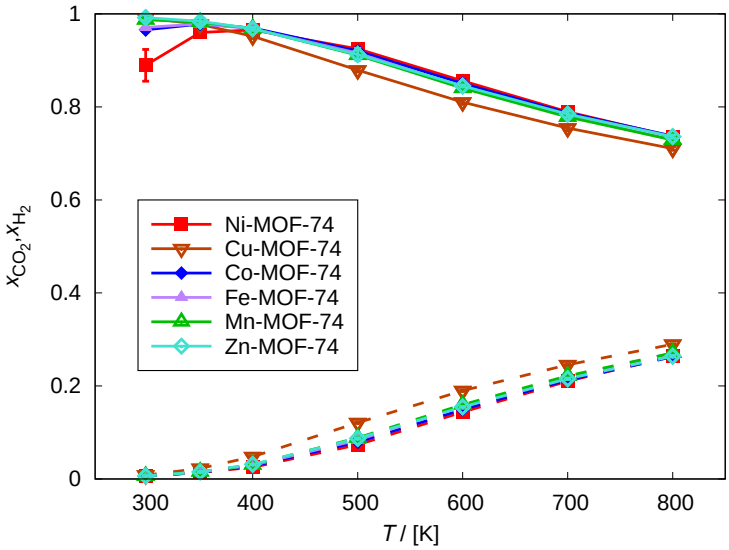

Fig. D.9. Mole fractions of CO_2 and H_2 computed from Monte Carlo simulations in the grand-canonical ensemble in M-MOF-74. The mole fractions computed from the Rx/CFC simulations are used as an input for the GCMC ensemble. The simulations were carried out at 298.15 - 800 K and 60 bar. The data points of CO_2 mole fractions are connected by the solid lines and the data points of H_2 mole fractions by the dashed lines to guide the eye. The mole fractions of CO_2 decrease with increasing temperature, except for Ni-, Co-, and Fe-MOF-74 at the temperature range 298.15 - 350 K, where the mole fraction of CO_2 slightly increases. The increase is caused by the large decrease in HCOOH production, affecting mole fractions of the other components. The number of adsorbed CO_2 molecules decreases throughout the range of studied temperatures. The mole fractions of H_2 increase with temperature.

Appendix E

Appendix E corresponds to Chapter 7 of this thesis.

- The experimental data for vapor-liquid equilibrium pressures and vaporization enthalpies of formic acid reported by the DIPPR database used for the optimization of the thermodynamic model;
- The change in Gibbs free energy and equilibrium constants of formic acid dimerization computed from Quantum Mechanics and umbrella sampling Monte Carlo simulations;
- Vapor-liquid equilibrium properties of formic acid computed from Monte Carlo simulations in the Gibbs ensemble.

Table E.1: The experimental data for P_{VLE} of formic acid reported by the DIPPR database [373] used for the optimization of the thermodynamic model.

T/[K]	P/[Pa]	T/[K]	P/[Pa]	T/[K]	P/[Pa]
323.15	15999	298.15	5733	374.39	103000
271.25	1333.2	267.92	1082.6	376.62	110000
283.35	2666.4	273.15	1487.9	382.41	130000
291.02	3999.7	281.4	2391.8	398.25	200000
296.75	5332.9	285.72	3029.1	299.79	6188
301.37	6666.1	293.15	4473	307.58	8881
311.63	10666	303.11	7247.4	310.03	9896
316.78	13332	313.04	11356	316.8	13293
326.62	19998	323.08	17345	324.84	18432
334.01	26664	333.13	25691	329.03	21830
345.08	39997	343.19	37410	336.16	28640
353.42	53329	353.08	52742	344.58	38845
360.2	66661	373.83	101660	349.13	45630
370.97	93325	383.77	135670	353.36	52449
373.71	101320	285.65	3000	357	59295
383.17	133320	291.15	4000	364.87	76343
389.75	159990	299.32	6000	374.78	103610
398.15	199980	310.31	10000	384.6	137770
283.45	2666.4	319.7	15000	392.65	172040
297.15	5332.9	326.74	20000		
305.55	7999.3	337.27	30000		
316.95	13332	345.2	40000		
334.55	26664	351.63	50000		
353.45	53329	357.09	60000		
373.75	101320	361.84	70000		
353.15	52240	366.08	80000		
413.15	291000	369.9	90000		
423.15	369100	371.68	95000		
453.15	706400	373.06	99000		
277.76	2000	373.39	100000		

Table E.2: The experimental data for $\Delta_{\text{vap}}H$ of formic acid reported by the DIPPR database [373] used for the optimization of the thermodynamic model.

$T/[\text{K}]$	$\Delta_{\text{vap}}H/[\text{kJ/kg}]$
298.15	432.37
580	204.23
300	438.89
400	493.20
450	504.07
500	491.03
550	401.95
315.35	444.34
337.65	457.74
373.65	483.25
298.15	436.71
250	404.77
300	438.89
400	493.20
450	504.07
500	491.03
550	401.95
560	362.84
570	317.21
353.15	458.22
413.15	501.24
423.15	506.67
453.15	509.06

Table E.3: The change in Gibbs free energy and equilibrium constants of HCOOH dimerization computed from Quantum Mechanics and both routes of umbrella sampling Monte Carlo simulations performed using Brick-CFCMC [143, 152]: dimer counting and potential of mean force computation (PMF). The subscripts show uncertainties computed as the standard deviation from five independent simulations.

T/[K]	QM	
	ΔG/[kJ/mol]	K
250	-25.98	267624.18
260	-24.60	87404.27
270	-23.22	31012.69
280	-21.84	11849.19
290	-20.46	4837.88
300	-19.08	2096.80
T/[K]	MC - Dimer counter	
	ΔG/[kJ/mol]	K
250	$-26.06_{0.05}$	279183.08_{6900}
260	$-25.21_{0.06}$	116139.11_{3100}
270	$-23.97_{0.06}$	43415.90_{1100}
280	$-22.51_{0.07}$	15856.94_{480}
290	$-20.96_{0.05}$	5966.76_{120}
300	$-19.26_{0.09}$	2257.39_{80}
T/[K]	MC - PMF	
	ΔG/[kJ/mol]	K
250	$-26.37_{0.07}$	322922.20_{12000}
260	$-24.88_{0.1}$	99964.41_{4800}
270	$-23.36_{0.1}$	33084.16_{1400}
280	$-21.86_{0.08}$	11970.10_{410}
290	$-20.91_{0.03}$	5835.63_{65}
300	$-18.80_{0.09}$	1880.98_{72}

Table E.4: Vapor-liquid equilibrium properties of HCOOH computed from Monte Carlo simulations in the Gibbs ensemble, performed using Brick-CFCMC [143, 152]: densities of the liquid and vapor phases, mole fractions of HCOOH monomer in the liquid and vapor phases, saturation pressure, enthalpy of vaporization, and the entropies of the liquid and vapor phases. The subscripts show uncertainties computed as the standard deviation from five independent simulations.

T /[K]	ρ_{liq} /[kg/m^3]	ρ_{vap} /[kg/m^3]	X_{liq}	X_{vap}
335	$1166.84_{0.19}$	$1.36_{0.19}$	$0.00892_{0.00010}$	$0.4600_{0.0008}$
360	$1132.99_{0.53}$	$3.01_{0.53}$	$0.01371_{0.00002}$	$0.5049_{0.0020}$
385	$1096.48_{0.34}$	$5.53_{0.34}$	$0.02040_{0.00006}$	$0.5051_{0.0005}$
410	$1056.91_{0.39}$	$10.14_{0.39}$	$0.02942_{0.00009}$	$0.5145_{0.0004}$
435	$1014.56_{0.54}$	$15.90_{0.54}$	$0.04100_{0.00006}$	$0.5235_{0.0003}$
460	$966.26_{0.43}$	$26.02_{0.43}$	$0.05636_{0.00026}$	$0.5305_{0.0003}$
485	$911.59_{0.41}$	$39.62_{0.41}$	$0.07598_{0.00011}$	$0.5341_{0.0038}$
510	$847.88_{0.31}$	$59.23_{0.31}$	$0.10111_{0.00017}$	$0.5214_{0.0015}$
535	$767.36_{2.57}$	$90.16_{2.57}$	$0.13448_{0.00061}$	$0.4977_{0.0081}$
560	$657.31_{5.33}$	$140.46_{5.33}$	$0.18185_{0.00154}$	$0.4587_{0.0095}$

T /[K]	P_{sat} /[bar]	$\Delta_{\mathrm{vap}}H$ /[kJ/kg]	s_{liq} /[kJ/kg K]	s_{vap} /[kJ/kg K]
335	$0.39_{0.14}$	746.58_{32}	$1.386_{0.04}$	$3.545_{0.08}$
360	$0.73_{0.18}$	674.92_{39}	$1.632_{0.04}$	$3.479_{0.10}$
385	$1.86_{0.09}$	649.11_{14}	$1.920_{0.01}$	$3.523_{0.03}$
410	$3.41_{0.05}$	603.45_{12}	$2.141_{0.002}$	$3.536_{0.03}$
435	$5.80_{0.06}$	$585.00_{9.0}$	$2.345_{0.001}$	$3.610_{0.02}$
460	$9.37_{0.07}$	$542.14_{4.6}$	$2.532_{0.001}$	$3.636_{0.01}$
485	$14.30_{0.11}$	$500.87_{2.6}$	$2.706_{0.001}$	$3.669_{0.005}$
510	$20.86_{0.15}$	$447.75_{1.3}$	$2.8710_{0.0005}$	$3.685_{0.002}$
535	$29.17_{0.18}$	$377.45_{6.4}$	$3.032_{0.002}$	$3.685_{0.01}$
560	$39.65_{0.26}$	$280.72_{9.3}$	$3.197_{0.003}$	$3.660_{0.01}$

Summary

There is a growing interest in economically attractive technologies for reducing carbon dioxide emissions while synthesizing a product with a wide range of applications. One of the possible routes for carbon dioxide conversion is the electrochemical reduction to formic acid (HCOOH) in an aqueous solution. This is not optimal due to the low solubility of carbon dioxide in water. It is crucial to investigate the possibilities of improving the solubility of carbon dioxide and thus the efficiency of the carbon dioxide conversion without decreasing the ionic conductivity of an electrolyte solution. Another method for formic acid production is the carbon dioxide hydrogenation reaction. The high free energy barrier of carbon dioxide hydrogenation in the gas phase indicates that a catalyst is needed to mediate the reduction. The cost of transition metal catalysts and the toxicity of the transition elements are two major limitations in their usage. The confinement effect of porous materials on the thermodynamical equilibrium of the reaction may be considered a cost-effective alternative to the transition metal catalysts, provided that the reaction free energy barrier is not too high. Due to the higher density of the pore phase compared to the gas phase by Le Chatelier's principle and the selective adsorption of favored components, the equilibrium distribution in the pore is different from that in the gas phase. In this work, advancements in formic acid production methods are proposed through force field-based Monte Carlo molecular simulation studies. The selected force field for formic acid was validated by reproducing the experimental densities, vapor-liquid equilibrium coexistence curve, and saturated vapor pressures. Implementation of the Continuous Fractional Component method for Monte Carlo simulations in the NVT/NPT ensembles enabled the direct calculation of chemical potentials. This allowed for the observation of increased carbon dioxide solubility with increasing formic acid fraction in the solution, suggesting formic acid production as a potential method to enhance carbon dioxide solubility. To study the thermodynamic confinement effects on the carbon dioxide hydrogenation to

formic acid, Monte Carlo simulations in the grand-canonical ensemble were performed in Metal-Organic Frameworks (MOFs), using gas-phase mole fractions of carbon dioxide, hydrogen, and formic acid at chemical equilibrium, obtained from Continuous Fractional Component Monte Carlo simulations in the Reaction Ensemble. By comparing the performance of MOFs with different pore size distributions and metal centers, it is found that the stronger confinement resulting from the smaller pores does not guarantee the improvement of formic acid production in the carbon dioxide hydrogenation reaction. The prevailing factor is the type of metal center in the metal-organic framework. Due to the presence of highly reactive open-metal sites, the M-MOF-74 series allows to fully investigate the dependence of formic acid production enhancement on the type of metal center, minimizing the effect of pore size. Non-polarizable carbon dioxide, and hydrogen force fields for adsorption in M-MOF-74 (M = Ni, Cu, Co, Fe, Mn, Zn), compatible with the formic acid force field are adjusted by scaling the Coulombic interactions of M-MOF-74 atoms and Lennard-Jones interaction potentials between the center of mass of hydrogen and the open-metal centers. The computed loadings, heats of carbon dioxide and hydrogen adsorption, and binding geometries in M-MOF-74 are in very good agreement with experimental data. The equilibrium geometries of formic acid in M-MOF-74 computed from force field-based simulations using Baker's minimization method are comparable to the results from DFT calculations. Depending on the metal center, the enhancement in formic acid production decreases in the same order as its isosteric heat of adsorption: Ni > Co > Fe > Mn > Zn > Cu. The strongest host-guest interaction of formic acid with Ni-MOF-74 causes the most significant influence on the carbon dioxide hydrogenation thermodynamics, enhancing formic acid production by ca. 10^5 times compared to the gas phase at 298.15 K, 60 bar. Ni-MOF-74 has the potential to be an alternative to transition metal catalysts for improving formic acid production due to the elimination of the high-cost temperature elevation, more valuable final product, and comparable final concentration of formic acid to the reported concentrations of formate obtained using transition metal catalysts. Additionally, this work introduces a multi-scale methodology integrating force field-based Monte Carlo simulations, Quantum Mechanics, and equations of state to characterize the thermodynamics of formic acid dimerization for the potential application as a new reactive fluid in thermodynamic cycles. This approach effectively predicts equilibrium constants, the enthalpy and entropy of dimerization, as well as phase equilibrium properties with high accuracy compared to experimental data. The methodology demonstrates strong agreement between different computational methods, showing its potential for predicting the thermodynamic properties of similar reactive systems.

Curriculum Vitae

Dominika O. Wasik

16.10.1994
Born in Wrocław, Poland

2013–2017
Bachelor's Degree in Chemical Technology (B.Sc. Eng.)
Wrocław University of Technology, Poland

2017–2018
Master's Degree in Chemical Technology (M.Sc. Eng.)
Wrocław University of Technology, Poland

2018–2020
Erasmus Mundus Joint Master Degree in Chemical Nano-Engineering (M.Sc. Eng.)
Aix-Marseille Université, France
Wrocław University of Technology, Poland
Università degli Studi di Roma 'Tor Vergata', Italy
Thesis: University of Missouri, Columbia, USA

07–08.2019
Research Internship
University of Queensland, Brisbane, Australia

2020–2024
Doctoral Degree in Materials Simulation and Modelling
Eindhoven University of Technology, The Netherlands

List of Publications

Publications included in this thesis

1. Wasik, D. O., Polat, H. M., Ramdin, M., Moultos, O. A., Calero, S., Vlugt, T. J. H. Solubility of CO_2 in Aqueous Formic Acid Solutions and the Effect of NaCl Addition: A Molecular Simulation Study. *Journal of Physical Chemistry C* **2022**, *126*, 19424-19434.

2. Wasik, D. O., Martín-Calvo, A., Gutiérrez-Sevillano, J. J., Dubbeldam, D., Vlugt, T. J. H., Calero, S. Enhancement of Formic Acid Production from Carbon Dioxide Hydrogenation Using Metal-Organic Frameworks: Monte Carlo Simulation Study. *Chemical Engineering Journal* **2023**, *467*, 143432.

3. Wasik, D. O., Vicent-Luna, J. M., Luna-Triguero, A., Dubbeldam, D., Vlugt, T. J. H., Calero, S. The Impact of Metal Centers in the M-MOF-74 Series on Carbon Dioxide and Hydrogen Separation. *Separation and Purification Technology* **2024**, *339*, 126539.

4. Wasik, D. O., Vicent-Luna, J. M., Rezaie, S., Luna-Triguero, A., Vlugt, T. J. H., Calero, S. The Impact of Metal Centers in the M-MOF-74 Series on Formic Acid Production. *ACS Applied Materials & Interfaces* **2024**, *16*, 45006-45019.

5. Wasik, D. O., Lasala, S., Herbinet, O., Vlugt, T. J. H., Calero, S. Multiscale Modelling of Dimerization Thermodynamics of Formic Acid (submitted **2024**).

Other publications

1. Polat, H. M., Salehi, H. S., Hens, R., Wasik, D. O., Rahbari, A., De Meyer, F., Houriez, C., Coquelet, C., Calero, S., Dubbeldam, D., Moultos, O. A., Vlugt, T. J. H. New Features of the Open Source Monte Carlo Software Brick-CFCMC: Thermodynamic Integration and Hybrid Trial Moves. *Journal of Chemical Information and Modeling* **2021**, *61*, 3752-3757.

List of Presentations

1. Presentation at Computational Methods in Nanothermodynamics workshop, Trondheim, Norway, 7–8.04.2022:
   'Solubility of CO_2 in Aqueous Formic Acid Solutions and the Effect of Adding NaCl Studied by Molecular Simulations'

2. Presentation at XLII Iberian Adsorption Meeting (42RIA), Valencia, Spain, 13–16.09.2022:
   'The Synthesis of Formic Acid from Carbon Dioxide by Hydrogenation in Metal-Organic Framework UiO-66 Studied by Molecular Simulations'

3. Presentation at Eleventh International Symposium Effects of Surface Heterogeneity in Adsorption, Catalysis and related Phenomena (ISSHAC-11), Zegrze, Poland, 18–22.09.2022:
   'Solubility of CO_2 in Aqueous Formic Acid Solutions and the Effect of NaCl Addition: A Molecular Simulation Study'

4. Presentation at XLIII Iberian Adsorption Meeting (43RIA), Porto, Portugal, 1–4.09.2024:
   'The Impact of Metal Centers in the Metal-Organic Frameworks on Carbon Dioxide Hydrogenation to Formic Acid'

Acknowledgments

I would like to express my deepest gratitude to my supervisors, Sofía and Thijs, for their guidance, and encouragement throughout this journey. Sofía, your insightful feedback and patience have been crucial in shaping this work. Thijs, your expertise and constructive critiques have consistently pushed me to refine my ideas and reach new heights. I am truly grateful for the time and effort you both invested in me and my research. This thesis would not have been possible without your dedication and mentorship.

I also want to thank the members of my thesis committee: prof.dr. P.A. Bobbert, prof.dr.ir. B. Kuchta, prof.dr. K. Hooman, and dr. D. Dubbeldam. My appreciation extends to the chairman, prof.dr. F. Toschi. I express my sincere gratitude to my colleagues in the Materials Simulation & Modelling group, especially Esteban, with whom I shared an office for four years. Thank you for being a great colleague and contributing to a positive work environment. I am grateful to all co-authors from my PhD studies — Vicent, Silvia, Olivier, Shima, Azahara, David, Juanjo, Ana, Mert, Otto, and Mahinder — for the excellent collaborations and invaluable contributions.

A special and heartfelt thanks go to my partner, Mairon Mahzoun. Thank you for being the best person, supporting me, and boosting my confidence in research while sharing memorable adventures, such as watching volcano explosions, kayaking near icebergs, searching for cassowaries, mountaineering, exploring sacred desert hills, and astronomical observations while camping in the wilderness. Your companionship make every journey, both in life and in science, truly extraordinary.

I thank my family, especially my mom, Sabina Szczupak-Wasik, for her support and encouragement in pursuing science. Thank you for always believing in me and for being a constant source of motivation and strength. I am also grateful to my grandma, Krystyna Szczupak, for placing great value on my education. Finally, I would like to thank my friends, Nikola, Kasia, Łukasz, and Norbert, for their support during stressful times, and ability to provide both a listening ear and a sense of humor.

References

[1] Peter, S. C. Reduction of CO_2 to Chemicals and Fuels: A Solution to Global Warming and Energy Crisis. *ACS Energy Letters* **2018**, *3*, p. 1557.

[2] Dowell, N. M., Fennell, P. S., Shah, N. and Maitland, G. C. The Role of CO_2 Capture and Utilization in Mitigating Climate Change. *Nature Climate Change* **2017**, *7*, pp. 243–249.

[3] Singh, N. B. *In Conversion of CO_2 into Useful Products. Industrial Waste: Characterization, Modification and Applications of Residues.* Ed. by H. Pöllmann. 4th ed. Berlin, Boston: De Gruyter, 2021, pp. 319–344.

[4] M. Aresta, ed. *Carbon Dioxide Recovery and Utilization.* 4th ed. Dordrecht: Kluwer Academic Publishers, 2010.

[5] Adams, D. and Boopathy, R. Use of Formic Acid to Control Vibriosis in Shrimp Aquaculture. *Biologia* **2013**, *68*, pp. 1017–1021.

[6] Cheremisinoff, N. P. and Rosenfeld, P. E. *Handbook of Pollution Prevention and Cleaner Production. Chapter 6 - Sources of air emissions from pulp and paper mills.* Oxford: William Andrew Publishing, 2010, pp. 179–259.

[7] Grasemann, M. and Laurenczy, G. Formic Acid as a Hydrogen Source – Recent Developments and Future Trends. *Energy & Environmental Science* **2012**, *5*, pp. 8171–8181.

[8] Hietala, J., Vuori, A., Johnsson, P., Pollari, I., Reutemann, W. and Kieczka, H. *Ullmann's Encyclopedia of Industrial Chemistry. Formic Acid.* 7th ed. John Wiley & Sons, Ltd, 2016, pp. 1–22. URL: https://onlinelibrary.wiley.com/doi/abs/10.1002/14356007.a12_013.pub3.

[9] Yasaka, Y., Yoshida, K., Wakai, C., Matubayasi, N. and Nakahara, M. Kinetic and Equilibrium Study on Formic Acid Decomposition in Relation to the Water-Gas-Shift Reaction. *Journal of Physical Chemistry A* **2006**, *110*, p. 11082.

[10] Ajingi, Y. S., Ruengvisesh, S., Khunrae, P., Rattanarojpong, T. and Jongruja, N. The Combined Effect of Formic Acid and Nisin on Potato Spoilage. *Biocatalysis and Agricultural Biotechnology* **2020**, *24*, p. 101523.

[11] Fathima, N., Rao, J. and Nair, B. Cost Effective Fixing Process for Post Tanning Operation. *Jalca* **2010**, *105*, pp. 100–106.

[12] Yang, H., Kaczur, J. J., Sajjad, S. D. and Masel, R. I. Electrochemical Conversion of CO_2 to Formic Acid Utilizing Sustainion^{TM} Membranes. *Journal of CO_2 Utilization* **2017**, *20*, pp. 208–217.

[13] Scibioh, M. and Viswanathan, B. Electrochemical Reduction of Carbon Dioxide: A Status Report. *Proceedings of the Indian National Science Academy* **2004**, *70*, p. 407.

[14] Lu, X., Leung, D. Y. C., Wang, H., Leung, M. K. H. and Xuan, J. Electrochemical Reduction of Carbon Dioxide to Formic Acid. *ChemElectroChem* **2014**, *1*, pp. 836–849.

[15] Hu, B., Guild, C. and Suib, S. L. Thermal, Electrochemical, and Photochemical Conversion of CO_2 to Fuels and Value-Added Products. *Journal of CO_2 Utilization* **2013**, *1*, pp. 18–27.

[16] König, M., Vaes, J., Klemm, E. and Pant, D. Solvents and Supporting Electrolytes in the Electrocatalytic Reduction of CO_2. *iScience* **2019**, *19*, pp. 135–160.

[17] Ramdin, M., Morrison, A. R. T., Groen, M. de, Haperen, R. van, Kler, R. de, Irtem, E., Laitinen, A. T., Broeke, L. J. P. van den, Breugelmans, T., Trusler, J. P. M., Jong, W. d. and Vlugt, T. J. H. High-Pressure Electrochemical Reduction of CO_2 to Formic Acid/Formate: Effect of pH on the Downstream Separation Process and Economics. *Industrial & Engineering Chemistry Research* **2019**, *58*, pp. 22718–22740.

[18] Moret, S., Dyson, P. and Laurenczy, G. Direct Synthesis of Formic Acid from Carbon Dioxide by Hydrogenation in Acidic Media. *Nature Communications* **2014**, *5*, p. 4017.

[19] Ghara, M. and Chattaraj, P. K. A Computational Study on Hydrogenation of CO_2, Catalyzed by a Bridged B/N Frustrated Lewis Pair. *Structural Chemistry* **2019**, *30*, pp. 1067–1077.

[20] *Cluster 5: Climate, Energy and Mobility. 2023*. Tech. rep. Access date: 5 June 2024. European Commission. URL: https://ec.europa.eu/info/research-and-innovation/funding/funding-opportunities/funding-programmes-and-open-calls/horizon-europe/cluster-5-climate-energy-and-mobility_en.

[21] *Global Energy Review 2019, Paris. 2020*. Tech. rep. Access date: 6 July 2024. IEA. URL: https://www.iea.org/reports/global-energy-review-2019.

[22] *CO_2 Emissions in 2023, Paris. 2024*. Tech. rep. Access date: 15 May 2024. IEA. URL: https://www.iea.org/reports/CO2-emissions-in-2023.

[23] *National Climate Agreement: The Netherlands. 2019*. Tech. rep. Access date: 26 June 2024. Government of the Netherlands. URL: https://www.klimaatakkoord.nl/documenten/publicaties/2019/06/28/national-climate-agreement-the-netherlands.

[24] European Commission. *An official website of the European Union*. Access date: 6 July 2024. 2023. URL: https://climate.ec.europa.eu/news-your-voice/news/fit-55-eu-reaches-new-milestone-make-all-new-cars-and-vans-zero-emission-2035-2023-03-28_en.

[25] Michele Aresta, A. D. and Quaranta, E. *Reaction Mechanisms in Carbon Dioxide Conversion*. 1st ed. Springer, 2016.

[26] *Formic Acid Market - Growth, Trends, COVID-19 Impact, and Forecasts (2023 - 2028)*. Tech. rep. Mordor Intelligence, 2023.

[27] Smith, R. M. and Martell, A. E. *Critical Stability Constants Volume 6: Second Supplement*. New York: Plenum Press, 1989.

[28] Chao, J. and Zwolinski, B. J. Ideal Gas Thermodynamic Properties of Methanoic and Ethanoic Acids. *Journal of Physical and Chemical Reference Data* **1978**, *7*, pp. 363–377.

[29] National Center for Biotechnology Information. *Formic Acid*. Accessed: 2024-07-06. 2021. URL: https://pubchem.ncbi.nlm.nih.gov/compound/Formic-acid.

[30] J. I. Kroschwitz, ed. *Kirk-Othmer Encyclopedia of Chemical Technology*. John Wiley & Sons, 2004.

[31] *Formic Acid Market Analysis By Concentration (Formic Acid of 85% Concentration, 90% Concentration, 94% Concentration, 99% Concentration), By Application (Formic Acid For Animal Feed, Agricultural Products, Leather Tanning), By Region - Global Insights 2021-2031. 2021.* Tech. rep. Access date: 20 August 2022. Fact.MR. URL: https://www.factmr.com/report/4279/formic-acid-market.

[32] Eppinger, J. and Huang, K.-W. Formic Acid as a Hydrogen Energy Carrier. *ACS Energy Letters* **2016**, *2*, p. 188.

[33] *Formic Acid Market Analysis By Formic Acid of 85% Concentration, 90% Concentration, 94% Concentration, and 99% Concentration from 2023 to 2033. 2023.* Tech. rep. Access date: 15 May 2024. Fact.MR, URL: https://www.factmr.com/report/4279/formic-acid-market.

[34] Rumayor, M., Dominguez-Ramos, A. and Irabien, A. Formic Acid Manufacture: Carbon Dioxide Utilization Alternatives. *Applied Sciences* **2018**, *8*, p. 914.

[35] O'Neill, B. J., Gürbüz, E. I. and Dumesic, J. A. Reaction Kinetics Studies of the Conversions of Formic Acid and Butyl Formate over Carbon-supported Palladium in the Liquid Phase. *Journal of Catalysis* **2012**, *290*, p. 193.

[36] Gibson, H. W. Chemistry of Formic Acid and Its Simple Derivatives. *Chemical Reviews* **1969**, *69*, p. 673.

[37] Dickson, S., Bakker, J. and Kitai, A. *Chemical Economics Handbook. Acetic acid.* March 1982 revised July 1982. Menlo Park, Calif: SRI International, 1982, pp. 6025020–6025021.

[38] Dubbeldam, D., Calero, S. and Vlugt, T. J. H. iRASPA: GPU-Accelerated Visualization Software for Materials Scientists. *Molecular Simulation* **2018**, *44*, pp. 653–676.

[39] Gattrell, M., Gupta, N. and Co, A. Electrochemical Reduction of CO_2 to Hydrocarbons to Store Renewable Electrical Energy and Upgrade Biogas. *Energy Conversion and Management* **2007**, *48*, pp. 1255–1265.

[40] Sternberg, A. and Bardow, A. Power-to-What? – Environmental Assessment of Energy Storage Systems. *Energy Environ. Sci.* **2015**, *8*, pp. 389–400.

[41] Rahbari, A., Ramdin, M., Broeke, L. J. P. van den and Vlugt, T. J. H. Combined Steam Reforming of Methane and Formic Acid To Produce Syngas with an Adjustable H_2:CO Ratio. *Industrial & Engineering Chemistry Research* **2018**, *57*, pp. 10663–10674.

[42] Bushuyev, O. S., De Luna, P., Dinh, C. T., Tao, L., Saur, G., van de Lagemaat, J., Kelley, S. O. and Sargent, E. H. What Should We Make with CO_2 and How Can We Make It? *Joule* **2018**, *2*, pp. 825–832.

[43] Luna, P. D., Hahn, C., Higgins, D., Jaffer, S. A., Jaramillo, T. F. and Sargent, E. H. What Would It Take for Renewably Powered Electrosynthesis to Displace Petrochemical Processes? *Science* **2019**, *364*, eaav3506.

[44] Le Chatelier, H. and Boudouard, O. On the Flammable Limits of Gas Mixtures. *Process Safety Progress* **2005**, *24*, pp. 3–5.

[45] Anawati, Frankel, G., Agarwal, A. and Sridhar, N. Degradation and Deactivation of Sn Catalyst Used for CO_2 Reduction as Function of Overpotential. *Electrochimica Acta* **2014**, *133*, pp. 188–196.

[46] Ramdin, M., Morrison, A. R. T., Groen, M. de, Haperen, R. van, Kler, R. de, Broeke, L. J. P. van den, Trusler, J. P. M., Jong, W. de and Vlugt, T. J. H. High Pressure Electrochemical Reduction of CO_2 to Formic Acid/Formate: A Comparison between Bipolar Membranes and Cation Exchange Membranes. *Industrial & Engineering Chemistry Research* **2019**, *58*, pp. 1834–1847.

[47] Duarte, M., De Mot, B., Hereijgers, J. and Breugelmans, T. Electrochemical Reduction of CO_2: Effect of Convective CO_2 Supply in Gas Diffusion Electrodes. *ChemElectroChem* **2019**, *6*, pp. 5596–5602.

[48] De Mot, B., Ramdin, M., Hereijgers, J., Vlugt, T. J. H. and Breugelmans, T. Direct Water Injection in Catholyte-Free Zero-Gap Carbon Dioxide Electrolyzers. *ChemElectroChem* **2020**, *7*, pp. 3839–3843.

[49] De Mot, B., Hereijgers, J., Duarte, M. and Breugelmans, T. Influence of Flow and Pressure Distribution Inside a Gas Diffusion Electrode on the Performance of a Flow-by CO_2 Electrolyzer. *Chemical Engineering Journal* **2019**, *378*, p. 122224.

[50] Duan, Z. and Sun, R. An Improved Model Calculating CO_2 Solubility in Pure Water and Aqueous NaCl Solutions from 273 to 533 K and from 0 to 2000 bar. *Chemical Geology* **2003**, *193*, p. 257.

[51] Liu, B., Mahmood, B. S., Mohammadian, E., Khaksar Manshad, A., Rosli, N. R. and Ostadhassan, M. Measurement of Solubility of CO_2 in NaCl, $CaCl_2$, $MgCl_2$ and $MgCl_2$ + $CaCl_2$ Brines at Temperatures from 298 to 373 K and Pressures up to 20 MPa Using the Potentiometric Titration Method. *Energies* **2021**, *14*, p. 7222.

[52] Koschel, D., Coxam, J.-Y., Rodier, L. and Majer, V. Enthalpy and Solubility Data of CO_2 in Water and NaCl(aq) at Conditions of Interest for Geological Sequestration. *Fluid Phase Equilibria* **2006**, *247*, p. 107.

[53] Liu, Y., Hou, M., Yang, G. and Han, B. Solubility of CO_2 in Aqueous Solutions of NaCl, KCl, $CaCl_2$ and Their Mixed Salts at Different Temperatures and Pressures. *Journal of Supercritical Fluids* **2011**, *56*, p. 125.

[54] Inoue, Y., Izumida, H., Sasaki, Y. and Hashimoto, H. Catalytic Fixation of Carbon Dioxide to Formic Acid by Transition-Metal Complexes Under Mild Conditions. *Chem. Lett.* **1976**, *5*, pp. 863–864.

[55] Ezhova, N. N., Kolesnichenko, N. V., Bulygin, A. V., Slivinskii, E. V. and Han, S. Hydrogenation of CO_2 to Formic Acid in the Presence of the Wilkinson Complex. *Russian Chemical Bulletin* **2002**, *51*, pp. 2165–2169.

[56] Graf, E. and Leitner, W. Direct Formation of Formic Acid from Carbon Dioxide and Dihydrogen Using the $[(Rh(Cod)Cl)_2]Ph_2P(CH_2)_4PPh_2$ Catalyst System. *Journal of the Chemical Society, Chemical Communications* **1992**, pp. 623–624.

[57] Gassner, F. and Leitner, W. Hydrogenation of Carbon Dioxide to Formic Acid Using Water-Soluble Rhodium Catalysts. *Journal of the Chemical Society, Chemical Communications* **1993**, pp. 1465–1466.

[58] Zhao, G. and Joó, F. Free Formic Acid by Hydrogenation of Carbon Dioxide in Sodium Formate Solutions. *Catalysis Communications* **2011**, *14*, pp. 74–76.

[59] Tanaka, R., Yamashita, M. and Nozaki, K. Catalytic Hydrogenation of Carbon Dioxide Using Ir(III)-Pincer Complexes. *Journal of the American Chemical Society* **2009**, *131*, pp. 14168–14169.

[60] Tanaka, R., Yamashita, M., Chung, L. W., Morokuma, K. and Nozaki, K. Mechanistic Studies on the Reversible Hydrogenation of Carbon Dioxide Catalyzed by an Ir-PNP Complex. *Organometallics* **2011**, *30*, pp. 6742–6750.

[61] Schmeier, T. J., Dobereiner, G. E., Crabtree, R. H. and Hazari, N. Secondary Coordination Sphere Interactions Facilitate the Insertion Step in an Iridium(III) CO_2 Reduction Catalyst. *Journal of the American Chemical Society* **2011**, *133*, pp. 9274–9277.

[62] Sanz, S., Benítez, M. and Peris, E. A New Approach to the Reduction of Carbon Dioxide: CO_2 Reduction to Formate by Transfer Hydrogenation in iPrOH. *Organometallics* **2010**, *29*, pp. 275–277.

[63] Sanz, S., Azua, A. and Peris, E. '(η^6-arene)Ru(bis-NHC)' Complexes for the Reduction of CO_2 to Formate with Hydrogen and by Transfer Hydrogenation with *i*PrOH. *Dalton Transactions* **2010**, *39*, pp. 6339–6343.

[64] Azua, A., Sanz, S. and Peris, E. Water-Soluble Ir^{III} N-Heterocyclic Carbene Based Catalysts for the Reduction of CO_2 to Formate by Transfer Hydrogenation and the Deuteration of Aryl Amines in Water. *Chemistry – A European Journal* **2011**, *17*, pp. 3963–3967.

[65] Himeda, Y., Onozawa-Komatsuzaki, N., Sugihara, H. and Kasuga, K. Simultaneous Tuning of Activity and Water Solubility of Complex Catalysts by Acid–Base Equilibrium of Ligands for Conversion of Carbon Dioxide. *Organometallics* **2007**, *26*, pp. 702–712.

[66] Hull, J. F., Himeda, Y., Wang, W.-H., Hashiguchi, B., Periana, R., Szalda, D. J., Muckerman, J. T. and Fujita, E. Reversible Hydrogen Storage Using CO_2 and a Proton-Switchable Iridium Catalyst in Aqueous Media Under Mild Temperatures and Pressures. *Nature chemistry* **2012**, *4*, pp. 383–388.

[67] Suna, Y., Ertem, M. Z., Wang, W.-H., Kambayashi, H., Manaka, Y., Muckerman, J. T., Fujita, E. and Himeda, Y. Positional Effects of Hydroxy Groups on Catalytic Activity of Proton-Responsive Half-Sandwich Cp*Iridium(III) Complexes. *Organometallics* **2014**, *33*, pp. 6519–6530.

[68] Wang, W.-H., Hull, J. F., Muckerman, J. T., Fujita, E. and Himeda, Y. Second-Coordination-Sphere and Electronic Effects Enhance Iridium(III)-Catalyzed Homogeneous Hydrogenation of Carbon Dioxide in Water Near Ambient Temperature and Pressure. *Energy & Environmental Science* **2012**, *5*, pp. 7923–7926.

[69] Wang, W.-H., Muckerman, J. T., Fujita, E. and Himeda, Y. Mechanistic Insight through Factors Controlling Effective Hydrogenation of CO_2 Catalyzed by Bioinspired Proton-Responsive Iridium(III) Complexes. *ACS Catalysis* **2013**, *3*, pp. 856–860.

[70] Turner, C. H., Johnson, J. K. and Gubbins, K. E. Effect of Confinement on Chemical Reaction Equilibria: The Reactions $2NO \rightleftarrows NO_2$ and $N_2+3H_2 \rightleftarrows NH_3$ in Carbon Micropores. *Journal of Chemical Physics* **2001**, *114*, pp. 1851–1859.

[71] Rowsell, J. L. and Yaghi, O. M. Metal–Organic Frameworks: a New Class of Porous Materials. *Microporous and Mesoporous Materials* **2004**, *73*, pp. 3–14.

[72] Ockwig, N. W., Delgado-Friedrichs, O., O'Keeffe, M. and Yaghi, O. M. Reticular Chemistry: Occurrence and Taxonomy of Nets and Grammar for the Design of Frameworks. *Accounts of Chemical Research* **2005**, *38*, pp. 176–182.

[73] Najafi Nobar, S. Cu-BTC Synthesis, Characterization and Preparation for Adsorption Studies. *Materials Chemistry and Physics* **2018**, *213*, pp. 343–351.

[74] Tomic, E. A. Thermal Stability of Coordination Polymers. *Journal of Applied Polymer Science* **1965**, *9*, pp. 3745–3752.

[75] Li, H., Eddaoudi, M., O'Keeffe, M. and Yaghi, O. M. Design and Synthesis of an Exceptionally Stable and Highly Porous Metal-Organic Framework. *Nature* **1999**, *402*, pp. 276–279.

[76] Yaghi, O. M., O'Keeffe, M., Ockwig, N. W., Chae, H. K., Eddaoudi, M. and Kim, J. Reticular Synthesis and the Design of New Materials. *Nature* **2003**, *423*, pp. 705–714.

[77] Stein, A., Keller, S. W. and Mallouk, T. E. Turning Down the Heat: Design and Mechanism in Solid-State Synthesis. *Science* **1993**, *259*, pp. 1558–1564.

[78] Vishnyakov, A., Ravikovitch, P. I., Neimark, A. V., Bülow, M. and Wang, Q. M. Nanopore Structure and Sorption Properties of Cu-BTC Metal-Organic Framework. *Nano Letters* **2003**, *3*, pp. 713–718.

[79] Groom, C. R., Bruno, I. J., Lightfoot, M. P. and Ward, S. C. The Cambridge Structural Database. *Acta Crystallographica Section B: Structural Science, Crystal Engineering and Materials* **2016**, *72*, pp. 171–179.

[80] Rosi, N. L., Eckert, J., Eddaoudi, M., Vodak, D. T., Kim, J., O'Keeffe, M. and Yaghi, O. M. Hydrogen Storage in Microporous Metal-Organic Frameworks. *Science* **2003**, *300*, pp. 1127–1129.

[81] Eddaoudi, M., Kim, J., Rosi, N., Vodak, D., Wachter, J., O'Keeffe, M. and Yaghi, O. M. Systematic Design of Pore Size and Functionality in Isoreticular MOFs and Their Application in Methane Storage. *Science* **2002**, *295*, pp. 469–472.

[82] Férey, G., Mellot-Draznieks, C., Serre, C., Millange, F., Dutour, J., Surblé, S. and Margiolaki, I. A Chromium Terephthalate-Based Solid with Unusually Large Pore Volumes and Surface Area. *Science* **2005**, *309*, pp. 2040–2042.

[83] Li, J.-R., Sculley, J. and Zhou, H.-C. Metal–Organic Frameworks for Separations. *Chemical Reviews* **2012**, *112*, pp. 869–932.

[84] Llabrés i Xamena, F. X., Abad, A., Corma, A. and Garcia, H. MOFs as Catalysts: Activity, Reusability and Shape-Selectivity of a Pd-Containing MOF. *Journal of Catalysis* **2007**, *250*, pp. 294–298.

[85] Alaerts, L., Séguin, E., Poelman, H., Thibault-Starzyk, F., Jacobs, P. A. and Vos, D. E. D. Probing the Lewis Acidity and Catalytic Activity of the Metal–Organic Framework $[Cu_3(btc)_2]$ (BTC=Benzene-1,3,5-tricarboxylate). *Chemistry – A European Journal* **2006**, *12*, pp. 7353–7363.

[86] Chen, Y., Li, P., Modica, J. A., Drout, R. J. and Farha, O. K. Acid-Resistant Mesoporous Metal–Organic Framework Toward Oral Insulin Delivery: Protein Encapsulation, Protection, and Release. *Journal of the American Chemical Society* **2018**, *140*, pp. 5678–5681.

[87] Wu, M.-X. and Yang, Y.-W. Metal–Organic Framework (MOF)-Based Drug/Cargo Delivery and Cancer Therapy. *Advanced Materials* **2017**, *29*, p. 1606134.

[88] Chen, Y., Li, P., Noh, H., Kung, C.-W., Buru, C. T., Wang, X., Zhang, X. and Farha, O. K. Stabilization of Formate Dehydrogenase in a Metal–Organic Framework for Bioelectrocatalytic Reduction of CO_2. *Angewandte Chemie International Edition* **2019**, *58*, pp. 7682–7686.

[89] Lian, X., Fang, Y., Joseph, E., Wang, Q., Li, J., Banerjee, S., Lollar, C., Wang, X. and Zhou, H.-C. Enzyme–MOF (Metal–Organic Framework) Composites. *Chemical Society Reviews* **2017**, *46*, pp. 3386–3401.

[90] Chen, B., Yang, Y., Zapata, F., Lin, G., Qian, G. and Lobkovsky, E. B. Luminescent Open Metal Sites Within a Metal–Organic Framework for Sensing Small Molecules. *Advanced Materials* **2007**, *19*, pp. 1693–1696.

[91] Kreno, L. E., Leong, K., Farha, O. K., Allendorf, M., Van Duyne, R. P. and Hupp, J. T. Metal-Organic Framework Materials as Chemical Sensors. *Chemical Reviews* **2012**, *112*, pp. 1105–1125.

[92] Gu, Q., Ng, H. Y., Zhao, D. and Wang, J. Metal–Organic Frameworks (MOFs)-Boosted Filtration Membrane Technology for Water Sustainability. *APL Materials* **2020**, *8*, p. 040902.

[93] Ye, J. and Johnson, J. K. Design of Lewis Pair-Functionalized Metal Organic Frameworks for CO_2 Hydrogenation. *ACS Catalysis* **2015**, *5*, pp. 2921–2928.

[94] Dubbeldam, D., Calero, S., Ellis, D. E. and Snurr, R. Q. RASPA: Molecular Simulation Software for Adsorption and Diffusion in Flexible Nanoporous Materials. *Molecular Simulation* **2016**, *42*, pp. 81–101.

[95] Dubbeldam, D., Torres-Knoop, A. and Walton, K. S. On the Inner Workings of Monte Carlo Codes. *Molecular Simulation* **2013**, *39*, pp. 1253–1292.

[96] Winarta, J., Shan, B., Mcintyre, S. M., Ye, L., Wang, C., Liu, J. and Mu, B. A Decade of UiO-66 Research: A Historic Review of Dynamic Structure, Synthesis Mechanisms, and Characterization Techniques of an Archetypal Metal–Organic Framework. *Crystal Growth & Design* **2020**, *20*, pp. 1347–1362.

[97] Kandiah, M., Nilsen, M. H., Usseglio, S., Jakobsen, S., Olsbye, U., Tilset, M., Larabi, C., Quadrelli, E. A., Bonino, F. and Lillerud, K. P. Synthesis and Stability of Tagged UiO-66 Zr-MOFs. *Chemistry of Materials* **2010**, *22*, pp. 6632–6640.

[98] DeCoste, J. B., Peterson, G. W., Schindler, B. J., Killops, K. L., Browe, M. A. and Mahle, J. J. The Effect of Water Adsorption on the Structure of the Carboxylate Containing Metal–Organic Frameworks Cu-BTC, Mg-MOF-74, and UiO-66. *Journal of Materials Chemistry A* **2013**, *1*, pp. 11922–11932.

[99] Ghosh, P., Colón, Y. J. and Snurr, R. Q. Water Adsorption in UiO-66: The Importance of Defects. *Chemical Communications* **2014**, *50*, pp. 11329–11331.

[100] Abid, H. R., Tian, H., Ang, H.-M., Tade, M. O., Buckley, C. E. and Wang, S. Nanosize Zr-Metal Organic Framework (UiO-66) for Hydrogen and Carbon Dioxide Storage. *Chemical Engineering Journal* **2012**, *187*, pp. 415–420.

[101] Abid, H. R., Pham, G. H., Ang, H.-M., Tade, M. O. and Wang, S. Adsorption of CH_4 and CO_2 on Zr-metal organic frameworks. *Journal of Colloid and Interface Science* **2012**, *366*, pp. 120–124.

[102] Tranchemontagne, D. J., Hunt, J. R. and Yaghi, O. M. Room Temperature Synthesis of Metal-Organic Frameworks: MOF-5, MOF-74, MOF-177, MOF-199, and IRMOF-0. *Tetrahedron* **2008**, *64*, pp. 8553–8557.

[103] Castillo, J. M., Vlugt, T. J. H. and Calero, S. Understanding Water Adsorption in Cu-BTC Metal-Organic Frameworks. *Journal of Physical Chemistry C* **2008**, *112*, pp. 15934–15939.

[104] Rowsell, J. L. C., Millward, A. R., Park, K. S. and Yaghi, O. M. Hydrogen Sorption in Functionalized Metal-Organic Frameworks. *Journal of the American Chemical Society* **2004**, *126*, pp. 5666–5667.

[105] Rowsell, J. L. C., Eckert, J. and Yaghi, O. M. Characterization of H_2 Binding Sites in Prototypical Metal-Organic Frameworks by Inelastic Neutron Scattering. *Journal of the American Chemical Society* **2005**, *127*, pp. 14904–14910.

[106] Panella, B. and Hirscher, M. Hydrogen Physisorption in Metal–Organic Porous Crystals. *Advanced Materials* **2005**, *17*, pp. 538–541.

[107] Li, Y. and Yang, R. T. Hydrogen Storage in Metal-Organic Frameworks by Bridged Hydrogen Spillover. *Journal of the American Chemical Society* **2006**, *128*, pp. 8136–8137.

[108] Sillar, K., Hofmann, A. and Sauer, J. Ab Initio Study of Hydrogen Adsorption in MOF-5. *Journal of the American Chemical Society* **2009**, *131*, pp. 4143–4150.

[109] Chui, S. S.-Y., Lo, S. M.-F., Charmant, J. P. H., Orpen, A. G. and Williams, I. D. A Chemically Functionalizable Nanoporous Material $[Cu_3(TMA)_2(H_2O)_3]_n$. *Science* **1999**, *283*, pp. 1148–1150.

[110] Zheng, C., Liu, D., Yang, Q., Zhong, C. and Mi, J. Computational Study on the Influences of Framework Charges on CO_2 Uptake in Metal-Organic Frameworks. *Industrial & Engineering Chemistry Research* **2009**, *48*, pp. 10479–10484.

[111] Sladekova, K., Campbell, C., Grant, C., Fletcher, A. J., Gomes, J. R. B. and Jorge, M. The Effect of Atomic Point Charges on Adsorption Isotherms of CO_2 and Water in Metal–Organic Frameworks. *Adsorption* **2020**, *26*, pp. 663–685.

[112] Moghadam, P. Z., Li, A., Wiggin, S. B., Tao, A., Maloney, A. G. P., Wood, P. A., Ward, S. C. and Fairen-Jimenez, D. Development of a Cambridge Structural Database Subset: A Collection of Metal–Organic Frameworks for Past, Present, and Future. *Chemistry of Materials* **2017**, *29*, pp. 2618–2625.

[113] Dietzel, P. D. C., Panella, B., Hirscher, M., Blom, R. and Fjellvåg, H. Hydrogen Adsorption in a Nickel Based Coordination Polymer with Open Metal Sites in the Cylindrical Cavities of the Desolvated Framework. *Chemical Communications* **2006**, *9*, pp. 959–961.

[114] Sanz, R., Martínez, F., Orcajo, G., Wojtas, L. and Briones, D. Synthesis of a Honeycomb-Like Cu-Based Metal–Organic Framework and Its Carbon Dioxide Adsorption Behaviour. *Dalton Transactions* **2013**, *42*, pp. 2392–2398.

[115] Dietzel, P. D., Morita, Y., Blom, R. and Fjellvåg, H. An In Situ High-Temperature Single-Crystal Investigation of a Dehydrated Metal–Organic Framework Compound and Field-Induced Magnetization of One-Dimensional Metal–Oxygen Chains. *Angewandte Chemie* **2005**, *117*, pp. 6512–6516.

[116] Bhattacharjee, S., Choi, J.-S., Yang, S.-T., Choi, S. B., Kim, J. and Ahn, W.-S. Solvothermal Synthesis of Fe-MOF-74 and Its Catalytic Properties in Phenol Hydroxylation. *Journal of Nanoscience and Nanotechnology* **2010**, *10*, pp. 135–141.

[117] Zhou, W., Wu, H. and Yildirim, T. Enhanced H_2 Adsorption in Isostructural Metal–Organic Frameworks with Open Metal Sites: Strong Dependence of the Binding Strength on Metal Ions. *Journal of the American Chemical Society* **2008**, *130*, pp. 15268–15269.

[118] Rosi, N. L., Kim, J., Eddaoudi, M., Chen, B., O'Keeffe, M. and Yaghi, O. M. Rod Packings and Metal-Organic Frameworks Constructed from Rod-Shaped Secondary Building Units. *Journal of the American Chemical Society* **2005**, *127*, pp. 1504–1518.

[119] Pham, T., Forrest, K. A., Banerjee, R., Orcajo, G., Eckert, J. and Space, B. Understanding the H_2 Sorption Trends in the M-MOF-74 Series (M = Mg, Ni, Co, Zn). *Journal of Physical Chemistry C* **2015**, *119*, pp. 1078–1090.

[120] Dietzel, P. D. C., Johnsen, R. E., Blom, R. and Fjellvåg, H. Structural Changes and Coordinatively Unsaturated Metal Atoms on Dehydration of Honeycomb Analogous Microporous Metal–Organic Frameworks. *Chemistry – A European Journal* **2008**, *14*, pp. 2389–2397.

[121] Rowsell, J. L. C. and Yaghi, O. M. Effects of Functionalization, Catenation, and Variation of the Metal Oxide and Organic Linking Units on the Low-Pressure Hydrogen Adsorption Properties of Metal–Organic Frameworks. *Journal of the American Chemical Society* **2006**, *128*, pp. 1304–1315.

[122] Queen, W. L., Hudson, M. R., Bloch, E. D., Mason, J. A., Gonzalez, M. I., Lee, J. S., Gygi, D., Howe, J. D., Lee, K., Darwish, T. A. et al. Comprehensive Study of Carbon Dioxide Adsorption in the Metal–Organic Frameworks M_2 (dobdc)(M= Mg, Mn, Fe, Co, Ni, Cu, Zn). *Chemical Science* **2014**, *5*, pp. 4569–4581.

[123] Bloch, E. D., Queen, W. L., Krishna, R., Zadrozny, J. M., Brown, C. M. and Long, J. R. Hydrocarbon Separations in a Metal-Organic Framework with Open Iron(II) Coordination Sites. *Science* **2012**, *335*, pp. 1606–1610.

[124] Liu, Y., Kabbour, H., Brown, C. M., Neumann, D. A. and Ahn, C. C. Increasing the Density of Adsorbed Hydrogen with Coordinatively Unsaturated Metal Centers in Metal-Organic Frameworks. *Langmuir* **2008**, *24*, pp. 4772–4777.

[125] Bloch, E. D., Murray, L. J., Queen, W. L., Chavan, S., Maximoff, S. N., Bigi, J. P., Krishna, R., Peterson, V. K., Grandjean, F., Long, G. J., Smit, B., Bordiga, S., Brown, C. M. and Long, J. R. Selective Binding of O_2 over N_2 in a Redox–Active Metal–Organic Framework with Open Iron(II) Coordination Sites. *Journal of the American Chemical Society* **2011**, *133*, pp. 14814–14822.

[126] Horike, S., Dincă, M., Tamaki, K. and Long, J. R. Size-Selective Lewis Acid Catalysis in a Microporous Metal-Organic Framework with Exposed Mn^{2+} Coordination Sites. *Journal of the American Chemical Society* **2008**, *130*, pp. 5854–5855.

[127] Tuckerman, M. E. *Statistical Mechanics: Theory and Molecular Simulation*. Oxford University Press, 2023.

[128] Frenkel, D. and Smit, B. *Understanding Molecular Simulation: From Algorithms to Applications*. 3rd ed. Elsevier, 2023.

[129] Allen, M. P. and Tildesley, D. J. *Computer Simulation of Liquids*. 2nd ed. Oxford University Press, 2017. ISBN: 9780198803195. DOI: 10.1093/oso/9780198803195.001.0001. URL: https://doi.org/10.1093/oso/9780198803195.001.0001.

[130] Chandler, D. *Introduction to Modern Statistical Mechanics*. New York: Oxford University Press, 1987. ISBN: 0-19-504276-X.

[131] Pathria, R. *Statistical Mechanics*. 2nd ed. Oxford: Butterworth-Heinemann, 1996, pp. 523–529.

[132] Metropolis, N., Rosenbluth, A. W., Rosenbluth, M. N., Teller, A. H. and Teller, E. Equation of State Calculations by Fast Computing Machines. *Journal of Chemical Physics* **1953**, *21*, pp. 1087–1092.

[133] Bowley, R. and Sánchez, M. *Introductory Statistical Mechanics*. Oxford University Press, 1999.

[134] Rothenberg, G. *Handbook of Porous Materials*. WORLD SCIENTIFIC, 2021. URL: https://www.worldscientific.com/doi/abs/10.1142/11909-vol2.

[135] Johnson, J. K., Panagiotopoulos, A. Z. and Gubbins, K. E. Reactive Canonical Monte Carlo. *Molecular Physics* **1994**, *81*, pp. 717–733.

[136] Smith, W. R. and Triska, B. The Reaction Ensemble Method for the Computer Simulation of Chemical and Phase Equilibria. I. Theory and Basic Examples. *Journal of Chemical Physics* **1994**, *100*, pp. 3019–3027.

[137] Smit, B. and Siepmann, J. I. Computer Simulations of the Energetics and Siting of n-Alkanes in Zeolites. *Journal of Physical Chemistry* **1994**, *98*, pp. 8442–8452.

[138] Rosenbluth, M. N. and Rosenbluth, A. W. Monte Carlo Calculation of the Average Extension of Molecular Chains. *Journal of Chemical Physics* **1955**, *23*, pp. 356–359.

[139] Shi, W. and Maginn, E. J. Continuous Fractional Component Monte Carlo: An Adaptive Biasing Method for Open System Atomistic Simulations. *Journal of Chemical Theory and Computation* **2007**, *3*, pp. 1451–1463.

[140] Shi, W. and Maginn, E. J. Improvement in Molecule Exchange Efficiency in Gibbs Ensemble Monte Carlo: Development and Implementation of the Continuous Fractional Component Move. *Journal of Computational Chemistry* **2008**, *29*, pp. 2520–2530.

[141] Rahbari, A., Hens, R., Ramdin, M., Moultos, O. A., Dubbeldam, D. and Vlugt, T. J. H. Recent Advances in the Continuous Fractional Component Monte Carlo Methodology. *Molecular Simulation* **2021**, *47*, pp. 804–823.

[142] Poursaeidesfahani, A., Hens, R., Rahbari, A., Ramdin, M., Dubbeldam, D. and Vlugt, T. J. H. Efficient Application of Continuous Fractional Component Monte Carlo in the Reaction Ensemble. *Journal of Chemical Theory and Computation* **2017**, *13*, pp. 4452–4466.

[143] Hens, R., Rahbari, A., Caro-Ortiz, S., Dawass, N., Erdős, M., Poursaeidesfahani, A., Salehi, H. S., Celebi, A. T., Ramdin, M., Moultos, O. A., Dubbeldam, D. and Vlugt, T. J. H. Brick-CFCMC: Open Source Software for Monte Carlo Simulations of Phase and Reaction Equilibria Using the Continuous Fractional Component Method. *Journal of Chemical Information and Modeling* **2020**, *60*, pp. 2678–2682.

[144] Torres-Knoop, A., Poursaeidesfahani, A., Vlugt, T. J. H. and Dubbeldam, D. Behavior of the Enthalpy of Adsorption in Nanoporous Materials Close to Saturation Conditions. *Journal of Chemical Theory and Computation* **2017**, *13*, pp. 3326–3339.

[145] Balaji, S. P., Gangarapu, S., Ramdin, M., Torres-Knoop, A., Zuilhof, H., Goetheer, E. L. V., Dubbeldam, D. and Vlugt, T. J. H. Simulating the Reactions of CO_2 in Aqueous Monoethanolamine Solution by Reaction Ensemble Monte Carlo Using the Continuous Fractional Component Method. *Journal of Chemical Theory and Computation* **2015**, *11*, pp. 2661–2669.

[146] Poursaeidesfahani, A., Torres-Knoop, A., Dubbeldam, D. and Vlugt, T. J. H. Direct Free Energy Calculation in the Continuous Fractional Component Gibbs Ensemble. *Journal of Chemical Theory and Computation* **2016**, *12*, p. 1481.

[147] Rappe, A. K., Casewit, C. J., Colwell, K. S., Goddard, W. A. and Skiff, W. M. UFF, a Full Periodic Table Force Field for Molecular Mechanics and Molecular Dynamics Simulations. *Journal of the American Chemical Society* **1992**, *114*, pp. 10024–10035.

[148] Mayo, S. L., Olafson, B. D. and Goddard, W. A. DREIDING: a Generic Force Field for Molecular Simulations. *Journal of Physical Chemistry* **1990**, *94*, pp. 8897–8909.

[149] Jorgensen, W. L., Maxwell, D. S. and Tirado-Rives, J. Development and Testing of the OPLS All-Atom Force Field on Conformational Energetics and Properties of Organic Liquids. *Journal of the American Chemical Society* **1996**, *118*, p. 11225.

[150] Jones, J. E. and Chapman, S. On the Determination of Molecular Fields. III.—-From Crystal Measurements and Kinetic Theory Data. *Proceedings of the Royal Society of London. Series A, Containing Papers of a Mathematical and Physical Character* **1924**, *106*, pp. 709–718.

[151] Wells, B. A. and Chaffee, A. L. Ewald Summation for Molecular Simulations. *Journal of Chemical Theory and Computation* **2015**, *11*, pp. 3684–3695.

[152] Polat, H. M., Salehi, H. S., Hens, R., Wasik, D. O., Rahbari, A., Meyer, F. de, Houriez, C., Coquelet, C., Calero, S., Dubbeldam, D., Moultos, O. A. and Vlugt, T. J. H. New Features of the Open Source Monte Carlo Software Brick-CFCMC: Thermodynamic Integration and Hybrid Trial Moves. *Journal of Chemical Information and Modeling* **2021**, *61*, pp. 3752–3757.

[153] Rahbari, A., Hens, R., Dubbeldam, D. and Vlugt, T. J. H. Improving the Accuracy of Computing Chemical Potentials in CFCMC Simulations. *Molecular Physics* **2019**, *117*, p. 3493.

[154] Schroer, W. and Pottlacher, G. Estimation of Critical Data and Phase Diagrams of Pure Molten Metals. *High Temperatures – High Pressures* **2014**, *43*, pp. 201–215.

[155] Polat, H. M., Meyer, F. de, Houriez, C., Moultos, O. A. and Vlugt, T. J. H. Solving Chemical Absorption Equilibria using Free Energy and Quantum Chemistry Calculations: Methodology, Limitations, and New Open-Source Software. *Journal of Chemical Theory and Computation* **2023**, *19*, pp. 2616–2629.

[156] McQuarrie, D. A. and Simon, J. D. *Physical Chemistry: A Molecular Approach*. 1st ed. Sausalito, California: University Science Books, 1997.

[157] Peng, D.-Y. and Robinson, D. B. A New Two-Constant Equation of State. *Industrial & Engineering Chemistry Fundamentals* **1976**, *15*, pp. 59–64.

[158] Farrusseng, D., Daniel, C., Gaudillère, C., Ravon, U., Schuurman, Y., Mirodatos, C., Dubbeldam, D., Frost, H. and Snurr, R. Q. Heats of Adsorption for Seven Gases in Three Metal-Organic Frameworks: Systematic Comparison of Experiment and Simulation. *Langmuir* **2009**, *25*, pp. 7383–7388.

[159] Jensen, F. *Introduction to Computational Chemistry*. 3rd ed. John Wiley & Sons, 2017.

[160] Baker, J. An Algorithm for the Location of Transition States. *Journal of Computational Chemistry* **1986**, *7*, pp. 385–395.

[161] Barham, H. N. and Clark, L. W. The Decomposition of Formic Acid at Low Temperatures. *Journal of the American Chemical Society* **1951**, *73*, p. 4638.

[162] Hänninen, V., Murdachaew, G., Nathanson, G. M., Gerber, R. B. and Halonen, L. Ab Initio Molecular Dynamics Studies of Formic Acid Dimer Colliding with Liquid Water. *Physical Chemistry Chemical Physics* **2018**, *20*, p. 23717.

[163] Jedlovszky, P. and Turi, L. Role of the C–H···O Hydrogen Bonds in Liquids: A Monte Carlo Simulation Study of Liquid Formic Acid Using a Newly Developed Pair-Potential. *Journal of Physical Chemistry B* **1997**, *101*, p. 5429.

[164] Soffientini, S., Bernasconi, L. and Imberti, S. The Hydration of Formic Acid and Acetic Acid. *Journal of Molecular Liquids* **2015**, *205*, p. 85.

[165] Zhou, Z., Shi, Y. and Zhou, X. Theoretical Studies on the Hydrogen Bonding Interaction of Complexes of Formic Acid with Water. *Journal of Physical Chemistry A* **2004**, *108*, p. 813.

[166] Kacar, G. and With, G. de. Parametrizing Hydrogen Bond Interactions in Dissipative Particle Dynamics Simulations: The Case of Water, Methanol and Their Binary Mixtures. *Journal of Molecular Liquids* **2020**, *302*, p. 112581.

[167] Chelli, R., Righini, R. and Califano, S. Structure of Liquid Formic Acid Investigated by First Principle and Classical Molecular Dynamics Simulations. *Journal of Physical Chemistry B* **2005**, *109*, pp. 17006–17013.

[168] Bakó, I., Hutter, J. and Pálinkás, G. Car-Parrinello Molecular Dynamics Simulation of Liquid Formic Acid. *Journal of Physical Chemistry A* **2006**, *110*, pp. 2188–2194.

[169] Rodziewicz, P. and Doltsinis, N. L. Formic Acid Dimerization: Evidence for Species Diversity from First Principles Simulations. *Journal of Physical Chemistry A* **2009**, *113*, pp. 6266–6274.

[170] Hanwell, M. D., Curtis, D. E., Lonie, D. C., Vandermeersch, T., Zurek, E. and Hutchison, G. R. Avogadro: An Advanced Semantic Chemical Editor, Visualization, and Analysis Platform. *Journal of Cheminformatics* **2012**, *4*, p. 17.

[171] Frisch, M. J., Trucks, G. W., Schlegel, H. B., Scuseria, G. E., Robb, M. A., Cheeseman, J. R., Scalmani, G., Barone, V., Mennucci, B., Petersson, G. A. et al. *Gaussian 09, Revision A.1.* Wallingford, CT: Gaussian, Inc., 2009.

[172] Schnabel, T., Cortada, M., Vrabec, J., Lago, S. and Hasse, H. Molecular Model for Formic Acid Adjusted to Vapor–liquid Equilibria. *Chemical Physics Letters* **2007**, *435*, p. 268.

[173] Niemann, T., Stange, P., Strate, A. and Ludwig, R. When Hydrogen Bonding Overcomes Coulomb Repulsion: From Kinetic to Thermodynamic Stability of Cationic Dimers. *Physical Chemistry Chemical Physics* **2019**, *21*, p. 8215.

[174] Salas, F. J., Nunez-Rojas, E. and Alejandre, J. Stability of Formic Acid/Pyridine and Isonicotinamide/Formamide Cocrystals by Molecular Dynamics Simulations. *Theoretical Chemistry Accounts* **2017**, *136*, pp. 1–12.

[175] Berendsen, H. J., Grigera, J. R. and Straatsma, T. P. The Missing Term in Effective Pair Potentials. *Journal of Physical Chemistry* **1987**, *91*, p. 6269.

[176] García-Sánchez, A., Ania, C. O., Parra, J. B., Dubbeldam, D., Vlugt, T. J. H., Krishna, R. and Calero, S. Transferable Force Field for Carbon Dioxide Adsorption in Zeolites. *Journal of Physical Chemistry C* **2009**, *113*, pp. 8814–8820.

[177] Aragones, J. L., Sanz, E. and Vega, C. Solubility of NaCl in Water by Molecular Simulation Revisited. *Journal of Chemical Physics* **2012**, *136*, p. 244508.

[178] Dawass, N., Langeveld, J., Ramdin, M., Pérez-Gallent, E., Villanueva, A. A., Giling, E. J. M., Langerak, J., Broeke, L. J. P. van den, Vlugt, T. J. H. and Moultos, O. A. Solubilities and Transport Properties of CO_2, Oxalic Acid, and Formic Acid in Mixed Solvents Composed of Deep Eutectic Solvents, Methanol, and Propylene Carbonate. *Journal of Physical Chemistry B* **2022**, *126*, pp. 3572–3584.

[179] Hempel, S., Fischer, J., Paschek, D. and Sadowski, G. Activity Coefficients of Complex Molecules by Molecular Simulation and Gibbs-Duhem Integration. *Soft Materials* **2012**, *10*, pp. 26–41.

[180] Poling, B. E., Prausnitz, J. M. and O'Connell, J. P. *Properties of Gases and Liquids*. Fifth Edition. New York, Chicago, San Francisco, Athens, London, Madrid, Mexico City, Milan, New Delhi, Singapore, Sydney, Toronto: McGraw-Hill Education, 2001.

[181] Hildebrand, F. B. *Introduction to Numerical Analysis*. New York: Dover Publications Inc.; McGraw-Hill, 1974.

[182] Dawass, N., Wanderley, R. R., Ramdin, M., Moultos, O. A., Knuutila, H. K. and Vlugt, T. J. H. Solubility of Carbon Dioxide, Hydrogen Sulfide, Methane, and Nitrogen in Monoethylene Glycol; Experiments and Molecular Simulation. *Journal of Chemical & Engineering Data* **2021**, *66*, pp. 524–534.

[183] Salehi, H. S., Hens, R., Moultos, O. A. and Vlugt, T. J. H. Computation of Gas Solubilities in Choline Chloride Urea and Choline Chloride Ethylene Glycol Deep Eutectic Solvents Using Monte Carlo Simulations. *Journal of Molecular Liquids* **2020**, *316*, p. 113729.

[184] Preston, J. M. and Starrock, V. *Partial Vapour Pressures and Activity Coefficients of GB and GD in Aqueous Solution. 1983*. Tech. rep. Defence Research Establishment Ottawa, pp. 1–24.

[185] Daubert, T. E. and Danner, R. P. *Physical and Thermodynamic Properties of Pure Chemicals Data Compilation*. Washington, D.C.: Taylor and Francis, 1989, p. 4904.

[186] Haynes, W. M. *CRC Handbook of Chemistry and Physics*. 91st ed. Boca Raton, FL: CRC Press Inc., 2010.

[187] Takagi, S. Boiling Points of the System of Formic Acid and Water. *Bulletin of the Chemical Society of Japan* **1939**, *14*, p. 508.

[188] Campbell, A. N. and Campbell, A. J. R. The Thermodynamics of Binary Liquid Mixtures: Formic Acid and Water. *Transactions of the Faraday Society* **1934**, *30*, pp. 1109–1114.

[189] Udovenko, V. V. and Aleksandrova, L. P. Vapor Pressure in Three-Component Systems. III. The Formic Acid-1,2-Di Chloroethane-Water System. *Russian Journal of Physical Chemistry A* **1960**, *34*, p. 655.

[190] Renon, H. and Prausnitz, J. M. Local Compositions in Thermodynamic Excess Functions for Liquid Mixtures. *AIChE Journal* **1968**, *14*, p. 135.

[191] Hayden, J. G. and O'Connell, J. P. A Generalized Method for Predicting Second Virial Coefficients. *Industrial & Engineering Chemistry Process Design and Development* **1975**, *14*, p. 209.

[192] Weisenberger, S. and Schumpe, A. Estimation of Gas Solubilities in Salt Solutions at Temperatures from 273 K to 363 K. *AIChE Journal* **1996**, *42*, p. 298.

[193] Apelblat, A. and Manzurola, E. Excess Molar Volumes of Formic Acid + Water Acetic Acid + Water and Propionic Acid + Water Systems at 288.15, 298.15 and 308.15 K. *Fluid Phase Equilibria* **1987**, *32*, p. 163.

[194] Mináry, P., Jedlovszky, P., Mezei, M. and Turi, L. A Comprehensive Liquid Simulation Study of Neat Formic Acid. *Journal of Physical Chemistry B* **2000**, *104*, p. 8287.

[195] Sander, R. Compilation of Henry's Law Constants (Version 4.0) For Water as Solvent. *Atmospheric Chemistry and Physics* **2015**, *15*, p. 4399.

[196] Weiss, R. F. Carbon Dioxide in Water and Seawater: The Solubility of a Non-ideal Gas. *Marine Chemistry* **1974**, *2*, p. 203.

[197] Harned, H. S. and Davis, R. The Ionization Constant of Carbonic Acid in Water and the Solubility of Carbon Dioxide in Water and Aqueous Salt Solutions from 0 to 50°. *Journal of the American Chemical Society* **1943**, *65*, p. 2030.

[198] Burgess, J. *Metal Ions in Solution*. Chichester, New York: Ellis Horwood; Distributed by Halsted Press, 1978.

[199] Samoilov, O. Y. A. New Approach to the Study of Hydration of Ions in Aqueous Solutions. *Discussions of the Faraday Society* **1957**, *24*, p. 141.

[200] Collins, K. D. Charge Density-dependent Strength of Hydration and Biological Structure. *Biophysical Journal* **1997**, *72*, p. 65.

[201] Zhang, X., Zhang, L., Jin, T., Pan, Z., Chen, Z., Zhang, Q. and Zhuang, W. Salting-in/Salting-out Mechanism of Carbon Dioxide in Aqueous Electrolyte Solutions. *Chinese Journal of Chemical Physics* **2017**, *30*, p. 811.

[202] Ganguly, P. and Vegt, N. F. A. van der. Convergence of Sampling Kirkwood–Buff Integrals of Aqueous Solutions with Molecular Dynamics Simulations. *Journal of Chemical Theory and Computation* **2013**, *9*, p. 1347.

[203] Jenkins, H. D. B. and Marcus, Y. Viscosity B-coefficients of ions in solution. *Chemical Reviews* **1995**, *95*, p. 2695.

[204] Joos, F. and Spahni, R. Rates of Change in Natural and Anthropogenic Radiative Forcing Over the Past 20,000 Years. *Proceedings of the National Academy of Sciences* **2008**, *105*, pp. 1425–1430.

[205] Dlugokencky, E. and Tans, P. *Trends in Atmospheric Carbon Dioxide, National Oceanic and Atmospheric Administration, Earth System Research Laboratory (NOAA/ESRL)*. Tech. rep. Access date: 11 March 2022. 2022. URL: http://www.esrl.noaa.gov/gmd/ccgg/trends/global.html.

[206] Wasik, D. O., Polat, H. M., Ramdin, M., Moultos, O. A., Calero, S. and Vlugt, T. J. H. Solubility of CO_2 in Aqueous Formic Acid Solutions and the Effect of NaCl Addition: A Molecular Simulation Study. *Journal of Physical Chemistry C* **2022**, *126*, pp. 19424–19434.

[207] Mömming, C. M., Otten, E., Kehr, G., Fröhlich, R., Grimme, S., Stephan, D. W. and Erker, G. Reversible Metal-Free Carbon Dioxide Binding by Frustrated Lewis Pairs. *Angewandte Chemie International Edition* **2009**, *48*, pp. 6643–6646.

[208] Ashley, A. E., Thompson, A. L. and O'Hare, D. Non-Metal-Mediated Homogeneous Hydrogenation of CO_2 to CH_3OH. *Angewandte Chemie International Edition* **2009**, *48*, pp. 9839–9843.

[209] Zhao, T., Hu, X., Wu, Y. and Zhang, Z. Hydrogenation of CO_2 to Formate with H_2: Transition Metal Free Catalyst Based on a Lewis Pair. *Angewandte Chemie International Edition* **2019**, *58*, pp. 722–726.

[210] Matito-Martos, I., García-Reyes, J., Martin-Calvo, A., Dubbeldam, D. and Calero, S. Improving Ammonia Production Using Zeolites. *Journal of Physical Chemistry C* **2019**, *123*, pp. 18475–18481.

[211] Trokhymchuk, A., Pizio, O. and Sokołowski, S. Solvation Force for an Associative Fluid in a Slit-like Pore. *Journal of Colloid and Interface Science* **1996**, *178*, pp. 436–441.

[212] Trokhymchuk, A., Henderson, D. and Sokołowski, S. Structure of Chemically Reacting Particles Near a Hard Wall from Integral Equations and Computer Simulations. *Canadian Journal of Physics* **1996**, *74*, pp. 65–76.

[213] Pizio, O., Henderson, D. and Sokołowski, S. Density Profiles of Chemically Reacting Simple Fluids near Impenetrable Surfaces. *Journal of Physical Chemistry* **1995**, *99*, pp. 2408–2411.

[214] Pizio, O., Henderson, D. and Sokołowski, S. Adsorption of Chemically Reacting Fluids on a Crystalline Surface. *Molecular Physics* **1995**, *85*, pp. 407–412.

[215] Müller, E. A., Vega, L. F., Gubbins, K. E. and Rull, L. F. Adsorption Isotherms of Associating Chain Molecules from Monte Carlo Simulations. *Molecular Physics* **1995**, *85*, pp. 9–21.

[216] Liu, X., Zhang, L. and Wang, J. Design Strategies for MOF-Derived Porous Functional Materials: Preserving Surfaces and Nurturing Pores. *Journal of Materiomics* **2021**, *7*, pp. 440–459.

[217] Wang, Z., Xu, X., Kim, J., Malgras, V., Mo, R., Li, C., Lin, Y., Tan, H., Tang, J., Pan, L., Bando, Y., Yang, T. and Yamauchi, Y. Nanoarchitectured Metal–Organic Framework/Polypyrrole Hybrids for Brackish Water Desalination Using Capacitive Deionization. *Mater. Horiz.* **2019**, *6*, pp. 1433–1437.

[218] Gómez-Lor, B., Gutiérrez-Puebla, E., Iglesias, M., Monge, M. A., Ruiz-Valero, C. and Snejko, N. Novel 2D and 3D Indium Metal-Organic Frameworks: Topology and Catalytic Properties. *Chemistry of Materials* **2005**, *17*, pp. 2568–2573.

[219] Yamada, Y. M. A., Maeda, Y. and Uozumi, Y. Novel 3D Coordination Palladium-Network Complex: A Recyclable Catalyst for Suzuki - Miyaura Reaction. *Organic Letters* **2006**, *8*, pp. 4259–4262.

[220] James, S. L. Metal-Organic Frameworks. *Chemical Society Reviews* **2003**, *32*, pp. 276–288.

[221] Ong, J. L., Loy, A. C. M., Teng, S. Y. and How, B. S. Future Paradigm of 3D Printed Ni-Based Metal Organic Framework Catalysts for Dry Methane Reforming: Techno-economic and Environmental Analyses. *ACS Omega* **2022**, *7*, pp. 15369–15384.

[222] Bambalaza, S. E., Langmi, H. W., Mokaya, R., Musyoka, N. M., Ren, J. and Khotseng, L. E. Compaction of a Zirconium Metal–Organic Framework (UiO-66) for High Density Hydrogen Storage Applications. *J. Mater. Chem. A* **2018**, *6*, pp. 23569–23577.

[223] Yang, Q., Wiersum, A. D., Llewellyn, P. L., Guillerm, V., Serre, C. and Maurin, G. Functionalizing Porous Zirconium Terephthalate UiO-66(Zr) for Natural Gas Upgrading: a Computational Exploration. *Chem. Commun.* **2011**, *47*, pp. 9603–9605.

[224] Ye, J. and Johnson, J. K. Screening Lewis Pair Moieties for Catalytic Hydrogenation of CO_2 in Functionalized UiO-66. *ACS Catalysis* **2015**, *5*, pp. 6219–6229.

[225] Yang, K. and Jiang, J. Computational Design of a Metal-Based Frustrated Lewis Pair on Defective UiO-66 for CO_2 Hydrogenation to Methanol. *J. Mater. Chem. A* **2020**, *8*, pp. 22802–22815.

[226] Rosch, T. W. and Maginn, E. J. Reaction Ensemble Monte Carlo Simulation of Complex Molecular Systems. *Journal of Chemical Theory and Computation* **2011**, *7*, pp. 269–279.

[227] Turner, C. H., Brennan, J. K., Lísal, M., Smith, W. R., Johnson, J. K. and Gubbins, K. E. Simulation of Chemical Reaction Equilibria by the Reaction Ensemble Monte Carlo Method: a Review. *Molecular Simulation* **2008**, *34*, pp. 119–146.

[228] Turner, C. H., Pikunic, J. and Gubbins, K. E. Influence of Chemical and Physical Surface Heterogeneity on Chemical Reaction Equilibria in Carbon Micropores. *Molecular Physics* **2001**, *99*, pp. 1991–2001.

[229] Borówko, M., Patrykiejew, A., Sokołowski, S., Zagórski, R. and Pizio, O. Chemical Reactions at Surfaces: Application of the Reaction Ensamble Monte Carlo Method. *Czechoslovak Journal of Physics* **1998**, *48*, pp. 371–388.

[230] Hansen, N., Jakobtorweihen, S. and Keil, F. J. Reactive Monte Carlo and Grand-Canonical Monte Carlo Simulations of the Propene Metathesis Reaction System. *Journal of Chemical Physics* **2005**, *122*, p. 164705.

[231] Lísal, M., Brennan, J. K. and Smith, W. R. Chemical Reaction Equilibrium in Nanoporous Materials: NO Dimerization Reaction in Carbon Slit Nanopores. *Journal of Chemical Physics* **2006**, *124*, p. 064712.

[232] Shimanouchi, T. *Tables of Molecular Vibrational Frequencies Consolidated Volume I*. National Bureau of Standards, 1972, pp. 1–160.

[233] Davies, P. R. and Orville-Thomas, W. J. Infrared Band Intensities and Bond Polarities. *Journal of Molecular Structure* **1969**, *4*, pp. 163–177.

[234] Person, W. B. and Zerbi, G. *Vibrational Intensities in Infrared and Raman Spectroscopy*. Amsterdam: Elsevier, 1982.

[235] Herzberg, G. *Electronic Spectra and Electronic Structure of Polyatomic Molecules*. 1st ed. New York: Van Nostrand, 1966.

[236] Huber, K. P. and Herzberg, G. *Molecular Spectra and Molecular Structure: IV. Constants of Diatomic Molecules. Constants of Diatomic Molecules*. Boston, MA: Springer US, 1979, pp. 8–689.

[237] Talu, O. and Myers, A. L. Molecular Simulation of Adsorption: Gibbs Dividing Surface and Comparison with Experiment. *AIChE Journal* **2001**, *47*, pp. 1160–1168.

[238] Jajko, G., Gutiérrez-Sevillano, J. J., Sławek, A., Szufla, M., Kozyra, P., Matoga, D., Makowski, W. and Calero, S. Water adsorption in ideal and defective UiO-66 structures. *Microporous and Mesoporous Materials* **2022**, *330*, p. 111555.

[239] Lemmon, E. W., Bell, I. H., Huber, M. L. and McLinden, M. O. *NIST Standard Reference Database 23: Reference Fluid Thermodynamic and Transport Properties-REFPROP, Version 10.0, National Institute of Standards and Technology*. 2018. URL: https://www.nist.gov/srd/refprop.

[240] Matito-Martos, I., Rahbari, A., Martin-Calvo, A., Dubbeldam, D., Vlugt, T. J. H. and Calero, S. Adsorption Equilibrium of Nitrogen Dioxide in Porous Materials. *Physical Chemistry Chemical Physics* **2018**, *20*, pp. 4189–4199.

[241] Taylor, J. R. *An Introduction to Error Analysis: The Study of Uncertainties in Physical Measurements*. 2nd ed. University Science Books, 1997.

[242] Builes, S., Sandler, S. I. and Xiong, R. Isosteric Heats of Gas and Liquid Adsorption. *Langmuir* **2013**, *29*, pp. 10416–10422.

[243] Darkrim, F. and Levesque, D. Monte Carlo Simulations of Hydrogen Adsorption in Single-Walled Carbon Nanotubes. *Journal of Chemical Physics* **1998**, *109*, pp. 4981–4984.

[244] Dubbeldam, D., Walton, K. S., Ellis, D. E. and Snurr, R. Q. Exceptional Negative Thermal Expansion in Isoreticular Metal–Organic Frameworks. *Angewandte Chemie International Edition* **2007**, *46*, pp. 4496–4499.

[245] Jajko, G., Kozyra, P., Gutiérrez-Sevillano, J. J., Makowski, W. and Calero, S. Carbon Dioxide Capture Enhanced by Pre-Adsorption of Water and Methanol in UiO-66. *Chemistry – A European Journal* **2021**, *27*, pp. 14653–14659.

[246] Gutiérrez-Sevillano, J. J., Dubbeldam, D., Bellarosa, L., López, N., Liu, X., Vlugt, T. J. H. and Calero, S. Strategies to Simultaneously Enhance the Hydrostability and the Alcohol–Water Separation Behavior of Cu-BTC. *Journal of Physical Chemistry C* **2013**, *117*, pp. 20706–20714.

[247] Wilmer, C. E., Kim, K. C. and Snurr, R. Q. An Extended Charge Equilibration Method. *Journal of Physical Chemistry Letters* **2012**, *3*, pp. 2506–2511.

[248] Hirschfelder, J. O., Curtiss, C. F. and Bird, R. B. *Molecular Theory of Gases and Liquids*. 1st ed. New York: J. Wiley, 1964.

[249] Martin-Calvo, A., Gutiérrez-Sevillano, J. J., Matito-Martos, I., Vlugt, T. J. H. and Calero, S. Identifying Zeolite Topologies for Storage and Release of Hydrogen. *Journal of Physical Chemistry C* **2018**, *122*, pp. 12485–12493.

[250] Zhang, X., Chen, Z., Liu, X., Hanna, S. L., Wang, X., Taheri-Ledari, R., Maleki, A., Li, P. and Farha, O. K. A Historical Overview of the Activation and Porosity of Metal-Organic Frameworks. *Chemical Society Reviews* **2020**, *49*, pp. 7406–7427.

[251] Furukawa, H., Cordova, K. E., O'Keeffe, M. and Yaghi, O. M. The Chemistry and Applications of Metal-Organic Frameworks. *Science* **2013**, *341*, p. 1230444.

[252] Irving, H. and Williams, R. J. P. The Stability of Transition-Metal Complexes. *Journal of the Chemical Society* **1953**, *637*, pp. 3192–3210.

[253] Yu, D., Yazaydin, A. O., Lane, J. R., Dietzel, P. D. C. and Snurr, R. Q. A Combined Experimental and Quantum Chemical Study of CO_2 Adsorption in the Metal–Organic Framework CPO-27 with Different Metals. *Chemical Science* **2013**, *4*, pp. 3544–3556.

[254] *Emission Database for Global Atmospheric Research (EDGAR)*. Tech. rep. Access date: 28 July 2023. European Commission Joint Research Centre (JRC)/Netherlands Environmental Assessment Agency (PBL). URL: http://edgar.jrc.ec.europa.eu.

[255] Radosz, M., Hu, X., Krutkramelis, K. and Shen, Y. Flue-Gas Carbon Capture on Carbonaceous Sorbents: Toward a Low-Cost Multifunctional Carbon Filter for "Green" Energy Producers. *Industrial & Engineering Chemistry Research* **2008**, *47*, pp. 3783–3794.

[256] Yeon, J. S., Lee, W. R., Kim, N. W., Jo, H., Lee, H., Song, J. H., Lim, K. S., Kang, D. W., Seo, J. G., Moon, D., Wiers, B. and Hong, C. S. Homodiamine-Functionalized Metal-Organic Frameworks with a MOF-74-Type Extended Structure for Superior Selectivity of CO_2 over N_2. *Journal of Materials Chemistry A* **2015**, *3*, pp. 19177–19185.

[257] Zurrer, T., Wong, K., Horlyck, J., Lovell, E. C., Wright, J., Bedford, N. M., Han, Z., Liang, K., Scott, J. and Amal, R. Mixed-Metal MOF-74 Templated Catalysts for Efficient Carbon Dioxide Capture and Methanation. *Advanced Functional Materials* **2021**, *31*, p. 2007624.

[258] Choe, J. H., Kim, H. and Hong, C. S. MOF-74 Type Variants for CO_2 Capture. *Materials Chemistry Frontiers* **2021**, *5*, pp. 5172–5185.

[259] Meng, W., Zeng, Y., Liang, Z., Guo, W., Zhi, C., Wu, Y., Zhong, R., Qu, C. and Zou, R. Tuning Expanded Pores in Metal–Organic Frameworks for Selective Capture and Catalytic Conversion of Carbon Dioxide. *ChemSusChem* **2018**, *11*, pp. 3751–3757.

[260] Chen, C., Feng, X., Zhu, Q., Dong, R., Yang, R., Cheng, Y. and He, C. Microwave-Assisted Rapid Synthesis of Well-Shaped MOF-74 (Ni) for CO_2 Efficient Capture. *Inorganic Chemistry* **2019**, *58*, pp. 2717–2728.

[261] Newsome, D. S. The Water-Gas Shift Reaction. *Catalysis Reviews Science and Engineering* **1980**, *21*, pp. 275–318.

[262] Qiao, Z., Wang, N., Jiang, J. and Zhou, J. Design of Amine-Functionalized Metal-Organic Frameworks for CO_2 Separation: the More Amine, the Better? *Chemical Communications* **2016**, *52*, pp. 974–977.

[263] Ruthven, D. M., Farooq, S. and Knaebel, K. S. *Pressure Swing Adsorption*. John Wiley & Sons, 1996.

[264] Rochelle, G. T. Amine Scrubbing for CO_2 Capture. *Science* **2009**, *325*, pp. 1652–1654.

[265] Iulianelli, A., Pirola, C., Comazzi, A., Galli, F., Manenti, F. and Basile, A. *Membrane Reactors for Energy Applications and Basic Chemical Production. 1 - Water gas shift membrane reactors*. Ed. by A. Basile, L. Di Paola, F. l. Hai and V. Piemonte. Woodhead Publishing, 2015, pp. 3–29.

[266] Hiller, H., Reimert, R., Marschner, F., Renner, H.-J., Boll, W., Supp, E., Brejc, M., Liebner, W., Schaub, G., Hochgesand, G., Higman, C., Kalteier, P., Müller, W.-D., Kriebel, M., Schlichting, H., Tanz, H., Stönner, H.-M., Klein, H., Hilsebein, W., Gronemann, V., Zwiefelhofer, U., Albrecht, J., Cowper, C. J. and Driesen, H. E. *Ullmann's Encyclopedia of Industrial Chemistry. Gas Production*. 6th ed. John Wiley & Sons, Ltd, 2006.

[267] Herm, Z. R., Swisher, J. A., Smit, B., Krishna, R. and Long, J. R. Metal–Organic Frameworks as Adsorbents for Hydrogen Purification and Precombustion Carbon Dioxide Capture. *Journal of the American Chemical Society* **2011**, *133*, pp. 5664–5667.

[268] Aksu, G. O., Daglar, H., Altintas, C. and Keskin, S. Computational Selection of High-Performing Covalent Organic Frameworks for Adsorption and Membrane-Based CO_2/H_2 Separation. *Journal of Physical Chemistry C* **2020**, *124*, pp. 22577–22590.

[269] Dietzel, P. D. C., Georgiev, P. A., Eckert, J., Blom, R., Strässle, T. and Unruh, T. Interaction of Hydrogen with Accessible Metal Sites in the Metal-Organic Frameworks M_2(dhtp) (CPO-27-M; M = Ni, Co, Mg). *Chemical Communications* **2010**, *46*, pp. 4962–4964.

[270] Brown, C. M., Ramirez-Cuesta, A. J., Her, J.-H., Wheatley, P. S. and Morris, R. E. Structure and Spectroscopy of Hydrogen Adsorbed in a Nickel Metal–Organic Framework. *Chemical Physics* **2013**, *427*, pp. 3–8.

[271] Rosnes, M. H., Opitz, M., Frontzek, M., Lohstroh, W., Embs, J. P., Georgiev, P. A. and Dietzel, P. D. Intriguing Differences in Hydrogen Adsorption in CPO-27 Materials Induced by Metal Substitution. *Journal of Materials Chemistry A* **2015**, *3*, pp. 4827–4839.

[272] Wong-Foy, A. G., Matzger, A. J. and Yaghi, O. M. Exceptional H_2 Saturation Uptake in Microporous Metal-Organic Frameworks. *Journal of the American Chemical Society* **2006**, *128*, pp. 3494–3495.

[273] Kapelewski, M. T., Geier, S. J., Hudson, M. R., Stück, D., Mason, J. A., Nelson, J. N., Xiao, D. J., Hulvey, Z., Gilmour, E., FitzGerald, S. A., Head-Gordon, M., Brown, C. M. and Long, J. R. M_2(m-dobdc) (M = Mg, Mn, Fe, Co, Ni) Metal–Organic Frameworks Exhibiting Increased Charge Density and Enhanced H_2 Binding at the Open Metal Sites. *Journal of the American Chemical Society* **2014**, *136*, pp. 12119–12129.

[274] Märcz, M., Johnsen, R. E., Dietzel, P. D. and Fjellvåg, H. The Iron Member of the CPO-27 Coordination Polymer Series: Synthesis, Characterization, and Intriguing Redox Properties. *Microporous and Mesoporous Materials* **2012**, *157*, pp. 62–74.

[275] Queen, W. L., Bloch, E. D., Brown, C. M., Hudson, M. R., Mason, J. A., Murray, L. J., Ramirez-Cuesta, A. J., Peterson, V. K. and Long, J. R. Hydrogen Adsorption in the Metal–Organic Frameworks Fe_2(dobdc) and $Fe_2(O_2)$(dobdc). *Dalton Transactions* **2012**, *41*, pp. 4180–4187.

[276] Wasik, D. O., Martín-Calvo, A., Gutiérrez-Sevillano, J. J., Dubbeldam, D., Vlugt, T. J. H. and Calero, S. Enhancement of Formic Acid Production from Carbon Dioxide Hydrogenation Using Metal-Organic Frameworks: Monte Carlo Simulation Study. *Chemical Engineering Journal* **2023**, *467*, p. 143432.

[277] Becker, T. M., Dubbeldam, D., Lin, L.-C. and Vlugt, T. J. H. Investigating Polarization Effects of CO_2 Adsorption in Mg-MOF-74. *Journal of Computational Science* **2016**, *15*, pp. 86–94.

[278] Becker, T. M., Heinen, J., Dubbeldam, D., Lin, L.-C. and Vlugt, T. J. H. Polarizable Force Fields for CO_2 and CH_4 Adsorption in M-MOF-74. *Journal of Physical Chemistry C* **2017**, *121*, pp. 4659–4673.

[279] Becker, T. M., Lin, L.-C., Dubbeldam, D. and Vlugt, T. J. H. Polarizable Force Field for CO_2 in M-MOF-74 Derived from Quantum Mechanics. *Journal of Physical Chemistry C* **2018**, *122*, pp. 24488–24498.

[280] Mercado, R., Vlaisavljevich, B., Lin, L.-C., Lee, K., Lee, Y., Mason, J. A., Xiao, D. J., Gonzalez, M. I., Kapelewski, M. T., Neaton, J. B. and Smit, B. Force Field Development from Periodic Density Functional Theory Calculations for Gas Separation Applications Using Metal–Organic Frameworks. *Journal of Physical Chemistry C* **2016**, *120*, pp. 12590–12604.

[281] Lin, L.-C., Lee, K., Gagliardi, L., Neaton, J. B. and Smit, B. Force-Field Development from Electronic Structure Calculations with Periodic Boundary Conditions: Applications to Gaseous Adsorption and Transport in Metal–Organic Frameworks. *Journal of Chemical Theory and Computation* **2014**, *10*, pp. 1477–1488.

[282] Buch, V. Path Integral Simulations of Mixed *para*-D_2 and *ortho*-D_2 Clusters: The Orientational Effects. *Journal of Chemical Physics* **1994**, *100*, pp. 7610–7629.

[283] Belof, J. L., Stern, A. C. and Space, B. An Accurate and Transferable Intermolecular Diatomic Hydrogen Potential for Condensed Phase Simulation. *Journal of Chemical Theory and Computation* **2008**, *4*, pp. 1332–1337.

[284] Harris, J. G. and Yung, K. H. Carbon Dioxide's Liquid-Vapor Coexistence Curve And Critical Properties as Predicted by a Simple Molecular Model. *Journal of Physical Chemistry* **1995**, *99*, pp. 12021–12024.

[285] Wilmer, C. E. and Snurr, R. Q. Towards Rapid Computational Screening of Metal-Organic Frameworks for Carbon Dioxide Capture: Calculation of Framework Charges via Charge Equilibration. *Chemical Engineering Journal* **2011**, *171*, pp. 775–781.

[286] Atkins, P., De Paula, J. and Keeler, J. *Atkins' Physical Chemistry*. 12th ed. Oxford University Press, 2023.

[287] Feynman, R. P., Hibbs, A. R. and Styer, D. F. *Quantum Mechanics and Path Integrals*. Courier Corporation, 2010.

[288] Bhatia, S. K. and Myers, A. L. Optimum Conditions for Adsorptive Storage. *Langmuir* **2006**, *22*, pp. 1688–1700.

[289] Deeg, K. S., Gutiérrez-Sevillano, J. J., Bueno-Pérez, R., Parra, J. B., Ania, C. O., Doblaré, M. and Calero, S. Insights on the Molecular Mechanisms of Hydrogen Adsorption in Zeolites. *Journal of Physical Chemistry C* **2013**, *117*, pp. 14374–14380.

[290] Kumar, A. V. A., Jobic, H. and Bhatia, S. K. Quantum Effects on Adsorption and Diffusion of Hydrogen and Deuterium in Microporous Materials. *Journal of Physical Chemistry B* **2006**, *110*, pp. 16666–16671.

[291] Sharma, S., Balestra, S. R. G., Baur, R., Agarwal, U., Zuidema, E., Rigutto, M. S., Calero, S., Vlugt, T. J. H. and Dubbeldam, D. RUPTURA: Simulation Code for Breakthrough, Ideal Adsorption Solution Theory Computations, and Fitting of Isotherm Models. *Molecular Simulation* **2023**, *49*, pp. 893–953.

[292] Langmuir, I. The Adsorption of Gases on Plane Surfaces of Glass, Mica and Platinum. *Journal of the American Chemical society* **1918**, *40*, pp. 1361–1403.

[293] Caldwell, S. J., Al-Duri, B., Sun, N., Sun, C.-g., Snape, C. E., Li, K. and Wood, J. Carbon Dioxide Separation from Nitrogen/Hydrogen Mixtures over Activated Carbon Beads: Adsorption Isotherms and Breakthrough Studies. *Energy & Fuels* **2015**, *29*, pp. 3796–3807.

[294] Myers, A. L. and Prausnitz, J. M. Thermodynamics of Mixed-Gas Adsorption. *AIChE Journal* **1965**, *11*, pp. 121–127.

[295] Luna-Triguero, A., Vicent-Luna, J. M., Madero-Castro, R. M., Gómez-Álvarez, P. and Calero, S. Acetylene Storage and Separation Using Metal–Organic Frameworks with Open Metal Sites. *ACS Applied Materials & Interfaces* **2019**, *11*, pp. 31499–31507.

[296] Li, W., Chuah, C. Y., Yang, Y. and Bae, T.-H. Nanocomposites Formed by In Situ Growth of NiDOBDC Nanoparticles on Graphene Oxide Sheets for Enhanced CO_2 and H_2 Storage. *Microporous and Mesoporous Materials* **2018**, *265*, pp. 35–42.

[297] Dietzel, P. D. C., Johnsen, R. E., Fjellvåg, H., Bordiga, S., Groppo, E., Chavan, S. and Blom, R. Adsorption Properties and Structure of CO_2 Adsorbed on Open Coordination Sites of Metal–Organic Framework Ni_2(dhtp) from Gas Adsorption, IR Spectroscopy and X-ray Diffraction. *Chemical Communications* **2008**, pp. 5125–5127.

[298] Chen, Y., Li, S., Pei, X., Zhou, J., Feng, X., Zhang, S., Cheng, Y., Li, H., Han, R. and Wang, B. A Solvent-Free Hot-Pressing Method for Preparing Metal–Organic-Framework Coatings. *Angewandte Chemie International Edition* **2016**, *55*, pp. 3419–3423.

[299] Chen, D.-L., Shang, H., Zhu, W. and Krishna, R. Transient breakthroughs of CO_2/CH_4 and C_3H_6/C_3H_8 mixtures in fixed beds packed with Ni-MOF-74. *Chemical Engineering Science* **2014**, *117*, pp. 407–415.

[300] Pu, S., Wang, J., Li, L., Zhang, Z., Bao, Z., Yang, Q., Yang, Y., Xing, H. and Ren, Q. Performance Comparison of Metal–Organic Framework Extrudates and Commercial Zeolite for Ethylene/Ethane Separation. *Industrial & Engineering Chemistry Research* **2018**, *57*, pp. 1645–1654.

[301] Al-Naddaf, Q., Thakkar, H. and Rezaei, F. Novel Zeolite-5A@MOF-74 Composite Adsorbents with Core–Shell Structure for H_2 Purification. *ACS Applied Materials & Interfaces* **2018**, *10*, pp. 29656–29666.

[302] Wang, N., Mundstock, A., Liu, Y., Huang, A. and Caro, J. Amine-modified Mg-MOF-74/CPO-27-Mg membrane with enhanced H_2/CO_2 separation. *Chemical Engineering Science* **2015**, *124*, pp. 27–36.

[303] Wasik, D. O., Vicent-Luna, J. M., Luna-Triguero, A., Dubbeldam, D., Vlugt, T. J. H. and Calero, S. The Impact of Metal Centers in the M-MOF-74 Series on Carbon Dioxide and Hydrogen Separation. *Separation and Purification Technology* **2024**, *339*, p. 126539.

[304] Vlugt, T. J. H., García-Pérez, E., Dubbeldam, D., Ban, S. and Calero, S. Computing the Heat of Adsorption using Molecular Simulations: The Effect of Strong Coulombic Interactions. *Journal of Chemical Theory and Computation* **2008**, *4*, pp. 1107–1118.

[305] Giannozzi, P., Baroni, S., Bonini, N., Calandra, M., Car, R., Cavazzoni, C., Ceresoli, D., Chiarotti, G. L., Cococcioni, M., Dabo, I. and al., et. QUANTUM ESPRESSO: A Modular and Open-Source Software Project for Quantum Simulations of Materials. *Journal of Physics: Condensed Matter* **2009**, *21*, p. 395502.

[306] Perdew, J. P., Burke, K. and Ernzerhof, M. Generalized Gradient Approximation Made Simple. *Physical Review Letters* **1996**, *77*, p. 3865.

[307] Johnson, E. R. and Becke, A. D. A Post-Hartree-Fock Model of Intermolecular Interactions: Inclusion of Higher-Order Corrections. *Journal of Chemical Physics* **2006**, *124*, p. 174104.

[308] Monkhorst, H. J. and Pack, J. D. Special Points for Brillouin-Zone Integrations. *Physical Review B* **1976**, *13*, p. 5188.

[309] Tan, K., Zuluaga, S., Gong, Q., Canepa, P., Wang, H., Li, J., Chabal, Y. J. and Thonhauser, T. Water Reaction Mechanism in Metal Organic Frameworks with Coordinatively Unsaturated Metal Ions: MOF-74. *Chemistry of Materials* **2014**, *26*, pp. 6886–6895.

[310] González-Galán, C., Balestra, S. R. G., Luna-Triguero, A., Madero-Castro, R. M., Zaderenko, A. P. and Calero, S. Effect of Diol Isomer/Water Mixtures on the Stability of Zn-MOF-74. *Dalton Transactions* **2021**, *50*, pp. 1808–1815.

[311] Tapiador, J., Leo, P., Rodríguez-Diéguez, A., Choquesillo-Lazarte, D., Calleja, G. and Orcajo, G. A Novel Zn-based-MOF for Efficient CO_2 Adsorption and Conversion under Mild Conditions. *Catalysis Today* **2022**, *390-391*, pp. 230–236.

[312] Gao, Z., Liang, L., Zhang, X., Xu, P. and Sun, J. Facile One-Pot Synthesis of Zn/Mg-MOF-74 with Unsaturated Coordination Metal Centers for Efficient CO_2 Adsorption and Conversion to Cyclic Carbonates. *ACS Applied Materials & Interfaces* **2021**, *13*, pp. 61334–61345.

[313] Zuluaga, S., Fuentes-Fernandez, E. M. A., Tan, K., Arter, C. A., Li, J., Chabal, Y. J. and Thonhauser, T. Chemistry in Confined Spaces: Reactivity of the Zn-MOF-74 Channels. *Journal of Materials Chemistry A* **2016**, *4*, pp. 13176–13182.

[314] Barakat, A., Lasala, S., Arpentinier, P. and Jaubert, J.-N. The Original and Impactful Exploitation of Chemical Energy in Heat Pumps. *Chemical Engineering Journal Advances* **2022**, *12*, p. 100400.

[315] Kosmadakis, G. Estimating the Potential of Industrial (High-Temperature) Heat Pumps for Exploiting Waste Heat in EU Industries. *Applied Thermal Engineering* **2019**, *156*, pp. 287–298.

[316] van de Bor, D., Ferreira, C. I. and Kiss, A. A. Low Grade Waste Heat Recovery Using Heat Pumps and Power Cycles. *Energy* **2015**, *89*, pp. 864–873.

[317] Khanlari, A., Sözen, A., Sahin, B., Nicola, G. D. and Afshari, F. Experimental Investigation on Using Building Shower Drain Water as a Heat Source for Heat Pump Systems. *Energy Sources, Part A: Recovery, Utilization, and Environmental Effects* **2020**, pp. 1–13.

[318] *Heat Pumps, Paris. 2021.* Tech. rep. Access date: 5 June 2024. IEA, URL: https://www.iea.org/energy-system/buildings/heat-pumps.

[319] Forman, C., Muritala, I. K., Pardemann, R. and Meyer, B. Estimating the Global Waste Heat Potential. *Renewable and Sustainable Energy Reviews* **2016**, *57*, pp. 1568–1579.

[320] Zhang, K., Shen, Y. and Duwig, C. Identification of Heat Transfer Intensification Mechanism by Reversible N_2O_4 Decomposition Using Direct Numerical Simulation. *International Journal of Heat and Mass Transfer* **2022**, *182*, p. 121946.

[321] Li, C. and Wang, H. Power Cycles for Waste Heat Recovery from Medium to High Temperature Flue Gas Sources – from a View of Thermodynamic Optimization. *Applied Energy* **2016**, *180*, pp. 707–721.

[322] Xu, Z., Wang, R. and Yang, C. Perspectives for Low-Temperature Waste Heat Recovery. *Energy* **2019**, *176*, pp. 1037–1043.

[323] Lasala, S., Privat, R., Herbinet, O., Arpentinier, P., Bonalumi, D. and Jaubert, J.-N. Thermo-Chemical Engines: Unexploited High-Potential Energy Converters. *Energy Conversion and Management* **2021**, *229*, p. 113685.

[324] Lasala, S., Samukov, K., Polat, H. M., Lachet, V., Herbinet, O., Privat, R., Jaubert, J.-N., Moultos, O. A., De Ras, K. and Vlugt, T. J. H. Application of Thermodynamics at Different Scales to Describe the Behaviour of Fast Reacting Binary Mixtures in Vapour-Liquid Equilibrium. *Chemical Engineering Journal* **2024**, *483*, p. 148961.

[325] Barakat, A., Lasala, S., Arpentinier, P., Tobaly, P. and Jaubert, J.-N. Understanding the Thermodynamic Effects of Chemically Reactive Working Fluids in the Stirling Engine. *Energy Conversion and Management: X* **2024**, *22*, p. 100573.

[326] Krasin, A. and Nesterenko, V. Dissociating Gases: a New Class of Coolants and Working Substances for Large Power Plants. *Atomic Energy Review* **1971**, *9*, pp. 177–194.

[327] Huang, H. M. and Govind, R. Use of Dissociating Gases in Brayton Cycle Space Power Systems. *Industrial & Engineering Chemistry Research* **1988**, *27*, pp. 803–810.

[328] Sorokin, A. Dissociating Nitrogen Tetroxide (N_2O_4) as a Working Fluid in Thermodynamic Cycles. *Nuclear Science and Engineering* **1979**, *72*, pp. 330–346.

[329] Stochl, R. J. *Potential Performance Improvement Using a Reacting Gas (Nitrogin Tetroxide) as the Working Fluid in a Closed Brayton Cycle*. Vol. 1060. US Department of Energy, 1979.

[330] Binotti, M., Invernizzi, C. M., Iora, P. and Manzolini, G. Dinitrogen Tetroxide and Carbon Dioxide Mixtures as Working Fluids in Solar Tower Plants. *Solar Energy* **2019**, *181*, pp. 203–213.

[331] Belkadi, A., Llovell, F., Gerbaud, V. and Vega, L. Modeling the Vapor–Liquid Equilibrium and Association of Nitrogen Dioxide/Dinitrogen Tetroxide and Its Mixtures with Carbon Dioxide. *Fluid Phase Equilibria* **2008**, *266*, pp. 154–163.

[332] Souza, L. E. S. de and Deiters, U. K. Modeling of the N_2O_4–NO_2 Reacting System. *Physical Chemistry Chemical Physics* **2000**, *2*, pp. 5606–5613.

[333] Manzolini, G., Binotti, M., Bonalumi, D., Invernizzi, C. and Iora, P. CO_2 Mixtures as Innovative Working Fluid in Power Cycles Applied to Solar Plants. Techno-Economic Assessment. *Solar Energy* **2019**, *181*, pp. 530–544.

[334] Seshadri, D. N., Viswanath, D. S. and Kuloor, N. R. Thermodynamic Properties of the System $N_2O_4 \rightleftharpoons 2NO_2 \rightleftharpoons 2NO + O_2$. *AIChE Journal* **1970**, *16*, pp. 420–425.

[335] Stai, D. F., Bizjak, F. and Stephanou, S. E. Thermodynamic Properties of Nitrogen Tetroxide. *Journal of Spacecraft and Rockets* **1965**, *2*, pp. 742–745.

[336] Bourasseau, E., Lachet, V., Desbiens, N., Maillet, J.-B., Teuler, J.-M. and Ungerer, P. Thermodynamic Behavior of the CO_2 + NO_2/N_2O_4 Mixture: A Monte Carlo Simulation Study. *Journal of Physical Chemistry B* **2008**, *112*, pp. 15783–15792.

[337] Lasala, S. Reactive Fluids for Intensified Thermal Energy Conversion. *Project Repository Journal* **2022**, *13*, pp. 102–105.

[338] Lasala, S. *ERC-REACHER*. access date: 5 July 2024. 2022. URL: `https://www.univ-lorraine.fr/erc-reacher/`.

[339] Slavchov, R. I., Novev, J. K., Mosbach, S. and Kraft, M. Vapor Pressure and Heat of Vaporization of Molecules That Associate in the Gas Phase. *Industrial & Engineering Chemistry Research* **2018**, *57*, pp. 5722–5731.

[340] Chocholoušová, J., Vacek, J. and Hobza, P. Potential Energy and Free Energy Surfaces of the Formic Acid Dimer: Correlated Ab Initio Calculations and Molecular Dynamics Simulations. *Physical Chemistry Chemical Physics* **2002**, *4*, pp. 2119–2122.

[341] Wasik, D. O., Vicent-Luna, J. M., Rezaie, S., Luna-Triguero, A., Vlugt, T. J. H. and Calero, S. The Impact of Metal Centers in the M-MOF-74 Series on Formic Acid Production. *ACS Applied Materials & Interfaces* **2024**, *16*, pp. 45006–45019.

[342] Hermida Ramón, J. M. and Rìós, M. A. A New Intermolecular Polarizable Potential for cis-Formic Acid. Introduction of Many-Body Interactions in Condensed Phases. *Chemical Physics* **1999**, *250*, pp. 155–169.

[343] Chameides, W. L. and Davis, D. D. Aqueous-Phase Source of Formic Acid in Clouds. *Nature* **1983**, *304*, pp. 427–429.

[344] Wang, B., Hou, H. and Gu, Y. New Mechanism for the Catalyzed Thermal Decomposition of Formic Acid. *Journal of Physical Chemistry A* **2000**, *104*, pp. 10526–10528.

[345] Turner, C. H. Monte Carlo Simulation of Formic Acid Dimerization in a Carbon Dioxide Solvent. *Journal of Physical Chemistry B* **2004**, *108*, pp. 11716–11721.

[346] Farfán, P., Echeverri, A., Diaz, E., Tapia, J. D., Gómez, S. and Restrepo, A. Dimers of Formic Acid: Structures, Stability, and Double Proton Transfer. *Journal of Chemical Physics* **2017**, *147*, p. 044312.

[347] Gantenberg, M., Halupka, M. and Sander, W. Dimerization of Formic Acid-An Example of a "Noncovalent" Reaction Mechanism. *Chemistry – A European Journal* **2000**, *6*, pp. 1865–1869.

[348] Brinkmann, N. R., Tschumper, G. S., Yan, G. and Schaefer, H. F. An Alternative Mechanism for the Dimerization of Formic Acid. *Journal of Physical Chemistry A* **2003**, *107*, pp. 10208–10216.

[349] Taylor, M. D. and Bruton, J. The Vapor Phase Dissociation of Some Carboxylic Acids. II. Formic and Propionic Acids[1,2]. *Journal of the American Chemical Society* **1952**, *74*, pp. 4151–4152.

[350] Nahringbauer, I. A Reinvestigation of the Structure of Formic Acid (at 98 K). *Acta Crystallographica Section B* **1978**, *34*, pp. 315–318.

[351] Berkovitch-Yellin, Z. and Leiserowitz, L. Atom-Atom Potential Analysis of the Packing Characteristics of Carboxylic Acids. A Study Based on Experimental Electron-Density Distributions. *Journal of the American Chemical Society* **1982**, *104*, pp. 4052–4064.

[352] Bhargava, B. L., Yasaka, Y. and Klein, M. L. Hydrogen Evolution from Formic Acid in an Ionic Liquid Solvent: A Mechanistic Study by ab Initio Molecular Dynamics. *Journal of Physical Chemistry B* **2011**, *115*, pp. 14136–14140.

[353] Weng, L., Chen, C., Zuo, J. and Li, W. Molecular Dynamics Study of Effects of Temperature and Concentration on Hydrogen-Bond Abilities of Ethylene Glycol and Glycerol: Implications for Cryopreservation. *Journal of Physical Chemistry A* **2011**, *115*, pp. 4729–4737.

[354] Allan, D. R. and Clark, S. J. Impeded Dimer Formation in the High-Pressure Crystal Structure of Formic Acid. *Physical Review Letters* **1999**, *82*, pp. 3464–3467.

[355] P. Jedlovszky I. Bakó, G. P. and Dore, J. Structural Investigation of Liquid Formic Acid. *Molecular Physics* **1995**, *86*, pp. 87–105.

[356] Nasr, S., Bellissent-Funel, M.-C. and Cortès, R. X-ray and Neutron Scattering Studies of Liquid Formic Acid DCOOD at Various Temperatures and Under Pressure. *Journal of Chemical Physics* **1999**, *110*, pp. 10945–10952.

[357] Bellamy, L., Lake, R. and Pace, R. Hydrogen Bonding in Carboxylic Acids—II. Monocarboxylic Acids. *Spectrochimica Acta* **1963**, *19*, pp. 443–449.

[358] Jedlovszky, P. and Turi, L. A New Five-Site Pair Potential for Formic Acid in Liquid Simulations. *Journal of Physical Chemistry A* **1997**, *101*, pp. 2662–2665.

[359] Vlugt, T. J. H., van der Eerden, J. P. J. M., Dijkstra, M., Smit, B. and Frenkel, D. *Introduction to Molecular Simulation and Statistical Thermodynamics*. Delft, The Netherlands: Delft University of Technology, 2008. URL: `https://thijsvlugt.github.io/website/imsst/`.

[360] Torrie, G. and Valleau, J. Nonphysical Sampling Distributions in Monte Carlo Free-Energy Estimation: Umbrella Sampling. *Journal of Computational Physics* **1977**, *23*, pp. 187–199.

[361] You, W., Tang, Z. and Chang, C.-e. A. Potential Mean Force from Umbrella Sampling Simulations: What Can We Learn and What Is Missed? *Journal of Chemical Theory and Computation* **2019**, *15*, pp. 2433–2443.

[362] Bansal, N., Zheng, Z., Cerutti, D. S. and Merz, K. M. On the Fly Estimation of Host–Guest Binding Free Energies Using the Movable Type Method: Participation in the SAMPL5 Blind Challenge. *Journal of Computer-Aided Molecular Design* **2017**, *31*, pp. 47–60.

[363] Yin, J., Henriksen, N. M., Slochower, D. R., Shirts, M. R., Chiu, M. W., Mobley, D. L. and Gilson, M. K. Overview of the SAMPL5 Host–Guest Challenge: Are We Doing Better? *Journal of Computer-Aided Molecular Design* **2017**, *31*, pp. 1–19.

[364] Sun, H., Tian, S., Zhou, S., Li, Y., Li, D., Xu, L., Shen, M., Pan, P. and Hou, T. Revealing the Favorable Dissociation Pathway of Type II Kinase Inhibitors via Enhanced Sampling Simulations and Two-End-State Calculations. *Scientific Reports* **2015**, *5*, p. 8457.

[365] Zhou, J.-K., Yang, D.-Y. and Sheu, S.-Y. The Molecular Mechanism of Ligand Unbinding from the Human Telomeric G-Quadruplex by Steered Molecular Dynamics and Umbrella Sampling Simulations. *Physical Chemistry Chemical Physics* **2015**, *17*, pp. 12857–12869.

[366] Wang, J. and Tingjun, H. Application of Molecular Dynamics Simulations in Molecular Property Prediction I: Density and Heat of Vaporization. *J Chem Theory Comput* **2011**, *7*, pp. 2151–2165.

[367] Hill, T. L. Thermodynamics of Small Systems. *Journal of Chemical Physics* **1962**, *36*, pp. 3182–3197.

[368] Grenzheuser, P. and Gmehling, J. An Equation of State for the Description of Phase Equilibria and Caloric Quantities on the Basis of the "Chemical Theory". *Fluid Phase Equilibria* **1986**, *25*, pp. 1–29.

[369] J. Gmehling, ed. *Chemical Thermodynamics for Process Simulation*. 2nd ed. Weinheim: Wiley-VCH, 2019.

[370] Lasala, S., Chiesa, P., Privat, R. and Jaubert, J.-N. VLE Properties of CO_2 – Based Binary Systems Containing N_2, O_2 and Ar: Experimental Measurements and Modelling Results with Advanced Cubic Equations of State. *Fluid Phase Equilibria* **2016**, *428*, pp. 18–31.

[371] Peng, D.-Y. and Robinson, D. *The Characterization of the Heptanes and Heavier Fractions for the GPA Peng-Robinson Programs*. Tech. rep. Gas Processors Association, 1978.

[372] Miyoshi, A. *GPOP Software*. 2002. URL: `http://akrmys.com/gpop/`.

[373] DECHEMA. *DIPPR 801 Database*. 2023. URL: `https://dechema.de/en/dippr801.html`.

[374] Scott, R. L. Models for Phase Equilibria in Fluid Mixtures. *Accounts of Chemical Research* **1987**, *20*, pp. 97–107.

[375] Konynenburg, P. H. van. "Critical Lines and Phase Equilibria in Binary Mixtures". PhD thesis. USA: University of California, Los Angeles, 1968.

[376] Konynenburg, P. H. van and Scott, R. L. Critical Lines and Phase Equilibriums in Binary Van der Waals Mixtures. *Philosophical Transactions of the Royal Society of London, Series A: Mathematical, Physical and Engineering Sciences* **1980**, *298*, pp. 495–540.

[377] Peneloux, A. and Rauzy, E. A Consistent Correction for Redlich-Kwong-Soave Volumes. *Fluid Phase Equilibria* **1982**, *8*, pp. 7–23.

[378] Rahbari, A. "Thermodynamics of Industrially Relevant Systems: Method Development and Applications". PhD thesis. Delft, The Netherlands: Delft University of Technology, 2020.

[379] Humphrey, W., Dalke, A. and Schulten, K. VMD: Visual Molecular Dynamics. *Journal of Molecular Graphics* **1996**, *14*, pp. 33–38.

[380] McRee, D. E. *Practical Protein Crystallography. 3 - Computational Techniques*. Second Edition. San Diego: Academic Press, 1999, p. 91.